New approaches for the real-time optimization of process systems under uncertainty

by

Gabriel David Patrón

A thesis
presented to the University of Waterloo
in fulfilment of the
thesis requirements for the degree of
Doctor of Philosophy
in
Chemical Engineering

Waterloo, Ontario, Canada, 2023

Examining Committee Membership

The following served on the Examining Committee for this thesis. The decision of the Examining Committee is by majority vote.

External examiner	Prashant Mhaskar Professor Chemical Engineering, McMaster University
Internal-external examiner	Houra Mahmoudzadeh Assistant Professor Management Sciences, University of Waterloo
Internal examiners	Hector Budman Professor Chemical Engineering, University of Waterloo
	Alexander Penlidis Professor Chemical Engineering, University of Waterloo
Supervisor	Luis Ricardez-Sandoval Associate Professor Chemical Engineering, University of Waterloo

Author's Declaration

This thesis consists of material all of which I authored or co-authored: see Statement of Contributions included in the thesis. This is a true copy of the thesis, including any required final revisions, as accepted by my examiners.

I understand that my thesis may be made electronically available to the public.

Statement of Contributions

All chapters herein are entirely written by me. My supervisor, Luis Ricardez-Sandoval, provided editing and feedback.

The results in Chapter 3 have been published in *Fuel*. Patrón, G.D., Ricardez-Sandoval, L.A. (2020). A robust nonlinear model predictive controller for a post-combustion CO_2 capture absorber unit. *Fuel*, 265, 116932. https://doi.org/10.1016/j.fuel.2019.116932.

Preliminary results for Chapter 4 can be found in Appendix B; these have been published in proceeding to the 21st IFAC world congress *IFAC-PapersOnline*. Patrón, G.D., Ricardez-Sandoval, L.A. (2020). Real-Time Optimization and Nonlinear Model Predictive Control for a Post-Combustion Carbon Capture Absorber. *IFAC-PapersOnline*, 53(2), 11595–11600. https://doi.org/10.1016/j.ifacol.2020.12.639.

The main results in Chapter 4 have been published in *Applied Energy.* Patrón, G.D., Ricardez-Sandoval, L.A. (2022). An integrated real-time optimization, control, and estimation scheme for post-combustion CO_2 capture. *Appl. Energy*, 308, 118302. https://doi.org/10.1016/j.apenergy.2021.118302.

The results in Chapter 5 have been published in *Industrial & Engineering Chemistry Research.* Patrón, G.D., Ricardez-Sandoval, L.A. (2022). Low-Variance Parameter Estimation Approach for Real-Time Optimization of Noisy Process Systems. *Ind. Eng. Chem. Res.*, 61(45), 16780–16798. https://doi.org/10.1021/acs.iecr.2c02897.

The results in Chapter 6 have been submitted to a journal and are under review.

The results in Chapter 7 have been submitted to a journal and are under review.

The results in Appendix E have been accepted for presentation at the *2023 IFAC World Congress* and will appear in proceeding to the 22nd IFAC world congress *IFAC-PapersOnline* under the title: Economic Model Predictive Control of a Recirculating Aquaculture System.

Abstract

In the process industry, the economical operation of systems is of utmost importance for stakeholders to remain competitive. Moreover, economic incentives can be used to drive the development of sustainable processes, which must be deployed to ensure continued human and ecological welfare. In the process systems engineering paradigm, model predictive control (MPC) and real-time optimization (RTO) are methods used to achieve operational optimality; however, both methods are subject to uncertainty, which can adversely affect their performance. Along with the challenges of uncertainty, formulations of economic optimization problems are largely problem-specific as process utilities and products vary significantly by application; thus, many nascent processes have not received a tailored economic optimization treatment.

In this thesis, the focus is on avenues of economic optimization under uncertainty, namely, the two-step RTO method, which updates process models via parameters; and the modifier adaptation (MA) method, which updates process models via error and gradient correction. In the case of parametric model uncertainty, the two-step RTO method is used. The parameter estimation (PE) step that accompanies RTO requires plant measurements that are often noisy, which can cause the propagation of noise to the parameter estimates and result in poor RTO performance. In the present work, a noise-abatement scheme is proposed such that high-fidelity parameter estimates are used to update a process model for economic optimization. This is achieved through parameter estimate bootstrapping to compute bounds and determine the measurement-set that results in the lowest parameter variation; thus, the scheme is dubbed low-variance parameter estimation (lv-PE). This method is shown to result in improved process economics through truer set points and reduced dynamic behaviour.

In the case of structural model mismatch (i.e., unmodelled phenomena), the MA approach is used, whereby gradient modifier (i.e., correction) terms must be recursively estimated until convergence. These modifier terms require plant perturbations to be performed, which incite time-consuming plant dynamics that delay operating point updates. In cases with frequent disturbances, MA may have poor performance well as there is limited time to refine the modifiers. Herein, a partial modifier adaptation (pMA) method is proposed, which selects a subset of modifications to be made, thus reducing the number of necessary perturbations. Through this reduced experimental burden, the operating point refinement process is accelerated resulting in quicker convergence to advantageous operating points. Additionally, constraint satisfaction during this refinement process can also result in poor performance via wasted below-specification products. Accordingly, the pMA method also includes an adjustment step that can drive the system to constraint-satisfying regions at each iteration. The pMA method is shown to economically outperform both the standard MA method as well as a related directional MA method in cases with frequent periodic disturbances.

The economic optimization methods described above are implemented in novel processes to improve their economics, which can incite further technological uptake. Post-combustion carbon capture (PCC) is the most advanced carbon capture technology as it has been investigated extensively. PCC takes industrial flue gases and separates the carbon dioxide for later repurposing or storage. Most PCC operating schemes make decisions using simplified models since a mechanistic PCC model is large and difficult to solve. To this end, this thesis provides the first robust MPC that can address uncertainty in PCC with a mechanistic model. The advantage of the mechanistic model in robust optimal control is that it allows for a precise treatment of uncertainties in phenomenological parameters. Using the multi-

scenario approach, discrete realizations of the uncertain parameters inside a given uncertainty region can be incorporated into the controller to produce control actions that result in a robust operation in closed-loop. In the case of jointly uncertainty activity coefficients and flue gas flowrates, the proposed robust MPC is shown to lead to improved performance with respect to a nominal controller (i.e., one that does not hedge against uncertainty) under various operational scenarios.

In addition to the PCC robust control problem, the mechanistic model is used for economic optimization and state estimation via RTO and moving horizon estimation (MHE) layers respectively. While the former computes economical set points, the latter uses few measurements to compute the full system state, which is necessary for the controller that uses a mechanistic model. These layers are integrated to operate the system economically via a new economic function that accounts for the most significant economic aspects of PCC, including the carbon economy, energy, chemical, and utility costs. A new proposed MPC layer is novel in its ability to enable flexible control of the plant by manipulating fresh material streams to impact CO_2 capture and the MHE layer is the first to provide accurate system estimates to the controller with realistically accessible measurements. A joint MPC-MHE-RTO scheme is deployed for PCC, which is shown to lead to more economical steady-state operation compared to constant set point counterfactuals under cofiring, diurnal operation, and price variation scenarios. The lv-PE scheme is also deployed for the PCC system where it is found to improve set point economics with respect to traditional PE methods. The improvements are observed to occur through reduced emissions and more efficient energy used, thus having environmental co-benefits. Moreover, the lv-PE algorithm is used for uncertainty quantification to develop a robust RTO that leads to more conservative set points (i.e., less economic improvement) but lower set point variation (i.e., less control burden).

The methodologies developed in this PhD thesis provide improvements in efficacy as well as applicability of online economic optimization in engineering applications, where uncertainty is often present. These can be deployed by both academic as well as industrial practitioners that wish to improve the economic performance on their processes.

Acknowledgements

I would like to thank the following people for their support in the past four years:

1. My supervisor, Luis Ricardez-Sandoval, who gave me the opportunity to work with him and has provided me the freedom to pursue my research interests. Your constant feedback has pushed me to become a better researcher and a more thoughtful person.
2. Steph and the Lettuce Club: Camilo, Dora, Natalie, Neha, and Ross. You have provided me with emotional support, a sounding board for my frustrations, distraction when needed, and constant encouragement.
3. Mi familia extendida de tíos y primos. Mis abuelos Alberto, Esperanza, Esperanza, and Luis. Su amor incondicional me hace sentir invencible.
4. Mi madre y padre, Marcela and Gabriel, quienes se mudaron a Canadá para darme un medioambiente en el que yo pudiera prosperar. Esto sería imposible sin ustedes.

Table of Contents

List of Figures

List of Tables

Nomenclature

Abbreviations

AC	Arrival Cost
CCS	Carbon Capture and Storage
CSTR	Continuously Stirred Tank Reactor
CV	Controlled Variable
dMA	Directional modifier adaptation
DR	Data Reconciliation
DAE	Differential Algebraic Equations
DV	Disturbance Variable
EKF	Extended Kalman Filter
EMPC	Economic Model Predictive Control
FDA	Finite difference approximation
GED	Gross Error Detection
HVAC	Heating, Ventilation and Air Conditioning
IC	Information Content
ISE	Integral Squared Error
KF	Kalman Filter
KKT	Karush-Kuhn-Tucker
lv	Low Variance
MA	Modifier Adaptation
MEA	Monoethanolamine
MHE	Moving Horizon Estimation
MPC	Model Predictive Control
MV	Manipulated Variable
NLP	Non-Linear Problem
PCC	Post-Combustion Capture
PE	Parameter Estimation
PID	Proportional, Integral, Derivative
pMA	Partial Modifier Adaptation
RAS	Recirculating Aquaculture System
RMPC	Robust Model Predictive Control
SS	Steady State
RRTO	Robust real-time optimization
RTO	Real-Time Optimization
SMPC	Stochastic Model Predictive Control
SSE	Sum of Squared Errors

W-O	Williams-Otto

General formulation symbols

$\mathbf{1}$	Matrix of ones
C	Control horizon
$\boldsymbol{d}$	Disturbance variables
$\overline{\boldsymbol{d}}$	Sample-averaged disturbances
$\boldsymbol{f}$	Mechanistic model
$\boldsymbol{g}$	Inequality constraints
$\boldsymbol{h}$	Observation model
$\boldsymbol{I}$	Identity matrix
$\boldsymbol{J}$	Jacobian matrix
N	Estimation window
P	Prediction horizon
$\boldsymbol{P}$	Weighting matrix
$\boldsymbol{Q}$	Weighting matrix
$\boldsymbol{R}$	Weighting matrix
$\boldsymbol{S}$	Total number of scenarios
t	Time
$\boldsymbol{u}$	Manipulated variables
$\overline{\boldsymbol{u}}$	Sample-averaged manipulated variables
$\boldsymbol{x}$	States
$\hat{\boldsymbol{x}}$	State estimates/predictions
$\boldsymbol{y}$	Controlled variables
$\hat{\boldsymbol{y}}$	Controlled variable predictions
$\boldsymbol{z}$	Measurements
$\hat{\boldsymbol{z}}$	Measurement prediction
$\bar{\boldsymbol{z}}$	Sample-averaged measurements
$\boldsymbol{v}$	Measurement noise
$\boldsymbol{\varphi}$	Arrival cost
$\boldsymbol{w}$	Process noise

lv-PE symbols

$\boldsymbol{K}$	Parameter estimation covariance matrix
$\boldsymbol{z_0}$	Initial measurement set
$\boldsymbol{\zeta}$	Partial measurement vector
$\hat{\boldsymbol{\zeta}}$	Partial measurement predictions
$\bar{\boldsymbol{\zeta}}$	Sample-averaged partial measurements

$\boldsymbol{\kappa}$	Partial covariance matrix
$\boldsymbol{\mu}$	Inequality KKT multipliers
$\boldsymbol{\lambda}$	Equality KKT multipliers
$\boldsymbol{\sigma}$	Standard deviations
ς	Aggregate information content

lv-PE robust RTO symbols

$\boldsymbol{P}$	Economic uncertainties
τ	t-value

pMA symbols

$\%\boldsymbol{I}$	Percent improvement
a_{max}	Maximum adjustment iterations
$\boldsymbol{A}$	Active constraint indicator matrix
B	Computational budget
m	Mass of material processed
P_{prod}	Process economics per unit mass
R	Total process economics
t_{viol}	Cumulative time violating constraints
U	Ordered set of inputs
$\boldsymbol{U}$	dMA direction matrix
$\boldsymbol{v}$	pMA modified input vector
V	Set of inputs used for modification
$\boldsymbol{V}$	pMA direction matrix
$\boldsymbol{w}$	pMA inputs not used for modification
W	Set of inputs not used for modification
$\boldsymbol{\alpha}$	Adjustment bounds
δ	Perturbation size
$\boldsymbol{\varepsilon}$	0^{th} order modifiers
$\boldsymbol{\zeta}$	Boundary for number of updated modifiers
$\boldsymbol{\lambda}$	Filter matrices
$\boldsymbol{\mu}$	1^{st} order modifiers
$\boldsymbol{\gamma}$	1^{st} order modifiers refined in pMA
τ	Perturbation time
T	Operating point change transient time
ϕ	Economic objective function
$\boldsymbol{\omega}$	1^{st} order modifiers not refined in pMA

General process symbols

A	Unit cross-sectional area (m^2)
c_p	Molar specific heat capacity
C	Concentration (mol/L)
D	Unit diameter (m)
F	Molar flowrate (mol/s)
h	Unit height (m)
h_{loss}	Heat loss coefficient
$\dot{m}$	Mass flowrate (tn/s)
n	Molar holdup (mol)
N	Molar flux ($mol/m^2/s$)
p	Pressure (kPa)
P	Price ($\$CAD/unit$)
Q	Duty (W)
T	Fluid temperatures (K)
u	Fluid velocity (m/s)
y	Gas molar fraction
z	Column height (m)
ΔH	Enthalpy (J/mol)
ρ	Density (mol/L)

PCC symbols

a_w	Wetted area of absorber (m^2/m^3)
LL	Lean loading (mol/mol)
$\%CC$	Percent carbon capture

Williams-Otto symbols

$F_{\{A,B,R\}}$	Mass flowrate of streams $\{A, B, R\}$
$k_{\{1,2,3\}}$	Rate of reactions $\{1,2,3\}$
W	Mass holdup
$X_{\{A,B,C,D,E,G\}}$	Mass fraction of species $\{A, B, C, D, E, G\}$

Evaporator Symbols

C_p	Fluid heat capacity
$F_{\{1,2,3,4,5,100,200\}}$	Molar flowrate of streams $\{1,2,3,4,5,100,200\}$
$F_{\{2,100\}}$	Pressure of streams $\{2,100\}$
Q_{100}	Evaporator heat duty
Q_{200}	Condenser heat duty
$T_{\{1,2,3,100,200\}}$	Temperature of streams $\{1,2,3,100,200\}$
UA_1	Jacket-evaporator heat transfer coefficient

UA_2	Condenser heat transfer coefficient
$X_{\{1,2\}}$	Mole percent of species $\{1,2\}$
κ	Fluid latent heat of evaporation
κ_s	Steam latent heat of evaporation

General formulation subscripts and superscripts

$annum$	Annum/year
c	Controller
d	Dynamic
e	Estimated quantity/estimation
f	Final time
F	Filtered quantity
fez	Finite elements in column height domain
h	Upper bound
l	Lower bound
m	Measured quantity
MHE	Moving horizon estimation
MSE	Mean squared error
$NMPC$	Nonlinear model predictive control
$payback$	Payback (period)
$plant$	Plant
$process$	Process
PCC	Post-combustion capture
RTO	Real-time optimization
s	Steady-state
sp	Set point
$\boldsymbol{SSE}$	Sum of squared errors
t	Current time period
T	True (i.e., not estimated) quantity
0	Initial condition/time

lv-PE subscripts and superscripts

$challenger$	Challenger PE problem
dyn	Dynamic operation phase
lv	Low variance estimation
opt	Optimal operation phase
r	Regular estimation
sub	Suboptimal operation phase

$true$	True optimum
z, min	Minimum number of measurements
$\theta(\boldsymbol{z})$	Measurement parameter estimates
$\theta(\boldsymbol{\zeta})$	Partial measurement parameter estimates

lv-PE subscripts and superscripts

$lv-PE$	Low variance parameter estimation
pe	Traditional parameter estimation
$rRTO$	Robust real-time optimization

pMA subscripts and superscripts

act	Active constraints
f	Filtered quantity
g	Constraint quantity
i	Index for constraints
in	Inactive constraints
j	Index for inputs
k	Index for time
l	Index for disturbances elapsed
lb	Lower bound
m	Model quantity
MA	Modified formulation
nom	Nominal quantity
ord	Ordered vector
p	Process (sampled) quantity
$pert$	Perturbed quantity
pMA	Partially modified formulation
t	Current time
ub	Upper bound
ϕ	Objective function quantity
∞	Upon convergence

PCC subscripts and superscripts

abs	Absorber
amb	Ambient
cap	Captured by absorber
$chem$	Chemical feeds
$cool$	Buffer tank cooling
$comp$	Chemical components/species

CO_2	Carbon dioxide
$elec$	Electricity sold to consumers
$energy$	Energy consumption
$flue$	Flue gas stream
g	Gas
H	Top of absorber column
H_2O	Water
in	Into unit
l	Liquid
$mkup$	Makeup stream
MEA	Monoethanolamine
nom	Nominal
N_2	Nitrogen gas
out	Out of unit
reb	Reboiler heating
rec	Recycle stream
rxn	Reaction
$sales$	Captured carbon sales
$steam$	Steam generated by power generation
$tank$	Buffer tank
vap	Vaporization of water
$vent$	Emitted from absorber in vent gas
0	Bottom of absorber column

Quote

All models are wrong, but some are useful.

- *George Box*

1. Introduction

As the chemical, manufacturing, and energy industries expand to meet growing demand, digitalization is being increasingly embraced and computational techniques are becoming necessary to remain competitive. This growth also incites further interconnectedness of processes and the markets, necessitating real-time decision-making regarding the operation of processes. In this competitive environment, process economics are paramount and online model-based optimization is emerging as an attractive option to update operating conditions subject to external factors (i.e., upstream processes changes, external disturbances, market prices). Additionally, economic mechanisms like carbon and energy pricing can promote sustainability. Figure 1-1 depicts the interaction of an online economic optimizer and a plant (e.g., manufacturing, process, energy). As depicted therein, the optimizer is subject to pricing dictated by the market. The optimizer also contains a mathematical model that predicts process phenomena and behaviour which, along with the pricing information, allow for an economic model of the plant to be formulated. The optimizer solves for cost-optimal decisions to convey to the plant; moreover, different optimizers could contain additional sub-layers that operate at different timescales. Nevertheless, the plant is operated using the optimizer-computed decisions subject to disturbances. Finally, sensor measurements are taken from the plant, whereby they are used to by optimizer to reconcile the process model with the plant. Among the most sophisticated model-based operational approaches being used today are real-time optimization (RTO) (Darby et al., 2011), model predictive control (MPC) (Mayne, 2014), and modifier adaptation (MA) (Marchetti et al., 2009). These methods are the common theme in the present thesis.

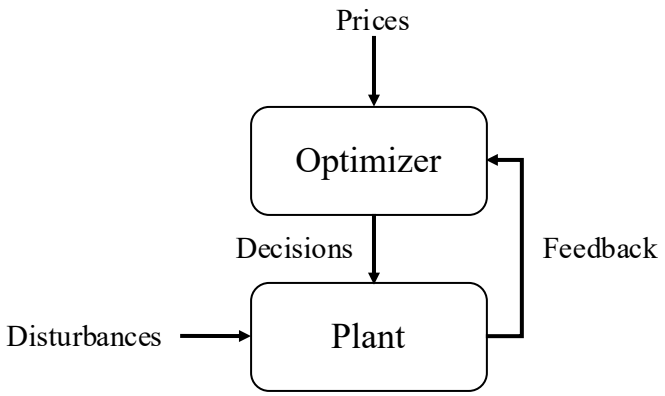

Figure 1-1: General flow of information for an online economic optimizer

RTO is commonly used in plants that deploy feedback control to regulate the system towards desired operating conditions. The most common implementation of RTO is the "two-step" approach, which uses time-averaged steady-state measurements to recursively estimate and update model parameters in the economic optimization layer. The economic optimization layer uses the same model as the parameter estimation (PE) layer; thus, the PE layer continually reconciles the optimization model with the latest plant data. The RTO economic optimization layer optimizes the plant operating conditions subject to an economic objective (e.g., revenue, cost, energy, emissions) and generates set points for the feedback controller to steer the plant towards.

Feedback control makes use of measurements or estimates of plant quantities to regulate the system towards the set points dictated by the RTO layer. Conventionally, classical control approaches like proportional-integral-derivative (PID) controllers have been used and continue to be prevalent in industry. However, these traditional PID controllers

are unable to consider process constraints and have difficulty in dealing with complex systems (e.g., with time-delays, nonlinearities, high-order dynamics). Resulting from these limitations, optimal control like MPC is increasingly being investigated, with a particular focus on its nonlinear version NMPC (i.e., an MPC that uses a nonlinear process model) to deal with troublesome dynamic behaviour. In principle, NMPCs (and MPCs more broadly) use a dynamic process model to predict future process behaviour and determine optimal control action based on the predicted process dynamics. The NMPC problems use feedback in the form of initial conditions to update its trajectory and execute its optimization problem at every time interval. NMPC solutions generate an optimal manipulated variable trajectory, and the first time-instance of this trajectory is provided to the plant. The plant is operated for another time interval and the initial conditions of the NMPC are updated to reflect the new measurements/estimates resulting in closed-loop operation. When integrated with RTO, an NMPC that uses a matching dynamic model to the RTOs steady-state model can also be updated upon the execution of a PE problem.

The initial conditions necessary to solve the MPC problem are not always readily measurable; this immeasurability is even more common in NMPC, where the process model is often detailed and requires information regarding many (sometimes all) system states. When this situation occurs, state estimation is deployed to use the available measurements to provide the necessary initial conditions to solve the NMPC problem. While many state estimation techniques exist (e.g., Kalman filter, Kalman, 1960; extended Kalman filter, Haseltine and Rawlings, 2005), MHE is of increasing interest for nonlinear systems to complement NMPC. MHE is effectively the inverse of MPC; instead of predicting the future to produce control actions, it uses historical trajectories to estimate the current state of the system. MHE achieves this by reconciling past measurements, estimates, and control actions to a dynamic model on a horizon, thus finding the optimal current state to match its predicted past trajectory. In doing predicting this current state, the MHE provides feedback to the NMPC, thus closing the loop. Like the RTO and NMPC, the MHE model can also be updated with a PE problem if it uses a matching model.

A commonality of all three approaches mentioned above is the use of a process model to make their respective decisions. All models make simplification and assumptions with respect to the actual system they represent; moreover, they require external inputs that may be unknown, measured, or estimated. These potential imperfections in the model can be lumped together as uncertainties. Uncertainties internal to the model are referred to as endogenous while those from external sources are known as exogeneous. In the case of the RTO/NMPC/MHE hierarchy as presented above, only parametric (endogenous and exogenous) uncertainty is generally addressed; this is sufficient if the model is of high quality as to be accurate across many operating conditions and capture most process phenomena. Moreover, the PE quality must be high, else erroneous predictions will be made by these models. If model quality is not high such that the plant and model cannot be reconciled via parameters, then structural uncertainty is present as the model's mathematical structure is awry from that of the plant.

In cases of structural model uncertainty MA is used to adapt the imperfect model to perform steady-state economic optimization. This is done through zeroth and first order "modifier" terms, which correct the optimization problem with respect to its constraints and gradients. By performing these corrections, MA can eventually converge to the true plan optimum upon refinement. A main difficulty in MA is the estimation of gradients for the first order correction. While model gradients are easy to estimate as the model is known by the modeller, the plant gradients are significantly

more difficult as they are not directly measurable from the plant. A common approach to estimate these gradients is to successively perturb plant inputs such that its local gradient with respect to each input can be estimated. However, this is difficult to do in practice in systems with slow dynamics, frequent disturbances, or many inputs.

To the author's knowledge, both two-layer RTO and MA algorithms contain points of weakness that can inhibit the economic performance of the systems they operate. In the case of the hierarchical RTO/NMPC/MHE approach, all three layers can be reliant on the fidelity of the parameter estimates generated by the PE problem. Poor parameter estimates can create problems in the RTO-generated set points leading to set point offset, as well as the NMPC/MHE control actions and state estimates leading to poor control performance and further offset. As the PE problem uses noisy data to generate its estimates, it is subject to propagation of that noise to the estimates. Moreover, the PE approach as commonly implemented does not verify the estimate quality before providing it to the other layers. In the case of the MA approach, the weakness occurs in the perturbation step whereby the optimal decisions made by the MA can be severely delayed. In a system where the disturbance dynamics are faster than the perturbation dynamics, the MA may not converge to or even approach the true plant set point.

In addition to the algorithmic gaps mentioned above, the economically optimal operation of many sustainable processes remains fully or partially unaddressed, especially as it pertains to addressing uncertainty. One such process is post-combustion carbon capture (PCC). For PCC, only a handful of online economic optimization studies have been published with significant limitations. PCC is a nascent process that has yet to reach widespread industrial update owing to its operating cost. Accordingly, online economic of the PCC process can be a factor to further induce operators to adopt this technology.

1.1. Research Objectives

This work attempts to address the issues regarding economic optimization under uncertainty listed above. New insights on ways to improve economic performance over existing uncertainty techniques will be presented in the context of RTO, NMPC, MHE, and MA. These will be applied to existing process benchmarks as well as budding processes that have not yet received attention in the optimal operation literature. Specifically, the current PhD thesis aims to achieve the following:

- Observe the propagation and effect of noise on the traditional two-layer RTO approach through its effect on parameter estimation and develop an operating scheme that abates noise.
- Examine MA in the context of high-frequency disturbances and slow dynamics; design an approach to deal with these circumstances and improve the economic performance of MA.
- Investigate the effects of uncertainty in the control, estimation, and economic optimization of post-combustion carbon capture (PCC) and propose a tiered economical operational scheme for its operation.

1.2. Contributions

To address the objectives listed above, this thesis will result in the following methodological contributions:

- A low-variance parameter estimation (lv-PE) approach integrated with RTO and NMPC to operate process systems under parametric uncertainty without propagation of noise to the process set points and control actions. A twofold algorithm will be presented, which chooses a favourable subset of measurements to reduce

noise propagation and ensures estimates are indeed accurate. Testing of the lv-PE scheme under known benchmark problems under the standard two-layer approach.

- A partial modifier adaptation approach to address structural model uncertainty in systems with slow dynamics and/or frequent disturbances. An algorithm to choose partial modification strategies that will lead to the best economic performance and evaluation of the algorithm in several systems with different structural characteristics. An ancillary problem to account for constraint violation is also proposed so the algorithm improves constraint adherence as well as economics.

Moreover, the following applied contributions are also described, which pertain to the PCC process:

- A robust NMPC that uses a mechanistic model for the PCC process and can address endogenous and exogenous uncertainty through the deployment of a scenario-based approach. Comparison of the proposed robust controller with a deterministic nominal controller under variations in the amount of uncertainty and variations the number of uncertain scenarios. Testing of the robust control scheme under step and a realistic power plant diurnal load variation scenario.
- A novel economic objective function that considers all significant operational cost in PCC for use in an RTO scheme integrated MHE and NMPC to operate the system under realistic measurability assumptions and relatively low cost. Use of a mechanistic PCC model in the three operating layers and testing of the scheme under realistic scenarios including: cofiring of fuels, diurnal load variations, and price fluctuations. The NMPC will allow for flexible operation of the PCC process while the MHE allows for a realistic subset of measurements to be required by the controller.
- Application of the lv-PE scheme to the PCC system and evaluation of its effect on process economics, energy consumption, emissions, and raw material usage over time. Additional evaluation of the effect of estimations fidelity on control performance as effected by NMPC and MHE layers. Study of PCC under time-of-use pricing scenarios across a wide set of possible disturbances. A robust RTO muti-scenario scheme to jointly address uncertain parameters and fluctuating prices will also be studied.

1.3. Structure of Thesis

The thesis presented herein is structured as follows:

Chapter 2 provides a literature in the pertinent research areas in economic optimization under model uncertainty including two-step approach and modifier adaptation. Moreover, methods to address uncertainty in MPC will also be outlined. Noise abatement methods for PE integrated with control and RTO will be examined. Lastly, online economic optimization methods for the novel PCC and RAS processes will be reviewed.

Chapter 3 presents the design of a robust NMPC for PCC under parametric uncertainty. The controller uses a dynamic mechanistic model, thereby enabling a precise treatment of uncertain model parameters and upstream disturbances. This controller is tested against a its nominal counterpart under step disturbances and diurnal load variation scenarios. The effect of number of scenarios and size of uncertainty region is also studied therein. This study was published in Fuel (Patrón and Ricardez-Sandoval, 2020a).

Chapter 4 introduces an RTO scheme for PCC by proposing a comprehensive cost function that included, energy, carbon tax, carbon sales, and utility costs. Moreover, a MHE is deployed along with a multi-variable NMPC to achieve

the set points dictated by the RTO with a realistic set of measurements. The proposed RTO is deployed in cofiring, diurnal variation, and price change scenarios with corresponding counterfactuals without RTO. This work was published in Applied Energy (Patrón and Ricardez-Sandoval, 2022a).

Chapter 5 proposes a scheme to abate the effect of measurement noise in the PE problem associated with RTO. The proposed algorithm chooses the lowest-variance subset of measurements prior to estimation and produces error bounds of the resulting estimates. This is motivated through a demonstration of the effect of parameter variation on the economic optimum and tested in two test cases. The scheme is designed to result in improved economics and reduced constraint violation through its effect of set point generation and NMPC parameter updates. This study was published in Industrial & Engineering Chemistry Research (Patrón and Ricardez-Sandoval, 2022b).

Chapter 6 applies the PE scheme presented in Chapter 5 to the PCC plant studied in Chapter 5. Two sets of uncertain parameters are considered: the flue gas CO_2 content and the activity coefficients. The PE scheme aims to make the PCC RTO more realistic by considering uncertainties. Moreover, fluctuating carbon and energy prices are also considered and addressed with a robust formulation. The effect of the pricing on the rate of carbon capture and process cost is studied and paired with varying disturbances.

Chapter 7 proposes a MA scheme, entitled partial MA (pMA), which is designed to abate the effect of uncertainty in cases of structural (i.e., not parametric) plant-model mismatch. This scheme aims to improve on the performance of the standard MA by selecting a subset of inputs for modification, instead of using all inputs, thus allowing for faster action. An algorithm for selecting the number of inputs as well as an ancillary problem to ensure constraint adherence are presented.

Chapter 8 presents concluding remarks as well as potential avenues for future works within the remit of the methods presented herein.

2. Background and Literature Review

The optimal process operations literature is vast and quickly evolving. This chapter reviews the variety of different methods used for optimal operation, how they have been applied to the sustainable processes of interest in the present thesis, and any gaps that may exist. The economic optimization under uncertainty literature is first reviewed in Section 2.1 with the context of RTO and MA. Moreover, the model predictive control literature is reviewed in Section 2.2 with a focus on uncertainty and economic control. Finally, the applications of these methods to the PCC are outlined in Section 2.3.

2.1. Online Economic Optimization of Process Systems

The economic operation of systems is of paramount importance in the chemical and process industries, which are becoming increasingly market-driven and competitive. To this end, model-based economic optimization has been an active field within the process systems engineering community in recent years.

2.1.1. Two-step Real-time Optimization

Chiefly among these methods is Real-Time Optimization (RTO: Darby et al., 2011), which has been deployed in a variety of applications: e.g., a laboratory-scale flotation column (Navia et al., 2016), hydrogen production network (Galan et al., 2019). RTO uses a process model as well as an economic model to determine the optimal operating point for the plant while addressing model uncertainty. These operating points are passed as set points to a control layer, which dynamically steers the plant towards the economic optimum.

RTO can either use steady-state or dynamic models to generate constant set points or set point trajectories, respectively. Dynamic RTO (DRTO) is used when systems can exhibit expensive dynamics, instability, or otherwise undesirable steady-state operation (Ramesh et al., 2021). Several variant of DRTO have been proposed, which include the use of stabilizing constraints (MacKinnon et al., 2022; Ramesh et al., 2021) and embedded closed-loop predictions (Dering and Swartz, 2022). While DRTO is beneficial in some cases, the typical steady-state RTO is often sufficient to achieve good performance and is the focus of this review.

Steady-state RTO typically employs detailed models that are a suitable reflection of the plant behaviour, often those models are subject to uncertainty, which can cause erroneous operating points that lead to economic suboptimality and constraint violations when implemented in the plant. Differences between the model and plant result in suboptimal plant economics as the model being optimized may not be fully equivalent with the plant it represents. The uncertainties present in RTO problems that cause these suboptimalities can be either structural (i.e., the model does not fully account for the phenomena occurring in the plant) or parametric (i.e., the model contains parameters that are not known precisely and/or may change over time) (Krasławski, 1989). While structural model uncertainty in RTO is also an active research area (Marchetti et al., 2009; Roberts and Williams, 1981), parametric uncertainty is of interest in the present study.

To mitigate the effects of parametric uncertainty and arrive near the “true” economic optimum (i.e., the optimum that corresponds to the plant), a Parameter Estimation (PE) step is typically implemented alongside the economic optimization step in RTO via the so-called two-step approach. The PE step uses steady-state process information (i.e., historical data on the steady-state measurements and manipulated variables) to perform a least squares optimization

problem, whereby the difference between measurements and the steady-state process model predictions are minimized with the uncertain parameters as the decision variables (Cox, 1964). These updated parameters are subsequently supplied to the RTO problem and can be also supplied to the controller (e.g., in a model-based control scheme that uses a dynamic version of the RTO model). Once a new set point is achieved, the PE step is repeated as new steady-state data becomes available. Thus, the procedure of executing PE and RTO is performed periodically such that the plant and the model are constantly being reconciled through the model parameters. This overall scheme is closed loop since the RTO set points are passed to a regulatory controller, which acts on the plant, whereby plant measurements are supplied to the PE problem and the controller. Note that the associated problem of identifying whether steady state has been reached (known as steady state identification (SSI: Cao and Rhinehart, 1995) is also a part of many RTO schemes. While SSI can be used to indicate when it is appropriate to begin collecting steady-state measurements, it does not otherwise interact with the PE and RTO in parameter estimation or set point generation, respectively; thus, its deployment is often omitted in the context of RTO for simplicity.

Issues arising from the use of experimental measurements often arise in practice, which could lead to performance loss in downstream operating layers. For instance, systematic measurement errors caused by instrumentation miscalibration, or faults can occur and lead to poor estimation, monitoring, and control performance. To address this, gross error detection (GED) methods have been proposed in the literature, e.g., hypothesis testing (Özyurt and Pike, 2004), error bounds (Bhat and Saraf, 2004), mixed integer programming (Arora and Biegler, 2001), and maximum *a posteriori* estimation (Yuan et al., 2015). In the presence of faults, the deployment of GED in the context of PE/RTO will ensure that estimated parameters and set points are consistent with the plant thereby preventing erroneous operating points.

In addition to gross error, random error is also present and difficult to eliminate from industrial systems. This type of error occurs as measurements are subject to fluctuations obeying an underlying statistical distribution that causes imprecision (Albuquerque and Biegler, 1996). In the context of RTO, variations in the set point produced by the RTO owed to noisy parameter estimates can occur (Quelhas et al., 2013); these are caused by noisy plant measurements that lead to ill-conditioning in the PE problem and propagation of noise into the estimates. This set point imprecision is detrimental to the process economics as the effect of deviating from the true optimum may accrue substantially many RTO iterations. Moreover, fluctuating set points also impose undue burden on the process control layer, which is preferably avoided. To address the accuracy/precisions of RTO set points, a variety of approaches have been proposed in the literature.

A probability constrained approach has been proposed (Zhang et al., 2002) to incorporate uncertain economics and constraints into a robust RTO formulation. Moreover, a Bayesian approaches for parameter estimation paired with uncertainty propagation (e.g., via polynomial chaos expansions; Mandur and Budman, 2014) have also been suggested to formulate robust economic objectives for optimization. However, robust approaches such as this sacrifice performance to find a solution that works well *regardless* of the true parameter realization. Other authors (e.g., Miletic and Marlin, 1998), have developed statistical approaches to decide when set point should be changed to avoid transients caused by insignificant parameter/disturbance changes. These use hypothesis testing and only perform model and set point updates upon the occurrence of significant changes in operating point; however, this does not

address the root issue of noisy measurements and only avoids frequent unnecessary unwarranted set point fluctuations. Data reconciliation (DR), which makes experimental data consistent with the process model (Albuquerque and Biegler, 1996; Arora and Biegler, 2001; Bhat and Saraf, 2004; Özyurt and Pike, 2004; Yuan et al., 2015), can also be employed to improve two-step RTO performance such that the measurement and parameter estimates are consistent with the RTO model and constraints; this may have some noise-filtering effects, thus reducing variability. However, the main issue being addressed in DR is measurement/model consistency, not random error, and any effect that it has on random error may be an ancillary benefit. Increasingly, joint parameter and state estimation has been investigated along with the use of dynamic data to improve RTO performance by increasing execution frequency. A recent work (Liu et al., 2021) performed dynamic estimation whereby the set of estimated variables changed depending on the operating conditions; other contributions (Krishnamoorthy et al., 2018; Matias and Le Roux, 2018; Valluru and Patwardhan, 2019) have coupled dynamic parameter estimation with steady-state economic optimization to achieve increased RTO frequency. Nevertheless, the issue of noise propagation can persist in joint parameter and state estimation if not addressed. Lastly, robust estimators (Albuquerque and Biegler, 1996; Arora and Biegler, 2001; Özyurt and Pike, 2004) have been proposed for GED, DR, and PE in chemical systems. These broadly aim to reduce the effects of outliers on parameter estimates by reformulation of the respective optimization problems (e.g., log-likelihood objectives); however, their effect on RTO has not been previously studied.

In general, the methods listed above require the implementation of new process layers (Bhat and Saraf, 2004; Liu et al., 2021; Matias and Le Roux, 2018) (e.g., Kalman filter or MHE) to generate outputs to the existing PE and RTO, thus further complicating an already stratified and intensive two-step approach. Other methods require sensitivity information (Liu et al., 2021; Miletic and Marlin, 1998), which is difficult to estimate in practice as it requires system perturbations; this is particularly difficult in the presence of significant noise. The additional complexity proposed by these methods may be undesirable in an industrial setting as operators are reticent to implement convoluted operating schemes. Moreover, no method in the literature aims to abate the effect of random error explicitly in the context of RTO. This leaves a gap for a scheme that directly targets the effect of random error owed process noise in the two-layer RTO scheme.

Two-step RTO can also be used in cases where structural plant-model mismatch is present (i.e., when parameter adaptation alone does not lead to convergence to true plant optima). For instance, Mandur and Budman (2015) propose a parameter gradient correction on the output model with simultaneous parameter estimation. This allows for convergence to the true process optimum and compares favourably to other structural mismatch adaptation schemes.

2.1.2. Modifier Adaptation

Increasingly, modifier adaptation (MA) (Gao and Engell, 2005; Marchetti et al., 2009) and its many variants (e.g., Marchetti et al., 2010; del Rio Chanona et al., 2021) are being investigated for situations of structural model uncertainty where robust and two-step approaches are not suitable. A comprehensive review of MA can be found in Marchetti et al (2016).

Instead of adapting model parameters, MA adapts the economic optimization problem via its objective function and inequality constraints. By introducing 0^{th} order bias terms and 1^{st} order gradient modifications with respect to the decision variables, MA has been proven to match plant and model KKT conditions (Marchetti et al., 2009). Assuming

full state accessibility, the bias terms are straightforward to compute; however, the gradient estimation is more intensive as it requires system perturbations. Imposing perturbations on the system requires small changes to be made on the input variables such that they produce a correspondingly small changes in the output variables in the neighbourhood of the current operating point. Note that perturbations can also refer to disturbances; henceforth we only use perturbations only to refer to small user-defined input changes. The gradient near the current operating point can then be estimated as the ratio of output to input perturbations, which allows for gradient modifiers to be computed and the process operating point to be updated. The gradient modifiers are then recomputed at the newly defined operating point as the local gradient changes with new operating points. This refinement process of updating operating points and gradients is repeated until the true (i.e., plant) operating point is reached by the model. If a disturbance occurs, the gradient computation and modifier refinement process can detect this mismatch such that the new plant optimal operating point is found again. Each input perturbation requires the system to undergo dynamic operation until the perturbed state is reached, thus delaying the operating point update. This can become detrimental if: i) there are many inputs such that many perturbations must occur; ii) the process dynamics are slow such that the gradient estimation is time consuming; and iii) the process disturbances occur at a high frequency. These conditions affect the amount of time it takes to converge to plant optimality. For instance, if disturbances are occurring frequently, the modifier refinement process may be interrupted before convergence to the optimum. Typically, layered RTO approaches are generally deployed for high-frequency disturbance scenarios (Bottari et al., 2020), whereby different timescales have individuated control schemes. More broadly, if the dynamics are slow, there are numerous inputs, or the disturbances occur at a high frequency, the system will not converge to an optimal solution in time to accrue the benefits of the true optimum. These represent the main weakness of the existing MA algorithms as constructed and deployed in the literature (Marchetti et al., 2016). A few MA variants have been proposed to circumvent the perturbation delay. Dual MA (Marchetti et al., 2010) has been proposed to estimate gradients using past operating points whereby new successive operating points are placed such that they contain sufficient information for gradient estimation. Gao et al., (2016) proposed the use of local approximations of the cost and constraint functions, which could be differentiated to produce gradient approximations. Some studies have taken the approach of using transient measurements to speed up the MA procedure (e.g., de Avila Ferreira et al., 2017; Marchetti et al., 2020). These generally use neighboring extremals, which assume that the uncertainty is parametric (François and Bonvin, 2014).

Most notably, directional MA (dMA; Costello et al., 2016), which updates the cost and constraint gradients according to "privileged" input directions chosen through sensitivity analysis of the Lagrangian function, has been proposed. dMA does not ensure KKT matching but ensures that the cost cannot be improved further in the privileged directions upon its convergence. dMA requires the knowledge of which parameters are uncertain, their distributions, and the sensitivity of the optima to these parameters. The main difficulty that arises when using dMA is the requirement of model Lagrangian cross derivatives with respect to inputs and uncertain parameters. Model derivatives are acquired through a perturbation process or analytically; however, these are only computed once and generate local sensitivities. Costello et al. (2016) compute their privileged directions based on local model sensitivities with respect to inputs and uncertain parameters. In reality, structurally mismatched problems may not contain uncertain parameters. Even for cases with uncertain parameters, their distributions are unlikely to be known *a priori* and their sensitivities are unlikely

to be the same across all potential operational points. Singhal et al. (2018) and Rodriguez et al. (2022) present a method to compute global (instead of local) parameter sensitivities; this allows for changing privileged directions at different operating points, which yields more flexibility to the dMA method. These global sensitivity methods also require parameter probability densities to be known *a priori*, which enable parameter Monte Carlo sampling. In addition to the assumptions regarding *a priori* knowledge of the uncertain parameters, these dMA methods compute directions based on the proposed predictive model, (i.e., not plant quantities), hence the directions that are privileged for the model may not necessarily be suitable for the actual plant. Despite this progress on gradient estimation and many-input systems, no prior MA scheme is aimed at frequent periodic disturbances.

Another issue in MA is that of constraint satisfaction during modifier refinement. MA only guarantees satisfaction upon convergence; however, satisfaction is not guaranteed in the modifier refinement iterations. Bunin et al. (2011) presented a method to determine upper bounds on filter gains such that satisfaction is guaranteed. However, limiting the filter gain may slow convergence speeds. Previous studies have also proposed schemes to ensure feasible-side convergence, whereby each iterate is guaranteed to be constraint-satisfying (Marchetti et al., 2017a). These require the constraint and objective function be made strictly convex upper-bounding functions via additional quadratic terms; to do so, the estimation of Hessian matrices is needed, which may be impractical. Furthermore, Marchetti et al. (2017b) also deployed robust constraint upper bounds, which result in backoff from the true constraint but ensure iteration feasibility in the presence of gradient uncertainty; this scheme also requires process Hessians. A gap exists in the literature for an MA constraint-satisfaction scheme that enables the use of little filtering and does not require Hessian information, which is difficult to acquire in practice.

2.2. Model Predictive Control

Process controllers aim to regulate controlled variables (CVs) to their desired set points by actuating the process manipulated variables (MVs). Model predictive control (MPC) is a well-established method to achieve the optimal control whereby a dynamic process model is used to predict future system behaviour while also receiving constant feedback from the plant by way of initial conditions. MPC poses a dynamic optimization problem given the feedback from the plant, which minimizes the sum of squared errors with respect to the set points across a prediction horizon (i.e., the fixed future time window in which the MPC model predicts plant behaviour). Accordingly, the MVs across a control horizon (which could be the same or shorter than the prediction horizon) are the decision variables for the MPC optimization problem. The first time-instance of these MVs is given to the plant such that it is controlled until the MPC is executed at the next sampling time. At every sampling time, feedback from the plant is acquired, thus making the scheme closed-loop by updating the process model on the current system state. Importantly, MPC can also include process constraints in their formulation; thus, ensuring the safety and viability of its decisions.

The set points provided to the MPC can be based on process knowledge/heuristics or determined by an RTO (as discussed in Section 2.1.1.). Control systems with various CVs require tuning of the various control objectives to ensure the desired dynamic behaviour occurs and the controller is effective for all CVs; tuning approaches (e.g., Shah and Engell, 2011) have also been studied. The feedback provided to the MPC is acquired by way of measurement or state estimation. Measurement simply relies on process instrumentation while state estimation is a very active field of research, which provides some of tools used in the present work. As state estimation is not the core topic of study

herein, the reader is referred to Afshari et al. (2017), Allgöwer et al. (1999), and Valipour and Ricardez-Sandoval (2021) for an in-depth discussion. The prediction horizon serves as a tuning parameter for MPC whereby better tracking performance is achieved by using longer horizons; however, this comes with increased computational effort as the dynamic optimization problem grows with longer predictions. Another way to improve control performance is the use of a nonlinear model for MPC (denoted NMPC); this can improve control performance in nonlinear systems whereby a linear model may be inaccurate. NMPCs are primarily of interest in the present work, which considers various variants on the traditional NMPC framework.

2.2.1. Model Predictive Control Under Model Uncertainty

As noted by Mesbah (2018), model uncertainty in MPC has been addressed with two techniques: robust MPC (RMPC) and stochastic MPC (SMPC). RMPC works on the principle that the uncertainties are bounded, and process constraints must be satisfied for all uncertainties within the bounds (Mayne, 2014). The uncertainties are assumed to be the set of all possible uncertainties in a finite bounded region, which is discretized into a finite number of realization. The simplest of these scenario-based approaches is the min-max MPC (Scokaert and Mayne, 1998), which assumes the worst-case uncertainty occurs and solves the MPC optimization subject to this pessimistic uncertainty realization. The min-max formulation results in significant conservativeness. To alleviate some the drawback of min-max, the multi-scenario approach (e.g., Huang et al., 2009; MacKinnon et al., 2021) builds a finite set of model realizations for which a single control trajectory is computed. The multi-scenario approach approximates an uncertain probability distribution through discretization of a probability density function and assigns each realization a probability *a priori* based on process knowledge. The multi-scenario approach results in less conservatism being built into the problem than min-max but still retains some performance sacrifices for constraint adherence as it prioritizes average performance across potential scenarios. However, the computational effort scales with the number of scenarios as the uncertainty is approximated with a higher resolutions. Most sophisticated among scenario-based approaches is the multi-stage approach (Lucia et al., 2013), which allows for uncertainty evolution and recourse actions occurring over time. The multi-stage formulation features a “robust horizon” that accommodates for changing uncertainties in the future whereby recourse may be taken. As with the multi-scenario approach, the multi-stage computational effort scales with the number of scenarios; however, it also scales with the length of the robust horizon, thus increasing the computational expense further.

In contrast to the scenario-based approaches SMPCs solve the dynamic optimization problem subject to constraint and parameter expectations that are not necessarily bounded (Saltık, 2018). In this way, the conservatism present in the scenario-based approaches is reduced with the trade-off that the hard constraints are softened through reformulation as chance constraints. In this case, a continuous probability density function is required for each uncertainty, which is not easy to acquire in practice (i.e., it may require process knowledge or Monte Carlo simulations; Mayne, 2016).

2.2.2. Economic Model Predictive Control

Economic MPC (EMPC) retains certain key characteristic of a traditional MPC such as the use of feedback, MVs, horizons, and constraints. The important difference lies in the use of an economic objective whereby a profit is

maximized, or a cost minimized over the prediction horizon. This control structure aims to bypass the need for set points and essentially merges the RTO and MPC layers into one. EMPC has been used for a variety of industrial applications, e.g., PCC (Decardi-Nelson et al., 2018), HVAC (Mendoza-Serrano and Chmielewski, 2012), and an air separation unit (Huang et al., 2012). However, this approach has some implications as it pertains to stability, which have spurred significant research on EMPC. As the set point regulation objective is no longer present, EMPC scheme can suffer from instability and capricious control actions. Under the standard formulation as presented in Ellis et al. (2014), stability cannot be guaranteed for EMPC-operated systems. Accordingly, several methods have been proposed to ensure stability including the use of infinite horizon approximations, terminal constraints, terminal cost, and Lyapunov-based EMPC. These methods are briefly reviewed herein; however, the reader is asked to refer to Ellis et al. (2014) for an extensive tutorial.

A general assumption that occurs in most MPC formulations is that of a finite horizon length. This assumption is made to make the dynamic optimization problem tractable when discretized; this is necessary as an infinite horizon would results in an infinite-dimensional problem. However, the truncation of the horizon results in the inability to guarantee stability as the full economic trajectory is unknown by the controller. Würth et al. (2007) propose the that a discount factor be used to account for the time value of money in EMPC. As a result of the long period of time needed to account for discounted economics, a long (i.e., effectively infinite) horizon is necessary. Accordingly, Würth et al. (2007) propose that time domain is made finite through a transformation of the time bounds. This poses the optimization problem to finite but introduces a singularity at one of the boundaries, which is handled using terminal constraints. Alternatively, Mendoza-Serrano and Chmielewski (2012) segmented the infinite horizon into a finite initial portion and a tail that is quantified by a quadratic regulator of the terminal state. By doing this, the EMPC problem is made independent on the finite horizon size and shown to be equivalent to the infinite horizon formulation. Lastly, Huang et al. (2012) showed that sufficiently long finite horizons could be used for EMPC in some cases to achieve the stability properties of infinite horizon.

Terminal constraints and costs are related methods to ensure EMPC stability in that they both impose system behaviour at the end of a finite time horizon. In the case of terminal constraints, this is done by imposing an end-point constraint on the horizon such that the system will always try to converge to a stable point (Diehl et al., 2011) or neighbourhood (e.g., Amrit et al., 2011). Choosing the terminal point is important as it must be stable; these are generally chosen based on off-line static process optimization (Angeli et al., 2012). The use of a terminal fixed point, however, can lead to small feasibility sets and inflexibility in the controller. Authors like Fagiano and Teel (2013) have suggested the used of terminal sets (regions) to abate this issue. In contrast, for terminal cost/penalty approaches, the objective function is formulated with a term to penalize the distance from a pre-specified terminal point. In general, the terminal cost takes the form of a quadratic Lyapunov function for which the weighing matrix satisfies the Lyapunov equations (Amrit et al., 2011). For this approach to work, the objective function must sometimes be regularized using quadratic regulator terms to satisfy dissipativity (Amrit et al., 2011) requirements.

Lastly, the Lyapunov-based EMPC (LEMPC; Heidarinejad et al., 2012) has also received significant attention as a means of stabilizing EMPC operation. LEMPC proposes the use of two distinct operational modes using an EMPC and an auxiliary controller, respectively. In the EMPC mode, the system uses a Lyapunov function to keep the state

trajectory within a pre-specific bounded set. This bounded set is chosen to guarantee stability is retained for any possible disturbance. If a disturbance drives the system outside of this bounded set, the system remains in a region of stability but the LEMPC switches to an auxiliary mode. In the auxiliary mode, a Lyapunov function is forced to decrease over time thereby steering the system back to the stability region or an equilibrium point. Using these two modes, stability is always guaranteed. As with the terminal cost approach, this requires the formulation of a Lyapunov function and regularization terms as previously mentioned. Moreover, Lyapunov functions can also be used to ensure robust stability (i.e., in the presence of model mismatch). For instance, Santander et al. (2016) propose the use of a polytopic model to characterize the model error across different operating conditions; this allows for the formulation of Lyapunov constraints with consideration of potential mismatches. They also perform online parameter updating as part of their EMPC procedure.

An application of EMPC in recirculating aquaculture systems, which was performed for this thesis but is not part of the main results, can be found in Appendix E.

2.3. Online Economic Optimization and Control of Post-combustion Carbon Capture

As global warming is increasingly in the forefront of public discourse, the drive to develop "green" technologies has never been greater. Chiefly among the causes of global warming is the large quantity of carbon dioxide (CO_2) produced in industrial combustion and emitted in flue gases. To this end, the development of mitigation strategies for CO_2 emissions is essential to restricting further global warming. An ever-increasing industrial demand bolsters worldwide greenhouse gas (GHG) emissions. CO_2 is the most abundant of the GHGs, totaling 73% of all emissions in 2017, mainly because of its production in the power generation and transportation sectors (Olivier and Peters, 2018). In particular, combustion sources make up 89% of the total CO_2 emissions subdivided by fuel type into coal (40%), oil (21%), and natural gas (18%) (Olivier and Peters, 2018). After a brief plateau in 2015 and 2016, CO_2 emissions continued their upward trend in 2017 owing to the increasing reliance of developing countries on coal as a convenient energy source (BP, 2019). Despite recent trends of waning coal use in in the developed world, worldwide reliance on other CO_2 emitters has been steadily increasing (Le Quéré et al., 2018); likely because of their abundance and low price. This is particularly essential for developing economies that must provide inexpensive and reliable energy to their populations. In 2019, combustibles accounted for ~79% of the world's energy supply (IEA, 2020), comprising mainly oil, natural gas, and coal. While it would be ideal to eliminate these emissions, this is not a realistic option because of the worldwide dependency on CO_2 emitting products, thereby necessitating the development of technologies to mitigate global CO_2 emissions.

Carbon capture and storage (CCS) is one of the technologies on the forefront of CO_2 emission mitigation. This technology aims to sequester CO_2 to avoid its release into the atmosphere, subsequently using it elsewhere or storing it in repositories. In particular, pre-combustion removal (Babu et al., 2013; Linga et al., 2007), post-combustion removal (Valencia-Marquez et al., 2015), chemical looping combustion (CLC) (Lucio and Ricardez-Sandoval, 2020; You et al., 2018) and oxy-combustion (Chansomwong et al., 2014a; 2014b) have received much attention.

Post-combustion CSS (PCC) is the most mature CCS technology that is ready for deployment. A major benefit of the technology is that it can be used to retrofit existing CO_2 emission sources for immediate removal. For PCC, several

methods of removing CO_2 from combustion products in industrial flue gases have been investigated, these include adsorption, physical absorption, chemical absorption, cryogenic separation, and membrane-based separation (Wang et al., 2017). Of these, chemical absorption by way of amine solvents has seen experimental contributions by way of pilot-scale (Dugas, 2006; Idem et al., 2006) and industrial-scale (Faramarzi et al., 2017; Huang et al., 2010) plants. Moreover, there have also been computational contributions in modelling, simulation and process design (Bahakim and Ricardez-Sandoval, 2014; 2015; Gaspar el al., 2016; 2017; Lawal et al., 2009; Mac Dowell et al., 2013; Nittaya et al., 2014). Despite the construction of these few plants, widespread uptake of PCC systems has been slow. The main factor hindering adoption of this technology remains the economic detriment it poses to the fuel-fired power plants to which it is connected; as the PCC process is expensive, it reduces the profit of the power plant. To this end, techno-economic analysis (e.g., Danaci et al., 2021; Li et al., 2016) and economic operation of the PCC process (e.g., Luu et al., 2015; Mechleri et al., 2017; Panahi and Skogestad, 2012) have been studied. These economical operation analyses and schemes will be critical in inducing emitters to consider PCC plants as viable.

Of the solvents possible for chemical absorption PCC, monoethanolamine (MEA) based solvents have received particular attention among the solvent alternatives because of their abundance, performance, and low price relative to other solvents (Hossein Sahraei and Ricardez-Sandoval, 2014). Consequently, MEA-based chemical absorption for CO_2 removal is very developed as a potential emerging technology since its chemistry and process have been extensively studied (Haimour and Sandall, 1984; Hikita et al., 1977; Hoff et al., 2004; Kvamsdal et al., 2009; Onda, et al., 1968). Importantly, these studies have allowed the development of transient mechanistic process models (Harun et al., 2012; Jayarathna et al., 2013; Schneider et al., 1999).

For real-life deployment of the MEA-based PCC, the process operation must be well understood to achieve safety and productivity. A crucial part of the operation is the implementation of a process control system to ensure set-point regulation and tracking. In an MEA-based PCC plant, the control system is conventionally used to ensure that CO_2 removal targets and energy consumption requirements are met in the presence of upstream disturbances, e.g. changes in the energy load. The successful fulfillment of these operational goals is especially pertinent in the PCC system as the CO_2 removal generally detracts from the profitability of the upstream plant. In addition to the control studies that consider conventional decentralized feedback controllers such as PI and PID (Luu et al., 2015; Mechleri et al., 2017), the development of the aforementioned PCC plant models has enabled the use of model-based control strategies. Previous studies have implemented model-based control featuring various levels of model sophistication and control envelopes. For the MEA-based PCC plant, Bedelbayev et al. (2008) implemented an MPC based on a linearized model of the absorber unit whereas Sahraei and Ricardez-Sandoval (2014) developed an MPC involving multiple inputs and outputs and compared their performance to a decentralized feedback PI-based control strategy. He et al. (2016) implemented another linearized MPC model integrated with scheduling for the full MEA-based PCC plant. Moreover, Panahi and Skogestad (2012) evaluated different control structures for the PCC plant and implemented a multivariable linear MPC. For increasingly complex models, Åkesson et al. (2012) considered a low-order nonlinear model and implemented a nonlinear MPC (NMPC) for the absorber unit in the PCC plant. Decardi-Nelson et al. (2018) also implemented an NMPC scheme for the complete post-combustion MEA-based CCS pilot-scale plant. Additionally, they also developed an economic MPC (EMPC) for the plant. Similarly, Chan and Chen (2018) also implemented an

EMPC scheme based on an Aspen Plus model of an entire MEA-based CSS plant whereby the process economics can be optimized and controlled with respect to changing feed qualities and utility prices. These are only selected few of the control studies for the MEA-based PCC plant, a review on this subject can be found elsewhere (Salvinder et al., 2019).

Recently, machine learning techniques (Altan et al., 2021; Karasu et al., 2020; Rangel-Martinez et al., 2021) applied to the prediction of systems with complex dynamics (Wang and Ricardez-Sandoval, 2020) such as PCC (Helei et al., 2021; Rahimi et al., 2021), this offers a balance between modelling accuracy and computational tractability. Literature on PCC control is vast; a recent review on this subject can be found in (Salvinder et al., 2019). A commonly proposed approach to achieve control flexibility in this system is through the manipulation of heating duty (Åkesson et al., 2012; He et al., 2016; Jung et al., 2020; Jung et al., 2021; Luu et al., 2015), which can enrich or dilute the PCC solvent as required but requires steam to be taken from the power plant. An aspect that has not been considered for control is the use of makeup streams to achieve the same flexibility while abating the use of steam that could otherwise be used for power generation.

For feedback control to be practically implementable, the plant states must be fully measurable or observable. Accordingly, state estimation is used as many system states required by the controller cannot be measured online; this is particularly important in complex systems that include several states. In comparison to the control literature for PCC, the available state estimation literature is sparse. Notably, Jung et al. (2020) paired a KF with linear and nonlinear MPCs for control of the PCC, respectively. The latter used a mechanistic control model and required the measurement of 74/110 system states and very low process noise for successful state estimation. Moreover, Yin, Decardi-Nelson and Liu (2019) used moving horizon estimation (MHE) to perform fault diagnosis, whereby the PCC absorber was decomposed into spatial subsystems (i.e., it was decomposed into five stages, each with its own estimator) and only gas temperatures were measured. MHE is an advanced estimation scheme well-suited to deal with nonlinearities and constraints. Its use in PCC, which is nonlinear and often constrained, could allow for more accurate and reliable state estimates than KF, leading to a more effective control layer. Despite these recent advances in the state estimation literature for the PCC process, only a single full MHE implementation, which requires a realistically achievable number of measurements without model decomposition, has yet to be implemented and engaged within a broader operational scheme (i.e., with MPC and RTO) for PCC plants. The only existing example of MHE for PCC was proposed by Yin et al. (2020); however, this was only used for monitoring purposes and not engaged with other operational layers. More broadly, there is also a gap for an integrated operating scheme that addresses the economic, control, and estimation problems simultaneously.

The ability to estimate plant states, which can subsequently be fed to a controller to steer the system towards desirable operating points, enables the implementation of optimal operation approaches. These can be put into two categories, both of which could use mechanistic process models: economic MPC (EMPC), in which an optimal control problem is formulated with an economic objective, thus providing economically-driven control actions directly to the plant; and real-time optimization (RTO), in which a steady-state problem is formulated with an economic objective, hence providing steady state set points that are passed to a control layer and are updated when significant disturbances occur. While RTO is a steady-state method, EMPC is inherently dynamical; as such, it often requires stabilization (e.g.,

terminal constraints/cost) and intensive computational effort per sampling interval (Ellis et al., 2014), making it difficult to implement online. The economically optimal operational approaches for PCC are summarized in Table 2-1:

Table 2-1: Summary of literature pertaining to the economically optimal operation of PCC processes.

Ref.	**Approach**	**Findings**	**Drawbacks**
Chan and Chen (2018)	EMPC	Approach for MEA-based plant provided ~10% cost reduction over a constant operating point. Disturbances in flue gas quality and utility costs were considered.	Full state access was assumed (no estimation). Only solvent and utility costs considered. MEA makeup manipulated.
Decardi-Nelson et al. (2018)	EMPC/ RTO	Approach for MEA-based plant provided ~6% cost savings over a constant operating point. EMPC and RTO were compared. RTO performance was found to approach EMPC performance if executed frequently. Disturbances in flue gas flowrate and steam price were considered.	Full state access was assumed (no estimation). Only carbon tax and thermal costs considered. Reboiler duty manipulated.
Akula et al. (2021)	RTO	Approach for MEA-based plant provided an analysis of the optimal steady-state operating point in part-load, full-load, and varying flue gas composition scenarios.	Dynamics were not considered (i.e., no control/estimation). Only pumping, heating, and cooling costs considered. Reboiler duty manipulated.

The following conclusions can be made from this review of the economically optimal operation literature: 1) the existing studies are tailored specifically to MEA-based plants, 2) the respective economic functions considered in the previous studies ignored key aspects of the process economics in their cost function (e.g., Decardi-Nelson, Liu and Liu (2018) included thermal and carbon tax costs but ignored solvent costs), 3) none of the previous studies have manipulated both MEA and water makeup streams to achieve solvent enrichment/dilution (e.g., Chan and Chen (2018) only manipulated the MEA makeup). This elucidates the following gaps in the literature: 1) the need for a generic operating scheme that can be applied to a general class of PCC plants to achieve economically optimal operation while promoting CO_2 removal, 2) the need for an economic function that is comprehensive through its inclusion of all significant economic aspects of PCC, 3) an advanced model-based control scheme that can manipulate PCC plants flexibly without solely relying on the energy-intensive reboiler, 4) an advanced model-based state estimation scheme that is accurate and reliable in terms of the measurements required.

A complicating factor embedded in the models that are used in model-based control approaches, including those using highly detailed nonlinear mechanistic models, is that the models will be subject to various types of uncertainty. These are caused by assumptions made in developing the model (structural), and error associated with estimating experimental parameters (parametric) (Krasławski, 1989). This uncertainty, which leads to mismatch between the plant and the model, can be either exogenous or endogenous. Exogenous uncertainty occurs due to factors not

embedded in the model, e.g., variations in inlet compositions, flowrates, changes in products demands; while endogenous uncertainties occur within the model's parameters or equations leading to plant-model mismatch, e.g. activity coefficients, heat transfer coefficients, rate constants. For model-based control, taking these uncertainties into account is crucial as neglecting them will lead to poor controller performance, which would translate into off-specification products, failure to meet commercial and regulatory process demands, and lost profits. To take these uncertainties into account, the closed-loop operation must be made insensitive to uncertainty, which can be achieved through stochastic or robust methods control, the latter of which will the focus of this study. A review of stochastic MPC methods can be found elsewhere (Mesbah, 2016). In this context, control actions must be determined such that the process will exhibit good performance in closed loop despite these uncertainties. The robust operation of the MEA-based PCC has been addressed using optimal control by a few authors. For instance, Panahi and Skogestad (2012) employed a robust linear MPC on the entire plant; while Zhang et al., (2018) implemented a H_∞ robust controller with a nonlinear NAARX model on the entire plant. Decardi-Nelson et al. (2018) evaluated the performance of their NMPC and EMPC schemes under upstream uncertainties; however, they did not make their controllers robust to those uncertainties. In a follow-up work, Decardi-Nelson and Liu (2022) used a zone tracking approach to design a robust PCC EMPC.

Uncertainty is particularly salient in PCC where a nonlinear carbon capture plant interacts with a nonlinear power plant. Accordingly, this topic has been investigated for several applications. The design of PCC under uncertainty has been addressed through ranking-based (Bahakim and Ricardez-Sandoval, 2015) and multi-scenario (Cerrillo-Briones and Ricardez-Sandoval, 2019) approaches. In the control layer, several robust controllers (Jung et al., 2020; Rúa et al., 2021a; Zhang et al., 2018) have been proposed and paired with state estimators (Yin et al., 2020); these often consider uncertain model structures, parameters, and unmeasurable/unmeasured variables. On longer timescales, scheduling (Zantye et al., 2019) and planning (Wu et al., 2015; Xuan et al., 2022; Zhang et al., 2019) schemes have been proposed for PCC, which generally address price and demand uncertainties. As per the literature, uncertainty has only been considered for online economic optimization of PCC in the context of EMPC (Decardi-Nelson and Liu, 2022); however, no study has considered uncertainty in an RTO-operated PCC process. The effect of uncertainty in real-time steady-state decision making (i.e., not scheduling or planning time horizons) for PCC is unknown.

While the models used in RTO are often mechanistic, there is no guarantee that the model parameters are near their true values; hence, parameters estimation schemes must be considered to improve the RTO's predictions. Indeed, for a PCC system being modelled mechanistically, Hughes et al. (2022) recently showed the importance of parameter accuracy through uncertainty quantification of mass transfer and kinetic parameters and their impacts on the effectiveness of carbon capture. To this end, RTO schemes typically employ the so-called 'two-step' approach, whereby a parameter estimation (PE) layer is employed to update RTO model parameters periodically. Previous RTO implementations for PCC, have not considered the estimation layer of the two-step approach (i.e., they have assumed perfect parameters and measurable disturbances). In most of the cases, this is a strong assumption as online measurement of some disturbances (e.g., compositions) or perfect knowledge of model parameters (e.g., thermodynamic activities or mass transfer parameters) are not realistic. As such, this assumption remains to be addressed such that the PCC RTO is fully implementable in a real-life scenario. In contrast, cases with rapidly

fluctuating parameters and economics make the two-step approach for RTO unsuitable as set points can quickly become suboptimal. Instead, a robust optimization approach could be deployed for this task. However, robust optimization, which has been an active research consideration for PCC in longer timescales, has also yet to be considered in context of RTO.

3. Robust Control of a CO_2 Capture Absorber

In this work, we focus on a monoethanolamine (MEA)-based chemical absorption PCC method, for which the chemistry and process have been extensively studied (e.g., Dugas, 2006; Hikita et al., 1997). These studies have enabled the development and verification of mathematical models, which in turn, can be used for model-based optimization and control as presented herein.

One optimization approach that has not been considered to make the MEA-based PCC plant robust through its control is the multi-scenario approach. In general, scenario-based approaches are commonly used when considering robust operation using MPC under uncertainty whereby an optimal controller considers multiple discrete realizations of uncertainty and aims to find optimal control actions that can accommodate all the pre-specified uncertainty realizations. The multi-scenario approach, as implemented in the present work, has previously been used for a large-scale nonlinear model of an air separation unit (Huang et al., Biegler, 2009), and linear hydrodynamic model for water resource management (Tian et al., 2017). To the authors' knowledge, the past robust controllers applied to the MEA PCC plant have used linear and reduced-order models while this study uses a nonlinear dynamic mechanistic model for this process. Such a model enables the controller to explicitly address uncertainty where it is most likely to occur; in parameters associated to specific chemical phenomena and in the process operating conditions dictated by upstream units.

The aim of this study is to use a mechanistic dynamic model to implement and assess the performance of a robust NMPC on the absorber in an MEA-based PCC pilot-scale plant. To the authors' knowledge, this is the first study that has implemented robust control in the MEA-based PCC process (or any other CCS process) with the multi-scenario approach while using the actual mechanistic model of the process. This work explicitly accounts for exogenous uncertainty that will affect the absorber daily owing to changes in operating policies of the upstream emission-producing plant (e.g. rapid changes in flue gas flowrates and uncertainty in flue gas composition); as well as endogenous parametric uncertainty in the plant model via its thermodynamic properties.

3.1. MEA-based Absorber Model

The dynamic mechanistic model used in this work was adapted from Harun et al. (2012) and describes an MEA-based CO_2 absorber unit in a PCC pilot plant as a packed column. The arrangement and operating conditions are based on the pilot plant studied by Dugas (2006). The model is a partial differential algebraic system of equations (PDAEs) as it is composed of ordinary (ODEs) and partial differential equations (PDEs) as well as algebraic equations (AEs).

The absorber, shown in Figure 3-1, operates at atmospheric inlet pressure and has four components: monoethanolamine (MEA), carbon dioxide (CO_2), water (H_2O), and nitrogen gas (N_2), which are denoted as the set $i = \{MEA, CO_2, H_2O, N_2\}$. The column has two inlet and two outlet streams located at the bottom and the top of the column's axial domain ($z(m)$), which are at $z = 0$ and $z = H$, respectively. The top inlet stream, referred to as the "lean" amine stream, consists of a liquid phase mixture of MEA, CO_2, and H_2O. In the full PCC plant, this stream comes from a storage tank that mixes fresh MEA with the recycled MEA from a downstream stripper that regenerates and recycles the solvent. The bottom inlet of the column, referred to as the flue gas stream, consists of CO_2, H_2O, and N_2. This gaseous mixture comes from an upstream combustion source and contains the CO_2 for removal. The top outlet stream, referred to as the vent gas, consists of unremoved CO_2 as well as H_2O and N_2. The bottom outlet stream,

referred to as the "rich" amine stream, consists of all four components and goes to the aforementioned stripper for isolation of the CO_2 and regeneration of the amine solvent. Inside the column, a small amount of gaseous CO_2 is naturally absorbed into the liquid phase from the gas phase. More importantly, the absorption relies on the reactive mechanism that takes advantage of the weak acid and base properties of the CO_2 and MEA (or other alkanolamines), respectively. These two components react to make a water-soluble salt containing the CO_2, which readily dissolves into the liquid phase rich amine solution. A detailed description of this mechanism can be found in (Vaidya and Kenig, 2007).

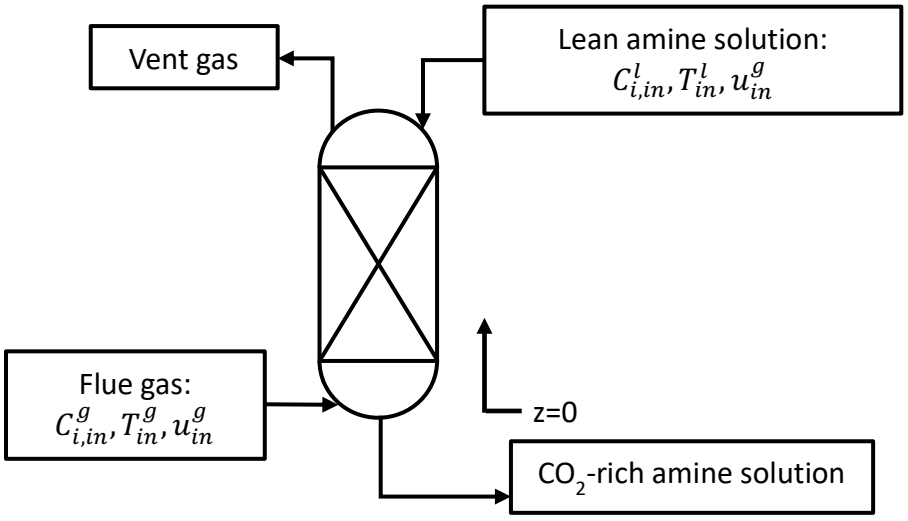

Figure 3-1: Absorber column arrangement with inputs and outputs. Components are MEA, CO_2, H2O, and N2

The absorber model considered in this study operates under the following assumptions:

1. There is turbulent flow within the column, which is approximated as plug flow.
2. The system is modelled as axially distributed and is assumed to be well-mixed in the radial direction.
3. The gas phase is ideal owing to low operating pressures.
4. The pressure drop along the height of the column is linear.
5. N_2 only exists in the gas phase, phase changes occur in all other components in both directions.
6. There is thermal equilibrium between the phases.
7. There is no accumulation in gas and liquid films.
8. The liquid phase has a constant velocity in the axial domain for a given inlet flowrate.

This model consists of molar component balances for the gas and liquid phases, energy balances for the gas and liquid phases, rate equations, chemical kinetic equations, equilibrium equations, and physical property descriptions. These are presented next.

3.1.1. Molar Component Material Balances

The molar component material balances describe the dynamics of the constituent component concentration in each phase owing to chemical reactions, changes in equilibria, and mass transfer. They are as follows:

$$\frac{dC_i^l}{dt} = u_l \frac{\partial C_i^l}{\partial z} + a_w N_i \tag{3-1}$$

$$\frac{dC_i^g}{dt} = -u_g \frac{\partial C_i^g}{\partial z} - a_w N_i - C_i^g \frac{\partial u_g}{\partial z} \tag{3-2}$$

where $C_i^l (mol/m^3)$ and $C_i^g (mol/m^3)$ are liquid and gas molar concentrations of component i, respectively; and $u_l (m/s)$ and $u_g (m/s)$ are liquid and gas velocities, respectively. $a_w (m^2/m^3)$ is the wetted area, while $N_i (mol/m^2/s)$ is the molar flux between phases for component i. The molar flux directions are defined as positive for gains of material in the liquid phase and, accordingly, negative for gains of material in the gas phase.

While the assumptions stated that there is a fixed liquid velocity along the height of the column for a given liquid inlet flowrate, the same is not assumed for the gas velocity since the gas phase is much less dense and loses substantially more momentum as it travels up the column. This decrease in velocity is expressed as a momentum balance for the gas phase:

$$\frac{\partial u_g}{\partial z} = \frac{u_g}{P}\frac{dP}{dz} + \frac{u_g}{T_g}\frac{dT_g}{dz} - \frac{a_w}{C_{tot}^g}\sum_{i=1}^{4} N_i \tag{3-3}$$

where $P(bar)$ is the absorber pressure as a function of position in the axial domain, $T_g(K)$ is the gas phase temperature, and $C_{tot}^g = \sum_{i=1}^4 C_i^g \ (mol/m^3)$ is the total gas concentration.

3.1.2. Energy Balances

The energy balances describe the dynamics of the temperatures of the two phases owing to chemical reactions, equilibria, and heat transfer. They are stated as follows:

$$\frac{dT_l}{dt} = u_l \frac{\partial T_l}{\partial z} - \frac{a_w}{\sum_{i=1}^4 c_{p,i}^l C_i^l}\left[h_{gl}\left(T_l - T_g\right) + \Delta H_{rxn} N_{CO_2} - \Delta H_{H_2O}^{vap} N_{H_2O} + h_{out}(T_l - T_{amb})\right] \tag{3-4}$$

$$\frac{dT_g}{dt} = -u_g \frac{\partial T_g}{\partial z} + \frac{a_w}{\sum_{i=1}^4 c_{p,i}^g C_i^g}\left[h_{gl}\left(T_l - T_g\right)\right] \tag{3-5}$$

where $T_l(K)$ is the liquid phase temperature, $h_{gl}(J/mol/K)$ is the interfacial heat transfer coefficient given by the Chilton-Colburn heat and mass transfer analogy (Geankoplis, 2003), and $T_{amb}(K)$ is the temperature of the surroundings. $c_{p,i}^l (J/mol/K)$ and $c_{p,i}^g (J/mol/K)$ are the liquid and gas specific heat capacities of component i, respectively; N_{CO_2} and N_{H_2O} are the molar fluxes of CO_2 and H_2O, respectively, calculated using the two-film mass transfer model. $\Delta H_{rxn}(J/mol)$ is the molar heat of reaction, $\Delta H_{H_2O}^{vap}(J/mol)$ is the molar heat of vaporization of water, and h_{out} (W/m^2/K) is the heat transfer coefficient between the absorber and its surroundings.

3.1.3. Mass Transfer

The two-film model gives the rate of mass transfer within the absorber for all components excluding N_2, as it is assumed to only occur in the gas phase. The model is stated as follows:

$$N_i = K_i^g (p_i - p_i^*) \tag{3-6}$$

$$\frac{1}{K_i^g} = \frac{1}{k_i^g} + \frac{He_i}{k_i^l E_{abs}} \tag{3-7}$$

where $K_i^g (mol/m^2/Pa/s)$ is the overall mass transfer coefficient for the gas phase while $k_i^g (mol/m^2/Pa/s)$ and $k_i^l (m/s)$ are the binary gas and liquid mass transfer coefficients for component i, respectively. $p_i (kPa)$ and $p_i^* (kPa)$ are the partial and equilibrium pressures for component i, respectively. $He_i (kPa\ m^3/mol)$ is the Henry's law constant for component i. The use of an overall mass transfer coefficient eliminates the need to calculate interfacial concentrations and, as stated earlier, transfer from the gas to the liquid phase was used as the convention for positive mass transfer. The model assumes that resistance to mass transfer for liquid H_2O and MEA is negligible because these components have a higher solubility; thus, most of their resistance to mass transfer occurs in the gas phase (Harun et al., 2012).

As mentioned above, the acid-base chemical reactions between CO_2 and MEA described by Austgen et al. (1989) dictates the amount of CO_2 absorbed in the liquid phase solvent. The effect of this increase is captured by the enhancement factor (E_{abs}), which represents an approximate analytical solution to the differential equations governing the diffusional mass transfer and chemical reactions occurring in the liquid film. The enhancement factor is valid under the pseudo-first order reaction scheme with respect to CO_2; which is valid in the situation where an alkanolamine is absorbing CO_2 in a packed column, owing to the increased mixing afforded by the packing (Kvamsdal et al. 2009). This scheme is facilitated by low CO_2 partial pressure, high reactant concentration, and short contact times; thus, ensuring that mass transfer is enhanced by the reactions while not depleting the amine concentration. The volume of amine is considered constant throughout the film and equal to that of the bulk phase. The enhancement factor is given by:

$$E_{abs} = \frac{\sqrt{k_2 C_{MEA}^* D_{CO_2}}}{k_{CO_2}^l} \tag{3-8}$$

where $k_2 (m^2/mol/s)$ is the second-order reaction rate constant and $C_{MEA}^* (mol/m^3)$ is the liquid molar concentration of free MEA, both calculated from Hoff et al. (2004). $D_{CO_2} (m^2/s)$ is the diffusivity of CO_2 in the MEA solution.

3.1.4. Equilibria

The dynamic model considers chemical and phase equilibria together. Chemical equilibrium describes the balance between ionic and molecular species in the liquid phase while phase equilibrium describes the balance between phases at the gas-liquid interface. For H_2O and MEA, the equilibrium pressure at the interface is expressed as follows:

$$p_i^* = x_i \gamma_i p_i^{vap} \tag{3-9}$$

where x_i, γ_i, and $p_i^{vap} (kPa)$ are the liquid fraction, activity coefficient, and vapor pressure of component i, respectively. Since the temperature of the system exceeds the supercritical temperature of CO_2, it does not exist in the liquid phase. Instead, the equilibrium pressure of CO_2 is calculated using Henry's law:

$$p_{CO_2}^* = He_{CO_2} C_{CO_2}^* \gamma_{CO_2} \tag{3-10}$$

where $C^*_{CO_2}(mol/m^3)$ is the liquid molar concentration of free CO_2 from Hoff et al. (2004), and γ_{CO_2} is the activity coefficient of CO_2.

3.1.5. Physical Properties, Absorber Design and Model Inputs

Table 3-1 lists the physical properties used in the model, their sources, and values (if constant). Variable physical properties are calculated using correlations provided in the corresponding reference. Table 3-1 also lists the packed column design characteristics as used in this study. Additionally, Table 3-2 lists the required inputs for the model, which come in the form of initial conditions and inlet (boundary) operating conditions. Initial conditions are obtained from measurements/estimates from the absorber while operating conditions are obtained from measurements/estimated from upstream units.

Table 3-1: Physical properties and design characteristics used for the absorber column model.

Physical Property	**Value**	**Source**
Ambient Temperature (K)	$T_{amb} = 297.6$	Harun et al. (2012)
Heat transfer coefficient between absorber and surroundings (W/m2/K)	$h_{out} = 430$	Kvamsdal and Rochelle (2008)
Molar heat of reaction (kJ/mol)	$\Delta H_{rxn} = 48$	Kvamsdal and Rochelle (2008)
Molar heat of vaporization (kJ/mol)	$\Delta H^{vap}_{H_2O} = 82$	Poling et al. (2007)
MEA activity coefficient	$\gamma_{MEA} = 0.677$	Aspen Property Package
CO_2 activity coefficient	$\gamma_{CO_2} = 0.381$	Smith et al. (2005)
H_2O activity coefficient	$\gamma_{H_2O} = 0.974$	Smith et al. (2005)
Wetted area (m^2/m^3)	a_w	Onda et al. (1968)
Liquid component heat capacity ($J/mol/K$)	$c^l_{p,i}$	Hilliard (2008)
Gas component heat capacity ($J/mol/K$)	$c^g_{p,i}$	Aspen Property Package
Liquid component mass transfer coefficient (m/s)	k^l_i	Onda et al. (1968)
Gas component mass transfer coefficient ($mol/m^2/Pa/s$)	k^g_i	Onda et al. (1968)
Component Henry's law constant ($kPa\ m^3/mol$)	He_i	Haimour and Sandall (1984)
Second-order reaction rate constant ($m^2/mol/s$)	k_2	Hikita et al. (1977)
CO_2 diffusivity in solvent solution (mol/m^3)	D_{CO_2}	Ko et al. (2001)
Component vapour pressure (bar)	p^{vap}_i	Aspen Property Package
Design Characteristics		

Column internal diameter (m)	0.43	Cerrillo-Briones and Ricardez-Sandoval (2019)
Packing height (m)	6.1	Cerrillo-Briones and Ricardez-Sandoval (2019)
Packing type	IMTP #40	Cerrillo-Briones and Ricardez-Sandoval (2019)

Table 3-2: Model inputs: initial and operating conditions required

	Initial Condition $(\mathbf{0} \leq \boldsymbol{z} \leq \boldsymbol{H}, \boldsymbol{t} = \mathbf{0})$	***Boundary Condition*** $(\boldsymbol{z} = \mathbf{0}, \boldsymbol{z} = \boldsymbol{H}, \boldsymbol{t} \geq \mathbf{0})$
Gas	$C_i^g(z,0) = C_{i,o}^g(z)$	$C_i^g(0,t) = C_{i,in}^g(t)$
	$T^g(z,0) = T_o^g(z)$	$T^g(0,t) = T_{in}^g(t)$
		$u^g(0,t) = u_{in}^g(t)$
		$P^g(0,t) = P_{in}^g(t)$
Liquid	$C_i^l(z,0) = C_{i,o}^l(z)$	$C_i^l(H,t) = C_{i,in}^l(t)$
	$T^l(z,0) = T_o^l(z)$	$T^l(H,t) = T_{in}^l(t)$
		$u^l(z,t) = u_{in}^l(t)$

The outlined PDEs that comprise the mass and energy balances (equations (3-1)–(3-5)) are denoted as $\boldsymbol{f_d}$ along with the AEs that comprise the process phenomena (equations (3-6)–(3-10)) and physical property (Table 3-1). This set of equations represent the mechanistic model for this process, which require the column design specifications and initial/boundary conditions presented in Table 3-1and Table 3-2, respectively.

3.2. Robust NMPC

In the present work, a nominal NMPC formulation will be implemented along with the multi-scenario formulation for comparison. By nominal NMPC, we refer to an NMPC controller that includes no measures for dealing with uncertainty in the formulation (it assumes that its parameters are known *a priori*). We begin by defining the multi-scenario NMPC and subsequently presenting the nominal NMPC as a special case. Generally, an NMPC uses a nonlinear dynamic process model to determine optimal control actions that minimize a loss function, e.g., set-point tracking errors in the controlled variables. In the case of the multi-scenario NMPC, the controller considers multiple realizations of the model's uncertain parameters, which results in instances of the process model denoted by the set "r". The operation of the NMPC in the feedback control strategy is depicted in Figure 3-2, which shows a control structure operating at a time t in the operation of a process where an NMPC receives measurements or estimates of the plant states $\boldsymbol{x_0}$ as initial conditions for the model, as well as the set points for the controlled variables $\boldsymbol{y_{sp}}$. This information is included in the formulation of the optimal control problem. For a multi-scenario discrete-time NMPC at sampling time t , this problem is as follows:

$$\min_{\boldsymbol{u_{t+i}} \forall i \in \{1,\dots,P\}} \sum_{r=1}^{S} \omega_r \sum_{i=1}^{P} \left\| \widehat{\boldsymbol{y}}_{\boldsymbol{t+i,r}} - \boldsymbol{y_{sp}} \right\|_{\boldsymbol{Q_c}}^2 + \sum_{i=1}^{P} \left\| \Delta \boldsymbol{u_{t+j}} \right\|_{\boldsymbol{R_c}}^2 \tag{3-11}$$

$s.t.$

$$\boldsymbol{f_{d,r}}\left(\widehat{\boldsymbol{x}}_{\boldsymbol{t+i,r}}, \boldsymbol{u_{t+j}}, \widehat{\boldsymbol{y}}_{\boldsymbol{t+i,r}}, \boldsymbol{\theta_r}\right) = \widehat{\boldsymbol{x}}_{\boldsymbol{t+i+1,r}} \qquad \forall i \in \{0, \dots, P-1\}, \forall r \in \{1, \dots, S\}$$

$$\widehat{\boldsymbol{x}}_{\boldsymbol{t}} = \boldsymbol{x_0}$$

$$\boldsymbol{g_{d,r}}\left(\widehat{\boldsymbol{x}}_{\boldsymbol{t+i,r}}, \boldsymbol{u_{t+j}}, \widehat{\boldsymbol{y}}_{\boldsymbol{t+i,r}}, \boldsymbol{\theta_r}\right) \leq \boldsymbol{0} \qquad \forall i \in \{1, \dots, P\}, \forall r \in \{1, \dots, S\}$$

$$\boldsymbol{u^l} \leq \boldsymbol{u_{t+j}} \leq \boldsymbol{u^h} \qquad \forall i \in \{1, \dots, P\}$$

$$\boldsymbol{u_{t+i+1}} = \boldsymbol{u_{t+i}} \qquad \forall i \in \{C, \dots, P-1\}$$

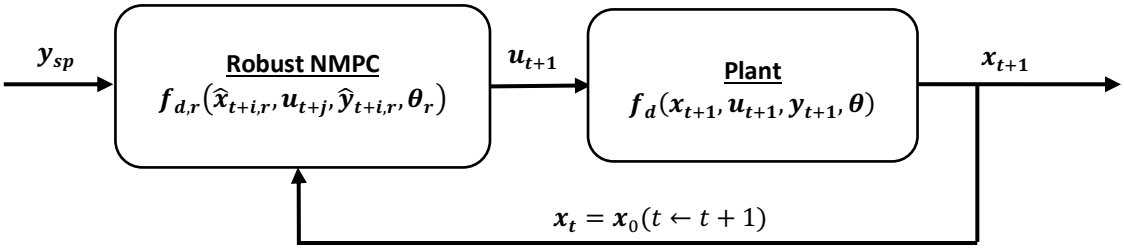

Figure 3-2: Feedback loop between the simulated plant and multi-scenario NMPC. NMPC dependent on "r" while plant is not.

where $\|\boldsymbol{X}\|_{\boldsymbol{A}}^2$ denotes a quadratic form on vector $\boldsymbol{X} \in \mathbb{R}^n$ with the weighting matrix $\boldsymbol{A} \in \mathbb{R}^{n \times n}$. $\widehat{\boldsymbol{x}}_{\boldsymbol{t+i,r}} \in \mathbb{R}^{n_x}$ represents the predicted states (differential variables) for each model realization, $\widehat{\boldsymbol{y}}_{\boldsymbol{t+i,r}} \in \mathbb{R}^{n_y}$ are the predicted controlled variables for each model realization, and $\boldsymbol{\theta_r} \in \mathbb{R}^{n_\theta}$ are the uncertain model parameters. Note that these variables are defined as across the set "r", representing the various model realizations corresponding to each realization in the uncertain parameters. $\boldsymbol{y_{sp}} \in \mathbb{R}^{n_y}$ are the user-defined set points for the controlled variables, and $\widehat{\boldsymbol{x}}_{\boldsymbol{t}} \in \mathbb{R}^{n_x}$ are the measured or estimated states used as the initial condition. Note that these variables are not indexed across the set "r" as they are externally acquired thus realization independent (they have the same value for all realizations). $\boldsymbol{x_0} \in \mathbb{R}^{n_x}$ is the state vector acquired from the simulated plant, which is set as equal to $\boldsymbol{x_t}$ for every NMPC execution thereby enabling feedback to the controller. $\Delta\boldsymbol{u_{t+i}} \in \mathbb{R}^{n_u}$ is the vector of changes in the manipulated variables ($\Delta\boldsymbol{u_{t+i}} = \boldsymbol{u_{t+i}} - \boldsymbol{u_{t+i-1}}$). The controller tuning parameters include diagonal positive semidefinite matrices $\boldsymbol{Q_c} \in \mathbb{R}^{n_y \times n_y}$ and $\boldsymbol{R_c} \in \mathbb{R}^{n_u \times n_u}$, which affect set-point tracking and control move suppression, respectively. P and C, which denote the prediction and control horizons as integer multiples of the sampling intervals, respectively, also serve as tuning parameters as they can affect the controller's performance. $\sum_{r=1}^{S} \omega_r = 1$ are nonnegative weights for different uncertainty realizations where M is the user-defined number of realizations that the NMPC considers. As mentioned above, these realizations represent instances of the process model that the NMPC simultaneously considers such that each realization has a unique combination of uncertain parameters. Of the total model parameters, only a user-defined subset is considered uncertain, this subset is chosen based on *a priori* process and model knowledge about which parameters are difficult to estimate**.**

By solving the open-loop problem (3-11), an optimal control sequence $\boldsymbol{u_{t+1}}, \dots, \boldsymbol{u_{t+C}}$ is obtained for the user-defined control horizon C; beyond this horizon, the manipulated variables are assumed constant, hence the last constraint in equation (3-11). The optimization problem from which this optimal sequence is acquired is subject to the system of constraints composed of the aforementioned DAE system $\boldsymbol{f_d}$ and $\boldsymbol{g_d}$, as well as input constraints $\boldsymbol{u^l} \leq \boldsymbol{u_{t+i}} \leq \boldsymbol{u^h}$. $\boldsymbol{f_{d,r}}$: $\mathbb{R}^{n_x} \times \mathbb{R}^{n_u} \times \mathbb{R}^{n_\theta} \rightarrow \mathbb{R}^{n_x}$ denotes the set of nonlinear differential equations describing the evolution of states in

the system, and $\boldsymbol{g_{d,r}}$: $\mathbb{R}^{n_x} \times \mathbb{R}^{n_u} \times \mathbb{R}^{n_\theta} \rightarrow \mathbb{R}^{n_g}$ denotes the set of inequality constraints imposed on the controller (aside from the manipulated variable contraints). $\boldsymbol{u^l}$ and $\boldsymbol{u^h} \in \mathbb{R}^{n_u}$ denote the lower and upper bounds for the manipulated variables and reflect the physical limitations of the process and its controllers. For the multi-scenario NMPC the DAE system composed of $\boldsymbol{f_{d,r}}$ and $\boldsymbol{g_{d,r}}$ contains "r" realizations of the uncertain parameters $\boldsymbol{\theta_r}$. This DAE system is used to predict the process' evolution for a user specified prediction horizon P for the given uncertainty realizations. This enables the objective function to determine the optimal control actions for the given control horizon. As shown in problem (3-11), the objective (loss) function contains two weighted terms: one minimizes quadratic deviation from specified set-points and the other penalizes changes in the control actions. From the optimal control sequence obtained by solving problem (3-11), the first control action $\boldsymbol{u_{t+1}}$ is passed to the plant as depicted in Figure 3-2. The plant is then simulated for a fixed interval Δt using the input $\boldsymbol{u_{t+1}}$ and a nonlinear process model. This simulation enables the plant states to evolve to $\boldsymbol{x_{t+1}}$ and, after the time interval Δt has elapsed, the process of obtaining and giving measurements/estimates to the NMPC is repeated. By using the evolved states $\boldsymbol{x_{t+1}}$ as feedback to solve problem (3-11) again recursively during each time interval Δt , the scheme becomes closed loop. This is shown in the feedback portion of Figure 3-2 where the initial condition is updated as $\boldsymbol{\hat{x}_t = x_0}$ after moving the horizon from t to $t + 1$. In this study, we assume full state and disturbance information availability (i.e., the relevant information needed by the NMPC can be precisely measured or estimated). State estimation for the MEA PCC system remains an open challenge that will be addressed in future work. Note that past NMPC studies on this system (e.g., Åkesson et al., 2012; Chan and Chen, 2018; Decardi-Nelson et al., 2018) have made similar assumptions. Also note that feedback does not necessarily need to occur at every sampling interval; however, more frequent feedback often leads to better control performance.

The mechanism by which the multi-scenario NMPC makes the controller robust is by finding a single optimal control sequence $\boldsymbol{u_{t+1}, \ldots, u_{t+C}}$ that minimizes the objective function for all model realizations given the feedback $\boldsymbol{x_t = x_0}$ from the plant. This unique optimal control sequence accommodates for the user-defined set of possible values that uncertainties parameters may manifest during operation. This makes the control actions robust to uncertainty in the sense that although the "true" parameter values are not ascertained by the NMPC controller, the actions will be well-suited for performance across the defined set of uncertain parameter realizations.

As mentioned above, the nominal NMPC occurs as a special case of the multi-scenario NMPC when only a single scenario is considered with no further safeguards against uncertainty. The single scenario corresponds to a nominal realization of the model uncertain parameters, i.e., $\boldsymbol{\theta_r}\ \forall r \in \{1\}$. This assumption simplifies the formulation and shrinks the model size as variables are no longer indexed across "r", however; it ignores model uncertainty by making the assumption that the model provides a perfect representation of the system. Unfortunately, this is often not the case in practice and may result in non-optimal operation because of poor controller performance. Worse still, this assumption may lead to infeasibility.

Both the nominal and multi-scenario NMPC controllers are implemented in a control loop with plant simulation containing a single realization of the uncertain parameters $\boldsymbol{\theta}$. The nominal and multi-scenario NMPC use the large-scale mechanistic model of the absorber column, consisting of $\boldsymbol{f_d}$ and $\boldsymbol{f_{d,r}}$, respectively. This model has been presented in Section 3.1.

3.3. Model Implementation and Validation

The nominal and multi-scenario NMPC optimization formulations are NLP and were implemented in the Pyomo environment, an optimization library in PYTHON (Hart et al., 2011). The axially distributed, continuous-time differential-algebraic system presented in Section 3.1 was discretized axially into ten finite elements using the backward finite difference method. This discretization was determined in the model validation stage by considering different numbers of finite elements for the axial domain. Since there is a tradeoff when considering discretization resolutions between model size and accuracy, a course axial discretization was used to prevent the model from becoming untenably large when discretized in time. The axially discretized absorber model has 80 states and 1,781 algebraic variables. Likewise, the model was discretized in time into eight elements to a step size of 12.5 seconds using three-point Radau collocation on finite elements for all experiments. The Radau collocation method was chosen because of its high accuracy and built-in functionality in Pyomo. The high-resolution discretization in time is necessary because fast responses are observed owing to the fact that the model represents a pilot-scale plant and disturbances are considered directly at the system boundaries. It was found that step sizes larger than 12.5 seconds presented difficulties to the solvers when solving the NMPC problem and smaller sizes would have increased the problem size, making it unnecessarily large. The interior-point optimization algorithm (IPOPT) (Wächter and Biegler, 2005) was used to search for local solutions of the nominal and robust optimization problems presented in (3-11). The studies presented in this section were performed on an Intel core i7-4770 CPU @ 3.4GHz. The nominal inlet conditions for the pilot-scale absorber model are adopted from Cerrillo-Briones and Ricardez-Sandoval (2019) and are presented in Table 3-3.

Table 3-3: Base case inlet operating conditions

	Flue Gas Inlet ($z = 0$)	***Lean Solution Inlet ($z = h$)***
$\boldsymbol{T_{in}(K)}$	319.17	314
$\boldsymbol{y_{in}^{MEA}/x_{in}^{MEA}(mol/mol)}$	0	0.1
$\boldsymbol{y_{in}^{CO_2}/x_{in}^{MCO_2}(mol/mol)}$	0.175	0.030
$\boldsymbol{y_{in}^{H_2O}/x_{in}^{H_2O}(mol/mol)}$	0.025	0.870
$\boldsymbol{y_{in}^{N_2}/x_{in}^{N_2}(mol/mol)}$	0.8	0
$\boldsymbol{u_{in}(m/s)}$	0.64	0.00473

In order to start the controller tests at realistic points, the inlet conditions stated in Table 3-3 were used to solve a steady-state version of the nominal absorber model. This steady state provided initial conditions for all undisturbed states at which to begin the dynamic plant simulations. Moreover, the NMPC model's performance in the solver is sensitive to how the algebraic variables are initialized in the solver. This is because the optimization problem is large, containing 64,488 nonlinear algebraic equations and 64,497 variables for the nominal (single-scenario) NMPC. Accordingly, prior to starting test scenarios, a feasibility problem is executed and the algebraic variables from this feasibility problem are used to initialize subsequent NMPC solves.

The model was validated at steady state using the base case operating conditions reported by Harun et al. (2012). These validation operating conditions differ from the base case operating conditions used in this study (shown in Table 3-3) as they have altered reference fluid velocities. The lower fluid velocities used in this study result in lower carbon capture rates than those considered in the Harun et al. (2012); however, the results obtained are nevertheless representative of the MEA PCC plant. The model was validated at steady state to compare the outputs to past implementation of the model, the validation outputs are displayed in Table 3-4. The outlet stream values were compared to Cerrillo-Briones and Ricardez-Sandoval (2019) and Harun et al. (2012). The latter of these studies was itself validated using experimental data from an MEA absorption CCS pilot-scale plant from Dugas (2006) and found to be in good agreement.

Table 3-4: Steady-state validation data for the current absorber model using the base case operating conditions from Harun et al. (2012). Model 1: Cerrillo-Briones and Ricardez-Sandoval (2019), Model 2: Harun et al. (2012).

	Vent gas			***Rich amine solution***		
	Current model	Model 1	Model 2	Current model	Model 1	Model 2
Temperature (K)	314.45	314.78	314.15	330.61	328.04	327.76
Total molar flowrate (mol/s)	3.49	3.53	3.47	32.87	31.68	32.87
Mole Fraction						
MEA	0.0001	0	0	0.0981	0.1044	0.1021
CO_2	0.0088	0.0108	0.0085	0.0555	0.0502	0.0503
H_2O	0.0717	0.0761	0.0651	0.8464	0.8452	0.8475
N_2	0.9193	0.9066	0.9264	0	0	0

As shown in Table 3-4, the current model implementation with the base case operating conditions from Harun et al. (2012) is in very good agreement for all output values with both models against which it was tested. The output values predicted by the present model have a 4.012% difference and 2.43% difference from model 1 and model 2, respectively; and there are no egregiously inaccurate values. This also validates the choice of resolution for the axial discretization mentioned above. Based on these results, the model was deemed fit for use in the study.

3.4. Results

In the PCC absorber model presented in Section 3.1, four parameters were considered uncertain. These included the species activity coefficients in the equilibrium pressure relations (γ_{MEA}, γ_{CO_2}, γ_{H_2O}) and the CO_2 flue gas inlet fraction ($y_{in}^{CO_2}$). To the authors' knowledge, this is the first study that explicitly considers uncertainty in these parameters for the post-combustion CO_2 absorber unit. The activity coefficients are featured in the equilibria model (equation (3-9)); an earlier study (Cerrillo-Briones and Ricardez-Sandoval, 2019) established their significant effect on the system's mass transfer rate. The activity coefficients were chosen as uncertain parameters because they typically exhibit

variation with changing operating conditions (Austgen et al., 1989). This potential variation is addressed in the proposed robust NMPC implementation by treating them as uncertain parameters. Meanwhile, the feed fraction is an inlet condition that is likely to be uncertain due to upstream variations in fuel quality (e.g., change in the type of coal) and demands as well as changes in the operating conditions of the fossil-fired power plants. For simplicity, changes in the CO_2 flue gas inlet mole fraction are reflected only in the H_2O gas inlet mole fraction, so they are treated as a single uncertain parameter. This is assumed because any changes in the upstream process will only affect the relative ratio of combustion products in the flue gas (CO_2 and H_2O), while the fraction of the two non-combustible components will be effectively fixed because there is no MEA in the flue gas and N_2 is inert. Table 3-5 contains the nominal values for the uncertain parameters considered in this study.

Table 3-5: Uncertain parameters and their nominal values

Uncertain Parameter ($\boldsymbol{\theta}$)	**Nominal Value ($\boldsymbol{\theta^{nom}}$)**
γ_{MEA}	0.677
γ_{CO_2}	0.381
γ_{H_2O}	0.974
$y_{in}^{CO_2}$	0.175

The nominal NMPC and the multi-scenario NMPC definition from (3-11) were applied to the CO_2 absorber model presented in Section 3.1. The formulation of the former will be omitted for brevity as the requisite assumptions were presented above; however, we define the optimization problem for the latter and is as follows:

$$
\begin{aligned}
&\min_{F_{in,t+i}^{l}\,\forall i\in\{1,\dots,P\}} \sum_{r=1}^{M} \omega_r \left(\sum_{i=1}^{P} \left(\%\widehat{CC}_{t+i,r}(\hat{\boldsymbol{x}}_{\boldsymbol{t+i,r}}) - \%CC_{t+i}^{sp} \right)^2 \right) + \sum_{j=1}^{P} \Delta F_{l,in_{t+i}}{}^2 \\
&s.t. \\
&\boldsymbol{f}_{\boldsymbol{d,r}}\left(\hat{\boldsymbol{x}}_{\boldsymbol{t+i,r}}, F_{l,in_{t+j}}, \boldsymbol{\theta}_{\boldsymbol{r}}\right) = \hat{\boldsymbol{x}}_{\boldsymbol{t+i+1,r}} \qquad \forall i \in \{0,\dots,P-1\}, \forall r \in \{1,\dots,S\} \\
&\hat{\boldsymbol{x}}_{\boldsymbol{t}} = \boldsymbol{x}_{\boldsymbol{0}} \\
&F_{l,in}^{l} \le F_{l,in_{t+i}} \le F_{l,in}^{h} \qquad \forall i \in \{1,\dots,P\}
\end{aligned}
\tag{3-12}
$$

where the manipulated variable is the total liquid feed flowrate F_{in}^{l}, with lower and upper bounds at $F_{l,in}^{l} = 10\ mol/s$ and $F_{l,in}^{h} = 80\ mol/s$, respectively. This input range provides a physically realistic range for the feed rate while allowing for fast control action. Note that the liquid inlet flowrate is typically used in conjunction with the reboiler duty as manipulated variables when considering an entire MEA PCC plant; in this study however, only the former is used however since it directly affects the absorber being studied and is better suited for disturbance rejection and fast control. As shown in Section 3.1, the states defined in the differential model equations $\boldsymbol{f}_{\boldsymbol{d}}$ for which initial conditions $\hat{\boldsymbol{x}}_{\boldsymbol{t}} = \boldsymbol{x}_{\boldsymbol{0}}$ are required are the component phase concentrations and phase temperatures corresponding to equations (3-1), (3-2), (3-4), and (3-5). Similarly, the model contain equations (3-3) and (3-6)–(3-10), along with physical property relations from Table 3-1. The control and prediction horizon were both set as 100 seconds, which discretized into eight time intervals ($P = C = 8$). This was determined based on preliminary uncontrolled step

disturbances tests where the most parsimonious discretization that provided an acceptable resolution for observing dynamics was obtained. The weighting matrices were set as identity matrices of proper dimensions ($\boldsymbol{Q} = I^{n_y \times n_y}$ and $\boldsymbol{R} = I^{n_u \times n_u}$) and, as no underlying distribution of the expected values of the uncertain parameters is available, the realization weighting parameter is assumed to be equal for all realizations ($\omega_1 = \omega_2 = \cdots = \omega_M$); the latter inherently assumes that the uncertain parameter values are uniformly distributed. The controlled output (variable) in the objective function is set as percentage of CO_2 captured from the flue gas, which will have a unique steady state for a given set of initial and operating conditions. This variable is defined as follows:

$$\%CC = \frac{F_{in}^{CO_2} - F_{out}^{CO_2}}{F_{in}^{CO_2}} \times 100\% \tag{3-13}$$

For the multi-scenario controllers tested, it is expected that there will be increasing loss in performance as the controller considers a larger number of scenarios. This performance deterioration manifests as less aggressive control actions and eventual set-point offsets. This effect can be examined by comparing the performance of a nominal NMPC under no plant-model mismatch (i.e., the case where the controller knows the plant parameters perfectly) to the performance of the multi-scenario NMPCs. Since the nominal NMPC has a perfect model of the plant, which results in off-set free tracking, it provides an upper limit for controller performance. Thus, for a given controller tuning, the performance of the nominal NMPC can be used as a benchmark to compare the performance of controllers that do result in offset (i.e., robust NMPC controllers and NMPC controllers that consider a plant-model mismatch). To quantify the performance degradation of the robust controller, the price of robustness was used, i.e., the percent difference in performance of the robust controller relative to the nominal NMPC controller. It is expected that the price of robustness (PoR) will increase to reflect increasing conservativeness of multi-scenario NMPCs as they consider more uncertainty realizations in their formulation. PoR is defined as follows:

$$PoR = \left| \frac{J_{robust} - J_{Nominal}}{J_{Nominal}} \right| \times 100\% \tag{3-14}$$

where "J_{robust}" and "$J_{nominal}$" are the performance indices of a given controller. This robust control PoR is designed to be analogous to the same concept used robust optimization, which quantifies the loss in performance incurred by computing a robust (as opposed to deterministic) solution (e.g., Schöbel and Zhou-Kangas, 2021). These terms are defined as the sum of squared errors with respect to a CO_2 removal percentage set-point over a time period (T), i.e.

$$J_c = \sum_{i=0}^{T} (\%CC_i - \%CC_{sp,i})^2, \quad \forall c = \{nominal, robust\} \tag{3-15}$$

Percent offsets from the desired set-point at the final steady state of simulation were also used for assessment of the robust NMPCs tested. Another factor to consider when using multi-scenario controllers is the increase in size of the multi-scenario NMPC optimization problem. The size of the problem increases proportionally to the number of realizations considered by the controller, thereby increasing the CPU time to solve each optimization problem. Accordingly, averaged CPU times for NMPC executions were also recorded to assess performance in a given simulation.

3.4.1. Effect of Size of Uncertainty Region

The effect of the size of the uncertainty region was investigated first. The uncertainty region refers to the symmetric interval box of *a priori* defined values around the nominal parameter values in which the uncertain parameters are bounded in a multi-scenario formulation (i.e., $\boldsymbol{\theta} \in [(1-\alpha)\boldsymbol{\theta^{nom}}, (1+\alpha)\boldsymbol{\theta^{nom}}]$), where the parameter α is used to represent the size of the uncertainty region. Given increasing sizes of uncertainty regions α, the robust controller performance is expected to degrade since the uncertain parameters are able to take on a wider range of values, which the controller must accommodate for. The source of the performance degradation is of interest as it could manifest as less aggressive control action or set-point offset.

As mentioned above, a nominal NMPC was designed with the uncertain parameter values set to their corresponding nominal parameters (Table 3-5), which were the same values used in the plant for this scenario. This corresponds to the operational case where the model describes the plant perfectly, which may rarely occur in practice. As can be seen in Table 3-6, the nominal NMPC has no set-point offset in the %CC controlled variable. As mentioned above, the performance of the nominal NMPC was used to determine the PoR to compare multiple three-realization multi-scenario NMPCs that were also tested in the plant simulation. The three-realization multi-scenario NMPCs tested had increasingly large uncertainty region sizes (i.e., increasing α value). The scenarios in the three-realization controllers were defined at the nominal ($\boldsymbol{\theta^{nom}}$), minimal ($\boldsymbol{\theta^{l}} = (1-\alpha)\boldsymbol{\theta^{nom}}$), and maximal ($\boldsymbol{\theta^{h}} = (1+\alpha)\boldsymbol{\theta^{nom}}$) values of each uncertain parameter for the given size of uncertainty region. These controllers were tested in a disturbance rejection scenario, where two subsequent 5% steps down in total flowrate of flue gas (F_{in}^{g}) were implemented 44 time-intervals (550 s) apart, as displayed in Figure 3-3. The 44 intervals between the steps were used to ensure sufficient time for the $\%CC$ output to reach steady state prior to disturbing the system again. Subsequent smaller steps down were implemented in favor of a single large step for ease of convergence in the IPOPT solver.

Table 3-6: Price of robustness, offset, and CPU time for increasing uncertainty region sizes

$\boldsymbol{\alpha}$	PoR (%)	Offset (%)	CPU time (s)
0 (nominal)	0	0	55.71
0.2	5.74	0.0253	183.14
0.25	9.57	0.0396	192.42
0.3	14.82	0.0568	192.74
0.35	21.77	0.0768	218.73
0.4	29.36	0.0968	208.27

Table 3-6 summarizes the results of these tests. As shown in this table, there is substantial performance degradation as reflected in the increasing PoR for increasing uncertainty region sizes. This degradation comes mostly in the form of offset as displayed in Figure 3-5. While the nominal NMPC shows no offset, each subsequent robust NMPC controller shows an increasing amount of offset with an increased uncertainty region size. A single-scenario NMPC with poorly chosen uncertain parameters (i.e., different than the nominal plant parameters), however, would not exhibit off-set free performance like the one exhibited by the nominal NMPC. This would be analogous to the case where a

NMPC no longer has a perfect plant model (plant-model mismatch) and is where multi-scenario approach can be beneficial; this type of behavior is investigated in the following sections. It can be also observed in Figure 3-4 and Figure 3-5 that the conservatism is not reflected in the aggressiveness (or lack thereof) of the control actions as each plant reaches its new steady state at approximately similar times for all the robust NMPC controllers. These figures also show that small changes in the manipulated variable reflect with quite substantial changes in the controlled variable. The results in Table 3-6 also suggest that there is an increasing price of robustness difference for constant increases in size of the uncertainty region. This nonlinear relationship highlights the need to define an uncertainty region size that covers the expected uncertainty but not so large as to squander the potential benefit of the multi-scenario approach. Moreover, a small increase in mean CPU time per simulation can generally be observed for increased sizes of uncertainty region. A similar effect was observed in a scheduling context by Li and Ierapetritou (2008) and is explained by a decrease in the size of the feasible region making it more difficult to find a solution as robustness requirements increase.

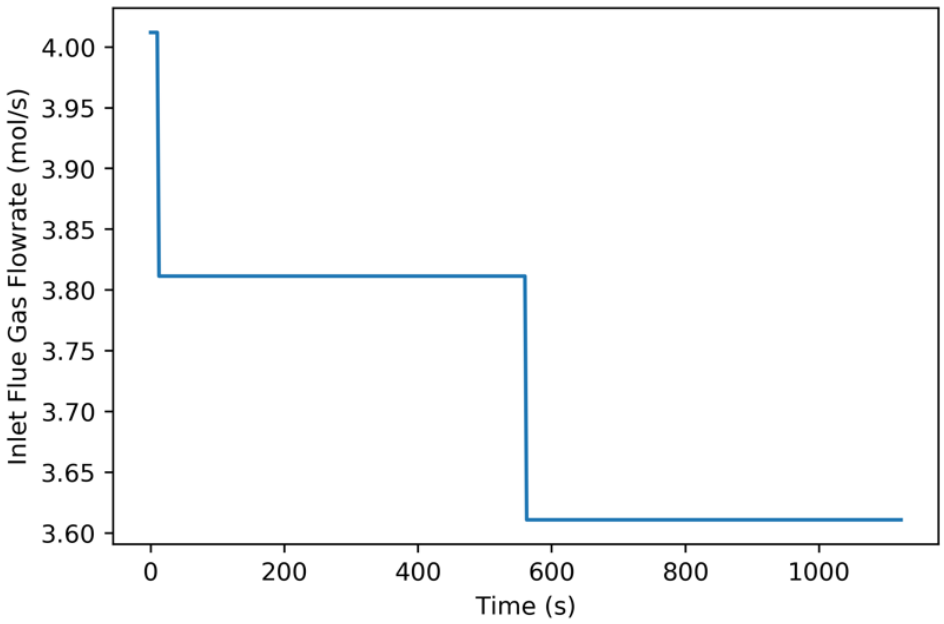

Figure 3-3: Inlet flue gas flowrate (disturbance) for Scenario A (5.1) and Scenario B (5.2)

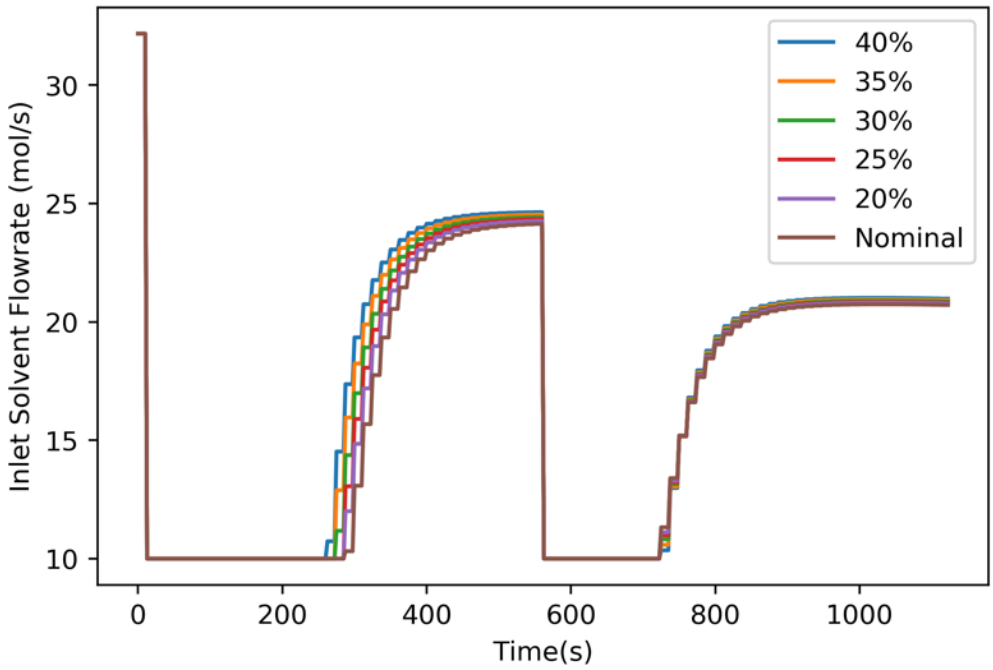

Figure 3-4: Inlet solvent flowrate (manipulated variable) for step-down simulations and increasing uncertainty region size

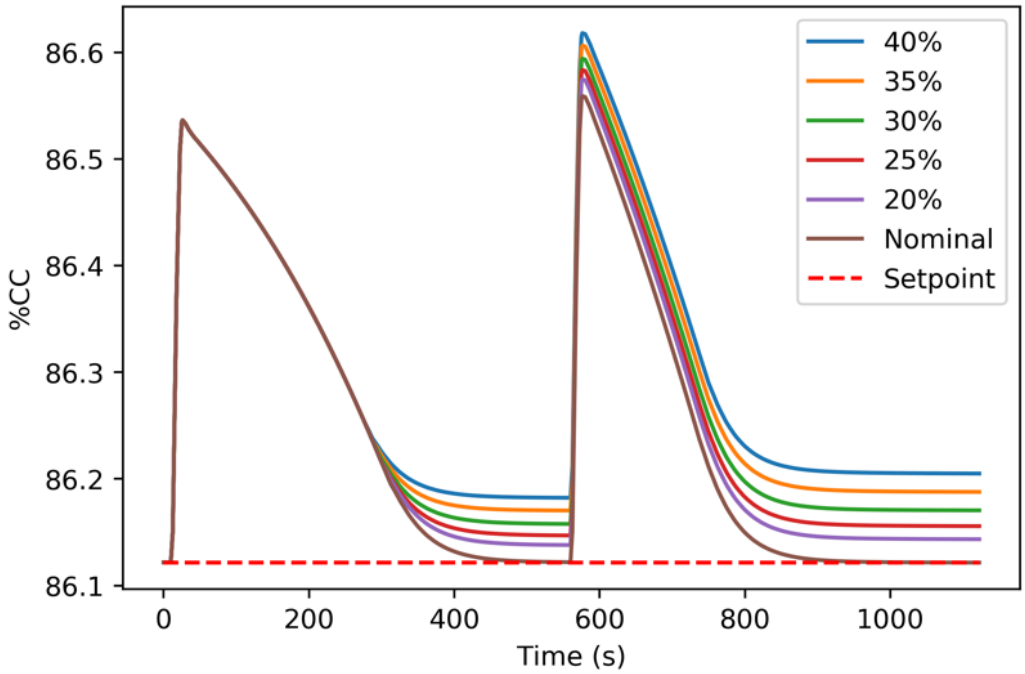

Figure 3-5: Percent Carbon capture (controller variable) for step-down simulations and increasing uncertainty region size

3.4.2. Effect of Number of Realizations

With the effect of uncertainty region size established, the effects of the number of scenarios considered by the controller on performance and CPU time were assessed. The size of the uncertainty region may be different for each parameter. In principle, historical plant data, seasonal and diurnal changes in the process, and process heuristics can be used to determine the size of the uncertainty. However, for the remainder of this work $\alpha = 0.3$ was chosen as the uncertainty region size for all of the uncertain parameters. This uncertainty region size was selected based on a preliminary analysis that showed that a 30% variation in the uncertain parameters represented significant process variability that is often observed during operation. Moreover, from the results of Scenario A, it was concluded that this uncertainty region size represents an acceptable trade-off between uncertainty region size (robustness) and PoR. Each of the uncertain parameters was discretized to its nominal, low or high values to limit the number of possible uncertainty realizations. Even with this limitation, since there exist four uncertain parameters that can occur at either θ^{nom}, θ^{l}, or θ^{h}; there are $3^4 = 81$ possible combinations of these parameters. However, including 81 realizations in a controller is unrealistic as the CPU time would become computationally intractable; thus, the maximum number of realizations allowed for a multi-scenario controller was chosen to be 7 based on observed CPU times and preliminary closed-loop simulations. These realizations are displayed in Table 3-7.

Table 3-7: Possible parameter realizations for the controllers and the plants

	S1 (P1)	**S2 (P2)**	**S3**	**S4 (P3)**	**S5**	**S6 (P4)**	**S7**
γ_{MEA}	θ^{nom}	θ^{h}	θ^{l}	θ^{h}	θ^{l}	θ^{l}	θ^{nom}
γ_{CO_2}	θ^{nom}	θ^{h}	θ^{l}	θ^{l}	θ^{l}	θ^{h}	θ^{nom}
γ_{H_2O}	θ^{nom}	θ^{h}	θ^{l}	θ^{h}	θ^{h}	θ^{nom}	θ^{nom}
$y_{in}^{CO_2}$	θ^{nom}	θ^{h}	θ^{l}	θ^{h}	θ^{h}	θ^{nom}	θ^{l}

These realizations were chosen with the goal of exploring a mix between expected and worst-case combinations of uncertain parameters. That is, the scenarios aim to represent (with only a few realizations), the full set of parameter realizations that may actually occur. It would be desirable to include a large number of these scenarios to make the controller robust; however, this number is limited by the CPU time. Note that the choice of these parameter realizations (as well as the number of realizations) in the controller can drastically affect closed-loop performance. Accordingly, the choice of realizations should be tailored to the specific application, especially when the operator has insight on the potential uncertainty. In this case specifically, each scenario was chosen as it represented a distinct combination of the uncertainty parameters that is significantly different from the other realizations in the uncertain parameter realization set.

While testing the performance of the multi-scenario controllers against a large sample of plants with different parameter realizations would be the best way to assess their benefit, time limitations required only simulating the controllers in a few plants, which itself still required significant computational effort. As such, a sample of four plants with different uncertain parameter realizations was chosen such that it would be as representative as possible to the potential variations in uncertain parameters and such that statistical measures approximately reflected the benefits of

the multi-scenario controller. The chosen simulated plants contained the parameter value realizations in Table 3-7 that correspond to S1, S2, S4, and S6, i.e., P1, P2, P3 and P4, respectively. With regards to the parameter values displayed in Table 3-7, S1 was chosen as it contained only nominal parameter values, S2 was chosen as all values were at the same (high) uncertain region boundaries, S4 was chosen as it contained values that were at different (high and low) uncertainty region boundaries, and S6 was chosen as it contained a mixture of nominal and uncertainty region boundary uncertain parameters.

Robust NMPC controllers with three, five, and seven scenarios were evaluated on the aforementioned plants. Also, an NMPC with uncertain parameters values different that the nominal uncertain parameters was considered. The performance of the robust controllers was tested using the same disturbance rejection tests as in Scenario A, shown in Figure 3-3, with a shorter simulation time of 950 seconds. The shorter simulation time was introduced to cut down on the computational effort required to obtain the results. Nevertheless, it proved to be more than sufficient time for the systems to reach their new-steady state after both disturbances are introduced as shown in the results from Scenario A. In this scenario, however, the controllers were compared based on their performance indices, as displayed in Table 3-8.

*Table 3-8: Performance indices of various NMPCs and multi-scenario NMPCs in different plants (i.e., with different uncertain parameter realizations). The average column represents the average performance index of a given controller in all plants simulated ($\bar{J}_c$), with their respective standard deviations (σ_{J_c}). *Plants where controllers exhibited ringing for the default tuning parameters*

Controller	**Scenario(s)**	J_c **(P1)**	J_c **(P2)**	J_c **(P3)**	J_c **(P4)**	**Average** $\bar{J}_c$	**Std. Dev** σ_{J_c}	**Mean CPU (s)**	**No. of Equations**
C1 (Nominal)	S1	13.044	19.250	14.576	11.940	14.703	3.218	50.9	64,488
C2	S2	32.020	11.126	31.646	20.581	23.843	10.00	57.7	64,488
C3	S1, S2, S3	14.977	15.455	16.475	11.163	14.518	2.322	192.3	193,416
C4	S1, S2, S3, S4, S5	14.679	17.657	15.469	11.969	14.944	2.349	385.7	322,344
C5	S1, S2, S3, S4, S5, S6, S7	15.161	15.700	16.537	11.350	14.687	2.295	718.6	451,272

The results in Table 3-8 show that the mean CPU time increases as the robust controllers takes more realizations into account. This is expected as the size of the problem grows proportionally to the number of scenarios as reflected in the number of equations, thus increasing the size of the search space that the NLP solver must consider. The degrees of freedom for each problem, however, remained fixed at eight (time intervals in the control horizon) regardless of the number of realizations considered in the controller. Nevertheless, since the total model size does grow with realizations, it is crucially important to determine whether the sacrifice in computational effort in the multi-scenario controllers is worth the increased robustness. For instance, consider C2 (an NMPC controller with parameters on the

high end of uncertainty region) and C5 (the seven-scenario controller). The mean performance index across all plants tested is ~1.62 times higher for C2 while the mean CPU time is time is ~12.45 times higher for C5. On face value, it appears that for the additional computational effort required for C5 to be justified, the operator must be placing significant priority to performance. However, this experiment only simulates approximately 16 minutes of plant operation. This is a relatively short amount of time where only two step-changes in the upstream process are introduced into the plant. A longer simulation time, which is unrealistic to perform for all controllers in all plants due to time constraints, would better illustrate the performance disparity between the two controllers. Nevertheless, in a real test scenario the PCC absorber could be operating continuously for days provided that the downstream combustion process is operating.

Despite the large computational cost of C5, very similar performance improvement over C2 was achieved with the three-scenario controller (C3) without as much additional computational burden. The mean performance of C2 is ~1.64 times higher than that of C3, while the mean computational time of C3 is a much more reasonable (compared to C5) ~3.33 times higher than that of C2. This, with C3 the operator would still be placing priority on performance over computational burden but not nearly as much as with C5. As mentioned above, this performance disparity would become increasingly large with longer test times as more error accrues in the performance indices. Although the performance of C3 and C5 are very similar despite much larger mean CPU times for C5, it should be noted that this is likely due to the small sample of plants used in this study. Across a larger set of plants, we would expect to see a clear benefit when using C5 since it is the most robust controller.

As indicated in previously, the uncertain parameters have been chosen to be uniformly distributed with their nominal parameter values in the center of the distribution. As a result, C1, which contains the uncertain parameters' nominal values that are centrally positioned in the uncertainty region; is expected to have some inherent robustness and therefore present good performance in most plant cases (as show in Table 3-8). This is analogous to the case where a NMPC is designed with well-chosen/estimated parameters and is reflected in C1s average performance index ($\overline{J_c}$ in Table 3-8), which is closer to that of the robust multi-scenario controllers (C3,C4, and C5) than that of the other single-scenario controller with large plant-model mismatch (i.e. C2). However, it is not always the case that parameters can be well chosen/estimated, i.e., when the parameter estimation problem is too large, not repeated frequently enough, or when variables are approximated as parameters. To contrast, C2 (i.e., the NMPC with parameter values at the high end of the uncertainty region) was observed to show substantially worse performance than C1, as reflected in the average performance index of C1 which is ~0.617 times that of C2. This is because C2 lacks the inherent robustness imparted on C1 by having centrally located parameter values in the uncertainty region and is analogous to the case where the NMPC is designed with poorly chosen/estimated parameters. Moreover, for C1 and C2, we observe a larger standard deviation in their performance across plants. This is particularly evident in C2 but still noticeable with C1. This means that these controllers show more variation in their performance in different plants (i.e., good performance in some plants and poor performance in others). Take for instance C1, which performs well relative to other controllers in P1 but less so in P2. C1s performance in P1 should be very good as its single scenario contains no plant-model mismatch to P1. However, its performance in P2 is worse because all the parameter values are largely mismatched; the converse can be said about C2. In contrast, the multi-scenario controllers show a more consistent performance

among the different plants tested as reflected in their low deviations for the plant sample although the mean performances indices are very similar to that of C1. Having consistent operation despite uncertainty, such as the proposed robust NMPC enables, is crucial for a process like PCC as its economics and emissions must be controllable to be attractive for industrial implementation. Load changes in the upstream power plant are common and cause these operational disturbances, making it important to consider them on a model level.

Since we are assessing the controllers based on their performance index, it is important to notice that the experiment designed in this section has two subsequent transients and little time for the $\%CC$(controlled variable) to be at steady-state. More time at steady-state and longer simulations times would allow the performance index to accrue more error and the benefits of the robust controllers would be even more pronounced as they would display reduced set point offset. This effect will be shown in the next section as we consider a prolonged test case that the controller might encounter in a real MEA-based PCC absorber's daily operation.

3.4.3. Diurnal Variation in Flue Gas

As stated above, the absorber's operation will occur downstream from a CO_2 emission source resulting in exogenous disturbances to the PCC plant operation. Coal-fired power plants are of specific interest to be retrofitted with PCC units and, as such, the coal-fired power plant will dictate the daily operational variation of the PCC plant. Conveniently, this provides a realistic test case under which the robust NMPC designed for the MEA PCC absorber can be evaluated for a longer operational period than in Section 3.4.2.

Due to diurnal variation in consumer demands, energy consumption occurs in a cyclical manner whereby the demand is highest in the middle of the day and lowest during the night. Similarly, for a region that is dependent on coal-fired power, the demand to the plant will also be cyclical leading to a periodic variation in the quantity of flue gas released. This periodic variation in the flue gas released by the plant provides a periodic disturbance to the MEA PCC plant. An example of region that is reliant on coal-fire power and experiences a diurnal demand variation is the Canadian province of Alberta. Based on single-day data from the Alberta Electric System Operator (AESO), the cycle amplitude of the province's daily internal load is ~8.95% of the midline (average load) (AESO, 2019).

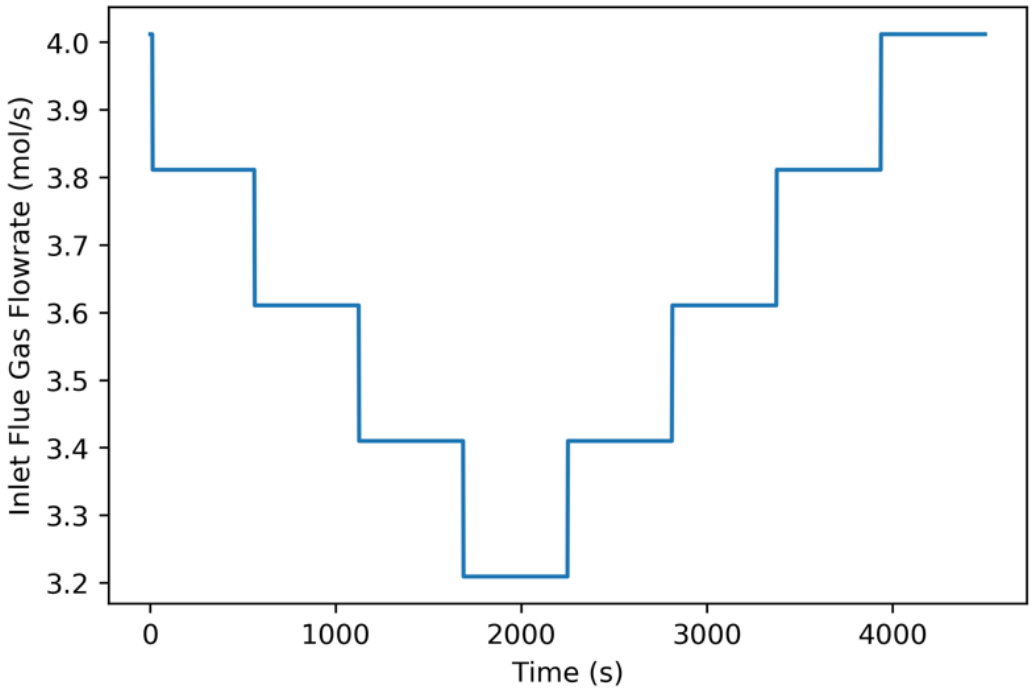

Figure 3-6: Diurnal Inlet flue gas flowrate variation (disturbance) for Scenario C (5.3)

As such, the disturbance in the flue gas flowrate shown in Figure 3-6 was used to approximate the single-day cycle in order to test the efficacy of several controllers for a single cycle. The periodic behavior was approximated as step changes in the flue gas flowrate to the absorber every 45 sampling intervals (~9.4 minutes). The amplitude of the variation in flue gas flowrate was assumed to be 10% of the midline flowrate based on the aforementioned daily observations from AESO. The cycle length was compressed to 75 minutes due to time limitations as a 24h simulation would be prohibitively long. Nonetheless, all controllers were shown to exhibit fast enough responses to reject each step disturbance before a subsequent one was introduced into the system.

For this test case, NMPC controllers involving one and three-scenarios ($\alpha = 0.3$) were implemented. The three-scenario robust NMPC controller was chosen as it could be shown to have benefits over single-scenario NMPCs with plant model-mismatch as demonstrated in Section 3.4.2 while maintaining more acceptable computational costs relative to higher-scenario controllers. Specifically, controllers C1, C2, and C3 (Table 3-8) were implemented in P1, i.e. plant with nominal uncertain parameters (Table 3-7). Moreover, to further elucidate the benefits of the multi-scenario controller more clearly, uncertain parameters values for a second test plant were randomly generated (based on a uniform distribution) inside the 30% uncertainty region. In addition to testing C1, C2, and C3 for a longer simulation in P1, the controllers were also implemented in this plant (P5) using random values in the uncertain parameters. The parameter values for P5 are displayed in Table 3-9.

Table 3-9: Randomly determined uncertain parameter realization for Plant 5

Uncertain Parameter (θ)	$\boldsymbol{\theta_{P5}}$
γ_{MEA}	0.846

γ_{CO_2}	0.453
γ_{H_2O}	1.062
$y_{in}^{CO_2}$	0.182

Table 3-10: Performance indices and CPU times for single-scenario (C1 & C2) and multi-scenario (C3) NMPCs in Plant 1 and Plant 5

Controller	***Scenario(s)***	J_c ***(P1)***	***Mean CPU (s)***	J_c ***(P5)***	***Mean CPU (s)***
C1 (Nominal)	S1	33.143	74.135	66.281	47.427
C2	S2	157.647	79.583	71.593	58.422
C3	S1, S2, S3	39.021	186.750	35.151	202.908

Table 3-10 summarizes the results for this scenario. As expected, the multi-scenario controller (C3) exhibited far better performance than the single-scenario NMPC with plant-model mismatch (i.e., C2) in P1. This was markedly illustrated by the longer simulation length of 75 minutes in this scenario compared to 18.75 minutes in the simulation from Scenario B. This is further exhibited in Figure 3-7,where the performance of C3 when employed in P1 is much more like the performance of the C1 (nominal controller) than that of C2 (controller with plant-model mismatch). Moreover, although the robust controller (C3) requires on average ~2.35 times the computational effort of C2, its performance index is ~0.25 times that of C2, thus justifying the additional computational effort. This reinforces the notion that the robust controller's benefits are more clearly observed over a longer operating window.

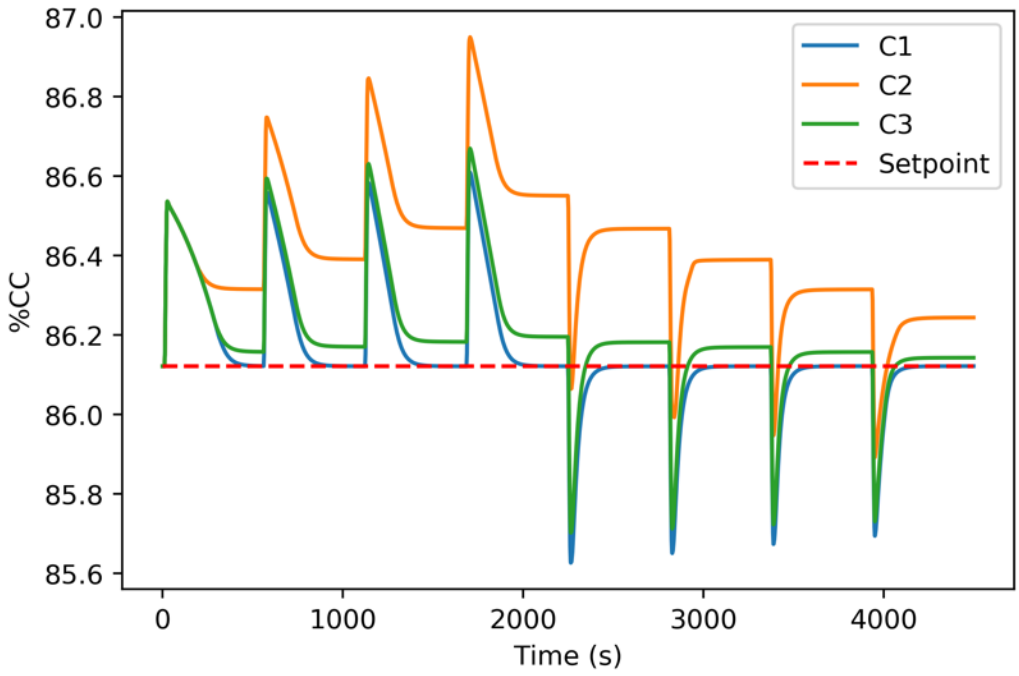

Figure 3-7: Percent Carbon capture for diurnal variation in flue gas simulations in P1

In P5 (random plant uncertain parameter realization), both C1 and C2 performed relatively similarly with respect to performance indices and CPU times as shown in Table 3-10. However, as with P1, the robust NMPC controller (C3) exhibited a better performance index that is half of that observed for C1 and C2. Note that in this case, C1 (nominal NMPC) has plant-model mismatch because plant P5 contains random realizations in the uncertain parameters, which no longer correspond to those in C1. This robustness came at a significant computational cost as each NMPC execution for C3 required ~4 times the CPU time relative to C1 and C2. Nevertheless, as shown in the simulations over a longer operational time, the benefits of a robust NMPC are evident even when only a small number of scenarios are considered. This performance benefit accrues over time and is significant in a plant that operates continuously for several hours or days such as a PCC plant. The simulations performed in this section, although longer than that shown in the previous scenario, are still relatively short compared to the operational time of a PCC plant. Consequently, real plant operation would see even more pronounced benefits from using the multi-scenario approach. As mentioned earlier, consistent performance despite uncertainty is essential to the PCC process. We have demonstrated in this scenario that, given a realistic load following experiment, the robust controller has superior regulatory performance for the %CC set-points. Having robust control, such as that presented in this work, makes the process industrially viable given the importance of economics and emissions.

3.5. Summary

The study herein presents a robust controller for a PCC absorber. This is the first explicit treatment of uncertainty associated with operating conditions and physical property descriptions in the MEA PCC process and it was enabled by the use of a dynamic mechanistic model. Uncertainties in activity coefficients are considered along with disturbance uncertainty in the flue gas inlet flowrate. The multi-scenario approach was used to address uncertainty and several aspects of this formulation where investigated. The size of the uncertainty region was first investigated with step experiments where it is found that increasing uncertainty leads to decreased control performance, primarily through off set. The effect of number of scenarios in the controller was also studies where overall (i.e., across potential uncertainty realizations) performance improvement is observed at the expense of large increased in computational effort. Lastly, a case of diurnal load variation from the power plant to the PCC plant is studied, and the robust controller is found to have better overall performance in this practical scenario. Overall, the deployment of robust controllers like the one presented herein can aid in the operation of PCC to ensure set points are reached accurately to maintain operation at economically optimal levels.

4. Integrated Operating Scheme of a CO_2 Capture System

The control system of the PCC process is crucial in ensuring its productive, safe, and cost-effective operation. As it currently stands, the use of PCC is of net economic detriment to the operation of the upstream power plant with which it is implemented. As such, the economically optimal controlled operation of this process is a crucial aspect that must be investigated to encourage widespread adoption of this technology. This can be achieved using what is known as the two-layer approach whereby real-time optimization (RTO) and model predictive control (MPC) are implemented hierarchically, which will be the focus of this study.

While there are many control studies that investigate the dynamic and controlled behaviour of the PCC system (e.g., Åkesson et al., 2012; Sahraei and Ricardez-Sandoval, 2014), the economically optimal operation of this process has not received as much attention. Some notable works in this field include the economically optimal operation of the entire PCC process by Panahi and Skogestad (2012); similarly, single-layer economic model predictive control (EMPC) strategies have been proposed by Chan and Chen (2018) and Decardi-Nelson et al. (2018). The literature, however, has not yet considered the implementation of a unit-based two-layer approach; whereby the major PCC units are operated with their own RTO and controller. A decentralized approach such as this allows for increased RTO execution frequency as the economic optimization can be performed upon a single unit reaching steady state (instead of the entire system).

Accordingly, the contributions of this chapter are as follows:

1) Jointly address the economic operation, control, and state estimation for general PCC plants operating downstream from fuel-fired power plants by using a mechanistic process model in RTO, NMPC, and MHE layers, respectively. To the authors' knowledge, this is the first operational scheme in PCC (or indeed any CCS) to use an optimal three-layer operational approach and a mechanistic process model in each of the manufacturing layers. The mechanistic process model is well-suited to perform this task as it produces highly accurate decisions and predictions in each of the layers, which results in an effective operation scheme in closed loop. Moreover, RTO is suitable for this system as it is computationally efficient and produces economically attractive set points.

2) Introduce a generalized economic objective function that can be adapted for all PCC plants (i.e., with different designs, solvents, prices, etc.). The proposed economic function brings together the aforementioned aspects of the economics for the first time (i.e., energy, chemical, utility), and includes novel carbon economy factors (i.e., social cost and recoups). A detailed economic model is key when many competing incentives can affect process costs such as in PCC. Using the proposed economic model, the RTO can provide realistic economically optimal steady states for different upstream power plant operations at which to maintain key variables while also incentivizing the removal of CO_2.

3) Design a centralized multivariable control approach for the PCC plant, which enables large disturbances from the power plant to be handled through the manipulation of makeup streams. The proposed NMPC control scheme is advantageous since the PCC system exhibits strong interactions between the manipulated and controlled variables. In addition, the manipulation of both makeup streams, which is a first in this the present study, helps in diluting/concentrating removal solvents to effectively manipulate the removal of CO_2.

4) Introduce the first model-based advanced estimation to be used within a control framework for PCC plants. The scheme consists of an MHE formulation that requires a realistic/accessible set of measurements and can accommodate for a substantial amount of noise. The mechanistic model applied to the estimation layer accurately captures the past process dynamics, which helps in producing highly accurate state estimates for the nonlinear dynamics exhibited in PCC.

The study herein employs the model used in Chapter 3 with some modifications (described in the following sections) to consider stripper-side effects. This economic operation scheme is applied to the absorber section of a pilot-scale PCC plant with approximations of the stripper section effects. The plant and scheme are subjected to scenarios that would occur in PCC plants owing to changes in the power plant including: A) co-firing of coal and biomass, such that the economics of each fuel under the new objective function can be observed; B) diurnal variation in flue gas quantities, which allows for assessment of the scheme performance under upstream power plant load variation; and C) price changes, such that the dependence of the economics on prices can be assessed. These scenarios are primarily assessed using their process economics as it pertains to the improvements in steady-state PCC cost and the associated energy penalty on the power plant imposed by the RTO.

4.1. Proposed Economic Operation Scheme and Formulations

PCC plants are subject to frequent disturbances, which impact the process operation and economics. Operating conditions that were once economically optimal become suboptimal thereby rendering the process set points outdated. For instance, a PCC system that requires a high CO_2 removal set point to maintain good process economics could be subject to a decrease in CO_2 composition in the flue gas. This disturbance would allow for a decrease in the removal set point because of the lower throughput of CO_2. In this situation, the lower removal set point would be an opportunity for savings from chemical materials (i.e., water and solvent consumption) as well as energy costs, which inflate the removal rate. As indicated above, economic detriment posed by the PCC to the upstream power plant remains the main factor in preventing adoption of this technology; thus, economical operating schemes are paramount in inciting its widespread uptake. Figure 4-1 outlines the flow of information of the proposed scheme, described next, which aims to operate the process in an economically optimal fashion while maintaining the closed-loop operation of the plant on target and using few available online measurements.

The PCC plant is subject to disturbances denoted as $\boldsymbol{d_t}$ in Figure 4-1. These disturbances cause the plant to deviate from its predefined set points, which can have economic and safety implications. An advanced model-based controller such as NMPC can be deployed to ensure that the plant meets its operational targets despite the occurrence of these disturbances. At every sampling interval, the NMPC requires access to the full set of model states (i.e., concentrations, temperatures, hold ups); however, only a small portion of the states are often available for online measurements ($\boldsymbol{z_t}$), which are typically corrupted with measurement noise $\boldsymbol{v_t}$. The lack of a full set of measured states to provide to the NMPC requires the use of a reliable state estimation framework that can operate for a wide range of operating conditions. In this work, MHE is employed since it can deal with process nonlinearities that are present in PCC. MHE comprises a dynamic optimization problem that uses the available noisy measurements ($\boldsymbol{z_t + v_t}$, as shown in Figure

4-1) to provide an estimate of the full set of plant states ($\hat{\boldsymbol{x}}_{\boldsymbol{t}}$) at the current time. These estimates are computed such that the model state predictions are consistent with historical process measurements and estimates.

Once the set of states are estimated by the MHE, they are fed to the NMPC as initial conditions ($\hat{\boldsymbol{x}}_{\boldsymbol{t,NMPC}} = \hat{\boldsymbol{x}}_{\boldsymbol{t,MHE}}$, as shown in Figure 4-1) to solve another dynamic optimization problem that determines control actions for the plant. The control actions are computed such that the controlled variables are regulated towards their set points by the process manipulated variables ($\boldsymbol{u}_{\boldsymbol{t+1}}$, as shown in Figure 4-1). The manipulated variables are subsequently passed to the plant, and after a time interval has elapsed (i.e., $t \leftarrow t + 1$), the procedure of measurement, estimation, and control is repeated. This repeated cycle provides constant feedback to the NMPC via the MHE so that the plant behaviour is properly regulated.

On a longer timescale, as the process operation varies significantly owing to the disturbances, operating points must be updated as noted above. When the closed-loop operation of the plant is at steady state, the RTO is triggered such that a new economically optimal steady-state operating point is defined for the plant. The RTO uses steady-state measurements ($\boldsymbol{z}_{\boldsymbol{t}} + \boldsymbol{v}_{\boldsymbol{t}}$) to provide updated controlled variables set points to the NMPC ($\boldsymbol{y}_{\boldsymbol{sp}} = \boldsymbol{y}_{\boldsymbol{RTO}}$, as depicted in Figure 4-1). These set point updates cause the NMPC layer to operate the system dynamically such that the updated controlled variables are eventually reached. Upon reaching these set points, the plant will be operating in an economically optimal manner until a new disturbance occurs. Each of the components of Figure 4-1 is discussed in further detail in the following subsections.

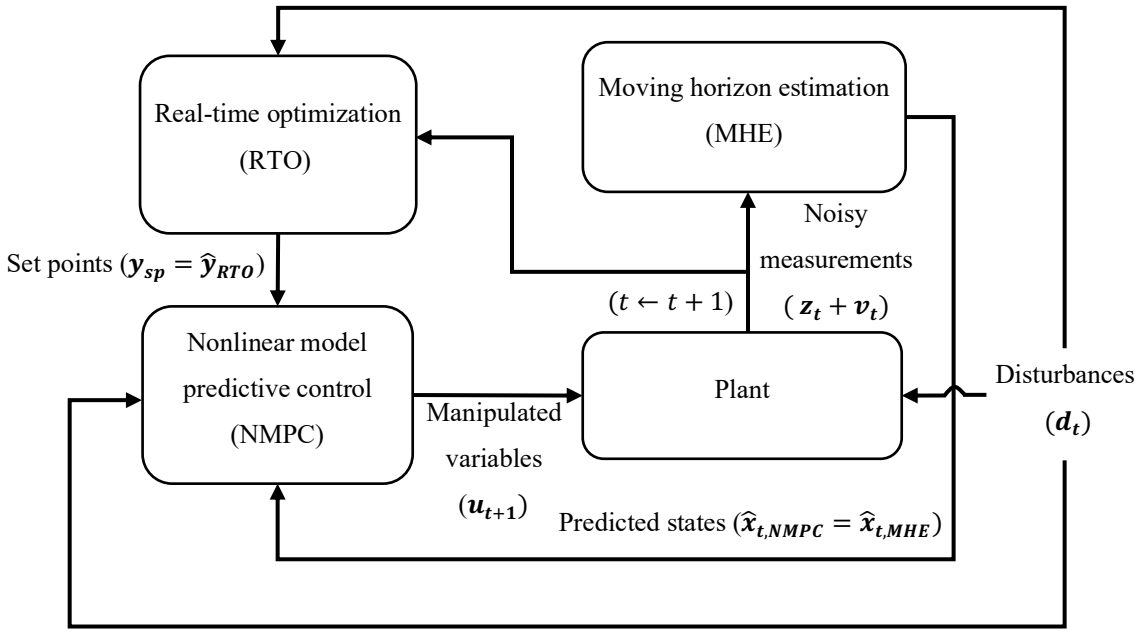

Figure 4-1: Proposed scheme for PCC plants.

4.1.1 RTO formulation

A novel RTO economic function for a general PCC process is introduced along with the RTO formulation, which provides updated set points to the NMPC as depicted in Figure 4-1. The RTO formulation proposed for PCC plants is as follows:

$$\min_{\hat{\boldsymbol{y}}} \sum_i P_{chem,i}\dot{m}_{chem,i}^{mkup}(\hat{\boldsymbol{x}}) + \zeta P_{sales}\dot{m}_{CO_2}^{cap}(\hat{\boldsymbol{x}}) + P_{CO_2}\dot{m}_{CO_2}^{vent}(\hat{\boldsymbol{x}}) + \sum_j P_{energy,j}Q_{energy,j}(\hat{\boldsymbol{x}}) + \sum_k P_{H_2O}\dot{m}_{H_2O,k}(\hat{\boldsymbol{x}})$$

$$s.t. \tag{4-1}$$

$$\boldsymbol{f_s}(\hat{\boldsymbol{x}}, \hat{\boldsymbol{y}}, \boldsymbol{u}, \boldsymbol{d}) = \boldsymbol{0}$$

$$\boldsymbol{g_s}(\hat{\boldsymbol{x}}, \boldsymbol{u}, \boldsymbol{d}) \leq \boldsymbol{0}$$

$$\boldsymbol{y^l} \leq \boldsymbol{y} \leq \boldsymbol{y^h}$$

$$\boldsymbol{u^l} \leq \boldsymbol{u} \leq \boldsymbol{u^h}$$

where $\boldsymbol{f_s}: \mathbb{R}^{n_u} \times \mathbb{R}^{n_d} \longrightarrow \mathbb{R}^{n_x} \times \mathbb{R}^{n_y}$ is the PCC model at steady state, which maps the disturbance variables ($\boldsymbol{d} \in \mathbb{R}^{n_d}$) to the steady states ($\hat{\boldsymbol{x}} \in \mathbb{R}^{n_x}$), manipulated variables ($\boldsymbol{u} \in \mathbb{R}^{n_u}$), and the controlled variables ($\boldsymbol{y} \in \mathbb{R}^{n_y}$). $\boldsymbol{g_s}: \mathbb{R}^{n_x} \times \mathbb{R}^{n_u} \times \mathbb{R}^{n_d} \longrightarrow \mathbb{R}^{n_g}$ denotes the set of inequality constraints (aside from upper and lower bounds) that determine the feasible region for the PCC plant in the RTO framework. $\boldsymbol{y^l}$ and $\boldsymbol{y^h} \in \mathbb{R}^{n_y}$ are the lower and upper bounds for the controlled variables, respectively, whereas $\boldsymbol{u^l}$ and $\boldsymbol{u^h} \in \mathbb{R}^{n_u}$ are the lower and upper bounds for the manipulated variables, respectively. The RTO procedure can also involve a parameter estimation step, which uses the available measurements to estimate uncertain parameters; this step is omitted for brevity.

The objective function lumps the major economic factors present in the PCC process into five categories. Firstly, it considers the fresh feeds of chemical solvents 'i' used for absorption, which are often expensive (e.g., CANSOLV, KS-1, AMP/PZ, etc., Danaci et al., 2021). These chemicals typically perform the removal of the CO_2 via various reactive absorption mechanisms. As such, the first (chemical) cost term is comprised of the fresh feeds of the various chemicals being fed to the process ($\dot{m}_{chem,i}^{mkup}$) along with their respective market price ($P_{chem,i}$).

The second term (sales) represents the recoups that can be made by selling the captured CO_2. This is the first time that this cost has been considered explicitly in an economic optimization function for PCC (it has previously only been considered in technoeconomic analyses e.g., Nwaoha and Tontiwachwuthikul, 2019). As CCS technologies become increasingly mature, a competitive market for the captured product will emerge, thus allowing for emitters to recover some of the losses incurred by the capture process. This term consists of the price of selling captured CO_2, (P_{sales}) and the capture rate of CO_2 ($\dot{m}_{CO_2}^{cap}$). This 'price' is negative as this term represents a profit (contrasted to the other terms which represent a cost). $\zeta \in [0,1]$ denotes an efficiency factor that quantifies the portion of the total CO_2 captured that can be sold.

The third term (carbon) consists of the social cost of carbon (SCC), which includes the market cost of emitting CO_2 as well the non-market negative externalities of emissions. Negative externalities are costs not typically borne by the emitter but by a third-party (e.g., the associated effects on human and environmental health and their remediation) and are largely ignored within most carbon tax frameworks. By taking the social cost into account, the economic burden of these externalities is shifted back to the emitter, thus representing a larger penalty than a carbon tax. This term consists of the price of emitting carbon (P_{CO_2}) and the CO_2 emission rate ($\dot{m}_{CO_2}^{vent}$) via the vent gas. This is the first time that SCC is used in the economic optimization of a PCC process to provide a more complete perspective of the

effects of emissions. Past studies have used simple carbon tax prices (Decardi-Nelson et al., 2018) however, a carbon tax will under-incentivize the removal of CO_2 as it ignores the negative externalities caused by the emission of CO_2.

The fourth (energy) term is comprised of all the energy-intensive units 'j' within the plant (e.g., reboilers, blowers, pumps, preheaters, etc.). This cost term is typically the most significant within PCC plant and is, in fact, the reason why their widespread uptake remains nascent. It consists of the unit price of energy (e.g., steam, electricity, etc., $P_{energy,j}$) as well as the energy consumption requirements (e.g., duty, load, etc., $Q_{energy,j}$). As the proposed scheme does not include a model of the power plant, this energy cost considers the energy requirements of the PCC plant but not its potential effects on the associated energy generation (i.e., the economic effect of taking steam for the PCC that could otherwise be used to produce energy). While the effects of PCC on the power plant are not considered in the RTO decisions, they are nonetheless assessed to ensure that the PCC is hindering the power generation unduly; this is discussed in the following sections.

The fifth (water) term is comprised of all the water-consuming units 'k' within the plant (e.g., makeups, condenser, etc.). This cost term is typically not very significant for PCC plants owing to the low price of water but it is included for completeness. This term consists of the price of water (P_{H_2O}) as well as the water consumption by individual units ($\dot{m}_{H_2O,k}$).

Using the economic function described in formulation (4-1), the RTO determines the set points for the controlled variables ($\boldsymbol{y_{sp}} = \boldsymbol{\hat{y}_{RTO}}$) to pass to the controller, as shown in Figure 4-1. These set points will change significantly as disturbances ($\boldsymbol{d}$) occur. The RTO problem is triggered when the PCC system reaches steady state; to detect steady state, there are various criteria that can be applied as outlined by Rhinehart (2013).

4.1.2 NMPC Formulation

The NMPC uses the dynamic process model to determine the control actions that are used by the plant at every sampling interval to regulate the process. For PCC plants, which are highly nonlinear, an NMPC rather than a linear MPC is preferred to provide quick control actions with little offset.

In NMPC, the manipulated variables act to regulate the controlled variables to the steady-state set points supplied by the RTO ($\boldsymbol{y_{sp}} \in \mathbb{R}^{n_y}$) in the presence of disturbances. The control actions are computed by solving an optimal control problem on a future time horizon whereby the sum of squared errors between the controlled variables and their set points as well as the squared changes in the manipulated variables are minimized. These, respectively, minimize set point offset and manipulated variable movement. To solve this dynamic problem, the mechanistic model requires the full set of process states as initial conditions, which acts as feedback from the plant to the controller; these are estimated by the MHE estimation framework based on the available plant measurements. With the initial conditions, the NMPC model is used to predict the future process behaviour on the future horizon $i \in \{1, \dots, P\}$ (i.e., $\boldsymbol{\hat{x}_{t+1}}, \dots, \boldsymbol{\hat{x}_{t+P}}$) and determine manipulated variable trajectories on the horizon $i \in \{1, \dots, C\}$ (i.e., $\boldsymbol{u_{t+1}}, \dots, \boldsymbol{u_{t+C}}$) that are optimal for the given objective function; these horizons are depicted as $t + P$ and $t + C$ in Figure 4-2, respectively. The first of these manipulated variables values (i.e., $\boldsymbol{u_{t+1}}$, shown at the $t + 1$ marker Figure 4-2) is passed to the plant, which is then operated for a sampling interval ($\Delta t = 1$ interval, as depicted in Figure 4-1). At this new interval, the NMPC is re-

computed, thus moving the horizon forward in time and creating a 'moving horizon'. In the case of a nominal NMPC (as opposed to robust in Chapter 3) with MHE estimates, the formulation solved at every time instance is as follows:

$$\min_{\boldsymbol{u_{t+i}}\forall i\in\{1,\dots,P\}} \sum_{i=1}^{P} \left\|\widehat{\boldsymbol{y}}_{\boldsymbol{t+i}} - \boldsymbol{y_{sp}}\right\|_{\boldsymbol{Q_c}}^2 + \sum_{i=1}^{P} \|\Delta \boldsymbol{u_{t+i}}\|_{\boldsymbol{R_c}}^2$$

$$s.t.$$

$$\begin{aligned}
&\boldsymbol{f_d}(\widehat{\boldsymbol{x}}_{\boldsymbol{t+i}}, \boldsymbol{u_{t+i}}, \boldsymbol{d_{t+i}}, \widehat{\boldsymbol{y}}_{\boldsymbol{t+i}}) = \widehat{\boldsymbol{x}}_{\boldsymbol{t+i+1}} && \forall i \in \{0, \dots, P-1\} \\
&\widehat{\boldsymbol{x}}_{\boldsymbol{t,NMPC}} = \widehat{\boldsymbol{x}}_{\boldsymbol{t,MHE}} && \\
&\boldsymbol{g_d}(\widehat{\boldsymbol{x}}_{\boldsymbol{t+i}}, \boldsymbol{u_{t+i}}, \boldsymbol{d_{t+i}}, \widehat{\boldsymbol{y}}_{\boldsymbol{t+i}}) \leq \boldsymbol{0} && \forall i \in \{1, \dots, P\} \\
&\boldsymbol{y^l} \leq \boldsymbol{y_{t+i}} \leq \boldsymbol{y^h} && \forall i \in \{1, \dots, P\} \\
&\boldsymbol{u^l} \leq \boldsymbol{u_{t+i}} \leq \boldsymbol{u^h} && \forall i \in \{1, \dots, P\} \\
&\boldsymbol{u_{t+i+1}} = \boldsymbol{u_{t+i}} && \forall i \in \{C, \dots, P-1\}
\end{aligned} \tag{4-2}$$

where $\|\boldsymbol{X}\|_{\boldsymbol{A}}^2$ denotes a quadratic form on vector $\boldsymbol{X} \in \mathbb{R}^n$ with the weighting matrix $\boldsymbol{A} \in \mathbb{R}^{n\times n}$. $\boldsymbol{f_d}$: $\mathbb{R}^{n_x} \times \mathbb{R}^{n_u} \times \mathbb{R}^{n_d} \longrightarrow \mathbb{R}^{n_x} \times \mathbb{R}^{n_y}$ is the dynamic mechanistic model (not at steady state as with the RTO). Inputs to problem (4-2) are the initial conditions ($\widehat{\boldsymbol{x}}_{\boldsymbol{t,NMPC}} \in \mathbb{R}^{n_x}$) and disturbances ($\boldsymbol{d_{t+i}} \in \mathbb{R}^{n_d}$) whereas the outputs are the states ($\widehat{\boldsymbol{x}}_{\boldsymbol{t+i}} \in \mathbb{R}^{n_x}$), manipulated variables ($\boldsymbol{u_{t+i}} \in \mathbb{R}^{n_u}$), and controlled variables ($\widehat{\boldsymbol{y}}_{\boldsymbol{t+i}} \in \mathbb{R}^{n_Y}$) on their respective horizon P or C. The disturbances $\boldsymbol{d_{t+i}}$ are denoted with the time index (compared to $\boldsymbol{d}$ in the RTO) as a trajectory of disturbances is required by the NMPC; however, this trajectory in the prediction horizon is assumed to be constant (i.e., $\boldsymbol{d_t} = \boldsymbol{d_{t+1}} = \cdots$) as knowledge of the disturbances cannot be known *a priori* to their occurrence. The feedback from the plant at the beginning of the horizon 't' ($\widehat{\boldsymbol{x}}_{\boldsymbol{t,MHE}} \in \mathbb{R}^{n_x}$) is comprised of measurements and estimates made by the MHE scheme as shown at the t marker in Figure 4-2. The terms $\boldsymbol{Q_c} \in \mathbb{R}^{n_Y \times n_Y}$ and $\boldsymbol{R_c} \in \mathbb{R}^{n_u \times n_u}$ are weights used to tune the controller such that its performance is acceptable. $\boldsymbol{g_d}$: $\mathbb{R}^{n_d} \times \mathbb{R}^{n_x} \times \mathbb{R}^{n_u} \times \mathbb{R}^{n_y} \longrightarrow \mathbb{R}^{n_g}$ denotes the set of inequality constraints (aside from upper and lower bounds) that can be applied to the NMPC-predicted trajectories. As with the RTO in equation (4-1), $\boldsymbol{y^l}$ and $\boldsymbol{y^h} \in \mathbb{R}^{n_y}$ are the lower and upper bounds for the controlled variables, respectively; and $\boldsymbol{u^l}$ and $\boldsymbol{u^h} \in \mathbb{R}^{n_u}$ are the lower and upper bounds for the manipulated variables, respectively; in the future horizon. The NMPC as described in formulation (4-2) provides the control actions ($\boldsymbol{u_{t+1}}$) to the plant by which the set points provided by the RTO can be tracked. It imposes dynamic operation on the plant to reject disturbances ($\boldsymbol{d_t}$) when occur and to change set points ($\boldsymbol{y_{sp}}$) when specified by the RTO. Each execution of the NMPC problem requires feedback from the plant via the MHE such that the full set of plant states are provided as inputs at each time interval (Δt) to the NMPC framework as shown in Figure 4-2. This NMPC differs from the one presented in Section 3.2. in that it only considers a single realization (i.e., it is not robust, hence no explicit dependence on model parameters is shown). This controller also has multiple manipulated and controlled variables; moreover, the tuning between the tracking and suppressions terms is significantly different as will be discussed in the next sections.

4.1.3 MHE Formulation

As noted with the NMPC, most PCC plants (and indeed most CCS processes) exhibit a highly nonlinear behaviour; hence, the state estimation is often subject to substantial process uncertainty for which linear filters (e.g., KF) may be

ill-suited. Moreover, measurements are corrupted with noise and PCC plants are subject to process constraints that must be satisfied during operation (e.g., safety bounds on temperature estimates). MHE is particularly well-suited for these types of problem as it enables the use of a detailed model to handle process nonlinearities, process constraints, and provides substantial smoothing of noise. In the proposed scheme, the MHE uses a dynamic process model to estimate the full state vector at every sampling interval ($\Delta t = 1$ interval) such that it can be supplied to the NMPC as feedback (i.e., $\hat{\boldsymbol{x}}_{\boldsymbol{t,MHE}} \in \mathbb{R}^{n_x}$ is used as initial conditions for the problem in equation (4-2)). This requires that plant measurements be supplied to the MHE at every execution such that it has updated information on the most recent (as well as past) states of the plant. In contrast to the NMPC, which makes future predictions of the process, the MHE esimates the current process state by building a horizon N time intervals into the past, i.e., $k \in \{0, \dots, N\}$ (depicted at the $t - N$ marker in Figure 4-2).

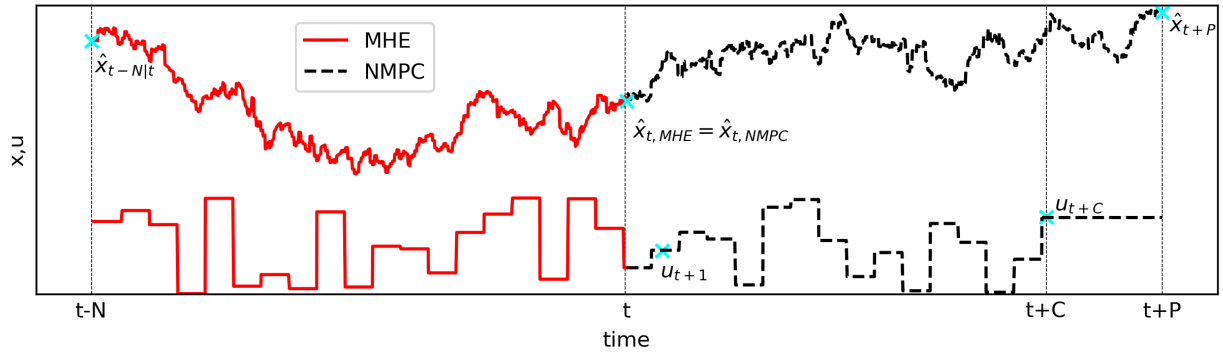

Figure 4-2: Relationship between MHE and NMPC. x denotes a state variable and u denotes a manipulated variable. Cyan X markers denote points of interest. Past of the process denoted in red, future of the process denotes in black.

In the past horizon, the history of the process can be reconstructed through its known measurements, estimates, and control actions; leading to a current state estimate that conforms with past plant behaviour. The MHE formulation solved at every time instance *t* and is as follows:

$$\min_{\substack{\hat{\boldsymbol{x}}_{\boldsymbol{t-N|t}}, \boldsymbol{v}_{\boldsymbol{t-i|t}}, \boldsymbol{w}_{\boldsymbol{t-i|t}} \\ \forall i \in \{0,\dots,N\}}} \sum_{i=1}^{N} \left\| \boldsymbol{v}_{\boldsymbol{t-i|t}} \right\|_{\boldsymbol{Q_e}}^2 + \sum_{i=0}^{N-1} \left\| \boldsymbol{w}_{\boldsymbol{t-i|t}} \right\|_{\boldsymbol{R_e}}^2 + \varphi_{t-N}$$

$s.t.$

$$\boldsymbol{f_d}\left(\hat{\boldsymbol{x}}_{\boldsymbol{t-i|t}}, \boldsymbol{u}_{\boldsymbol{t-i}}, , \boldsymbol{d}_{\boldsymbol{t-i}}, \hat{\boldsymbol{y}}_{\boldsymbol{t-i|t}}\right) = \hat{\boldsymbol{x}}_{\boldsymbol{t-i+1|t}} + \boldsymbol{v}_{\boldsymbol{t-i+1|t}} \qquad \forall i \in \{1, \dots, N\} \qquad (4\text{-}3)$$

$$\boldsymbol{h_d}\left(\hat{\boldsymbol{x}}_{\boldsymbol{t-i|t}}\right) = \boldsymbol{z}_{\boldsymbol{t-i}} + \boldsymbol{w}_{\boldsymbol{t-i|t}} \qquad \forall i \in \{0, \dots, N-1\}$$

$$\boldsymbol{g_d}\left(\boldsymbol{x}_{\boldsymbol{t-i|t}}, \boldsymbol{u}_{\boldsymbol{t-i}}, \boldsymbol{d}_{\boldsymbol{t-i}}, \hat{\boldsymbol{y}}_{\boldsymbol{t-i|t}}\right) \leq \boldsymbol{0} \qquad \forall i \in \{0, \dots, N\}$$

$$\boldsymbol{y^l} \leq \hat{\boldsymbol{y}}_{\boldsymbol{t-i|t}} \leq \boldsymbol{y^h} \qquad \forall i \in \{0, \dots, N\}$$

where $\boldsymbol{z}_{\boldsymbol{t-i}} \in \mathbb{R}^{n_z}$ is the history of the process measurements for the past N time intervals until the time 't' at which the MHE is executed. $\boldsymbol{v}_{\boldsymbol{t-i+1|t}} \in \mathbb{R}^{n_x}$ and $\boldsymbol{w}_{\boldsymbol{t-i|t}} \in \mathbb{R}^{n_z}$ are the process and measurement noise terms on the past horizon, respectively; the square of these noise terms is minimized in the objective function. $\boldsymbol{h_d}$: $\mathbb{R}^{n_x} \longrightarrow \mathbb{R}^{n_z}$ is the observation model and, as with the NMPC, $\boldsymbol{f_d}$: $\mathbb{R}^{n_x} \times \mathbb{R}^{n_u} \times \mathbb{R}^{n_d} \times \mathbb{R}^{n_y} \longrightarrow \mathbb{R}^{n_x}$ is the dynamic mechanistic process model. The inputs to problem (4-3) are the manipulated variable ($\boldsymbol{u}_{\boldsymbol{t-i}} \in \mathbb{R}^{n_u}$), disturbance variable ($\boldsymbol{d}_{\boldsymbol{t-i}} \in \mathbb{R}^{n_d}$),

measurement ($\boldsymbol{z_{t-i}}$), and state ($\boldsymbol{\hat{x}_{t-i|t}}$) histories on the horizon N and the output the current system state ($\boldsymbol{\hat{x}_{t|t}} \in \mathbb{R}^{n_x}$). $\boldsymbol{Q_e} \in \mathbb{R}^{n_x \times n_x}$ and $\boldsymbol{R_e} \in \mathbb{R}^{n_z \times n_z}$ are weighting matrices for the objective function; these are inversely proportional to the process and measurement noise covariances, respectively. Both $\boldsymbol{Q_e}$ and $\boldsymbol{R_e}$ are estimated at every sampling interval based on previous estimates and measurements, respectively. As with the NMPC and RTO, $\boldsymbol{y^l}$ and $\boldsymbol{y^h} \in \mathbb{R}^{n_y}$ are the lower and upper bounds for the controlled variables, respectively. $\boldsymbol{g_d}$: $\mathbb{R}^{n_d} \times \mathbb{R}^{n_x} \times \mathbb{R}^{n_u} \times \mathbb{R}^{n_y} \longrightarrow \mathbb{R}^{n_g}$ denotes the set of inequality constraints (aside from upper and lower bounds) to which the MHE estimates must adhere. $\varphi_{t-N} \in \mathbb{R}$ denotes the arrival cost, which penalizes the MHE for truncating the horizon to a finite length, this can be estimated using a variety of filters as explored in Valipour and Ricardez-Sandoval (2021).

The first (process noise) term in the objective function represents the process uncertainty within the MHE horizon. Moreover, the second (measurement noise) term represents the errors in the MHE state estimates with their associated historical measurements within the estimation horizon. The arrival cost accounts for previous information discarded in the MHE since it was gathered before the current estimation horizon (i.e., historical information of the process prior to $t - N$). By embedding prior available measurements within the MHE problem, the objective function ensures that the current state estimates are consistent with prior state measurements. The resulting MHE state estimates for a given time interval are provided to the NMPC and used as the initial conditions to solve the corresponding optimal control problem. Hence, the future state trajectories predicted by the NMPC begin at the MHE-estimated operating point of the system (as shown where the two trajectories meet in Figure 4-2). Given the estimates provided by MHE at the current time interval 't' ($\boldsymbol{\hat{x}_{t,MHE}}$), the NMPC problem provides the optimal control actions to run the process plant and perform MHE for the next time interval '$t \leftarrow t + 1$'. That is, once the new measurements are available (from the process plant), MHE uses these measurements together with the control actions provided by NMPC to estimate the states that are needed to initialize the NMPC problem. Note that inaccurate initial conditions provided by the MHE would likely result in inaccurate control actions predicted by the NMPC thus resulting in an undesirable or even unstable closed-loop operation of the system. Likewise, inaccurate control actions provided by NMPC may lead to a significant loss of performance in the MHE scheme and therefore inaccurate estimations. Thus, a high performance of both the NMPC and MHE schemes is required to avoid intensifying the errors and to achieve a proper closed-loop performance.

Using the formulations presented in this section, information is exchanged between the operational layers as depicted in Figure 4-1 and in Figure 4-2 for the NMPC and MHE schemes. The RTO provides economically optimal set point updates ($\boldsymbol{y_{sp}}$) to the NMPC upon the occurrence of disturbances ($\boldsymbol{d_t}$). These set points are achieved by the NMPC through the manipulated variables ($\boldsymbol{u_{t+1}}$), which are used to control the plant. The NMPC is provided with the current states as feedback to determine optimal control actions; these states are estimated by the MHE ($\boldsymbol{\hat{x}_{t,MHE}}$) using the available noisy measurements ($\boldsymbol{z_t + v_t}$). The control/estimation procedure is repeated at every sampling interval (Δt), while the RTO procedure is performed less often when the system reaches steady state.

4.2. PCC Absorber Section Case Study

The PCC model presented in Section 3.1 was adapted to consider stripper-side effects as shown herein. The PCC plant operates as described next. An MEA/water solution is outputted through the bottom of the stripper for which a reboiler

determines the ratio of this solvent solution that is recycled between the buffer tank and stripper; higher reboiler duty leads to increased CO_2 desorption in the stripper. The buffer tank recycle stream containing MEA, water, and traces of CO_2 goes through the cross-heat exchanger where it pre-heats the colder rich amine solution. The recycle stream then reaches the tank where it is mixed with two makeup streams of fresh water and fresh MEA such that the solution is concentrated or diluted as required. The recycled amine solution enters the buffer tank at 366.5 K (Nittaya, 2014); thus, the tank contents are cooled using an internal coil through which water is circulated.

As shown Figure 4-3, PCC plants are composed of absorber and stripper sections, which provide a natural partition for operational schemes. In this study, the absorber section is primarily being studied (Figure 4-3, left dashed box), with some approximations on the behaviour of the stripper section reboiler (Figure 4-3, right dashed box). The focus was placed mainly on the absorber section as it is where the carbon capture from the flue gas occurs; thus, it is the most important unit from a processing perspective. This partition was necessary as to restrict the size (thus, the computational time) of the simulated plant as assessment of the entire plant would have been prohibitively protractive. As RTO is an inherently steady-state method, the decision was made that steady-state approximations of the stripper section were sufficient for its assessment. Accordingly, the stripper section economics (particularly those of the reboiler), which are important to the process, are considered through steady-state approximations elaborated upon in this section. Moreover, changes in the stripper section are assumed to occur as disturbances to the absorber section, elaborated upon in Section 4.2.2; this way the stripper side operation and associated dynamics are considered in the present analysis. The NMPC and MHE implemented in the present case study, moreover, are quite general and could be applied in the larger context of a PCC plant scenario if the stripper section behaviour could be considered.

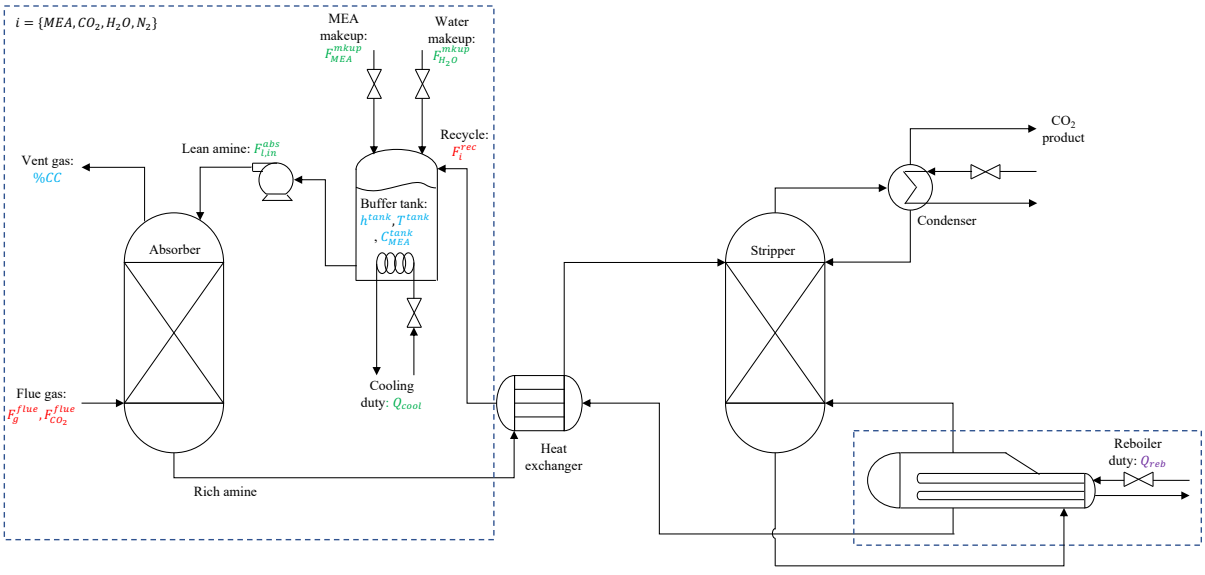

Figure 4-3: PCC plant. Dashed lines denote the units being considered in this study (i.e., the absorber section and reboiler). Blue font denotes controlled variables, purple font denotes additional RTO decision variables, green font denotes manipulated variables, and red font denotes disturbance variables (outlined in Section 4.2.3).

The dynamic mechanistic model for the absorber section of the PCC plant used for the layers in this study was adapted from Harun et al. (2012) and Nittaya (2014), which was based the operating conditions for the process on the pilot plant data and configuration from Dugas (2006). The model comprises a set of partial differential equations (PDEs),

ordinary differential equations (ODEs), and algebraic equations (AEs) to describe the system dynamics and phenomena; together these are a partial differential-algebraic system of equations (PDAEs). The process model consists of material balances, energy balances, and physical property models for both units, which are presented in the next subsections. Additionally, the absorber model consists of rate equations, chemical kinetics equations, and equilibrium equations; these, along with the assumptions made in developing the absorber model, are omitted for brevity, a full description of this model is provided in Chapter 3.

4.2.1 Buffer Tank Model

As shown within the left dashed box in Figure 4-3, the inputs to the tank are the recycled solvent coming from the stripper as well as the fresh water and MEA makeups. The output from the tank is the lean solvent going to the absorber. Component material balances for the buffer tank account for changes in molar holdup caused by control actions on the inlet and outlet flowrates. Moreover, changes in molar holdup also occur upon disturbances in the recycled flowrates coming from the stripper section as depicted in Figure 4-3. Nitrogen is assumed to be insoluble in the amine solvent; thus, the buffer tank does not contain this component as in the absorber, i.e., $n_{tank} = n_{comp} - 1$. The material balances for the tank are differential molar balances for each soluble component where no reaction is taking place and the well-mixed assumption holds (stirred tank). The molar holdups are modelled as follows:

$$\frac{dn_{MEA}^{tank}}{dt} = F_{MEA}^{rec} + F_{MEA}^{mkup} - F_{MEA,out}^{tank} \tag{4-4}$$

$$\frac{dn_{CO_2}^{tank}}{dt} = F_{CO_2}^{rec} - F_{CO_2,out}^{tank} \tag{4-5}$$

$$\frac{dn_{H_2O}^{tank}}{dt} = F_{H_2O}^{rec} + F_{H_2O}^{mkup} - F_{H_2O,out}^{tank} \tag{4-6}$$

where F_{MEA}^{mkup} and $F_{H_2O}^{mkup}(mol/s)$ denote the fresh MEA and water flowrates, respectively. $n_i^{tank}(mol)$ denotes the tank holdup component moles. $F_{l,in}^{tank} = \sum_{i=1}^{n_{tank}} F_i^{rec}$ and $F_{l,in}^{abs} = \sum_{i=1}^{n_{tank}} F_i^{out}\ (mol/s)$ (as shown in Figure 4-3) denote the total recycled and tank outlet molar flowrates of species i, respectively.

In addition to the component molar balances, an overall material balance is required to model the tank's holdup as it can also change significantly because of the control actions taken to regulate the PCC system and due to changes in the recycled stream. For instance, a control action may impose an increase in the makeup flowrates which, if not adequately accounted for in the outlet flowrate, may cause the tank level to continually rise. Tracking the tank's liquid level is a necessary safety requirement to avoid overflows or emptying of the tank (i.e., for inventory management). The inventory requirements of the tank must be coordinated with the removal requirements of the absorber (i.e., changing the makeup flowrates may affect the liquid level while also affecting the amount of absorption occurring). Hence, a centralized multi-variable controller such as NMPC is well suited to handle this interaction. This balance is performed under the assumption of constant inlet liquid densities in the makeup streams, which are valid as inlet stream are assumed to have constant compositions and temperatures. In contrast, the recycle and outlet density stream densities are modelled using the physical property models presented in the next section, as the composition of these

streams may vary due to changes in the operation of the stripper section. As such, the tank liquid level is modelled as follows:

$$A^{tank}\frac{dh^{tank}}{dt} = \frac{F_{l,in}^{tank}}{\rho^{rec}} + \frac{F_{MEA}^{mkup}}{\rho_{MEA}} + \frac{F_{H_2O}^{mkup}}{\rho_{H_2O}} - \frac{F_{l,in}^{abs}}{\rho^{tank}} \tag{4-7}$$

where $h(m)$ denotes the tank liquid level and $A^{tank}(m^2)$ denotes the tank cross-sectional area. ρ^{rec}, ρ_{MEA}, ρ_{H_2O}, and $\rho^{tank}(mol/m^3)$ denote the total recycle, fresh MEA, fresh water, and total outlet stream molar densities, respectively. In addition to the component and overall material balances, an energy balance is required for the tank. Within this unit, streams of different temperatures are mixed, and cooling is applied. Hence, temperature tracking is needed because thermodynamic changes in the tank can lead to changes in the removal rate of the subsequent absorber unit. The temperature changes within the tank are modelled as follows:

$$\begin{aligned}\left(\sum_{i=1}^{n_{tank}} c_{p,l,i}^{tank} n_i^{tank}\right)\frac{dT^{tank}}{dt} \\ = F_{total}^{rec} c_{p,l}^{rec}(T^{tank} - T_l^{rec}) + F_{MEA}^{mkup} c_{p,l,MEA}^{mkup}(T^{tank} - T_{MEA}^{mkup}) \\ + F_{H_2O}^{mkup} c_{p,l,H_2O}^{mkup}(T^{tank} - T_{H_2O}^{mkup}) + Q_{cool}\end{aligned} \tag{4-8}$$

where $c_{p,i}^{tank}(J/mol/K)$ denotes the tank component specific molar heat capacities. $T^{tank}(K)$ denotes the bulk tank temperature while $T_l^{recycle}$, T_{MEA}^{mkup}, and $T_{H_2O}^{mkup}(K)$ denote the inlet recycled, fresh MEA, and fresh water temperatures, respectively. Likewise, $c_{p,l}^{rec}$, $c_{p,l,MEA}^{mkup}$, and $c_{p,l,H_2O}^{mkup}(J/mol/K)$ denote the specific molar heat capacities of the recycled, fresh MEA, and fresh water streams, respectively. $Q_{cool}(W)$ denotes the cooling duty supplied to the tank through a coil.

Table 4-1 contains physical property models, parameters, and design characteristics associated with the tank model described herein.

Table 4-1: Physical property and design characteristics for the tank model.

Physical Property	**Value**	**Source**
Stream heat capacity $(J/mol/K)$	$c_{p,l}$	Hilliard (2008)
Recycled stream molar density (mol/L)	ρ^{rec}	Weiland et al. (1998)
Tank liquid molar density (mol/L)	ρ^{tank}	Weiland et al. (1998)
MEA molar density (mol/L)	$\rho_{MEA} = 5.05 \times 10^{-5}$	Aspen Property Package
Water molar density (mol/L)	$\rho_{H_2O} = 1.87 \times 10^{-5}$	Aspen Property Package
Design Characteristics		
Internal diameter (m)	$D^{tank} = 2$	Harun et al. (2012)
Height (m)	$h^{tank} = 2$	Harun et al. (2012)

4.2.2 Stripper Section Approximation

For the RTO layer to find an economically optimal point, approximations regarding the steady-state stripper section behaviour are made herein for a more realistic representation of the process and its economics. These additional

equations were included as part of the RTO model to consider the stripper-side reboiler steam and solvent depletion costs.

The largest cost in the PCC plant is incurred by the steam supplied to the stripper section reboiler, which is energy-intensive and often draws the required heating steam from the upstream power plant. To consider the reboiler cost, simulated steady-state data between reboiler duty and lean loading from Nittaya (2014) was correlated to yield:

$$LL = a_{reb} + b_{reb} Q_{reb} \tag{4-9}$$

where $LL(mol/mol)$ denotes the lean loading in the recycled stream and $Q_{reb}(W)$ denotes stripper-side reboiler duty as shown in Figure 4-3. To correlate the data in this range, a linear model was found to accurately fit the data available with $R^2 = 0.97$ (see Figure A-1in Appendix A), thus not requiring a more sophisticated regression model. In this case, the nominal reboiler duty value of $153{,}600\ W$ corresponds to the nominal operation outlined in Nittaya (2014) and the data were within $\pm 5\%$ of this nominal value. A sensitivity analysis performed by Nittaya (2014) also established that the $\pm 5\%$ range provides ample flexibility for the reboiler to affect the lean loading (i.e., the loading is very sensitive to the reboiler duty and this range of heat duties varies the loading from ~ 0.23 to $\sim 0.32\ mol/mol$, which is a typical range for a pilot-scale PCC unit). Accordingly, the reboiler duty (Q_{reb}) was also constrained within this range in the RTO, where it becomes an additional decision variable. The reason for inclusion of reboiler duty as a decision variable in the RTO through the simplified model in equation (4-9) was to consider the significant reboiler cost and to understand its effect on the optimal RTO-determined controlled variables.

Solvent depletion also occurs in the stripper section due to the condenser (top right of Figure 4-3), which outputs some solvent with the purified CO_2. The absorber section does not contain the condenser; thus, no solvent depletion is explicitly being accounted for in the RTO model. The depleted MEA and water, while not as expensive as the reboiler steam, need to be considered so that the system has incentive to supply makeups at steady state; thus, necessitating the modelling of solvent depletion by further approximating the behavior in the stripper section. If depletion were not considered in the absorber section it would be assumed that all the solvent can be regenerated and remain in the system; in this case, the RTO would not have incentive to feed fresh makeups at steady state owing to the high cost of the solvent chemicals (particularly MEA); this situation would be unrealistic. Accordingly, additional equations were added to model the steady-state depletion of MEA and water in the stripper and to connect the enrichment effect of the reboiler in equation (4-9) to the recycled stream flowrates. These equations were designed rather than fitted, such that they accounted for the contributions made by all 'fresh' inlets of the depleting species (i.e., the makeup MEA and water as well as flue gas water content). In the absence of data regarding this behaviour, the depletion was assumed to increase proportionally to the fresh feeds provided and subsequently approach constant depletion as the fresh feeds approach their nominal value; this behaviour was approximated using exponential functions for use within the RTO optimization problem.

Together with the reboiler approximation in equation (4-9), the RTO steady-state stripper is approximated to affect the recycle stream going from the stripper into the tank as follows:

$$F_{MEA}^{rec} = a_{MEA} - b_{MEA} exp(c_{MEA} F_{MEA}^{mkup}) \tag{4-10}$$

$$F_{CO_2}^{rec} = F_{MEA}^{rec} LL = F_{MEA}^{rec}(a_{reb} + b_{reb} Q_{reb}) \quad (4\text{-}11)$$

$$F_{water}^{rec} = a_{H_2O} + y_{H_2O}^{flue} F_g^{flue} - b_{H_2O} exp(c_{H_2O}(F_{H_2O}^{mkup} + y_{H_2O}^{flue} F_g^{flue})) \quad (4\text{-}12)$$

where the parameters for equations (4-10)–(4-12) are listed in Table 4-2.

Table 4-2: Additional RTO model parameters.

i	a_i	b_i	c_i
Reboiler	1.19	-5.94e-6	-
MEA	3.2096	3.2096	-55000
Water	27.68	27.68	-5000

Due to the lack of data regarding species depletion in this specific pilot-scale system, the constants for the recycled stream parameters in equations (4-10) and (4-12) were designed such that the depletion follows the behaviour expected in a complete PCC plant. That behaviour is as follows: the MEA recycled from the absorber depletes exponentially to zero as less makeup MEA is added since this stream is the only source of fresh MEA into the system. In contrast, the recycled water depletes exponentially to a constant value specified by the flue gas water content as fresh water enters the system through both the makeup and flue gas streams. The pre-exponential coefficient for MEA (a_{MEA}) was chosen such that the recycle flowrates were effectively zero if no fresh feeds were provided, while the decay rate (b_{MEA}) was chosen to approximate linear increases in depletion that reach an asymptote as the makeup stream approaches its nominal value, this behaviour can be seen in Figure A-2a in Appendix A. For consistency, the behaviour of the water recycle was also modelled with an exponential function. However, since there are two fresh water streams (i.e., within the flue gas and the makeup stream), there will always be water in the recycled stream (as water vapour is a by-product of combustion). As such, the pre-exponential and decay rates for water (a_{water}, b_{water}, respectively) were chosen such that the water content in the recycle would increase approximately linearly with increased makeup, as shown in Figure A-2b in Appendix A. The behaviour approximated herein inherently assumes that the condenser duty (hence the depletion) remains constant. In principle, the condenser duty would be one of the manipulated variables in the stripper section, but this unit is out of the scope of the present study as noted previously.

Note that these correlations approximate the steady-state effect of the reboiler and condenser on the makeup streams and do not attempt to capture dynamics. To account for the impact of these correlations on the recycle stream in the transient domain, a ramp disturbance is assumed to occur such that the recycled stream flowrate and composition are updated from their pre-RTO values to RTO-optimized values; these are described in detail in the following sections. The assumption of the recycle stream as a ramp is made here to reflect a typical operating condition of the stripper section. Note that the proposed operational framework is not limited to this assumption and can be extended to consider other profiles entering the absorber section from the recycle stream. With the treatments of stripper section effects as disturbances; the important effect of the stripper section on process dynamics is not disregarded.

4.2.3 Model Solution and Nominal Operation

The set of PDAEs representing the PCC absorber section presented previously require the inputs outlined in Table 4-3 whereby the steady-state version requires only boundary conditions, and the dynamic version requires initial and boundary conditions. The models are implemented in the Pyomo environment, an optimization modelling package for PYTHON (Hart et al., 2011). The absorber model is discretized in the axial (z) domain in the steady-state version while additional discretization in the time (t) domain is required in the dynamic model. This enables the differential equations comprising the continuous time/space models to be efficiently solved. The discretization is performed using four-point orthogonal Radau collocations on finite elements in the time domain and backward finite differences in the axial domain. Collocations were chosen for the time domain because of their accuracy and built-in functionality within Pyomo. To achieve an accurate dynamic model, this discretization was prioritized such that the time interval $\Delta t = 12.5\ s$ (i.e., 8 intervals in a 100 second time horizon) was chosen as the finite element size in both absorber and tank models. A more parsimonious $n_{fez} = 10$ finite elements were used in the absorber axial domain to keep the model size as small as possible without sacrificing accuracy in the solution.

Table 4-3: Inputs required by the absorber section model

	Initial conditions $(\mathbf{0 \le z \le H, t = 0})$	***Boundary conditions*** $(\mathbf{z = 0, z = H, t \ge 0})$
Absorber (gas)	$C_i^g(z,0) = C_{i,0}^g(z)$	$C_i^g(0,t) = C_{i,in}^g(t)$
	$T_g(z,0) = T_{g,0}(z)$	$T_g(0,t) = T_{g,in}(t)$
		$u^g(0,t) = u_{in}^g(t)$
Absorber (liquid)	$C_i^l(z,0) = C_{i,0}^l(z)$	$C_i^l(H,t) = C_{i,in}^l(t)$
	$T_l(z,0) = T_{l,0}(z)$	$T_l(H,t) = T_{l,in}(t)$
		$u^l(z,t) = u_{in}^l(t)$
Tank	$T^{tank}(0) = T_0^{tank}$	
	$h(0) = h_0$	
	$n_i(0) = n_{i,0}$	

Prior to discretization, the models (i.e., absorber and tank) have a collective 16 states and 210 algebraic variables, which grows to 116 states and 1,977 algebraic variables with absorber axial discretization (i.e., when solving the RTO problem). This further grows to 3,712 states and 63,168 algebraic variables with axial discretization of the absorber and time discretization of the entire absorber section (i.e., when solving the NMPC and MHE problems). The states of the system are the differential variables in the previously presented differential equations (i.e., the liquid and gas concentrations and temperatures in the absorber as well as the molar holdups, liquid level, and temperature in the tank). The algebraic variables correspond to all other phenomenological and physical property models in the system. An interior-point algorithm (Wächter and Biegler, 2005) was used to solve the large-scale optimization problems described in the following sections on an Intel core i7-4770 CPU @ 3.4 GHz. Both steady-state and dynamic versions

of the models described in this Section 3.1 and Section 4.2 (in the steady-state case) are used in the proposed scheme. The collective vector of equations representing the discretized models is denoted as $\boldsymbol{f_s}$ in its steady-state version and $\boldsymbol{f_d}$ its dynamic version.

In addition to the initial and boundary conditions, the PCC absorber section case study considered herein also requires additional inputs in the form of the manipulated variables and the disturbance variables. In the PCC absorber section, the manipulated variables which act as control actions are the flowrate of solvent solution into the absorber, the fresh MEA makeup flowrate into the tank, the fresh water makeup flowrate into the tank, and the tank cooling duty; i.e., $\boldsymbol{u} = [F_{l,in}^{abs} \quad F_{MEA}^{mkup} \quad F_{water}^{mkup} \quad Q_{cool}]^{\mathbf{T}}$ as depicted in Figure 4-3. Manipulation of both makeup streams is a key novelty within this work as they can significantly impact the economics and operation of the absorber section of this plant. For this purpose, a centralized MPC approach is best suited as it can model and account for the interaction between the makeup streams, the amount of carbon captured, and the tank level.

The operation of an actual PCC system is subjected to disturbances that can have significant effects on the process behaviour and economics. In this study, the main disturbances being considered are: 1) the flue gas flowrate, which varies based on the load variation in the upstream power plant; 2) the flue gas CO_2 content, which varies based on the fuels being used in the upstream power plant; and 3) the recycle stream flowrates, which vary based on the makeup fed to the system and the operation of the stripper section reboiler. Changes in the flue gas CO_2 content are assumed to be reflected by changes in the flue gas water content (i.e., a 0.01 fraction increase in CO_2 is accompanied by a 0.01 fraction decrease in H_2O in the flue gas); hence, changes in the fractions are treated as a single disturbance variable. Accordingly, the disturbances considered in this work are denoted as $\boldsymbol{d} = [F_g^{flue} \quad y_{CO_2}^{flue} \quad F_{MEA}^{rec} \quad F_{CO_2}^{rec} \quad F_{H_2O}^{rec}]^{\mathbf{T}}$; these are depicted in Figure 4-3.

In the PCC absorber section, the controlled variables comprise the percent carbon capture ($\%CC$), the MEA concentration in the lean solvent ($C_{MEA}^{tank}(mol/L)$) from buffer tank to absorber, the buffer tank temperature ($T^{tank}(K)$), and the buffer tank level ($h^{tank}(m)$); i.e., $\boldsymbol{y} = [\%CC \quad C_{MEA}^{tank} \quad T^{tank} \quad h^{tank}]^{\mathbf{T}}$. The percent carbon capture is defined in.

This nominal operation occurs at the nominal values for the manipulated variables $\boldsymbol{u_{nom}} = [32.17 \quad 0.0002 \quad 0.2 \quad 139{,}000]^{\boldsymbol{T}}$ and the nominal values for the disturbances $\boldsymbol{d_{nom}} = [4.012 \quad 0.175 \quad 3.2098 \quad 0.98 \quad 27.78]^{\boldsymbol{T}}$; these correspond to the nominal controlled variables $\boldsymbol{y_{nom}} = [96.23 \quad 4847 \quad 314 \quad 1]^{\boldsymbol{T}}$ (Harun et al., 2012; Nittaya et al., 2012; Nittaya, 2014). The complete stream data for the nominal conditions as predicted by the current model can be found in Table A-1 (Appendix A). Combinations of nominal disturbance variables and nominal manipulated variables are used as the initial or final operating conditions for several of the operational cases presented in Section 4.3.

4.2.4 Model Validation

The model presented in the previous section was validated using different sources of data available in the literature as a single set of comprehensive data for this system is unavailable. Table 4-4 presents a comparison of outlet stream predictions for the nominal operation (i.e., corresponding to $\boldsymbol{u_{nom}}$, $\boldsymbol{d_{nom}}$, and $\boldsymbol{y_{nom}}$) of the absorber model as implemented in this study and of a previous mechanistic model reported in Harun et al. (2012). The authors of the

prior model provided detailed data on the outlet streams at the nominal operating condition defined previously and in Table A-1 (Appendix A); this included compositions, flowrates, and temperatures; these can be compared to predictions of the present model.

Table 4-4: Comparison of absorber output predictions against previously reported mechanistic model implementation. Error of predictions of present study with respect to Harun et al. (2012) also presented.

	Vent gas		**Rich solvent**	
	Present study	**Harun et al. (2012).**	**Present study**	**Harun et al. (2012).**
Temperature (K)	314.06	314.15	319.89	327.76
Flowrate (mol/s)				
MEA	0.0000	0.0000	3.2098	3.3560
CO_2	0.0427	0.0295	1.6393	1.6534
Water	0.2340	0.2259	27.8460	27.8573
N_2	3.2100	3.2146	0.0000	0.0000
Total	3.4867	3.4700	32.6951	32.87
Mean error (%)		8.1641		1.3638

As shown in Table 4-4, the predictions made by the current model conform well with previous model predictions (mean output predictions $< 8.2\ \%$ error). In particular, the error of the vent gas stream is elevated by the CO_2 composition; nevertheless, this composition is very small in magnitude ($\sim 1\ mol\%$) so small inaccuracies tend to inflate the error. This suggests that the absorber column boundaries (i.e., outlets) are being predicted well without making conclusions as to the accuracy along the absorber height. While having validation at the nominal operation is acceptable, a complete validation at various operating conditions is necessary to conclude that the model is valid for a range of operations. Two key process variables for which there is experimental as well as simulated data across several operating conditions are the solvent temperature and the $\%CC$. By analyzing solvent temperature profiles, the existence of the so-called temperature bulge, which is characteristic of the reactive mechanism in the PCC absorber, can be verified. Moreover, the conformance of the absorber predictions can be assessed. Although a set of experimental data of compositions along the absorber height is not available due to the intractability of online composition analysis for this system, the $\%CC$ can be obtained from the boundary compositions and has been reported. By analyzing the $\%CC$, it can be verified that this key performance variable is indeed being predicted accurately; this is particularly important in the RTO and NMPC layers where the $\%CC$ is being used explicitly to define set points. Kvamsdal and Rochelle (2008) present two experimental data sets (temperature profiles and corresponding $\%CC$) and an additional two simulated temperature profiles (generated by their own model). The former are named case 1 and 2 in the present study while the latter simulated profiles are referred to as case 3 and 4 in the present study. The temperature profiles that comprise cases 3 and 4 were sampled at regular intervals to generate individual data points. Each case represents a significant change in operating conditions via the flue gas flowrate, composition, and temperature; the lean solvent flowrate, composition, and temperature; as well as the column packing height. The inlet

compositions required to achieve these profiles along with their naming conventions in Kvamsdal and Rochelle (2008) can be found in Appendix A, Table A-2. Figure 4-4 shows the temperature profiles predicted by the present model along with data for temperatures from Kvamsdal and Rochelle (2008) for the four different operational cases while Table 4-5 presents the error in the predictions made by the model in the present study with respect to the data from Kvamsdal and Rochelle (2008).

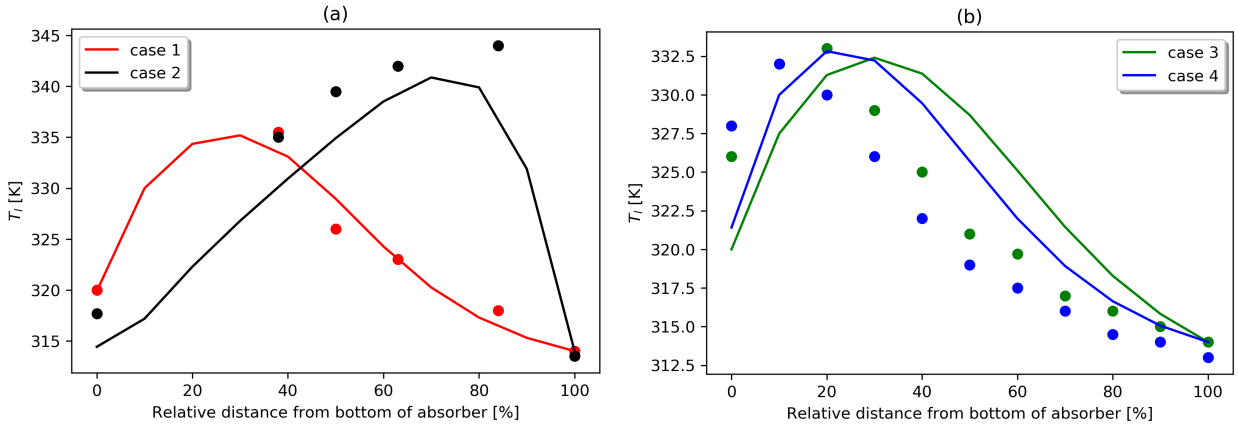

Figure 4-4: Temperature profile prediction for various operating cases. a) experimental data, b) simulated data.

Table 4-5: Comparison of absorber temperature profiles and %CC predictions against previously reported data. Error of predictions of present study with respect to Kvamsdal and Rochelle (2008) also presented.

Case #	**%CC present study**	**%CC (Kvamsdal and Rochelle, 2008)**	**Error in %CC (%)**	**Mean error in T_l (%)**
1	95.03	93.85	1.257	0.310
2	72.07	70.95	1.578	3.781
3	86.77	86.20	0.661	2.700
4	93.61	93.35	0.278	2.892

As shown in Figure 4-4, the temperature profiles align closely with the data from Kvamsdal and Rochelle (2008), this is corroborated by the low mean errors in T_l presented in Table 4-5 ($< 4\%$ across all operating conditions). The present model slightly underestimates the profiles for the entire length of the column in case 2 while, in cases 3 and 4, the present model underestimates the profiles prior to the bulge and overestimates after the bulge. Moreover, they key $\%CC$ predictions made by the present model conform with the data from Kvamsdal and Rochelle (2008) even more closely ($< 2\%$ across all operation conditions). This close agreement in temperature and $\%CC$ predictions compared to Kvamsdal and Rochelle (2008) are well within the range of acceptability for the wide range of operating conditions summarized in Table B2. Moreover, the accuracy of outlet stream predictions compared to Harun et al. (2012) summarized in Table 4-4 given further confidence in the accuracy of the model as it is an independent data set. These findings suggest that the current absorber model conforms with past models as well as experimental data, thus it is adequate for use in the present study. Additionally, the simplified reboiler correlation in Section 4.2.2 was also shown

to accurately correlate reboiler duty to lean loading (which serves as an input to the absorber as show in Table B2) within the range being considered in this study with $R^2 = 0.97$, implying small residuals and highly correlated data.

4.3. Scheme Implementation and Assessment

The specifics of the implementation of the model presented in Sections 3.1 and 4.2.2 to the scheme proposed in Section 4.1 are presented next along with the assessment tools used for different layers within the scheme.

4.3.1. RTO Implementation and Assessment

The RTO uses the economic function presented in equation (4-1) along with a steady-state version of the mechanistic process model and stripper approximations to determine the economically optimal steady state for the controlled variables. State measurements are typically fed to the RTO such that a parameter estimation problem is solved prior to the economic optimization procedure. In this study, we assume no parametric mismatch, thus not requiring the parameter estimation step. However, the steady-state wait-time associated with the parameter estimation step is enforced using the following heuristic for triggering of the RTO:

$$\boldsymbol{y_t - y_{t-i} < 0.005 y_{nom}} \qquad \forall i \in \{1, \dots, 10\} \qquad (4\text{-}13)$$

which declares that the system is at steady state when the controlled variables are changing at a rate of less than 0.5% of their nominal value from the current sampling interval to the previous ten sampling intervals. A simple heuristic such as this is assumed to be acceptable for the present PCC case study; for more sophisticated methods, the field of steady-state detection provides ways to automate this trigger (e.g., Rhinehart, 2013).

The additional correlations (5-9)–(5-12) are included within the steady-state model $\boldsymbol{f_s}$ such that decisions can made regarding the reboiler operation without explicitly considering it in the control scheme. With the inclusion of the stripper section approximations within $\boldsymbol{f_s}$, the RTO objective function in equation (4-1) as it pertains to the system described in Section 4.1 simplifies to:

$$C_{process} = P_{MEA}\dot{m}_{MEA}^{mkup} + P_{sales}(\dot{m}_{CO_2,in}^{g} - \dot{m}_{CO_2,out}^{g}) + P_{CO_2}\dot{m}_{CO_2,out}^{g} + P_{steam}Q_{reb} \qquad (4\text{-}14)$$

where $C_{process}(\$CAD/s)$ is the cost of operating the PCC absorber section. $\dot{m}_{MEA}^{makeup}(tn/s)$ is the flowrate of fresh makeup MEA into the system as shown in Figure 4-3; this is the only chemical cost considered in this case. $\dot{m}_{CO_2}^{cap} = \dot{m}_{CO_2,in}^{g} - \dot{m}_{CO_2,out}^{g}(tn/s)$ and $\dot{m}_{CO_2,out}^{g}(tn/s)$ are the flowrate of carbon captured and emitted, respectively, by the absorber. $Q_{reb}(W)$ is the reboiler duty as modelled by steady-state lean loading equation (4-9), which is an additional decision variable aside from the controlled variables; this is the only energy cost considered in this case. In this case study, the efficiency factor introduced in equation (4-1) was assumed to be $\zeta = 1$ for simplicity. Moreover, pumping and water costs are assumed to be negligible.

Another consideration when optimizing the PCC plant is the impact it has on the upstream power plant. Namely, operating the PCC plant with higher reboiler duty decreases the power plant profits by using steam that could otherwise be used for power generation. To analyze the impact, the lost profits owed to reboiler operation were estimated as:

$$C_{energy} = \Delta Q_{reb}(P_{elec} - P_{steam})\eta \quad (4\text{-}15)$$

where $C_{energy}(\$CAD/yr)$ are the lost profits (energy penalty) owing to reduced energy generation, $\Delta Q_{reb}(MW)$ denotes the difference between the current reboiler duty and its previous or nominal value, P_{elec} is the price of electricity sold to consumers. The efficiency factor (η) accounts for the losses in converting thermal energy from combustion-generated steam to electrical energy for consumers. For the present absorber section case-study, this factor is defined as $\eta = 0.4$ (Mac Dowell and Shah, 2013); however, this user-defined parameter may vary depending on the power plant. The price term uses the difference between the electrical sales cost and the steam cost to evaluate the losses not already considered within $C_{process}$; in this way, only sales cost mark-up is considered (i.e., the raw steam cost is not double counted). This additional energy penalty to the power plant can be compared against the savings achieved by the PCC RTO to have a more complete perspective on the economic impact. The prices associated with equations (4-14) and (4-15) are summarized in Table 4-6.

Table 4-6: Prices for economic terms, adjusted for inflation and converted to $CAD.

Term	**Value**	**Source**
MEA (P_{MEA})	2420 $\$CAD/tn\ fresh\ MEA$	Straathof and Bampouli (2017)
Sales (P_{sales})	-50 $\$CAD/tn\ CO_2\ sold$	Nwaoha and Tontiwachwuthikul (2019)
CO_2 (P_{CO_2})	176 $\$CAD/tn\ CO_2\ removed$	Nordhaus (2017)
Steam (P_{steam})	0.065 $\$CAD/kWh$	Karimi et al. (2011)
Electricity (P_{elec})	0.115 $\$CAD/kWh$	OEB (2021)

There is little consensus on the true SCC, and various models have been proposed in the literature (Nordhaus, 2017). In this work, we estimated the price using the DICE-2016R with a 2.5% discount rate. Note that this is the first time this cost is used in the economic optimization of a PCC process.

The lower and upper bounds for the controlled variables ($\boldsymbol{y^l}$ and $\boldsymbol{y^h}$) are set as follows:

$$0 \leq \%CC \leq 100 \quad (4\text{-}16)$$

$$3000 \leq C_{MEA}^{tank}\ (mol/L) \leq 6000 \quad (4\text{-}17)$$

$$300 \leq T^{tank}\ (K) \leq 345 \quad (4\text{-}18)$$

$$0.05h^{tank} \leq h\ (m) \leq 1.95h^{tank} \quad (4\text{-}19)$$

The constraint on the controlled variable for the tank level is an important safety constraint to avoid overflowing and imposes that the tank level's set point does not exceed the physical tank dimensions (within a 5% safety factor). Moreover, the tank temperature constraint ensures that the absorber feed temperature is within an acceptable range for this operation.

Using the new economic function described in equation (4-1) applied to this case study in equation (4-14), the RTO passes updated controlled variables as set points (i.e., $\boldsymbol{y_{sp}} = \boldsymbol{y}$) to the NMPC upon its execution which, as mentioned, requires for the controlled variables to be steady in time by the criteria described in equation (4-13).

In addition to the set point update, the execution of the RTO also incites a ramp disturbance in the recycle flowrates through the approximated model described in Section 4.2.2. In other words, the recycled flowrates ramp from their outdated values to those specified by the RTO. A ramp is used such that there is a delay between making stripper side decisions and their effect on the absorber as these changes would not occur instantaneously in the plant. As mentioned in Section 4.2.2, the recycled stream is treated as a disturbance for the NMPC to reject when the set points are changed. The treatment as a disturbance is necessary as the NMPC does not have a stripper section model to predict the behaviour of the recycle stream. The ramp begins when the RTO is executed and last for 200 time intervals (i.e.~40 minutes), when the recycle stream reaches its new flowrate and composition as specified by the RTO. This number of sampling intervals (~40 minutes) was chosen to model the time-delay between changes on the absorber/stripper sections and their effect on the recycled stream (i.e. changes in makeup streams and heat duty will not have immediate effects on the recycle stream). A similar delay was observed in open-loop tests by Nittaya (2014), thus supporting the assumption that stripper section dynamics would occur gradually.

For the overall integrated scheme, the performance is economically driven, thus the process economics are assessed through an annualized version of the RTO objective function in equation (4-14) at every sampling interval. Additionally, the payback period $t_{payback}(h)$ is used to quantify the amount of time that the process must be operated at a new steady state for to justify the execution of the RTO. This term is defined as follows:

$$t_{payback} = \tau_{annum} \frac{\int_{t_0^{RTO}}^{t_f^{RTO}} C_{PCC} dt}{C_{PCC}^0 - C_{PCC}^f} \tag{4-20}$$

where t_0^{RTO} and $t_f^{RTO}(hr)$ denote the initial and final times at which a given RTO execution imposes dynamic operation on the plant, respectively (i.e., t_0^{RTO} is the time at which the RTO is executed and t_f^{RTO} is the time at which the set point change is completed). C_{PCC}^0 and $C_{PCC}^f(\$CAD/yr)$ denote the initial (unoptimized) and the final (optimized) steady-state cost of the plant operation. τ_{annum} ($8760\ hr/yr$) is used to convert the annualized costs to payback periods in hours.

4.3.2. NMPC Implementation and Assessment

In the proposed NMPC controller, the horizons are set to be equivalent and equal to 100 seconds (i.e., $P = C = 100s$), these were previously found to provide good control performance (Chapter 3). The first term in the objective function in problem (4-2) is weighted using the diagonal matrix $\boldsymbol{Q_c} = diag(4,2,3 \times 10^4, 5 \times 10^{-4})$, which aims to regulate the system towards its set points. The second term in the objective function is weighted by the diagonal matrix $\boldsymbol{R_c} = diag(3.5 \times 10^7, 2 \times 10^3, 30, 2 \times 10^{-8})$, which supresses sudden changes in the manipulated variables. The dynamic performance of the proposed scheme is dependent on these tuning parameters as they balance tracking speed with aggressive changes in the manipulated variables. These must be balanced as fast tracking is desired for good performance, but overly quick control actions put undue burden on process equipment (i.e., manipulated variables).

For this case study, preliminary closed-loop simulations as well as RGA analysis were used to tune the controller weights. The former helped in tuning the move-suppression matrix to ensure unrealistically fast control actions were supressed, while the latter served as a guideline to assess interactions between variables such that high interaction was avoided while evenly prioritizing the control objectives. This unique tuning and structure of the controller makes it difficult to compare to previous control approaches, which have different control mechanisms and priorities.

As with the RTO, $\boldsymbol{y^l}$ and $\boldsymbol{y^h}$ are the lower and upper bounds for the controller variables, respectively, as outlined in equations (4-16)–(4-19), and $\boldsymbol{u^l}$ and $\boldsymbol{u^h}$are the lower and upper bounds for the manipulated variables, respectively. The manipulated variable bounds are defined as follows:

$$0 \leq F_{l,in}^{abs}\ (mol/s) \leq 100 \tag{4-21}$$

$$0 \leq F_{MEA}^{mkup}\ (mol/s) \leq 5 \tag{4-22}$$

$$0 \leq F_{water}^{mkup}\ (mol/s) \leq 2 \tag{4-23}$$

$$-500{,}000 \leq Q_{cool}\ (W) \leq 0 \tag{4-24}$$

These bounds are chosen such that they provide the manipulated variables with a realistic range, while still providing operational flexibility. Note that the cooling duty in equation (4-24) is negative as heating is positive in the convention used herein. Using this NMPC tuning, horizon, and bounds, the economically important controlled variables (i.e., carbon capture and MEA content going to the absorber) can be tracked quickly and flexibly using makeup streams while also considering safety limitations (i.e., in the tank level and temperature).

Assessment of the control scheme is performed by analyzing the transient times and shape of the responses observed in the system. Moreover, the sum of squared errors (SSE) between each controlled variable and its respective set point is computed as follows:

$$\boldsymbol{SSE} = \sum_{i=1}^{n} \left(\boldsymbol{y_i} - \boldsymbol{y_{i,sp}}\right)^2 \tag{4-25}$$

where n is the number of sampling intervals un a given scenario and $\boldsymbol{SSE} \in \mathbb{R}^{n_y}$ denotes the vector of SSE for the controlled variables. The tracking performance of each variable is assessed separately as they have largely different magnitudes and controller tunings, thus prohibiting their direct comparison. Using SSE, the performance of the controller is quantified through its tracking performance.

4.3.3. MHE Implementation and Assessment

In the present work, the MHE is formulated such that only a few realistically achievable measurements are required for state estimation; this is enabled by the mechanistic MHE model. This is the first MHE implementations for any PCC plant that uses a mechanistic model, few measurements, and does not require decomposition of the column axial domain into subdomains with their own estimators.

The discretization necessary to solve the axially distributed absorber model poses a measurability challenge because each of the n_{fez} discretization point along height domain requires an initial condition to solve the NMPC problem. For instance, online measurement of the concentrations along the column height is not practical because analysis of stream compositions is time and resource intensive. Accordingly, only the inlet stream (boundary) compositions into the absorber are assumed to be measurable; this leaves the compositions along the $n_{fez} - 2$ remaining column heigh discretization points to be estimated. Conversely, the temperatures at every spatial discretization point in the column are assumed to be measurable. Having several temperature measurements is realistic since only conventional thermocouples are only required. Furthermore, the states in the storage tank are comparatively fewer as they only include the level, temperature, and molar holdup. The temperature measurement in the tank is realistic as it only requires a thermocouple, while measuring level is also commonplace using pressure transmitters/transducers. In total, 32/116 system states are assumed to be measured online and are as follows:

$$\boldsymbol{z_t} = [\boldsymbol{T_l^{abs^T}} \quad \boldsymbol{C_{n_{fez}}^{l,abs^T}} \quad \boldsymbol{T_g^{abs^T}} \quad \boldsymbol{C_0^{g,abs^T}} \quad T_l^{tank} \quad h_l^{tank}]^{\mathbf{T}} \tag{4-26}$$

where $\boldsymbol{T_l^{abs}}$ and $\boldsymbol{T_g^{abs}} \in \mathbb{R}^{n_{fez}}$ denote the liquid and gas temperature measurements along the absorber column height, respectively. $\boldsymbol{C_{n_{fez}}^{l,abs}}$ and $\boldsymbol{C_0^{g,abs}} \in \mathbb{R}^{n_{comp}}$ denote the liquid and composition measurements at the absorber column boundaries, respectively. T_l^{tank} and $h_l^{tank} \in \mathbb{R}$ denote the tank temperature and level measurements, respectively.

The molar holdup in the tank is readily observable as it is assumed that the composition of inlet from tank to absorber is measurable; thus, the concentration of the tank is also known due to the well-mixed assumption. This is estimated as follows:

$$\boldsymbol{n^{tank}} = \pi(D^{tank}/2)^2 h_l^{tank} \boldsymbol{C_{n_{fez}}^{l,abs}} \tag{4-27}$$

where $\boldsymbol{n^{tank}} \in \mathbb{R}^{n_{comp}}$ denotes the molar holdup in the tank. In the present PCC absorber section case study, as some of the states are directly measured and some can be calculated, $\boldsymbol{h_d}$ is effectively a diagonal matrix of proper dimensions augmented with the tank holdup equation (4-27) (i.e., $\boldsymbol{h_d} \in \mathbb{R}^{(N_z+n_{comp})\times N_z}$).

The MHE horizon used in this study was set to be of the same length as the NMPC horizons (i.e., $N = P = C = 100s$). This horizon was determined through preliminary closed-loop tests and was found to be long enough to achieve a good state estimate without the approximation of an arrival cost that is often required in MHE problems (Valipour and Ricardez-Sandoval, 2021). A shorter horizon resulting in a more parsimonious MHE problem would be enabled by the inclusion of arrival cost; however, this is out of the scope of the present study.

In the present scheme, the measured/calculated buffer tank states are passed directly to the NMPC while the estimated absorber states must be solved for by the MHE and then passed to the NMPC. Since the tank measurement are noisy as they do not experience the filtering effects of the MHE, a first-order filter with a constant of $\lambda = 0.5$ is imposed on the states of the tank provided to the NMPC to mitigate the noise effects in the control actions, i.e.:

$$\begin{aligned} T_{l,t}^{tank,F} &= \lambda T_{l,t-1}^{tank,F} + (1-\lambda) T_{l,t}^{tank,m} \\ h_{l,t}^{tank,F} &= \lambda h_{l,t-1}^{tank,F} + (1-\lambda) h_{l,t}^{tank,m} \\ \boldsymbol{n_t^{tank,F}} &= \lambda \boldsymbol{n_{t-1}^{tank,F}} + (1-\lambda) \boldsymbol{n_t^{tank,m}} \end{aligned} \tag{4-28}$$

where superscripts F and m denote a filtered and a measured value, respectively.

Using the observation strategy and horizon outlined, the scheme can provide accurate state estimates for the NMPC to produce effective control actions. The quality of these estimates is assessed by analyzing the mean squared error (MSE) between the estimated and true $\%CC$. MSE is defined as follows:

$$MSE = \frac{1}{n}\sum_{i=1}^{n}\left(\%CC_{i,T} - \%CC_{i,e}\right)^2 \tag{4-29}$$

where n is the number of sampling intervals in a given scenario (or for a given time span) and the subscripts T and e denote the true and estimated $\%CC$ for sample i, respectively. The MSE of $\%CC$ is used as a proxy to assess the performance of the MHE as only the absorber states are estimated and $\%CC$ is the most crucial output from the absorber portion of the model.

4.4. Results and Discussion

To evaluate the performance of a real-life PCC plant, the proposed closed-loop scheme shown in Figure 4-1 was implemented in the pilot-scale system described previously. The transient operation of the system is described using the dynamic model $\boldsymbol{f_d}$, where noise is added to the process and the measurements. Process noise (i.e., owed to unmodelled fluctuations in the system) is inserted via the initial conditions between one simulation interval and the next, while measurement noise (i.e., owed to instrumentation errors) is inserted via the measured states passed to the MHE. Both of these noises are assumed to be zero mean, normally distributed, with a standard deviation of 0.02% of the corresponding nominal state values, i.e. $\mathcal{N}(0, (0.0002\boldsymbol{x_{nom}})^2)$ where $\boldsymbol{x_{nom}}$ is the state vector corresponding to the nominal operation indicated in Table B1.

As noted previously, the model parameters used herein are experimentally determined from prior studies. Accordingly, the present work assumes that they manifest at their nominal value in both the plant and the mechanistic models used in the proposed scheme (i.e., no structural or parametric mismatch was assumed). However, if parametric uncertainty were observed, the scheme would experience some deterioration owing to a loss in control, estimation, and RTO performance.

4.4.1. Scenario A: Cofiring of Fuels

Cofiring refers to the operation of a power plant that combusts different types of fuels within the same operating period to lessen the environmental impact of a highly emissive fuel. One such emissive fuel is coal and, as there is a greater shift to renewables, the potential of cofiring with biomass (Yang et al., 2019) is being increasingly investigated in terms of feasibility and benefits. However, this operational case (co-firing) has yet to be examined through an economic optimization framework, which can help to further reduce emissions as well as cost.

In this scenario, the cofiring of biomass and coal is illustrated through its impact on the flue gas composition being supplied by the power plant to the downstream PCC absorber section. The scheme presented in this work is particularly well-suited for this scenario as the RTO can find new economically optimal steady states depending on the fuel used in the combustion process. In this scenario, only the transition between 100% biomass and 100% coal firing is studied; however, the proposed RTO framework for this case study is suited to determine set points for any fuel ratio in

between. The starting point for this scenario corresponds to the nominal manipulated variables values presented in Section 4.2.3 and the PCC plant operating downstream from a biomass-fired plant ($y_{CO_2} = 0.12$). From this initial operation, coal ($y_{CO_2} = 0.175$) is introduced into the upstream power plant with the fuel ramping up from 0% coal content to 100% coal content within a span of 200-time intervals (~40 minutes). This is reflected in a flue gas CO_2 fraction that ramps from 0.12 (fully biomass-fired) to 0.175 (fully coal-fired), as shown in Figure 4-5a. The controller first rejects the disturbance imposed on the flue gas composition by the change in fuel, reaching a new steady state at ~7.5 hours as determined by meeting the criteria in equation (4-13). At this time, the RTO is executed such that an economically optimal set point is found for the new flue gas composition corresponding to coal-firing.

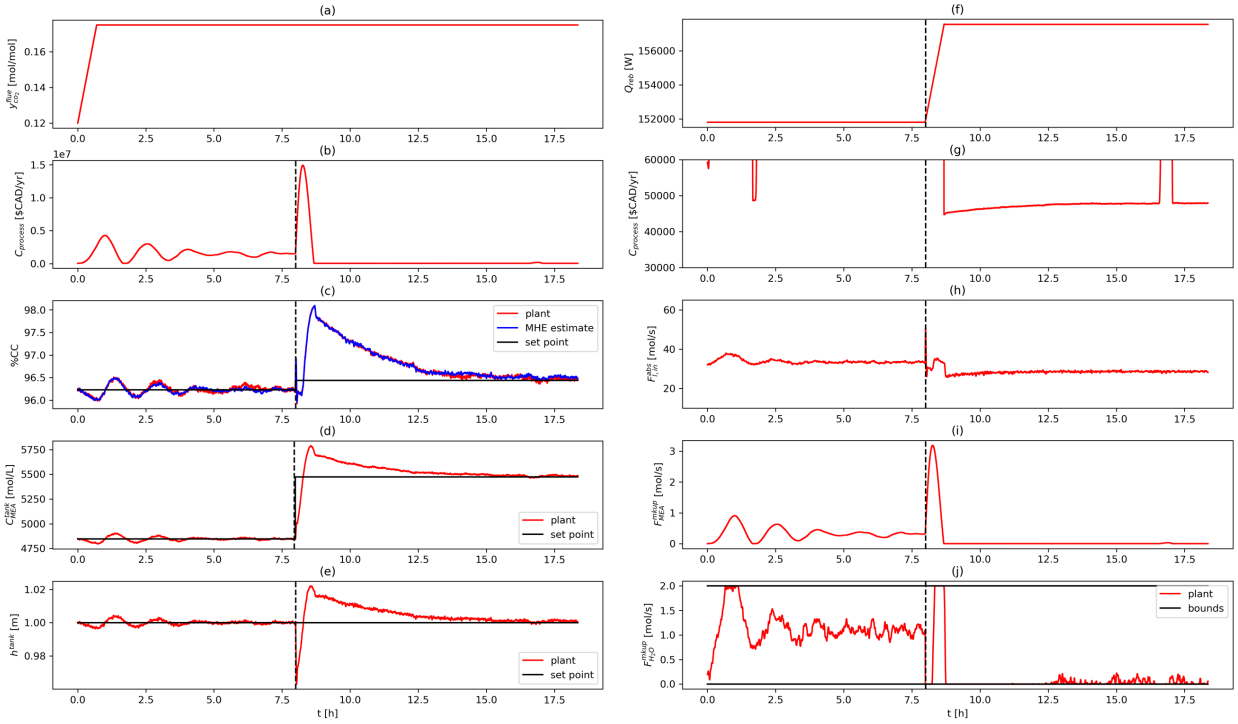

Figure 4-5: Flue gas CO_2 content, process cost (b shows full profile, g shows zoomed in profile), controlled variables, and manipulated variables for a cofiring scenario. Dashed vertical lines represent times at which the RTO was executed, thus inciting a set point change.

The responses on the buffer tank temperature and cooling duty in this scenario can be found in Figure A-3 (Appendix A). In general, the temperature is tracked quickly and has little impact on the process economics. Contrastingly, the other controlled variables (i.e., $\%CC$, C_{MEA}^{tank}, and h^{tank}; Figure 4-5c, d, e, respectively) are tracked more slowly. This occurs as the tank inlet and outlet flowrates, which affect the level, interact with the removal rate and MEA concentration; thus, a slower coordinated response is made by the NMPC to track these interacting controlled variables.

Figure 4-5c shows the plant $\%CC$ along with the MHE-estimated $\%CC$; for this scenario, the MHE estimates were observed to be in good agreement with the true plant with an $MSE = 1.239 \times 10^{-3}$. This is the case for all scenarios in the present study and is owed to the use of the mechanistic model in this layer and the use of a long horizon in the MHE framework. Nevertheless, the MHE occasionally drifts from the true states as can be seen during some time

periods in Figure 4-5c (i.e., $t \cong 6\,h \rightarrow 6.9\,h$ with $MSE = 6.830 \times 10^{-2}$ and $t \cong 13.7\,h \rightarrow 14.4\,h$ with $MSE = 5.160 \times 10^{-2}$).

To gain further insight into the effect of the proposed RTO framework, a 'no-MHE' case was performed whereby the cofiring scenario is repeated with the assumption of full access to the system states. This occurs when all the true plant states can be measured thus making the state estimation framework (i.e., MHE) unnecessary. In principle such a 'no-MHE' case is unrealistic as composition measurements are difficult to perform online for the PCC absorber; nevertheless, it is valuable to assess the performance of the proposed scheme under this assumption to assess the impact and need of a reliable estimation scheme. Note that previous economic operation studies in PCC have not considered an estimation scheme and hence have not addressed the issue of state accessibility. Since the MHE provides state estimates to the NMPC, which may differ from the true plant states, the controller and economic performance can be affected by using estimation. Hence, the 'no-MHE' case enables observation of the deterioration that an estimation scheme causes on the operational framework. For the present 'no-MHE' case, the first-order filter with $\lambda = 0.5$ is imposed on all states to smooth noise and the RTO is assumed to be executed at the same time as the MHE scenario. As the SSE described in equation (4-25) quantifies the tracking performance of the NMPC, this measure can be used to assess the controller performance under the MHE and 'no-MHE' cases. To make a fair comparison, the NMPC controller tuning parameters, and characteristics remain the same for both scenarios. Table 4-7 summarizes the tracking performance under the MHE and 'no-MHE' scenarios.

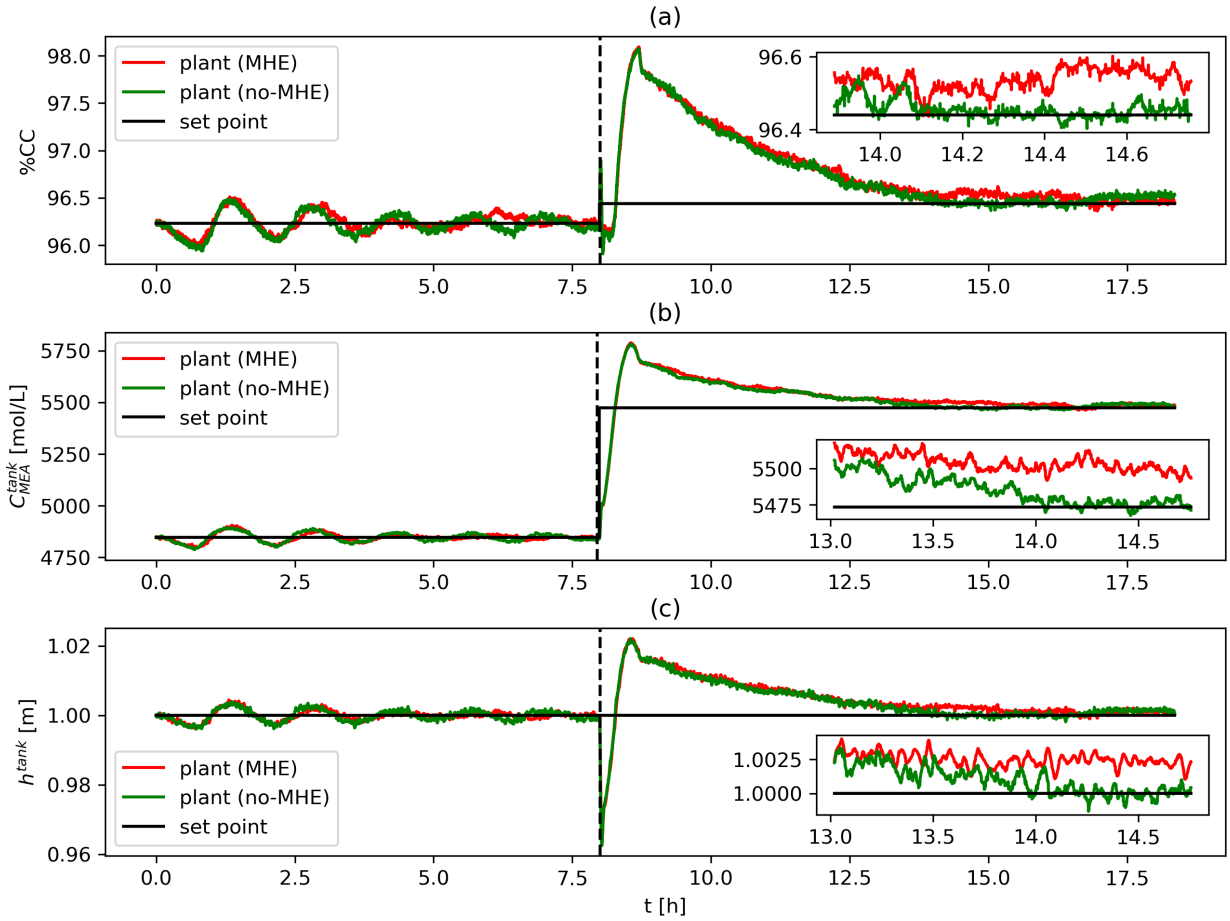

Figure 4-6: Controlled variables in MHE and no-MHE cases for Scenario A. Sub-windows display ranges in which MHE-induced performance loss is most severe.

Table 4-7: Effect of MHE on control and economic performance for Scenario A.

Controlled variable	***SSE*** **(MHE)**	***SSE*** **(no-MHE)**	**Performance loss** (%)
$\%CC$ (%)	3827	3657	4.649
C_{MEA}^{tank} (mol/L)	1.530×10^8	1.416×10^8	8.051
T^{tank} (K)	30.68	23.56	30.22
$h^{tank}(m)$	0.7931	0.7376	7.524
Economics	**Cost (MHE)**	**Cost (no-MHE)**	
$\int_0^{18h} C_{process} dt$ $(\$CAD)$	9018	8977	0.4567

As displayed in Table 4-7 and the drift observed in the controlled variable plots (Figure 4-6a, b, c, particularly the sub-windows), the tracking performance is better in all 'no-MHE' controlled variables as reflected by lower SSE values in Table 4-7. The 'no-MHE' case provides an upper bound for controller performance as it has access to the true plant states and, in principle, the control performance is best when true plant states can be measured. In contrast,

the MHE estimates were shown to sometimes drift from the actual plant states, thus adversely affecting performance. As such, the percent error of the MHE case with respect to the 'no-MHE' case reflects the loss in controller performance owed to the MHE. Nevertheless, the MHE case reflects a more realistic condition since most of plant states are often not available for online control. These losses due to the MHE estimation are generally low ($< \sim 8\%$) except for that of the tank temperature; however, the temperature dynamics are fast compared to other controlled variables and the deviations from the set points are primarily due to noise as shown in Figure A-3 (Appendix A). The speed of the tank temperature dynamics, and the fact that there is little deviation from its set point in both MHE and 'no-MHE' cases (SSE is on the order of $20–30$ across the entire simulation while the nominal tank temperature is on the order of $314\ K$) suggest that the deterioration in tank temperature tracking performance caused by the MHE is negligible in reality because the deviations are caused by noise, thus this variables will not have a significant impact on the rest of the process. In terms of economics, there is little difference in the total process cost as reflected by the cost integral in Table 4-7 whereby the economic loss of the MHE case with respect to the 'no-MHE' case is low. This implies that the loss in tracking performance caused by the MHE does not propagate to the economics because the economic improvements are being achieved in the steady-state phase. That is, the MHE was able to track the true plant states accurately using only a low number of measurements available in the plant. While at steady state, the behaviour of the controlled variables in the MHE and 'no-MHE' cases in Figure 4-6 are observed to have essentially no offset (hence no economic loss). Additionally, Figure 4-5c displays the true $\%CC$ and the MHE-estimated $\%CC$, which again show virtually no offset while at steady state. These results highlight the benefits in using an advanced state estimation scheme such as MHE for the optimal operation of PCC plants. We can conclude that the deterioration from a control and economic perspective caused by the MHE is acceptable considering how few measurements are used and the level of noise. Thus, the MHE performs well in estimating the system states and its application is not a significant detriment on the larger scheme. This result is of prime importance since state estimation will always be necessary for plants such as the PCC system since many plant states cannot be measured online.

As shown in Figure 4-5c, d, and e, following the ramp disturbance at $t = 0\ h$, the NMPC was able to track the system back to its original set points by $t \cong 7.5\ h$ with a few damped oscillations. The initial ramping in the flue gas content from 0 to $t \cong 0.7\ h$ hours cause the flowrate manipulated variables (i.e., Figure 4-5h, i, and j) to also ramp to minimize the effect of the disturbance on the controlled variables. Once the ramp has been completed, hysteresis from this initial ramping action causes the NMPC to modulate the manipulated variables to quickly track the set points. A less aggressive controller tuning (i.e., more weight on control move suppression terms) could have resulted in less oscillation at the expense of control speed; however, due to the stable nature of the PCC system these small oscillations are deemed acceptable.

The increase in CO_2 content in flue gas initially disturbs the system such that the original $\%CC$ cannot be maintained with the pre-disturbance MEA content in the solvent fed to the absorber; thus, rejecting the disturbance to the $\%CC$ is achieved through the increase of the MEA makeup flowrate, as shown in Figure 4-5i. While the initial makeup flowrate is merely $0.0002\ mol/s$, the flowrate after the disturbance rejection is $\sim 0.4\ mol/s$, thus constituting a two thousandfold increase in the flowrate. Despite the relatively low unit price of MEA, the disturbance rejection phase of the scenario leads the process to a very economically disadvantageous combination of controlled and manipulated

variables as the high MEA makeup flowrate is not accompanied by a commensurate increase in the $\%CC$ because of the disturbance. Accordingly, this makeup stream is the primary driver of a drastic increase in process economics following the disturbance rejection compared to the initial process cost ($\sim 59{,}000\ \$CAD/yr$ at $t = 0\ h$ to $\sim 1.5M\ \$CAD/yr$ $t \cong 7.5\ h$; Figure 4-5g and b, respectively). That is, despite MEA being seemingly inexpensive per unit volume, the makeup flowrate is drastically elevated as to have a significant negative impact on the economics. The MEA cost as the primary driver of this condition is also confirmed by the similarity of trajectories of process economics and MEA makeup flowrate in Figure 4-5b and i, respectively. For the proposed NMPC structure to reject the large flowrate disturbance, this behaviour is unavoidable as the only way to substantially maintain $\%CC$ on target is through the MEA makeup. These poor steady-state economics last until corrective action is taken by the RTO to find a new suitable set point for the system.

The RTO is executed at $t \cong 8\ h$ to re-optimize the plant economics under the new operating conditions. To achieve the new set points, which in principle represent a more economical operating point, the process must first undergo another dynamic phase while control actions are imposed. These dynamics are observed to be expensive; during this transient, a process cost peak occurs at $t \cong 8.5\ h$, which is caused by a similar peak in the MEA makeup flowrate. The peak occurs as the RTO imposes an increase in $\%CC$ and C_{MEA}^{tank} set points, which are quickly acted upon by an increase in MEA makeup flowrate. This increased cost period is brief, however, and after the dynamics associated with the increase in reboiler duty shown in Figure 4-5f have elapsed, the MEA makeup decreases back to a near-zero value as the lean loading is decreased through the recycle stream; thus, a large amount of MEA makeup is no longer necessary to maintain the new $\%CC$ set point. These expensive dynamics suggest that the approach presented herein should be applied especially when the system experiences significant and sustained disturbances. The set point increases in $\%CC$ and C_{MEA}^{tank} take advantage of the fact that an increased composition of CO_2 in the flue gas makes it economically advantageous to remove more CO_2 to be sold at the expense of a small increase in reboiler cost, which allows for the reduction of the MEA makeup flowrate as the associated cost. After this initial peak, the controlled variables approach their set point at $t \cong 18\ h$ and the new RTO-defined operating point for the process has a low operating cost of $\sim 48{,}000\ \$CAD/yr$ with respect to the operating cost of pure biomass firing.

The original $\sim 59{,}000\ \$CAD/yr$ (biomass) steady-state cost is broken down into $\sim 86{,}000\ \$CAD/yr$ from reboiler steam, $\sim -32{,}000\ \$CAD/yr$ from CO_2 sales, $\sim 4{,}000\ \$CAD/yr$ from SCC, and $\sim 1{,}000\ \$CAD/yr$ from MEA costs. This is compared to the final $\sim 48{,}000\ \$CAD/yr$ (coal) steady-state cost broken down into $\sim 90{,}000\ \$CAD/yr$ from reboiler steam, $\sim -47{,}000\ \$CAD/yr$ from CO_2 sales, $\sim 5{,}000\ \$CAD/yr$ from SCC, and $\sim 0\ \$CAD/yr$ from MEA costs. This breakdown shows that the RTO increases reboiler duty to achieve more capture (thus sales) despite the increased amount of CO_2 content in the flue gas; this is reflected in an increased reboiler cost and an increased sales profit from the initial to the final steady state. This increased reboiling will typically have implications on the operation of the upstream power plant (e.g., reduction of the power plant's energy output). As a consequence of increased reboiling, the absorber enrichment in the latter (coal-fired) state is primarily achieved through the reboiler rather than the makeup stream, leading to a low MEA makeup cost. The increase in sales profit seen here exemplifies the importance of a carbon economy where CO_2 is treated as a sellable product rather than an unwanted biproduct as noted by Nwaoha and Tontiwachwuthikul (2019), thereby encouraging higher capture rates. Moreover, an increase in SCC

is observed due to the increased CO_2 content in the flue gas, which leads to more total emissions as reflected in the cost (but less relative emissions considering that more CO_2 is being fed to the absorber). This breakdown reflects the large effect that recoups can have to strengthen the incentive to remove CO_2 as well as make the PCC process more economically feasible. From an energy standpoint, the execution of the RTO increases the reboiler duty from an original $\sim 151{,}800\, W$ to $\sim 157{,}500\, W$. As per equation (4-15), this increase constitutes approximately a $1315\ \$CAD/h$ decrease in power plant profits, which is entirely justified considering the $\sim 11{,}000\$CAD/h$ (i.e., $\sim 12\%$ energy penalty) decrease in the optimal steady-state PCC operating cost.

In summary, the net (i.e., including energy penalties) optimal steady state cost for coal is $\sim 19\%$ cheaper than the optimal steady state cost associated with biomass. This occurs as the increased CO_2 content in the flue gas from coal combustion allows for more carbon to be captured and sold at the expense of a minor increase in reboiler duty. Moreover, the evolution of the process economics in this scenario provides new insights with regards to the NMPC and RTO behaviour. The NMPC structure used in this study, while working well to reject disturbances, can lead to drastically increased steady-state operating costs as evidenced in the disturbance rejection phase of the scenario where a significant amount of MEA is required. These high costs, however, are quickly alleviated through the execution of the RTO which lessens the solvent enrichment caused by the MEA makeup and increases the solvent enrichment caused by the reboiler. Moreover, the process dynamics imposed by the NMPC when tracking a new set point can also be expensive because of brief peaks in the MEA makeup; these dynamics are acceptable as they are relatively short-term and are necessary to achieve a more economical operating point. Despite the expensive transients achieved by the proposed scheme, the manipulated variables make a coordinated response as the NMPC is a centralized (multi-variable) control scheme. In contrast, decentralized control strategies would likely lead to even more expensive transient costs as interactions between various control loops would not be accounted for leading to slower control actions; this is a further benefit of the proposed NMPC-based control structure in the case-study. Nevertheless, the losses incurred while operating dynamically to reach a new RTO-defined steady state are justified as they will be recovered in the long term provided that the system is operated at steady state for a sufficiently long period thereafter. For instance, in this case the payback period is $t_{payback} \cong 18\, h$. Moreover, with this control structure, the post-disturbance steady state costs and dynamic costs are inflated due to the unavailability of reboiler duty as a manipulated variable and the high price of MEA. Lifting this restriction and manipulating the reboiler duty as well as makeup stream would likely shorten the payback period by making the dynamics less expensive; however, this is out of the scope of the present study. Still, the approach proposed in this work was shown effective for the cofiring of fuels, which is an increasingly common operational scheme in fuel-fired power plants, while incurring an acceptable energy penalty.

4.4.2. Scenario B: Diurnal Variation of Inlet Flowrate

It is common for power plants to respond to changing energy demands. Diurnal variation is one case that occurs over the course of the weekday for load-changing power plants, whereby the energy demand of the plant varies cyclically. Peak hours often occur in the late mornings, afternoon, and early night; while low demand occurs the late night, and early mornings. To accommodate cycling energy demands, the quantity of fuel combusted, and thus the quantity of

flue gas, both undergo similar diurnal cycles. This scenario has been investigated before (Akula et al., 2021; Harun et al., 2012). In our previous works (Chapter 3 and Appendix A), however, the controller had limited flexibility as it only considered the absorber, thus the solvent could became easily saturated with CO_2, limiting size of disturbances that could be rejected. Through the integration of the control layer in the absorber and buffer tank in this work, larger fluctuations in flue gas flowrate can be rejected as the solvent entering the absorber can be readily concentrated or diluted using the makeup streams.

In this scenario, the cyclic behaviour is modelled as steps around a nominal flue gas flowrate as displayed in Figure 4-7a; this signal has an amplitude equal to 40% of the nominal flue gas flowrate (i.e., there is a 20% step up and a 20% step down from the nominal flue gas flowrate), which exceeds the amplitude explored in previous studies. Following each disturbance, the controller tracks to its outdated set point. Upon reaching an outdated steady state, the RTO is executed such that an updated operating point is defined. This procedure of disturbance rejection and set point tracking would be repeated daily; for the sake of brevity, only a single cycle is performed in this work.

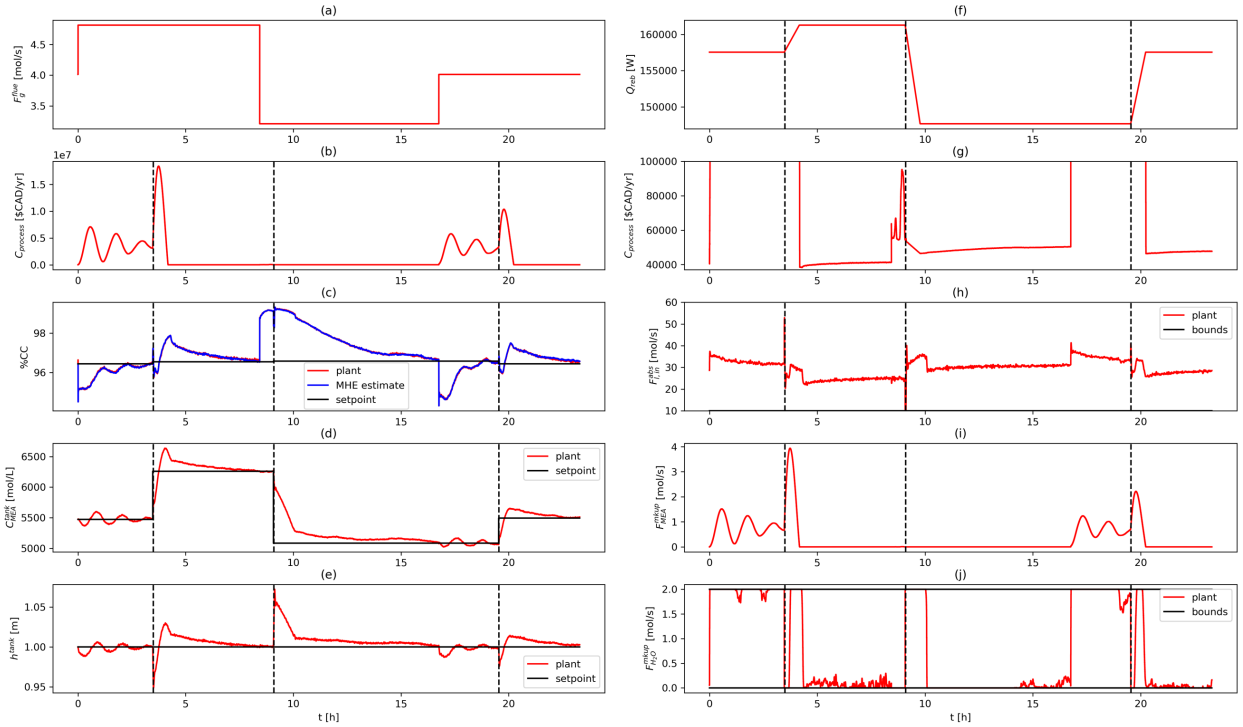

Figure 4-7: Flue gas flowrate, process cost (b shows full profile, g shows zoomed in profile), controlled variables, and manipulated variables for a diurnal variation scenario. Dashed vertical lines represent times at which the RTO was executed, thus inciting a set point change.

The responses on the buffer tank temperature and cooling duty in this scenario can be found in Figure A-4 (Appendix A). For this scenario, the MHE estimates were observed to be in good agreement with the true plant with an $MSE = 7.076 \times 10^{-4}$ and the similar trajectories displayed in Figure 4-7c. While a 'no-MHE' case was not performed in scenario B as in scenario A for brevity, an MSE on the same order as the scenario A suggests that the MHE performance is similarly good, thus allowing the NMPC to have good performance.

This scenario begins at the economically optimal operating point corresponding to the nominal disturbances outlined in Section 4.2.3. A first disturbance is imposed at $t = 0\ h$ and constitutes a 20% step up in flue gas flowrate, thus

beginning the 'peak' hours. Such a disturbance would cause the $\%CC$ to decrease drastically as the amount of solvent being fed into the absorber would no longer be sufficient; however, the disturbance is rejected by the controller through an increase in the MEA makeup flowrate, which enriches the solvent going into the absorber thereby accounting for the excess flue gas. The first disturbance is rejected by $t \cong 4\ h$ with a few brief damped oscillations; however, the resulting process economics are unfavourable because of the new MEA makeup flowrate of $\sim 0.7\ mol/s$ as shown in Figure 4-7i. This is also reflected in the increase of process cost from $\sim 48{,}000\ \$CAD/yr$ (Figure 4-7g) pre disturbance rejection to $\sim 3.1M\ \$CAD/yr$ (Figure 4-7b) post disturbance rejection. At this point ($t \cong 4\ h$), the RTO is executed and leads to a transient lasting until $t \cong 9\ h$, whereby the reboiler duty is increased (Figure 4-7f) to enrich the recycle stream, thus allowing the system to maintain a high $\%CC$ with a lower makeup flowrate. This quickly reduces the process cost to $\sim 42{,}000\ \$CAD/yr$ (Figure 4-7g). This new set point is accompanied by an energy penalty to the upstream power plant of $654\ \$CAD/yr$ owed to the increase in reboiler duty; this is acceptable considering the price reduction from the previous optimal steady state of $\sim 6000\ \$CAD/yr$. Without executing the RTO, the process would have remained at the elevated post-disturbance cost; thus, the cost maintaining the outdated set point (i.e., doing nothing) would be substantial.

At $t \cong 9\ h$, a second 40% step down in flowrate is imposed, thus ending the peak hours. The controller works to reject this disturbance but as shown in Figure 4-7c, d, and e, there is a flattening of the controlled variables at $t \cong 10\ h$. At this point, the (40%) step-down disturbance makes the pre-disturbance $\%CC$ set point too low to be reached by the controller as the high reboiler duty elevates the plant $\%CC$. Despite the MEA flowrate being near its lower bound (Figure 4-7i) and the water flowrate being at its upper bound (Figure 4-7j), there remains a nearly $2\%CC$ upward offset as the size of the disturbance makes the outdated set point unreachable for the current reboiler duty. In addition to this offset, the system quickly reaches a point where the cost fluctuates noisily as a result of modulation of the MEA makeup near its lower bound (as reflected in Figure 4-7g at $t \cong 9\ h \rightarrow 10\ h$). This occurs owing to the strong interaction between the MEA makeup and its simultaneous (and conflicting) effect on both the tank level and the $\%CC$. Despite the MEA makeup still varying, it has very little effect on the controlled variables as they are nearly constant by ~10 hours. Moreover, the process cost is still varying at this point with a minimum of $\sim 60{,}000\ \$CAD/yr$. As the controlled variables have flattened by $t \cong 10\ h$, the RTO is executed whereby a new reachable set point is computed and the system undergoes a transient that lasts until $t \cong 17\ h$ hours and reduces the steady-state cost to $\sim 50{,}000\ \$CAD/yr$. The transient associated with this set point change ($t \cong 10\ h \rightarrow 17\ h$) is longer than the previous set point change ($t \cong 4\ h \rightarrow 9\ h$) as the system starts far from its optimal operating point because the previous set point corresponds to a flue gas flowrate that is 40% higher. Despite the new optimal steady state having a cost that is $\sim 8000\ \$CAD/yr$ higher than the previous steady state, the energy penalty incurred to the upstream power plant is $-2385\ \$CAD/yr$ because of the reduction in reboiler duty. In this case, the RTO decision helps the power plant operation as well as the PCC since ~30% of the losses imposed by the new disturbance on the system will be offset by increased power plant profits owing to the reduction of steam being routed to the PCC plant.

At $t \cong 17\ h$, a third 20% step up in flowrate is imposed, thus returning the system to its nominal flue gas flowrate. This disturbance is successfully rejected by $t \cong 20\ h$ but results in another high operating cost of $\sim 2.6M\ \$CAD/yr$ due to the high MEA makeup flowrate of $\sim 0.5\ mol/s$. The RTO is executed again at $t \cong 20\ h$, whereby the process

cost is returned to its original $\sim 48{,}000\ \$CAD/yr$ in just under $t \cong 24\ h$, thus completing a cycle. This new set point is accompanied by an energy penalty to the upstream power plant of $1731\ \$CAD/yr$, which is substantial as it negates $\sim 87\%$ of the price reduction from the previous optimal steady-state cost of $\sim 2000\ \$CAD/yr$.

As with the Scenario A, large MEA makeup flowrates following disturbance rejection phases are observed. This re-emphasizes the large economic effects that MEA cost can have despite its relatively low price. In contrast to Scenario A, the disturbances in the present scenario occur relatively frequently, resulting in a plant that is in the disturbance rejection phase more often. This leads to frequent dynamic operation, which was observed to be expensive. Despite this, when the RTO is executed the dynamic process cost (i.e., when a new set point is being tracked) typically decreases drastically following a peak as the NMPC often reduces the MEA makeup quickly.

In the three RTO periods associated with a daylong operation with three disturbances observed in the present scenario, the optimal process cost decreases by $\sim 6000\ \$CAD/yr$, increases by $\sim 8000\ \$CAD/yr$, and decreases by $\sim 2000\ \$CAD/yr$ for each RTO period, respectively. The first cost decrease is enabled by the increase in flue gas flowrate, which allows for substantially more carbon to be captured and sold per unit time with only a slight increase in reboiler duty. It is associated with a sizable net (considering energy penalty) cost improvement of $\sim 12\%$ with respect to the pre-disturbance process cost. The second RTO period and its associated increase in cost occurs because of the significant decrease in flue gas flowrate, which allows for less sales recoups. Despite this, the RTO still enables the reduction of steady state cost from the post-disturbance steady state by $\sim 17\%$; that is, while there is an increase of steady state cost with respect to the previous disturbance in this case, the RTO still results in significant loss abatement from the second disturbance-rejection phase. Furthermore, the third RTO period observed a more modest $\sim 0.6\%$ of net cost improvement over the previous RTO period because of a large energy penalty as noted above. Dynamically, for the three RTO periods observed in this scenario, the payback periods were calculated to be $t_{payback} \cong 8\ h$, $t_{payback} \cong 12\ h$, and $t_{payback} \cong 7\ h$ in chronological order. Thus, none of the RTO periods are operated at steady state for a sufficiently long time to justify the expensive dynamics as the payback period is not completed before a new disturbance is imposed. For a scenario such as this where the system has little time to settle before more disturbances are imposed, an EMPC structure may be more well-suited for the dynamic costs to be considered; however, EMPC also has disadvantages as stated in the introduction. Nevertheless, this scenario showed that the execution of the RTO decreased the steady-state costs from the disturbance-rejection phase cost in all three RTO periods observed herein, and that the scheme can handle very large disturbances in flue gas flowrate (with the caveat of expensive dynamics). For slower power plants that do not impose such large load changes on the PCC process, this approach would be more suitable. Moreover, the energy penalty of the power plant was relatively small or negative for two of the RTO periods; even when the penalty was large, it did not exceed the savings incurred by the RTO.

4.4.3. Scenario C: Variation in Prices

To assess the effect of the pricing of RTO economic cost terms on the system's operation, disturbances were imposed on the prices associated with the two primary cost terms (i.e., those that incur the biggest profit or loss during nominal operation as established in the cost breakdown in scenario A). Accordingly, the largest contributors to the overall cost

were found to be the reboiler steam cost and CO_2 sales profit. These prices were varied within ±10% of their nominal value in a series of steps over five RTO periods as depicted in Figure 4-8a.

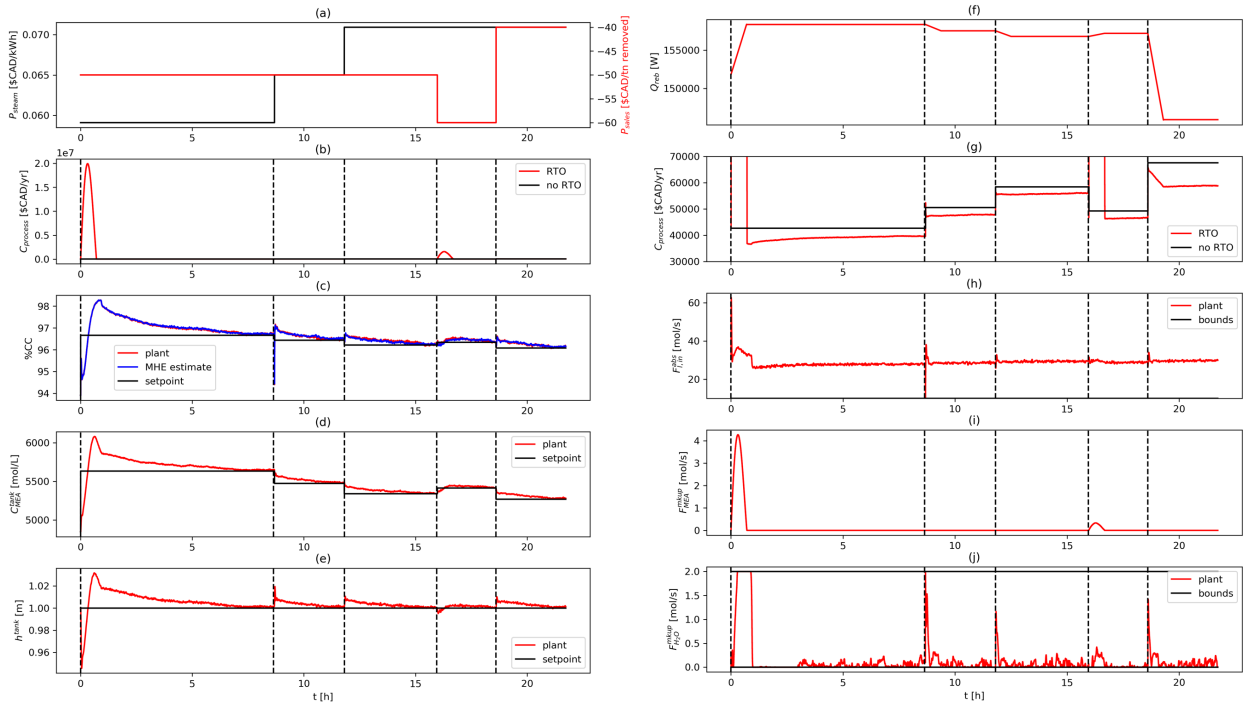

Figure 4-8: Price profiles, process cost, controlled variables (b shows full profile, g shows zoomed in profile), and manipulated variables for price variation scenario. Dashed vertical lines represent times at which the RTO was executed, thus inciting a set point change.

The responses on the buffer tank temperature and cooling duty in this scenario can be found in Figure A-5 (Appendix A). As with the previous scenarios, the MHE estimates were observed to be in good agreement with the true plant with an $MSE = 1.075 \times 10^{-3}$. Moreover, a 'no-MHE' case was performed for this scenario as summarized in Appendix A (Figure A-6 and Table A-3). The control and economic performance loss in this scenario were found to be similarly small to that observed in Scenario A; hence, it is deemed acceptable under the assumptions considered for the present MHE scheme.

The starting point for this scenario corresponds to the nominal conditions outlined in Section 4.2.3 and Table A-1 (Appendix A), in which the system starts far from its economically optimal steady state as reflected in the long initial transient (~8.5 hours) in $\%CC$, C_{MEA}^{tank}, and h^{tank} (Figure 4-8c, d, and e, respectively). Once the system reaches its new operating condition at the end of this transient, the subsequent dynamics related to price changes are comparatively short as they represent adjustments near the optimum rather than a move into a radically different operating point. This is reflected in the small magnitude of the adjustments and brief dynamics made on the $\%CC$ and h^{tank} in RTO periods 2–5.

Figure 4-8b and g show the process cost after execution of the RTO with updated pricing and the subsequent tracking to the newly defined set points that were observed. This profile is compared to the process cost profile of a 'no RTO' case (also shown in Figure 4-8b and g) where the controlled and manipulated variables are maintained at their nominal values (i.e., $\boldsymbol{Y_{nom}}$ and $\boldsymbol{u_{nom}}$, respectively). This way, the economic benefit of executing the RTO over remaining at

the nominal operating conditions suggested in the literature (Nittaya, 2014) can be assessed. The RTO always supplies economically advantageous operating points; however, the amount of improvement over the nominal scenario depends on the specific pricing as summarized in Table 4-8. These improvements range from modest (RTO period 3, nominal sales prices and high reboiler price) to substantial (RTO period 5, low sales price and high reboiler price).

Table 4-8: PCC savings, energy penalty, and net savings for different RTO periods (price combinations) with respect to the 'no RTO' case.

RTO period	**PCC savings** ($\$CAD/yr$)	**Energy penalty** ($\$CAD/yr$)	**Net savings (%)**
1	3047	1149	4.45
2	2776	1005	3.50
3	2417	876	2.64
4	2608	946	3.38
5	8742	−1032	14.47

The second and third RTO periods, after the system reaches its first economic optimum and only reboiler prices are disturbed, provide modest economic advantages over the 'no RTO' operation. This suggests the economic optimum is only mildly dependent on the price of steam although steam comprises a large part of the total cost. The importance of steam price is corroborated by the increase in cost from $\sim 39{,}000\ \$CAD/y$ to $\sim 56{,}000\ \$CAD/y$ upon the two steam price increases, which represents a significant economic penalty. In other words, the reboiler cost makes up a large part of the process economics, but the RTO can only provide modest improvements to offset changes in this price if the system begins at an optimum. Nevertheless, these improvements are worthwhile if the price holds for a long time thereafter. These increases in reboiler cost also cause the RTO to generate lower $\%CC$ set points as the removal of $\%CC$ is disincentivized since it becomes more expensive for the reboiler to provide a MEA-rich recycle stream. Moreover, with the reboiler prices increasing during the second and third RTO periods, the system experience successive decreases in savings and energy penalty. The energy penalty to the power plant is decreased as the RTO dictates that less duty is required as the steam price becomes more expensive while the PCC savings also decrease as less carbon is captured as a result. In both periods, the decreases in PCC savings outpaces the decreases in energy penalty, resulting in lower net savings.

During the fourth RTO period in which the sales price is increased, an increasing incentive to remove CO_2 is observed through a slight increase in $\%CC$ set point. This occurs along with a significant drop in process cost to $\sim 46{,}000\ \$CAD/y$ as more economic benefits can be recouped through CO_2 sales. This period also represents an increase in the improvement over the no RTO case from the previous period as displayed in Table 4-8, which suggests that there is a larger economic benefit to be gained by executing the RTO upon sales prices changes. In this fourth period, the energy penalty increases owing to the increased recoup price, which incentivizes removal and higher reboiler duty. In contrast to the previous two periods, the increase in PCC savings is greater than the increase in energy penalty, hence an increase in net savings is observed.

The notion of potentially large savings to be made upon changes in sales price is further reinforced in the fifth RTO period, which represents the most substantial cost improvement over the 'no RTO' case. This occurs with a low sales

price, which decreases the $\%CC$ set point by drastically decreasing the reboiler duty leading to a large price increase. In this period, the RTO allows less CO_2 to be removed since the economic incentive of selling the capture material is significantly reduced. This is reflected in the process economics as there is a decrease in the money recouped through sales, causing the process cost to increase to a high of $\sim 65{,}000\ \$CAD/y$. A substantial decrease in reboiler duty such that it goes below the reboiler duty in the 'no RTO' case is dictated by the RTO in this period; hence the negative energy penalty as shown in Table 4-8. In this case, the savings are substantial as they are made with respect to both the PCC and the power plant, hence the large net savings.

As observed in this scenario, there can be a significant dependence of optimal process cost on the material and energy prices as shown in Figure 4-8g ranging from $\sim 39{,}000\ \$CAD/y$ to $\sim 56{,}000\ \$CAD/y$. However, these all represented improvements with respect to the nominal operating point reported by Nittaya (2014) with net savings ranging from $\sim 3 - 14\%$ as summarized in Table 4-8 (i.e., net because the associated energy penalties are accounted for). As in previous scenarios, the dynamics associated with some set point changes were observed to be costly during some periods of time. This was observed at the beginning of RTO periods 1 and 4 where there are short (~ 40 minute) spikes in MEA makeup. Accordingly, the RTO should be primarily executed if the prices are expected to hold thereafter such that the detriment from the spikes can be made up for by the improved steady-state economics. As in the previous scenarios, the energy penalty to the power plant never exceeded the RTO savings, thus justifying the use of an RTO framework. Day-to-day variations in typical commodity/energy prices are often noisy and small, thus they would not warrant set point changes. In contrast, price variation on the order observed in this scenario (i.e., $\pm 10\%$) would occur less regularly; these would warrant the execution of the RTO as doing nothing would represent significant additional costs as shown by the comparison to the no RTO case in Table 4-8. That is, large price changes as observed in this scenario are outside the tolerance of noise and occur when there is a market change; these price changes would justify the use of RTO such that the payback period is short given the expensive dynamics observed.

The averaged computational times for the RTO, NMPC, and MHE in the proposed scheme for this scenario are $4.33\ s$, $55.43\ s$, and $64.65\ s$, respectively. The CPU times do not change significantly across test scenarios as the optimization problems are of the same size and were carried out using the same hardware; thus, these times are representative for all scenarios. As can be observed in the CPU times for the dynamic optimization problems, the implementation of a large model as in the present study requires significant computational effort; this is one of the drawbacks of using a mechanistic model. Despite having the same number of equations, the MHE problem requires more CPU time than the NMPC problem, owing to an increased number of decision variables (i.e., manipulated variables trajectories in NMPC vs. state trajectories in MHE). The long computational times of the dynamic optimization problems used herein warrant adjustments in the solution strategy for the scheme to be used in a real plant. One option is to accept the computational delay caused by these long CPU times and asses its effect on the control and estimation layers; however, this can have detrimental effects on performance. Previous studies have proposed the use of terminal conditions to mitigate this issue (Chen et al., 2000), but this increases the implementational complexity of the control scheme. More attractively, a reduction in this computational effort can be achieved through efficient reformulations such as the advanced-step NMPC presented by (Zavala and Biegler, 2009).

4.4.4. Remarks

The scheme was implemented on an MEA-solvent pilot-scale PCC absorber section and a mechanistic process model was used for the layers comprised in the proposed scheme. The absorber section and proposed scheme were subjected to test scenarios including cofiring, diurnal variations, and price variations to assess performance. A ∼19% improvement in process cost was observed in the cofiring scenario (A) with only a small (∼0.5%) of economic performance deterioration caused by the MHE. The diurnal variation scenario (B) revealed improvement in steady-state economics upon the introduction of each new disturbance from ∼12% cost improvements (in the cases where disturbances caused the cost to improve) to ∼17% loss abatement (in the cases where the disturbances caused the cost to increase). Furthermore, a ∼3% to ∼14% cost improvement with respect to maintaining a constant set point was observed for different economic incentives (through price variations) in the scenario C.

Dynamically, the NMPC layer was shown to track the RTO-supplied economically optimal set points quickly in all scenarios while maintaining non-economic variables, such as temperature and level, steady. Occasionally, the control actions in the NMPC were observed to be expensive because of the use of MEA makeup as a manipulated variable; this would make the proposed scheme expensive to execute for plants subject to continuous disturbances where steady-state operation is not sustained for long periods. This finding is consistent with the fact that RTO is a steady-state optimization method, which does not consider dynamics when determining set points. Nevertheless, the payback periods for the scenarios observed in this work were found to be reasonable with respect to the RTO period lengths (i.e., the payback period were of similar lengths to the RTO periods). Moreover, the MHE was observed to provide consistently acceptable estimates of the absorber as observed through the NMPC performance, which showed little deterioration compared to when full state access was assumed. The fidelity of the estimates was also evidenced by the low error in the MHE-estimated $\%CC$ with respect to the true $\%CC$.

From a process economics perspective, it was found through the test scenarios that there is a substantial potential to recoup costs through CO_2 sales; this was most salient at high inlet CO_2 concentrations (i.e., with very emissive fuels) and high flue gas throughputs, whereby the PCC plant was operated at a high $\%CC$. Furthermore, the energy penalty to the upstream power plant was always lower than the economic benefit incurred by the RTO; thus, justifying the execution of the RTO even if the energy consumption led to some reduction of its potential cost improvements. It is thus evident that the RTO, while not having a model of the power plant, is able to make sensible decisions regarding the energy use of the PCC plant such that the power plant does not experience an undue energy burden because of carbon capture.

4.5. Summary

An operating scheme was proposed for the economic optimization of PCC. The RTO layer introduces a novel economic function, which provides a comprehensive consideration of process economics through its inclusion of SCC, CO_2 sales profit, chemical cost, and energy cost; this provides realistic and economical set points to the control layer through its use of the proposed economic function. The NMPC layer enables the centralized control of the absorber and buffer tank while keeping the system inside its physical and safety constraints. Moreover, the control structure in the case study provides adequate control flexibility because of its ability to concentrate and dilute the absorber feed

using the buffer tank makeup streams. The MHE layer provides accurate estimates of the states required to execute the previous two layers while only requiring a realistic number of measurements and ensuring that the estimates adhere to constraints. The case study results demonstrate that the operational approach presented herein do, in fact, provide an economically optimal operating approach for PCC operating downstream from fuel-fired power plants. Approaches such as this will be paramount in achieving economic viability in PCC such that fuel-firing can become environmentally viable.

5. Low-variance Parameter Estimation

To the authors' knowledge, a scheme to abate the effect of noise directly in parameter estimates in RTO has not been proposed in the literature. The present study introduces a low-variance PE (lv-PE) algorithm coupled with RTO for the economic operation of noisy processes. The lv-PE scheme reduces the error in parameter estimates with a twofold strategy. Firstly, the available measurements are probed for their information content to ensure low parameter variability (i.e., high precision) by performing "challenger" PE problems with different measurement combinations; this ensures that most of the information-rich measurements are used for PE. Secondly, a filter is introduced to reduce the frequency of high-error estimates by establishing parameter bounds; this prevents estimates beyond realistic bounds to be implemented in the system. Using the measurement-probing and data-filtering steps, the proposed method results in low measurement-to-parameter noise propagation and elimination of high-error estimates. The deployment of the proposed method does not entail a fundamental redesign of the two-layer RTO scheme that is prevalent in industry; this makes it an attractive way to augment RTO performance in any system that uses the two-layer approach. As will be shown in the following sections, the method only requires additional computations to be performed using the recurrently sampled measurements which would be collected nonetheless. Notably, this approach is not mutually exclusive with any aforementioned technique (i.e., GED, DR, robust estimation) since it chooses favourable measurements (pre-estimation) and filters noise from the resulting estimates (post-estimation). The proposed method can be used to improve the efficacy of robust estimators in noisy conditions and be included as an extra data-processing step with data reconciliation, gross error detection, or any online estimation task (e.g., state estimation).

The study is structured as follows: preliminary notation and standard definitions are defined at the outset; Section 5.1 outlines the regular formulations for RTO, PE, and NMPC to expound on the arising issues with PE and provide context for the proposed algorithm. Section 5.2 presents, and rigorously motivates the proposed algorithm, also providing frameworks to analyze process economics and constraint violations in RTO-operated systems. Section 5.3 illustrates the implementation of the proposed algorithm through two case studies: an evaporator process and the Williams-Otto process. Section 5.4 summarizes the findings and provides areas of future work.

Preliminaries

Bolded letters denote matrices and vectors, while plain letter done scalars. Lower-case bolded letters denote vectors, while upper-case bolded letters denote matrices. $\boldsymbol{I}_{n_i} \in \mathbb{R}^{n_i \times n_i}$ denotes an identity matrix of dimensions $n_i \times n_i$. $\boldsymbol{I}_{n_i:j} \in \mathbb{R}^{n_i \times (n_i+1)}$ denotes a matrix composed of the identity matrix of dimensions $i \times i$ with a zero vector of length i inserted as column j, e.g.:

$$\boldsymbol{I}_{3:3} = \begin{bmatrix} 1 & 0 & 0 & 0 \\ 0 & 1 & 0 & 0 \\ 0 & 0 & 0 & 1 \end{bmatrix} \tag{5-1}$$

Given a generic vector $\boldsymbol{x} = [x_1 \quad \cdots \quad x_n]^{\boldsymbol{T}}$, some operations on the vector are defined. $\|\boldsymbol{x}\|_{\boldsymbol{A}}{}^2$ denotes a quadratic form on the vector $\boldsymbol{x} \in \mathbb{R}^{n_x}$ with the weighting matrix $\boldsymbol{A} \in \mathbb{R}^{n_x \times n_x}$. $\hat{\boldsymbol{x}} \in \mathbb{R}^{n_x}$ denotes model prediction of $\boldsymbol{x} \in \mathbb{R}^{n_x}$. Model predictions are not inputs to the model nor the decision variables; rather, they are generated while solving optimization problems but not conveyed to any other layers unless explicitly stated. $\{\boldsymbol{x}_{\boldsymbol{t-i}}\}_{i=0}^{N}$ denotes a discrete

sequence of the vector $\boldsymbol{x}$ from the present time t to time $t-N$. $\bar{\boldsymbol{x}} \in \mathbb{R}^{n_X}$ denotes the average of the sequence and $\boldsymbol{\sigma_x}$ denotes the standard deviation of that sequence, i.e.:

$$\bar{\boldsymbol{x}} = \frac{1}{N}\sum_{i=-N}^{0} \boldsymbol{x_{t+i}} \tag{5-2}$$

$$\boldsymbol{\sigma_x} = \sqrt{\frac{\sum_{i=-N}^{0}(\boldsymbol{x_{t+i}} - \bar{\boldsymbol{x}})^2}{N-1}} \tag{5-3}$$

Similarly, the covariances of elements within the vector $\boldsymbol{x}$ given their discrete sequence $\{\boldsymbol{x_{t-i}}\}_{i=0}^{N}$ is estimated as follows:

$$K_{i,j} = \frac{1}{N}\sum_{k=0}^{N}(x_{i,t-k} - \bar{x}_i)(x_{j,t-k} - \bar{x}_j) \qquad \forall i \in \{1,\dots,n_x\}, \forall j \in \{1,\dots,n_x\} \tag{5-4}$$

The latter expression can be used to construct the covariance matrix $\boldsymbol{K_x} \in \mathbb{R}^{n_x \times n_x}$. Lastly, this study uses *US*$ as the monetary basis.

5.1 Real-time Optimization of Controlled Plants

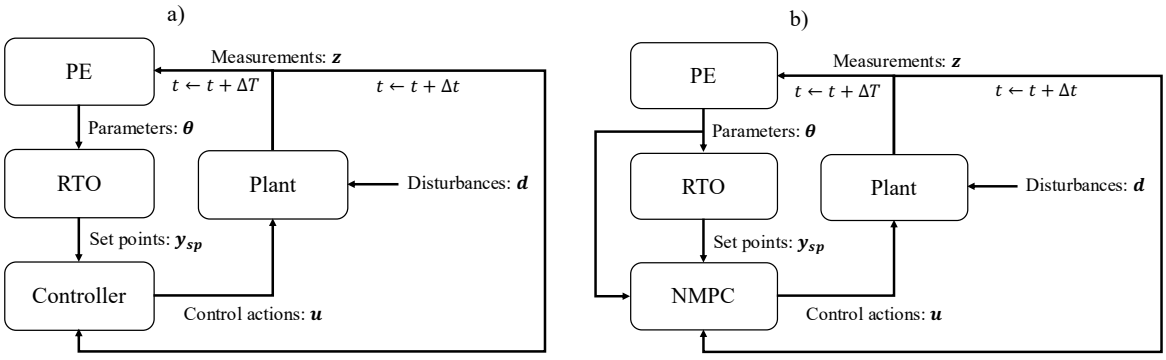

Figure 5-1: Typical RTO scheme for a controlled plant with a) independent optimization and control models, b) equivalent optimization and control models.

Figure 5-1 depicts the exchange of information between the plant, RTO, PE, and controller via the two-step approach. Herein, a continuous plant is assumed to be subject to measurable disturbances ($\boldsymbol{d} \in \mathbb{R}^{n_d}$). Note that this assumption is made for simplicity (i.e., measurability is not necessary for the proposed method as will be discussed later in this section). Measurements ($\boldsymbol{z} \in \mathbb{R}^{n_z}$) can be acquired from the plant such that enough new data is collected to perform the PE problem at every RTO period ΔT. The PE problem supplies the RTO economic optimization problem with updated model parameters ($\boldsymbol{\theta} \in \mathbb{R}^{n_\theta}$) which, in turn, supplies the controller with set points ($\boldsymbol{y_{sp}} \in \mathbb{R}^{n_y}$). Note that $\boldsymbol{y}$ denotes the controlled variables that are regulated towards their respective set points ($\boldsymbol{y_{sp}}$). The controller regulates the plant towards the RTO-supplied set points at every sampling interval Δt such that the plant is kept on target. Note that $\Delta T = k\Delta t$ where $k \in \mathbb{Z}^+$ (i.e., the RTO period is a positive integer multiple of the sampling interval), and typically $\Delta T \gg \Delta t$. Moreover, while state accessibility is often an issue in process plants, we assume that the required measurements are accessible for the purposes of this work (i.e., full state access is considered); this is not necessary for the scheme but done for simplicity and to remove confounding factors.

Two controller implementations are possible as depicted in Figure 5-1, a) when the controller uses an individual internal model/scheme and, b) when the RTO, PE, and controller models are equivalent (i.e., they use dynamic and steady state versions of the same model). The latter case is of primary interest as parameter updates are passed to both RTO and controller, thus affecting the scheme's performance in a twofold manner. For the purposes of this study, the parameter estimates are passed to both layers; however, they need only be passed to the RTO or NMPC layers to affect the system operation. Indeed, in larger systems where the online mechanistic control problem is expensive to compute, the use of a mechanistic MPC may be impractical such that the controller will be incompatible with PE. The use of equivalent models often necessitates that the controller uses detailed process models to match the PE and RTO layers, which are typically nonlinear, hence the use of nonlinear model predictive control (NMPC), as depicted in Figure 5-1b. The NMPCs employed herein use a dynamic version of the steady-state model deployed in the RTO and PE. Indeed, the interaction between NMPC and RTO has been studied previously (Adetola and Guay, 2010; Diehl et al., 2002); to the authors' knowledge, studies addressing a reduction of parameter variability owed to measurement noise are not available in the literature. Generally, RTO problems are formulated as follows:

$$\begin{aligned} &\min_{\hat{\boldsymbol{y}}} \Phi \\ &s.t. \\ &\boldsymbol{f_s}(\hat{\boldsymbol{x}}, \hat{\boldsymbol{y}}, \boldsymbol{u}, \boldsymbol{d}, \boldsymbol{\theta}) = \boldsymbol{0} \\ &\boldsymbol{g_s}(\hat{\boldsymbol{x}}, \boldsymbol{u}, \boldsymbol{d}) \leq \boldsymbol{0} \\ &\boldsymbol{y^l} \leq \boldsymbol{y} \leq \boldsymbol{y^h} \\ &\boldsymbol{u^l} \leq \boldsymbol{u} \leq \boldsymbol{u^h} \end{aligned} \tag{5-5}$$

where $\Phi \in \mathbb{R}$ denotes the economic model for which the process is optimized. In formulation (5-5), it is assumed that Φ is an economic loss function being minimized; however, maximization of a revenue function also occurs. The inputs to the RTO formulation (5-5) are the current process disturbances ($\boldsymbol{d}$) and the uncertain model parameters ($\boldsymbol{\theta}$), while the outputs are the economically optimal controlled variables ($\boldsymbol{y} \in \mathbb{R}^{n_y}$). The process state predictions ($\hat{\boldsymbol{x}} \in \mathbb{R}^{n_x}$) and the manipulated variables ($\boldsymbol{u} \in \mathbb{R}^{n_u}$) corresponding to the optimal set points are also generated by the model. $\boldsymbol{f_s}: \mathbb{R}^{n_u} \times \mathbb{R}^{n_d} \times \mathbb{R}^{n_\theta} \longrightarrow \mathbb{R}^{n_x} \times \mathbb{R}^{n_y}$ denotes the steady-state process model. $\boldsymbol{y^l}$ and $\boldsymbol{y^h} \in \mathbb{R}^{n_y}$ are lower and upper bounds for the set points, respectively, while $\boldsymbol{u^l}$ and $\boldsymbol{u^h} \in \mathbb{R}^{n_u}$ are lower and upper bounds, respectively, for the manipulated variables. $\boldsymbol{g_s}: \mathbb{R}^{n_x} \times \mathbb{R}^{n_u} \times \mathbb{R}^{n_d} \longrightarrow \mathbb{R}^{n_g}$ are any constraints (aside from those on the inputs and set points) to which the economic optimum must adhere. The RTO supplies the controlled variable set points to the controller (i.e., $\boldsymbol{y_{sp}}$). Although the RTO may provide a set point that is challenging to match by the controller because of model uncertainty in both layers, the set point is nonetheless conveyed between the layers as it approximates the economic optimum (with some error); this point is described in the following section. Executing the RTO (and corresponding PE) problem too frequently would put undue computational burden on the plant and may not necessarily lead to drastic improvement in performance. Accordingly, the RTO problem is executed every RTO period ΔT as specified by the user, such that the set point is periodically being updated as more plant data becomes available. In contrast, the controller acts on the plant at every sampling interval Δt.

The controller is tasked with regulating the controlled variables towards the RTO-defined set points. In the case of an equivalent model between layers (Figure 5-1b) an NMPC can be considered. NMPC (or MPC more generally) takes plant state measurements or estimates at every sampling interval Δt and uses them as initial conditions for a process

model to predict plant behaviour on the horizon P. The manipulated variables are used as decision variables on the horizon C such that the NMPC generates the sequence $\{\boldsymbol{u_{t+i}}\}_{i=1}^{C}$ ($C \leq P$ such that $\boldsymbol{u}$ is assumed to remain constant beyond C). The first instance of manipulated variables from this sequence $\boldsymbol{u_{t+1}}$ are subsequently provided to the plant such that the system is controlled. The NMPC problem is formulated as follows:

$$\min_{\boldsymbol{u_{t+i}} \forall i \in \{1,\dots,P\}} \sum_{i=1}^{P} \left\| \boldsymbol{y_{sp}} - \boldsymbol{\hat{y}_{t+i}} \right\|_{\boldsymbol{Q_c}}^{2} + \sum_{j=1}^{P} \left\| \Delta \boldsymbol{u_{t+i}} \right\|_{\boldsymbol{R_c}}^{2}$$

$$s.t.$$

$$\begin{aligned}
&\boldsymbol{f_d}(\boldsymbol{\hat{x}_{t+i}}, \boldsymbol{\hat{y}_{t+i}}, \boldsymbol{u_{t+i}}, \boldsymbol{d_{t+i}}, \boldsymbol{\theta}) = \boldsymbol{\hat{x}_{t+i+1}} && \forall i \in \{1, \dots, P-1\} \\
&\boldsymbol{\hat{x}_t} = \boldsymbol{x_0} && \\
&\boldsymbol{g_d}(\boldsymbol{\hat{x}_{t+i}}, \boldsymbol{u_{t+i}}, \boldsymbol{d_{t+i}}) \leq \boldsymbol{0} && \forall i \in \{1, \dots, P\} \\
&\boldsymbol{y^l} \leq \boldsymbol{\hat{y}_{t+i}} \leq \boldsymbol{y^h} && \forall i \in \{1, \dots, P\} \\
&\boldsymbol{u^l} \leq \boldsymbol{u_{t+i}} \leq \boldsymbol{u^h} && \forall i \in \{1, \dots, P\} \\
&\boldsymbol{u_{t+i+1}} = \boldsymbol{u_{t+i}} && \forall i \in \{C, \dots, P-1\}
\end{aligned} \tag{5-6}$$

where all variables are defined as in the RTO with an additional dependence on time. The first term of the objective function represents a minimization of the sum of squared errors between the controlled variables and their set points over the horizon P, while the second term minimizes the squared changes in the manipulated variables from one time period to the next (i.e., $\Delta \boldsymbol{u_{t+i+1}} = \boldsymbol{u_{t+i+1}} - \boldsymbol{u_{t+i}}\ \forall i \in \{1, \dots, C\}$). These objective function terms affect control performance and manipulated variable speed, and are subject to the diagonal weighting matrices $\boldsymbol{Q_c} \in \mathbb{R}^{n_y \times n_y}$ and $\boldsymbol{R_c} \in \mathbb{R}^{n_u \times n_u}$, respectively, which are determined from prior tuning. $\boldsymbol{f_d}: \mathbb{R}^{n_x} \times \mathbb{R}^{n_u} \times \mathbb{R}^{n_d} \times \mathbb{R}^{n_\theta} \longrightarrow \mathbb{R}^{n_x} \times \mathbb{R}^{n_y}$ denotes the dynamic process model. $\boldsymbol{g_d}: \mathbb{R}^{n_x} \times \mathbb{R}^{n_u} \times \mathbb{R}^{n_d} \longrightarrow \mathbb{R}^{n_g}$ are the set of inequality constraints (aside from the controlled and manipulated variable constraints) that are imposed on the predicted trajectories. The inputs to the NMPC dynamic optimization problem are the initial conditions $\boldsymbol{x_0} \in \mathbb{R}^{n_x}$, which are state measurements or estimates; as well as the disturbance trajectories ($\boldsymbol{d_t} = \cdots = \boldsymbol{d_{t+P}}$) and the model parameters ($\boldsymbol{\theta}$), which are assumed to remain constant at the latest disturbance and PE-defined value for the entire controller prediction horizon, respectively. The outputs of this problem are the optimal manipulated variable trajectory ($\boldsymbol{u_{t+i}} \in \mathbb{R}^{n_u}$) as well as the predicted state ($\boldsymbol{\hat{x}_{t+i}} \in \mathbb{R}^{n_x}$) and controlled variable trajectories ($\boldsymbol{\hat{y}_{t+i}} \in \mathbb{R}^{n_y}$). Only the first time-instance of the manipulated variables trajectory (i.e., $\boldsymbol{u_{t+1}}$) is implemented in the plant. After this, the plant is operated for a sampling interval Δt whereby new measurements are given to the NMPC as feedback and the formulation in equation (5-6) is re-solved; therefore, the process of sampling and solving the NMPC problem is repeated recursively, and the scheme becomes closed-loop.

The uncertain model parameters ($\boldsymbol{\theta}$) associated with formulations (5-5) and (5-6) must be estimated prior to every execution of the RTO problem (5-5) to reconcile the plant model with the current steady state operating conditions. The PE optimization problem is based on Bayesian inference, which allows for the embedding of prior information and determination of weighting terms in a statistically rigorous manner. This assumes that measurements (and thus the noise associated with measurements) obey a Gaussian distribution; the complete outline of the probabilistic

interpretation can be found elsewhere (Cox, 1964). As such, the work herein is limited to Gaussian noise, which is indeed a very common assumption in process systems.

The PE problem uses a measurement sequence $\{\boldsymbol{z_{t-i}}\}_{i=0}^{M}$, whereby the past M steady-state samples are considered. This allows for averaged measurements ($\bar{\boldsymbol{z}} \in \mathbb{R}^{n_z}$) to be computed using equation (5-2) along with the measurement covariance matrix ($\boldsymbol{K} \in \mathbb{R}^{n_z \times n_z}$) using equation (5-4). The PE problem is as follows:

$$
\begin{aligned}
&\min_{\boldsymbol{\theta}} \|\hat{\boldsymbol{z}} - \bar{\boldsymbol{z}}\|_{\boldsymbol{K}^{-1}}{}^2 \\
&s.t. \\
&\boldsymbol{f_s}\left(\hat{\boldsymbol{x}}, \hat{\boldsymbol{y}}, \bar{\boldsymbol{u}}, \bar{\boldsymbol{d}}, \boldsymbol{\theta}\right) = \boldsymbol{0} \\
&\boldsymbol{h_s}\left(\hat{\boldsymbol{x}}, \bar{\boldsymbol{u}}, \bar{\boldsymbol{d}}\right) = \hat{\boldsymbol{z}} \\
&\boldsymbol{g_s}\left(\hat{\boldsymbol{x}}, \bar{\boldsymbol{u}}, \bar{\boldsymbol{d}}\right) \leq \boldsymbol{0} \\
&\boldsymbol{\theta^l} \leq \boldsymbol{\theta} \leq \boldsymbol{\theta^h}
\end{aligned}
\tag{5-7}
$$

$\boldsymbol{f_s}: \mathbb{R}^{n_u} \times \mathbb{R}^{n_d} \times \mathbb{R}^{n_\theta} \longrightarrow \mathbb{R}^{n_x} \times \mathbb{R}^{n_y}$ is the steady-state process model that also corresponds to the model used in formulation (5-5). $\boldsymbol{\theta^l}$ and $\boldsymbol{\theta^h} \in \mathbb{R}^{n_\theta}$ are lower and upper bounds, respectively, for the parameter estimates. $\boldsymbol{g_s}: \mathbb{R}^{n_x} \times \mathbb{R}^{n_u} \times \mathbb{R}^{n_d} \longrightarrow \mathbb{R}^{n_g}$ are any constraints (aside from those on the inputs and set points) to which the estimates must adhere. Moreover, $\boldsymbol{h_s}: \mathbb{R}^{n_x} \times \mathbb{R}^{n_u} \times \mathbb{R}^{n_d} \longrightarrow \mathbb{R}^{n_z}$ denotes the function between the model inputs and measurement prediction. The measurements can coincide with the states or be functions of the model inputs/states. The objective function in problem (5-7) minimizes the differences between the model measurement predictions and the sample-averaged measurements by using the model parameters as the decision variables. The inverse covariance matrix ($\boldsymbol{K}^{-1}$) weights the objective function such that high-variance measurements are assigned low weights with the converse occurring for low-variance measurements. By performing the sampling and averaging, less noisy reconciliation between plant and model are achieved; however, some noise will still propagate to the parameter estimates as experimental data are used. In executing this formulation, the plant and model are reconciled for current operating conditions as the latest available steady-state plant data including the measurements, manipulated variables, and disturbances are used. As such, the inputs to this problem are the averaged measurements ($\bar{\boldsymbol{z}}$), averaged manipulated variables ($\bar{\boldsymbol{u}}$), and disturbances ($\bar{\boldsymbol{d}}$) while the outputs are the parameter estimates ($\boldsymbol{\theta}$). While a large M would be preferable for its averaging effect (especially in the presence of noise), this can lead to the use of measurements that are not truly at steady state (e.g., owing to drift or subtle control actions over time); thus, the size of M is typically limited. Note that this formulation can also be adapted for disturbance estimation or joint parameter/disturbance estimation; however, this work is restricted to cases involving parameter estimation.

As both RTO and NMPC layers are privy to the parameter estimates, poor PE performance can lead to suboptimal operation via inaccurate RTO set points and set point offset in the NMPC layer when compared to the true optimum. Given the formulations presented above, the importance of the PE problem becomes clear from the dependence of the RTO and NMPC on $\boldsymbol{\theta}$. Moreover, the gaps for a method to deal with variation in parameter estimates can be expounded upon:

1) More information (i.e., measurements) do not necessarily mean that the PE problem (5-7) will yield better estimates as covariances ($\boldsymbol{K}$) may, in fact, weigh the problem unevenly such that it becomes ill-conditioned.

Typically, all available measurements ($\boldsymbol{z}$) are used when solving PE problems; accordingly, there is need for a method that can choose a favourable subset of measurements to provide to the PE step.

2) Problem (5-7) uses a sample of measurements ($\{\boldsymbol{z_{t-i}}\}_{i=0}^{M}$), which are subject to noise through the sample average $\bar{\boldsymbol{z}}$ and the covariance matrix $\boldsymbol{K}$. The propagation of noise from the measurements to the parameter estimates can cause economic losses, which accrue in the long-term. There remains a gap for a method to ensure this does not occur by filtering for erroneous estimates.

To address these issues, the low-variance PE procedure is introduced herein and presented in the following section. This comprises an algorithm that determines favourable measurements to embed in the PE problem as well as a filter to reject instances where the parameters are poorly estimated.

5.2 Low-variance Parameter Estimation (lv-PE)

The proposed low-variance PE (i.e., lv-PE) scheme works by reducing the variability in parameter estimates with respect to their expected value, which is equivalent to their true value provided that the system is absent of systematic errors (see assumption 3 below). Accordingly, any single estimate may not be more accurate at a given PE/RTO iteration; however, the estimates over time will be more precise, thus benefits will accrue over many RTO periods. In this section, the scheme is motivated through analysis of the set point error, which is attributed to parameter error. Then, the algorithm comprising the scheme is discussed step-by-step. Moreover, the economic implications of the method are discussed, with a novel algebraic and geometric interpretation of RTO economics. Assessment metrics for the scheme are introduced at the end of this section.

The following assumptions are made herein:

1) The time operating at steady state far exceeds the time operating dynamically. This is an underlying assumption in systems that operate with RTO (Darby et al., 2011) (i.e., not specific to the proposed approach) as the principle of steady-state optimization is that cost-optimal operating policy is steady while dynamic operation is expensive and should be minimized.
2) The measurement noise is additive Gaussian and occurs owing to random errors. As noted earlier, this is an underlying assumption of standard PE in equation (5-7) as the least-squares objective embedded with prior measurements arises from Bayesian inference in the presence of Gaussian noise (Cox, 1964).
3) Plant–model mismatch is owed to PE error. This is a standard assumption in the two-layer RTO ((Darby et al., 2011) whereby a mechanistic model is assumed to provide an adequate representation of the system and only requires parameter estimates to match the plant. Mechanistic process models are increasingly common and available for RTO; however, in cases where such model is not available, other approaches (Marchetti et al., 2009; Roberts and Williams, 1981) can be considered. The PE error herein is owed to large amounts of noise to which the measurements are subjected. Measurement bias and similar systematic errors are not addressed herein as they would require GED. In principle, GED could also be addressed within the proposed scheme but would require an extra processing layer as indicated in the introduction. However, as this is the first study to use the proposed approach, extra layers were not considered to explicitly assess the benefits and limitations of the method.

5.2.1. Effect of Parameter Errors on Set Point Tracking

A theoretical argument is first made to motivate the proposed approach, which connects parameter error to set point error for an RTO-operated system. Consider a single RTO period during which the process loss is minimized (alternatively, revenue can be maximized). For a constrained RTO to operate the process at its "true" economic optimum (i.e., the economic optimum corresponding to the plant, not the mismatched model) the controlled variables must fulfill the Karush-Kuhn-Tucker (KKT) conditions, i.e.:

$$\begin{aligned} &\nabla\Phi\left(\boldsymbol{y}_{\boldsymbol{sp}}^{\boldsymbol{true}}\right) + \boldsymbol{J}_{\boldsymbol{f}}\left(\boldsymbol{y}_{\boldsymbol{sp}}^{\boldsymbol{true}}\right)^{T}\boldsymbol{\lambda} + \boldsymbol{J}_{\boldsymbol{g}}\left(\boldsymbol{y}_{\boldsymbol{sp}}^{\boldsymbol{true}}\right)^{T}\boldsymbol{\mu} = \mathbf{0} \\ &\boldsymbol{f}\left(\boldsymbol{y}_{\boldsymbol{sp}}^{\boldsymbol{true}}\right) = \mathbf{0} \\ &\boldsymbol{g}\left(\boldsymbol{y}_{\boldsymbol{sp}}^{\boldsymbol{true}}\right) = \mathbf{0} \\ &\boldsymbol{\mu}^{T}\boldsymbol{g}\left(\boldsymbol{y}_{\boldsymbol{sp}}^{\boldsymbol{true}}\right) = 0;\ \boldsymbol{\mu} \geq \mathbf{0} \end{aligned} \tag{5-8}$$

where $\boldsymbol{J}_{\boldsymbol{f}} \in \mathbb{R}^{n_x \times n_y}$ and $\boldsymbol{\lambda} \in \mathbb{R}^{n_x}$ are the Jacobian matrix and KKT multipliers of the process model, respectively. Moreover $\boldsymbol{J}_{\boldsymbol{g}} \in \mathbb{R}^{n_g \times n_y}$ and $\boldsymbol{\lambda} \in \mathbb{R}^{n_g}$ are the Jacobian matrix and KKT multipliers of the process constraints, respectively. $\boldsymbol{y}_{\boldsymbol{sp}}^{\boldsymbol{true}} \in \mathbb{R}^{n_y}$ in equation (5-8) denotes the controlled variables set points that achieve a true economic optimum (i.e., plant KKT conditions). In practice, the true economic optimum $\boldsymbol{y}_{\boldsymbol{sp}}^{\boldsymbol{true}}$ is difficult to achieve because of mismatch between the plant and RTO model. As such, the performance of an RTO optimizer can be assessed by the difference between the actual controlled variables achieved by the system and the true set points. Over time, this can be quantified using an error metric; herein the integral square error (ISE) is considered owed to its common use in control systems. Accordingly, the error is quantified over the single RTO operating period ($T_{RTO} = \Delta T$):

$$ISE = \int_{0}^{T_{RTO}} \left\| \boldsymbol{y}^{\boldsymbol{RTO}} - \boldsymbol{y}_{\boldsymbol{sp}}^{\boldsymbol{true}} \right\|_{\boldsymbol{I}_{n_y}}^{2} dt \tag{5-9}$$

where $\boldsymbol{y}^{\boldsymbol{RTO}} \in \mathbb{R}^{n_y}$ denotes the actual controlled variables achieved by the RTO-operated system. $\boldsymbol{y}_{\boldsymbol{sp}}^{\boldsymbol{true}}$ and $\boldsymbol{y}^{\boldsymbol{RTO}}$ are distinct as the RTO may not operate the system at the theoretical optimum owing to modelling errors, thus the gap between the achieved set point and the true optimum is expressed by the error metric in equation (5-9). The set point offsets in equation (5-9) provide a way to analyze the efficacy of an RTO-operated system on a theoretical basis. As values of $\boldsymbol{y}^{\boldsymbol{RTO}}$ are not known a priori, the effect of offset is analyzed under several hypothetical scenarios as shown next.

The operation of process plants is composed of many RTO periods; however, taking a more granular view as done here, a single RTO operating period can be segmented into distinct phases: the suboptimal phase, the dynamic phase, and the optimal phase; these are depicted in Figure 5-2. The suboptimal phase corresponds to the time before the RTO is executed and the system is operating at a point that is outdated/suboptimal ($\boldsymbol{y}^{\boldsymbol{sub}} \in \mathbb{R}^{n_y}$), the dynamic phase occurs once the RTO has been executed and the system is in a transient state ($\boldsymbol{y}^{\boldsymbol{dyn}} \in \mathbb{R}^{n_y}$), and the optimal phase occurs once the system is operating at its RTO-defined set point ($\boldsymbol{y}^{\boldsymbol{opt}} \in \mathbb{R}^{n_y}$). Note that the "optimal phase" here corresponding to $\boldsymbol{y}^{\boldsymbol{opt}}$ refers to optimal as achieved by the PE/RTO-operated system and may, in fact, not be the true plant optimum $\boldsymbol{y}_{\boldsymbol{sp}}^{\boldsymbol{true}}$ as the RTO can result in offset with respect to the true set point as show in equation (5-9). The segmentation of the RTO period into three phases allows for $\boldsymbol{y}^{\boldsymbol{RTO}}$ as defined previously to be decomposed into $\boldsymbol{y}^{\boldsymbol{sub}}$,

$\boldsymbol{y^{dyn}}$, and $\boldsymbol{y^{opt}}$. These phases have durations t_{sub}, t_{dyn}, and t_{opt}, such that for a single RTO period $T_{RTO} = t_{sub} + t_{dyn} + t_{opt}$.

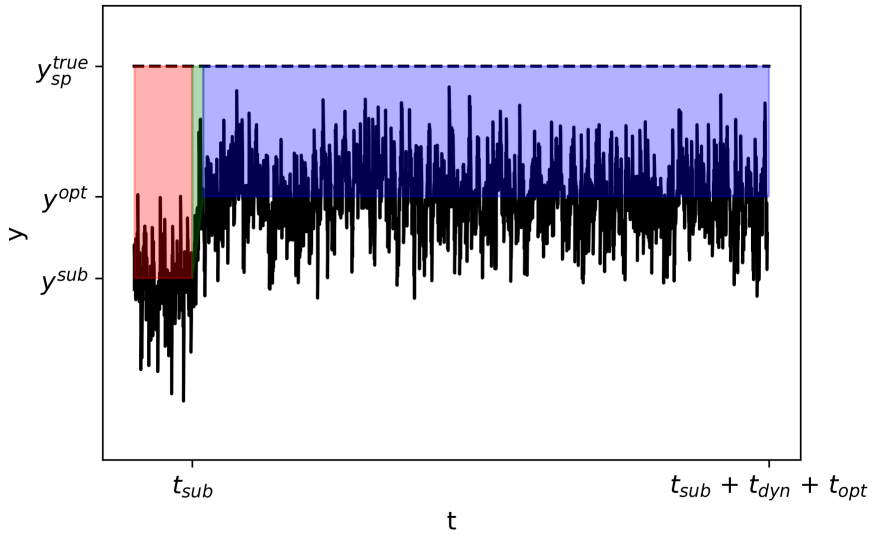

Figure 5-2: Segmentation of RTO period. Dotted (--) line denotes the true (theoretical) optimum. The integral of differences between true optimum and actual phase values highlighted red (suboptimal phase), green (dynamic phase), and blue (optimal phase).

This allows for equation (5-9) to be segmented into phases, for which the set point difference in each phase is shown in Figure 5-2 as follows:

$$ISE = \int_0^{t_{sub}} \left\| \boldsymbol{y^{sub}} - \boldsymbol{y_{sp}^{true}} \right\|_{\boldsymbol{I}_{n_y}}^{\ 2} dt + \int_{t_{sub}}^{t_{dyn}+t_{sub}} \left\| \boldsymbol{y^{dyn}} - \boldsymbol{y_{sp}^{true}} \right\|_{\boldsymbol{I}_{n_y}}^{\ 2} dt + \int_{t_{sub}+t_{dyn}}^{t_{sub}+t_{dyn}+t_{opt}} \left\| \boldsymbol{y^{opt}} - \boldsymbol{y_{sp}^{true}} \right\|_{\boldsymbol{I}_{n_y}}^{\ 2} dt \tag{5-10}$$

Since RTO is inherently a steady state method, assumption 1 outlined above is made; indeed, predominantly steady state operation is largely the case for many process plants. This leads to $t_{sub}, t_{opt} \gg t_{dyn} \Longrightarrow T_{RTO} \cong t_{sub} + t_{opt}$, thus simplifying equation (5-10) to:

$$ISE = \int_0^{t_{sub}} \left\| \boldsymbol{y^{sub}} - \boldsymbol{y_{sp}^{true}} \right\|_{\boldsymbol{I}_{n_y}}^{\ 2} dt + \int_{t_{sub}}^{t_{sub}+t_{opt}} \left\| \boldsymbol{y^{opt}} - \boldsymbol{y_{sp}^{true}} \right\|_{\boldsymbol{I}_{n_y}}^{\ 2} dt \tag{5-11}$$

The RTO-defined controlled variables can be partitioned into the true value (as defined above) and their deviation from the true value ($\boldsymbol{\sigma} \in \mathbb{R}^{n_y}$), which allows for the expansion into:

$$ISE = \int_0^{t_{sub}} \left\| \boldsymbol{y_{sp}^{true}} + \boldsymbol{\sigma^{sub}} - \boldsymbol{y_{sp}^{true}} \right\|_{\boldsymbol{I}_{n_y}}^{\ 2} dt + \int_{t_{sub}}^{t_{sub}+t_{opt}} \left\| \boldsymbol{y_{sp}^{true}} + \boldsymbol{\sigma^{opt}} - \boldsymbol{y_{sp}^{true}} \right\|_{\boldsymbol{I}_{n_y}}^{\ 2} dt \tag{5-12}$$

which simplifies to:

$$ISE = \int_0^{t_{sub}} \left\|\boldsymbol{\sigma}^{\boldsymbol{sub}}\right\|_{I_{n_y}}{}^2 dt + \int_{t_{sub}}^{t_{sub}+t_{opt}} \|\boldsymbol{\sigma}^{\boldsymbol{opt}}\|_{I_{n_y}}{}^2 dt \; \boldsymbol{\mu}^T \boldsymbol{g}\left(\boldsymbol{y}_{\boldsymbol{sp}}^{\boldsymbol{true}}\right) = 0; \boldsymbol{\mu} \geq \mathbf{0} \tag{5-13}$$

Moreover, as only steady state periods are being analyzed, the deviations from the true values are constant for a single given RTO period (i.e., not a function of time) as show geometrically in Figure 5-2. The solution of equation (5-13) provides a definition of the ISE performance metric for RTO:

$$ISE = \left\|\boldsymbol{\sigma}^{\boldsymbol{sub}}\right\|_{I_{n_y}}{}^2 t_{sub} + \|\boldsymbol{\sigma}^{\boldsymbol{opt}}\|_{I_{n_y}}{}^2 t_{opt} \tag{5-14}$$

Using equation (5-14), the performance of two operating schemes can be compared: the first (lv), which reduces the set point deviation; and the second (r), which is the regular RTO problem:

$$ISE_{lv} - ISE_r = \left\|\boldsymbol{\sigma}_{\boldsymbol{lv}}^{\boldsymbol{sub}}\right\|_{I_{n_y}}{}^2 t_{sub,lv} + \left\|\boldsymbol{\sigma}_{\boldsymbol{lv}}^{\boldsymbol{opt}}\right\|_{I_{n_y}}{}^2 t_{opt,lv} - \left\|\boldsymbol{\sigma}_{\boldsymbol{r}}^{\boldsymbol{sub}}\right\|_{I_{n_y}}{}^2 t_{sub,r} - \left\|\boldsymbol{\sigma}_{\boldsymbol{r}}^{\boldsymbol{opt}}\right\|_{I_{n_y}}{}^2 t_{opt,r} \tag{5-15}$$

To have an equivalent assessment of the schemes, it can be assumed that both operating schemes in equation (5-15) begin at the same suboptimum (i.e., $\boldsymbol{\sigma}_{\boldsymbol{lv}}^{\boldsymbol{sub}} = \boldsymbol{\sigma}_{\boldsymbol{r}}^{\boldsymbol{sub}}$) and can act at the same time (i.e., $t_{sub,lv} = t_{sub,r} = t_{sub}$ and $t_{opt,lv} = t_{opt,r} = t_{opt,}$), thus:

$$ISE_{lv} - ISE_r = \left(\left\|\boldsymbol{\sigma}_{\boldsymbol{lv}}^{\boldsymbol{opt}}\right\|_{I_{n_y}}{}^2 - \left\|\boldsymbol{\sigma}_{\boldsymbol{r}}^{\boldsymbol{opt}}\right\|_{I_{n_y}}{}^2\right) t_{opt} \tag{5-16}$$

Which, since $t_{opt} > 0$ by definition, leads to:

$$ISE_{lv} - ISE_r < 0 \Leftrightarrow \left\|\boldsymbol{\sigma}_{\boldsymbol{lv}}^{\boldsymbol{opt}}\right\|_{I_{n_y}}{}^2 < \left\|\boldsymbol{\sigma}_{\boldsymbol{r}}^{\boldsymbol{opt}}\right\|_{I_{n_y}}{}^2 \tag{5-17}$$

Following assumption 3, it can be concluded that by reducing the error in parameter estimates ($\boldsymbol{\theta}$), the deviations from the set points are also minimized as the uncertain parameters represent the only source of plant–model mismatch, thus:

$$ISE_{lv} - ISE_r < 0 \Leftrightarrow \left\|\boldsymbol{\sigma}_{\boldsymbol{\theta},\boldsymbol{lv}}^{\boldsymbol{opt}}\right\|_{I_{n_y}}{}^2 < \left\|\boldsymbol{\sigma}_{\boldsymbol{\theta},\boldsymbol{r}}^{\boldsymbol{opt}}\right\|_{I_{n_y}}{}^2 \tag{5-18}$$

Since the set point corresponding to $\boldsymbol{y}_{\boldsymbol{sp}}^{\boldsymbol{true}}$ is indeed an economic optimum by definition, the minimization of parameter deviations will lead to improved economics as effected through the set points. This can be generalized to multiple RTO periods if the deviations $\boldsymbol{\sigma}$ are re-defined as standard deviations, thus they represent the mean deviation across many RTO periods. An algorithm to achieve this lowering of parameter deviation, which fulfills the assumptions made herein is presented next.

5.2.2. Proposed Approach (lv-PE)

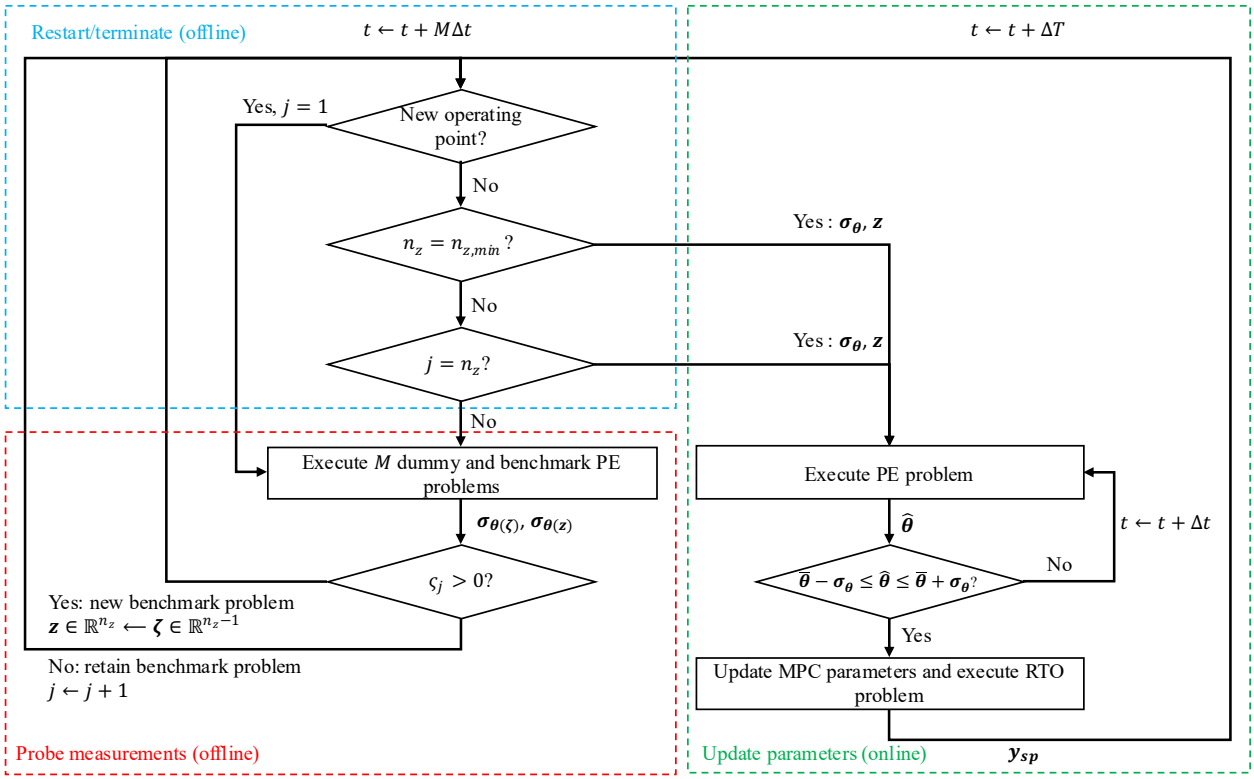

Figure 5-3: The proposed low-variation parameter estimation algorithm for RTO. The blue block denotes the restarting criteria for the measurement-probing block (in the red block). The green block denotes the parameter update procedure in the RTO and NMPC.

The proposed algorithm to lower the variability in the parameter estimates is depicted in Figure 5-3 and divided into three blocks to facilitate discussion. The key idea is to test available measurements sequentially for whether they help or hinder the variability of the parameter estimates by performing "challenger" PE problems (i.e., potential PE formulations of which the results are not implemented in the RTO or NMPC). The parameter estimates of the challenger problems are compared to those of a benchmark problem, whereby the challenger problem is a version of the benchmark problem with an omitted measurement. If the challenger problem performs better with the omitted measurement, it becomes the new benchmark problem. At the first iteration of the algorithm, the benchmark problem contains all available measurements, this way they may all be probed as the algorithm progresses; as the progression occurs, each successive benchmark problem will have a lower parameter variability. The removal of measurements is preferable to the addition of measurements as addition will require an initial subset of fixed measurements to be chosen *a priori.* Both challenger and benchmark problems are executed several times; accordingly, data regarding the parameter estimates is collected to calculate their statistical parameters. These are used twofold: 1) to determine the combination of measurements that leads to the lowest $\boldsymbol{\sigma_\theta^{opt}}$; 2) as filters to discard inaccurate parameter estimates (i.e., those outside of the tightest $\pm\boldsymbol{\sigma_\theta^{opt}}$).

The scheme can begin at any point in the operation of a process by going through the restart/terminate block in Figure 5-3 (i.e., checking if an operating point change has occurred and if all conditions for the measurement-probing procedure are met). Once these conditions are met, the measurement-probing block in Figure 5-3 is activated (the

activation conditions will be explained in detail at the end of this section). Upon activation, a counter is set to $j = 1$ and all measurements are assumed to be used (i.e., $\boldsymbol{z_0} \in \mathbb{R}^{n_{z_0}}$ where $n_z = n_{z_0}$). The challenger problems as shown in the measurement-probing block of Figure 5-3 and defined in formulation (5-19) are solved M times over M sampling intervals Δt such that each problem has a data window with a new measurement added and an old measurement discarded with respect to the previous problem. This process of executing M challenger problems is performed by excluding a measurement from the benchmark PE problem via the formulation in equation (5-19). The challenger problems are performed offline such that their estimates are never conveyed to the other layers. At $j = 1$, the benchmark is the regular PE problem as defined in equation (5-7) with $\boldsymbol{z_0}$, and it is also solved M times over M sampling intervals. This benchmark problem will change if a better formulation is found by the challenger problem, otherwise is it kept.

The challenger PE problems are formulated as a modified PE problem where the variables are defined as in equation (5-7) except for $\boldsymbol{\zeta} \in \mathbb{R}^{n_z-1}$. The challenger problems are as follows:

$$
\begin{aligned}
&\min_{\boldsymbol{\theta}} \left\| \hat{\boldsymbol{\zeta}} - \bar{\boldsymbol{\zeta}} \right\|_{\boldsymbol{\kappa}^{-1}}^{2} \\
&s.t. \\
&\boldsymbol{f_s}\left(\hat{\boldsymbol{x}}, \hat{\boldsymbol{y}}, \bar{\boldsymbol{u}}, \bar{\boldsymbol{d}}, \boldsymbol{\theta}\right) = \boldsymbol{0} \\
&\boldsymbol{h_s}\left(\hat{\boldsymbol{x}}, \bar{\boldsymbol{u}}, \bar{\boldsymbol{d}}\right) = \hat{\boldsymbol{z}} \\
&\boldsymbol{I_{n_z-1:j}}\hat{\boldsymbol{z}} = \hat{\boldsymbol{\zeta}} \\
&\boldsymbol{g_s}\left(\bar{\boldsymbol{u}}, \bar{\boldsymbol{d}}, \hat{\boldsymbol{x}}\right) \leq \boldsymbol{0} \\
&\boldsymbol{\theta^l} \leq \boldsymbol{\theta} \leq \boldsymbol{\theta^h}
\end{aligned}
\tag{5-19}
$$

where $\hat{\boldsymbol{\zeta}}$ excludes measurement j from the PE problem using $\boldsymbol{I_{n_z-1:j}} \in \mathbb{R}^{(n_z-1)\times n_z}$ such that only a subset of measurements $\boldsymbol{\zeta}$ are used with the respective covariance matrix $\boldsymbol{\kappa} \in \mathbb{R}^{(n_z-1)\times(n_z-1)}$ and averages $\bar{\boldsymbol{\zeta}} = \boldsymbol{I_{n_z-1:j}}\,\bar{\boldsymbol{z}}$.

After M executions of problem (5-19), the parameter sequence $\left\{\boldsymbol{\theta(\zeta)_{,t-i}}\right\}_{i=0}^{M}$ is available, allowing for the calculation of the standard deviation of that sequence $\boldsymbol{\sigma_{\theta(\zeta)}}$. Moreover, M executions of a benchmark PE problem (i.e., with the full set of measurements $\boldsymbol{z}$) have also been performed to obtain the sequence $\{\boldsymbol{\theta(z)_{t-i}}\}_{i=0}^{M}$ with variation benchmark $\boldsymbol{\sigma_{\theta(z)}}$. Note that M is a system parameter and is limited by the RTO period size as it will determine the computational time associated with the proposed scheme along with the number of challenger problems required; more details about this parameter are provided in the following section.

The information content ($IC \in \mathbb{R}$) metric introduced by Vrugt et al. (2001) is adapted for PE as follows:

$$
IC_{i,k} = 1 - \frac{\sigma_{\theta(\zeta),i,k}}{\sigma_{\theta(\boldsymbol{z}),i,k}} \quad \forall i \in \{1, \dots, n_\theta\} \tag{5-20}
$$

where $k = j + n_{z_0} - n_z$ denotes the number of measurements probed hitherto.

The IC metric in equation (5-20) quantifies if, and by how much, the exclusion of a measurement helps in the decrease of parameter variability. $IC_{i,k} > 0$ implies that the removal of a measurement helps reduce variability while $IC_{i,k} < 0$ implies that the removal increases the variation. The IC metric was chosen due to its simplicity and the fact that it does not require plant perturbations such as alternatives metrics like the sensitivity matrix (Kravaris et al., 2013). In essence, equation (5-20) determines whether each measurement is beneficial or detrimental to the expected error of

the PE problem via parameter standard deviations. The deviations are used in evaluating a benchmark problem (i.e., with lowest variance set of measurements found thus far in the measurement probing phase) and a challenger problem (i.e., with a potentially better set of measurements). To quantify the aggregate effect of measurement exclusion in systems with many parameters, the overall IC ($\varsigma_k \in \mathbb{R}$) is defined as follows:

$$\varsigma_k = \sum_{i=1}^{n_\theta} IC_{i,k} \tag{5-21}$$

This is depicted within the measurement-probing block of Figure 5-3 to determine whether to exclude or keep a measurement as follows:

If $\varsigma_k > 0$, the exclusion of the measurement is deemed beneficial as cumulative impact of the exclusion is net positive across all estimated parameters in the system (i.e., the variation in some parameters may decrease while the variance in other may increase; however, the net effect is of decrease in variation). As such, the measurement *j* being tested is removed from the PE formulation and the challenger formulation becomes the new benchmark problem, thereby reducing the dimension of the measurements vector by one i.e.,

$$n_z \longleftarrow n_z - 1 \Longrightarrow \boldsymbol{z} \in \mathbb{R}^{n_z} \longleftarrow \boldsymbol{\zeta} \in \mathbb{R}^{n_z - 1}$$

following this, the probing process then proceeds whereby the previous second measurement, which is now the first measurement (i.e., $z_1 \longleftarrow z_2$), is probed for its information content.

If $\varsigma \leq 0$, the exclusion of the measurement is not beneficial, thus the measurement is retained, and a new exclusion candidate is chosen i.e., $j \longleftarrow j + 1$.

This process is then repeated sequentially for available measurements $k \in \{1, \dots, n_{z_0}\}$ until either of the three conditions in the restart/terminate block of Figure 5-3 is fulfilled: 1) the operating point changes as dictated by a sudden disturbance to the system, thus interrupting the measurement-probing process and setting $j = 1$, 2) the minimum number of allowable measurements are reached as specified by the user based on identifiability analysis (Guillaume et al., 2019) or process knowledge or, 3) the scheme has gone through all the available measurements and chosen only to exclude a small subset. The latter two conditions are reflected in the following:

$$n_z = n_{z,min} \tag{5-22}$$

$$n_z = j \tag{5-23}$$

where $n_{z,min}$ is the minimum number of measurements required for the system to be identifiable. Condition (5-22) ensures that the minimum number of measurements needed (conversely, the maximum number of measurements that can be excluded) are retained. Additionally, condition (5-23) stops the data acquisition when all original measurements have been analyzed as reflected by the index k being equivalent to the original number of measurements n_{z_0} (and condition (5-22) has not yet been fulfilled). Condition (5-22) is predominant as reflected in Figure 5-3 whereby it is checked before condition (5-23); this is to ensure sufficient measurements always remain such that the system is identifiable.

Once the measurement-probing block of the algorithm in Figure 5-3 is completed, the information-rich measurement vector $\boldsymbol{z}$ is known and the filter bounds $[\overline{\boldsymbol{\theta}} - \boldsymbol{\sigma}_{\boldsymbol{\theta}(\boldsymbol{z})}, \overline{\boldsymbol{\theta}} + \boldsymbol{\sigma}_{\boldsymbol{\theta}(\boldsymbol{z})}]$ can be calculated using the parameter sample $\{\boldsymbol{\theta}(\boldsymbol{z})_{\boldsymbol{t-i}}\}_{i=0}^{M}$ from the final benchmark problem (i.e., the one corresponding to the subset of measurements that were chosen to be used in the PE problem implemented in the RTO and NMPC). The sample of parameter estimates corresponding to the chosen subset of measurements is used to calculate these bounds as the standard deviation. Since the standard deviation is the average difference between the expected parameter value and the individual estimates within the sample, future estimates outside of the bounds established by the standard deviation (i.e., those with higher-than-average distance from the expected parameter) are deemed unacceptable. This avoids potential high-error estimates whereby noisiness may be propagating excessively to the estimates. With this information, the PE problem (5-7) can be performed and implemented at every RTO period ΔT with the chosen subset of measurements $\boldsymbol{z}$ as depicted in the update block of Figure 5-3. This PE problem corresponds to the one with the final $\boldsymbol{z}$ determined by the measurement-probing block of the algorithm and generates the estimates $\widehat{\boldsymbol{\theta}}$, which are assessed with the filter bounds. If the estimates are outside the filter bounds, they are not accepted, and another sampling interval is taken to collect measurements; this process is repeated until an acceptable set of parameter estimates are generated. If the estimates are inside the filter bounds, the parameters are used to update the NMPC and execute the RTO problem.

The update procedure is not repeated for another RTO period (i.e., $t \longleftarrow t + \Delta T$) unless a new operating point is introduced as depicted by the upper decision block in Figure 5-3, which restarts the measurement-probing process. When a sudden operating point change occurs, as indicated by a sudden large change in control actions or process economics, the measurement-probing block of the algorithm in Figure 5-3 is reactivated by the restart /terminate block. This is done to ensure that favourable measurements are being used for the PE problem under the new operating conditions. Note that 'favourable' measurements may not mean optimal as stopping criteria (5-22) may halt the algorithm before all measurements are probed for IC. Nevertheless, the subset of 'favourable' measurements chosen by the proposed scheme will always lead to parameter estimates that are equally accurate or more accurate than the original set of measurements. Alternatively, the measurement-probing block can also be activated through the restart/terminate block if there is a sudden change occurs as the measurement probing procedure is proceeding, this is checked for after every new challenger problem is introduced (i.e., $t \longleftarrow t + M\Delta t$).

In summary, the algorithm proceeds as follows:

lv-PE algorithm applied to RTO:	
1.	New operating point?
a.	Yes: activate measurement-probing block, go to step 4
b.	No: go to step 2
2.	$n_z = n_{z,min}$?
a.	Yes: activate parameter update block, go to step 5
b.	No: go to step 3
3.	$n_z = j$?
a.	Yes: activate parameter update block, go to step 5

b.	No: activate measurement-probing block, go to step 4
4.	Measurement-probing, set $j = 1$
a.	Execute M challenger and benchmark problems (5-19) and (5-7), respectively
i.	If $\varsigma_k > 0$: $j = 1$, measurement excluded, new benchmark problem established, go to step 1
ii.	Else: $j \mathrel{+}= 1$, measurement retained, keep old benchmark problem, go to step 1
5.	Parameter update
a.	Execute actual PE problem
i.	If $\overline{\boldsymbol{\theta}} - \boldsymbol{\sigma}_{\boldsymbol{\theta}} \leq \widehat{\boldsymbol{\theta}} \leq \overline{\boldsymbol{\theta}} + \boldsymbol{\sigma}_{\boldsymbol{\theta}}$: update RTO and MPC parameters, $t \mathrel{+}= \Delta T$, return to step 1
ii.	Else: $t \mathrel{+}= \Delta t$, return to step 5a

It should be noted that the algorithm presented above is designed to reduce parameter variation across RTO periods, not to detect gross errors. However, the method could be adjusted for GED through hypothesis testing (Özyurt and Pike, 2004) of the parameter estimate means generated by the benchmark and challenger problems in the lv estimation algorithm. Accordingly, a test statistic could be used to determine whether measurement removal in the probing procedure generates shifting means, thus identifying gross errors. The lv-PE, as proposed herein, has two major advantages over the regular PE applied to RTO: firstly, the most information-rich subset of measurements is chosen to reduce parameter variability; secondly, the parameter filter avoids RTO periods with poorly estimated parameters. As shown in the previous section, this will result in lower set point error and, in turn, better process economics. Importantly, the information content procedure only requires sampling and can be performed offline as its solutions are not implemented in the system being operated. The only time at which the proposed scheme interacts with the process control loop is when the RTO set points are updated. Otherwise, only an additional independent computer/processor is necessary for repeated execution of the PE problems, which do not interfere with the regular process control loop; this makes the requirements for implementation relatively simple, hence its appeal of industrial systems. The information content procedure may be adjusted through sample sizes such that it can fully occurs within the RTO period; the assessment of this computational expense to the PE computer will be elaborated on in the following section.

5.2.3. Scheme Assessment and Economic Analysis

The proposed scheme is mainly analyzed through variation, the process economics, and constraint violations; these are the factors that affect the PE, NMPC, and RTO problems, which the scheme aims to improve upon. The variation is captured through the standard deviation of parameters, the economics are calculated using the process revenues/losses and their rates, and the constraint violations can be quantified through their cumulative magnitude.

As shown in Section 5.2.1, the ISE of the operation of an RTO system is linearly dependent on the operating time; thus, the cumulative error can be written as a linear combination of the error terms of each individual RTO period. The same follows for the process economics $R(\$)$, where a revenue is made if $R > 0$ or a loss is incurred if $R < 0$. This occurs as the operation is a combination of constant rates $P(\$/time)$. $P > 0$ is a profit rate and occurs when the

operator is selling produced commodities; in contrast $P < 0$ is a price rate and occurs when a process is operating at a loss.

As stated previously, the RTO period consists of three phases ($T_{RTO} = t_{sub} + t_{dyn} + t_{opt}$). These correspond to suboptimal operation before the set points are updated t_{sub} $(time)$, a fast (i.e., negligible) dynamic operation, and RTO-optimal operation once the set points are updated t_{opt} $(time)$. The respective suboptimal, dynamic, and optimal process profit/cost rates are $P_{sub,i}$, $P_{dyn,i}$, and $P_{opt,i}$ $(\$/time)$ are dependent on the specific RTO period i. This enables calculation of the cumulative process economics (i.e., as the process progresses), i.e.,

$$R = \sum_{i=0}^{N} \int_{0}^{T_{RTO}} P_i \, dt \tag{5-24}$$

Again, this can be segmented into three phases: suboptimal, dynamic, and optimal, i.e.:

$$R = \sum_{i=0}^{N} \int_{0}^{t_{sub}} P_{sub,i} \, dt + \int_{t_{sub}}^{t_{sub}+t_{dyn}} P_{dyn,i} \, dt + \int_{t_{sub}+t_{dyn}}^{t_{sub}+t_{dyn}+t_{opt}} P_{opt,i} \, dt \tag{5-25}$$

As the RTO operation is inherently steady state, the dynamics are assumed to ensure quickly, thus simplifying to:

$$R = \sum_{i=0}^{N} \int_{0}^{t_{sub}} P_{sub,i} \, dt + \int_{t_{sub}}^{t_{sub}+t_{opt}} P_{opt,i} \, dt \tag{5-26}$$

Both suboptimal and optimal phases are composed of constant profit/loss rates whereby the time that is not spent operating optimally during the RTO period is spent operating suboptimally instead, this can be expressed as:

$$R = \sum_{i=0}^{N} t_{sub} P_{sub,i} + t_{opt} P_{opt,i} \tag{5-27}$$

Substituting back the expression $t_{opt} = T_{RTO} - t_{sub}$, whereby the time that is not spent operating optimally during the RTO period is spent operating suboptimally instead, both terms can be expressed in terms of the total RTO period length and the suboptimal time:

$$R = \sum_{i=0}^{N} t_{sub} P_{sub,i} + (T_{RTO} - t_{sub}) P_{opt,i} \tag{5-28}$$

For a single RTO period, equation (5-28) could be used to build forecasting tools such as payback periods as exemplified in the Appendix B (payback period). If the system were not to act promptly (i.e., be delayed beyond the regular suboptimal time), the time operating suboptimally would be protracted, thus causing diminished economic performance. For instance, suppose the delay incurred at a given RTO period is τ, this causes further suboptimal operating time expressed as:

$$R = \sum_{i=0}^{N} P_{sub,i}\left(t_{sub,i} + \tau_i\right) + P_{opt,i}\left(T_{RTO} - t_{sub,i} - \tau_i\right) \tag{5-29}$$

This situation is best avoided as the $T_{RTO} - t_{sub,j} - \tau_i$ term diminishes the potential benefit of an RTO scheme over time. This is especially important in the lv-PE/RTO system as offline computations must be performed before set point updates. As a result, the computational burden, which is associated with the information content procedure must also be considered in order to avoid the delay.

The size of M (i.e., the number of samples used for averaging in problems (5-7) and (5-19)) will determine whether delay occurs in the proposed lv-PE/RTO scheme through the information content procedure occurring in the PE computer. If M is small, the estimation formulation (5-7) will not benefit from the smoothing of noise of a large sample size, thus resulting in high variance estimate. In contrast, a large M may capture slow dynamics such as drift or, as noted above, computational delays in the execution of the RTO problem (5-5). Drift would result in high-error estimates as the data collected would not be dynamic, thus the steady-state estimation problem would aim to fit parameters to dynamic data using a steady-state model. Computational delays would result in performance deterioration that could become significant if they delay persists over time as shown in equation (5-29).

The time required to perform $k = j + n_{z_0} - n_z$ sets of challenger problems (as shown in Figure 5-3) each requiring M samples, depends on the length of the sampling time (Δt) with respect to the CPU time of each challenger problem ($\Delta t_{challenger}$). Whichever time is greater limits the speed of the information content procedure, i.e.,

$$t_{comp} = \begin{cases} kM\Delta t & if \quad \Delta t > \Delta t_{challenger} \\ kM\Delta t_{challenger} & if \quad \Delta t_{challenger} > \Delta t \end{cases} \tag{5-30}$$

In the case studies considered in this work, M was sized based on equation (5-30) such that the delayed revenue case in represented by equation (5-29) would be avoided. To do so, it is assumed that $t_{comp} \coloneqq \Delta T$ such that the maximum allowable computational time (assuming no parallelization, which can also be considered through an integer multiple of equation (5-30)) was equal to the RTO period, as to avoid any delay. Moreover, $k \coloneqq n_{z_0}$ was assumed such that all available measurements are assumed to be probed via challenger problems. The time-limiting conditions can be verified through preliminary PE executions, and it was found that $\Delta t > \Delta t_{challenger}$ for both case studies herein (i.e., the sampling period is longer than the computational time to execute a PE problem). Accordingly, the M for each case study was determined by rearranging equation (5-30) and substituting the aforementioned definitions ($\coloneqq$) as follows:

$$M = \frac{\Delta T}{\Delta t n_{z_0}} \tag{5-31}$$

such that RTO delays are avoided.

Furthermore, the proposed scheme also helps to avoiding constraint violations. To quantify this effect, the sum of absolute constraint violations is considered, i.e.,

$$SAV = \sum_{t=0}^{T_f} \left| g_{plant,t} - g \right| \tag{5-32}$$

where $T_f(time)$ is the total time for which the system is operated while $g_{plant,t}$ and g are the actual (measured) and bound values for the constraints being violated, respectively. The absolute sum is used as it gives a good physical sense of the amount by which the constraint is being exceeded cumulatively over time. SAV is preferred to an alternative metric like sum of squares, which also quantifies the violation but does not correspond to an actual plant quantity because of the squaring.

5.3 Case Studies

The proposed scheme was tested for updating the RTO and NMPC parameters as depicted in Figure 5-1b with matching optimization and control models (however, they need only be passed to one of these layers to influence the process operation). Two simulated case studies are performed: a forced circulation evaporator (Lee et al., 1989) case exemplifies the benefit of avoiding constraint violations and the Williams-Otto CSTR (Williams and Otto, 1960) shows the economic benefit of the lv-PE/RTO scheme. Each case study is tested under different parameter realizations (i.e., where the plant manifests distinct parameter values/combinations) whereby both regular PE and lv-PE schemes must repeatedly estimate the parameters to feed to the RTO and NMPC. The initial conditions (i.e., at $T = 0, t = 0$) for all scenarios within each case study correspond to the optimal operating point given by the nominal parameter(s). Note that this is only the starting point, and each scheme then proceeds to pursue the true optimum corresponding to the actual parameters for a given scenario. A consistent starting point for both PE/RTO schemes (i.e., the regular and low-variance) and across all scenarios ensures comparability in the dynamic domain such that no scheme/scenario starts at a more advantageous point. As a result, the plant is assumed to have arrived at a new operating point in both case studies, thus progressing through the restart/terminate block in Figure 5-3 and triggering the measurement-probing block. Both case studies assume full state accessibility as to not confound the performance of the proposed method with the performance of a potential state estimator. Nevertheless, many industrial systems require state estimation for unmeasured states; these estimators (e.g., Kalman filter, extended Kalman filter, and moving horizon estimation) also use noisy process measurements. As the proposed method targets measurement noise, it can be adapted to be compatible with the state estimators and improve the quality of estimates (provided that the system is both identifiable and observable).

In both case studies, the time intervals (i.e., sampling times) are chosen based on literature values (Amrit et al., 2013). Moreover, the RTO intervals were chosen to be significantly longer than the transient times as to satisfy assumption 1 (Section 5.2). The noise levels are set to be sufficiently high to cause large errors in PE, the minimum number of measurements were based on preliminary tuning experiments, and the sample size M was for each case was determined using equation (5-31). The proposed scheme will be denoted as "RTO (lv-PE)" while the regular RTO will be denoted as simply "RTO".

The scheme is deployed for various combinations of uncertain parameter(s) as different scenarios within in each case study; the goal of the RTO is to repeatedly estimate the uncertain parameters and operate the system as close to the true optimum as possible. During this time, disturbances were assumed to be measurable and steady as to be able to assess the scheme in the neighbourhood of the optimal operating point and not in large transients; since RTO is a steady state scheme, significant dynamics could confound the analysis. As such, any dynamics observed are owed to set point fluctuations and control actions incited by changing parameter estimates in the RTO and NMPC layers, respectively.

The schemes were assessed on three factors: parameter variability, process cost, and constraint violation (in cases where this occurs). Metrics to quantify these factors are computed *a posteriori* to each simulated case study for both RTO-operated systems with the standard PE and the lv-PE. Firstly, the variability is captured through the standard deviation of parameter estimates computed using formulations (5-7) and (5-19). The standard deviation of parameter

estimates is central to the proposed approach as it is the main factor effected by the IC procedure in Section 5.2.2, which reduces variability using equation (5-21). As the system is repeatedly estimating parameters for each realization, the variability measures how much these parameters vary by PE execution such that low variability is desired. Secondly, the process economics, which the reduced parameter variability improves upon, are computed through the cumulative process revenue/cost in equation (5-28) divided by the total operating time of a given scenario. As the system should operate primarily at steady state, this mean process cost should approximate the RTO-optimal steady state cost achieved for each case/scenario. Furthermore, constraint violations can occur as previously mentioned; the cumulative violation is computed using equation (5-32). As these violations are undesirable, the constraint violation metric used herein is ideally minimized by estimating parameters that yield non-violating set points in the RTO layer. Both case studies were simulated and optimized in the Pyomo environment, which is a modelling package for PYTHON (Hart et al., 2011). Both dynamic simulations were discretized in the time domain using four-point Radau collocations on finite elements per sampling interval. The optimization problems were solved using the MA27 IPOPT solver from the HSL library on an Intel core i7-4770 CPU @ 3.4 GHz.

5.3.1. Forced Circulation Evaporator

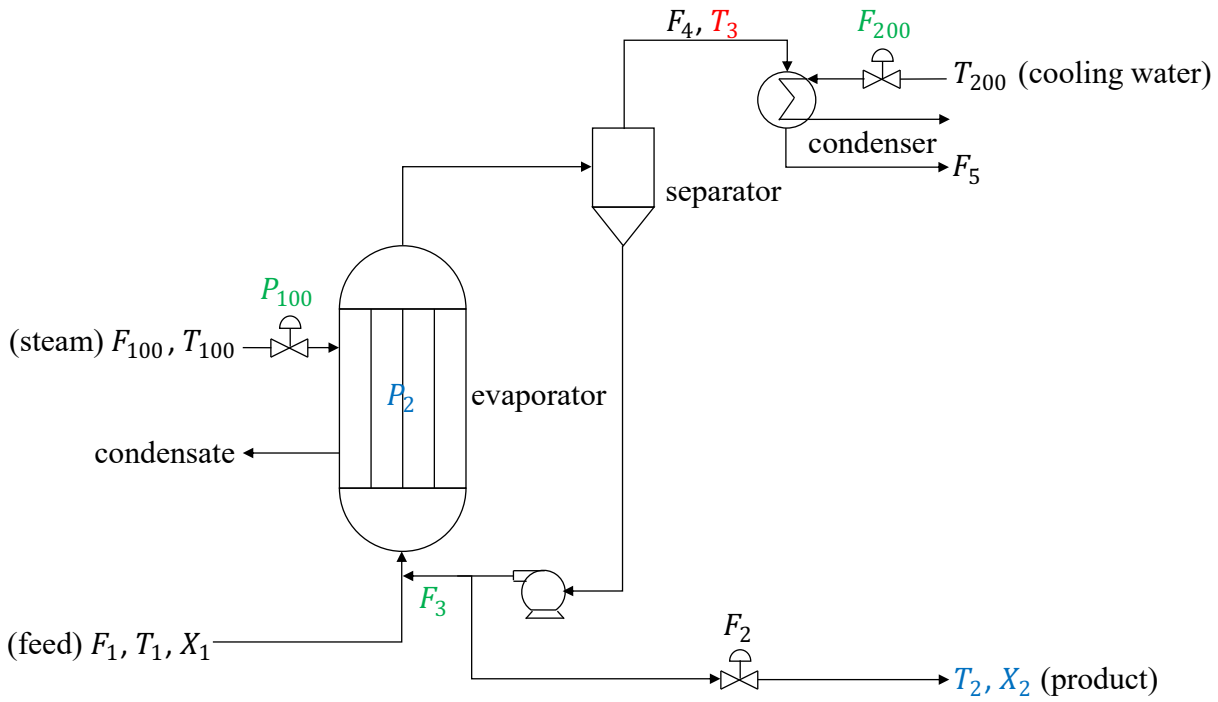

Figure 5-4: Forced-circulation evaporator process. Blue denotes controlled variables, green denotes manipulated variables, and red denotes additional measurements (i.e., aside from the controlled variables) as implemented in the present study.

The forced circulation evaporator (Figure 5-4) is a common unit in chemical plants; the mechanistic process model, along with its use in simulation studies, was first introduced by Lee et al. (1989). The system is of particular interest in the process control literature because of its nonlinearity and many potential control loops owed to the number of possible manipulated/controlled variable pairings (Govatsmark and Skogestad, 2001). Moreover, the optimal operating point of the system has been observed to occur at an active constraint, hence it provides a good setting in

which to investigate the effect of parameter estimates under a potential RTO constraint violation. The evaporator model consists of the following material balances:

$$H\frac{dX_2}{dt} = F_1X_1 - F_2X_2 \tag{5-33}$$

$$K\frac{dP_2}{dt} = F_4 - F_5 \tag{5-34}$$

$$F_2 = F_1 - F_4 \tag{5-35}$$

where F_1, F_2, F_4, and F_5 (kg/min) are the stream mass flowrates outlined in Figure 5-4; X_1 and $X_2(\%)$ are the feed and product compositions of the product chemical, respectively, and $P_2(kPa)$ is the evaporator pressure. Note that the third material balance (33-3) implies a constant mass holdup in the evaporator, which is reflected in the constant holdup term $H(kg)$. The energy balance over the entire process is modelled as follows:

$$T_2 = 0.5616P_2 + 0.3126X_2 + 48.43 \tag{5-36}$$

$$T_3 = 0.507P_2 + 55 \tag{5-37}$$

$$F_4 = \frac{Q_{100} - F_1C_p(T_2 - T_1)}{\kappa} \tag{5-38}$$

where T_1, T_2, and T_3 $(°C)$ are the stream temperatures as outlined in Figure 5-4 whereas $Q_{100}(kW)$ is the steam jacket heat duty. The steam jacket energy balance is modelled as follows:

$$T_{100} = 0.1538P_{100} + 90 \tag{5-39}$$

$$Q_{100} = UA_1(T_{100} - T_2) \tag{5-40}$$

$$UA_1 = 0.16(F_1 + F_3) \tag{5-41}$$

$$F_{100} = \frac{Q_{100}}{\kappa_s} \tag{5-42}$$

where $T_{100}(°C)$, $P_{100}(kPa)$, and $F_{100}(kg/min)$ are the saturated steam temperature, pressure, and mass flowrate, respectively. $UA_1(kW/°C)$ is the heat jacket heat transfer coefficient. The condenser is modelled as follows:

$$Q_{200} = \frac{UA_2(T_3 - T_{200})}{1 + \frac{UA_2}{2C_pF_{200}}} \tag{5-43}$$

$$F_5 = \frac{Q_{200}}{\kappa} \tag{5-44}$$

where $T_{200}(°C)$, $Q_{200}(kW)$, and $F_{200}(kg/min)$ are the cooling water temperature, cooling duty, and mass flowrate, respectively. In this case, the manipulated variables are the steam pressure, cooling water flowrate, and recirculation

flowrate (i.e., $\boldsymbol{u} = [P_{100} \quad F_{200} \quad F_3]^T$); the controlled variables are the product composition, temperature, and evaporator pressure (i.e., $\boldsymbol{y} = [X_2 \quad P_2 \quad T_2]^T$); the uncertain parameter is the condenser heat transfer coefficient (i.e., $\boldsymbol{\theta} = [UA_2]^T$). The initial measurements are the controlled variables, as well as the separator outlet temperature (i.e., $\boldsymbol{z_0} = [X_2 \quad P_2 \quad T_2 \quad T_3]^T$). The process losses are to be minimized according to the following objective function:

$$\Phi = P_e(F_2 + F_3) + P_s F_{100} + P_w F_{200} \tag{5-45}$$

where P_e, P_s, and P_w are the electricity, steam, and cooling water prices, respectively, in Table B-1 (Appendix B). The RTO and NMPC problems (5-5) and (5-6) are subject to the following constraints on the controlled variables:

$$25 \leq X_2(\%) \leq 100 \tag{5-46}$$

$$40 \leq P_2(kPa) \leq 80 \tag{5-47}$$

Moreover, the RTO and NMPC problems are also subject to constraints on the manipulated variables:

$$10 \leq P_{100}(kPa) \leq 400 \tag{5-48}$$

$$10 \leq F_{200}(kg/min) \leq 400 \tag{5-49}$$

$$1 \leq F_3(kg/min) \leq 100 \tag{5-50}$$

Lastly, following constraints are imposed on the estimated parameters in problems (5-7) and (5-19):

$$0.1 \leq UA_2(kW/°C) \leq 20 \tag{5-51}$$

Table B-1 (Appendix B) presents the model parameters and nominal values used in this study.

The proposed scheme was implemented for this case study using the process model, controlled variables, manipulated variables, constraints, and uncertain parameters described in this section. The system is operated for $833\ h$ with an RTO period of $\Delta T = 16\ hours$ and a sampling interval of $\Delta t = 4\ minutes$. $n_{z,min} = 1$ was chosen based on prior identifiability analysis and the process and measurement noises ($\boldsymbol{w}, \boldsymbol{v}$; owed to mismatch and instrumentation error, respectively) are additive and zero-mean with 0.1% of the nominal state values as variance $\mathcal{N}(0, (0.001\boldsymbol{x_{nom}})^2)$. The NMPC controller tuning for formulation (5-6) is $\boldsymbol{Q} = diag(1,1,1)$, $\boldsymbol{R} = diag(0.09, 15, 20)$ and $P = C = 200\Delta t$; these are based on preliminary manual tuning to balance tracking speed and stability. Table 5-1 presents the formulations to the corresponding optimization problems (5-5), (5-6), and (5-7) associated with this case study.

*Table 5-1: PE, RTO, and NMPC formulations for evaporator case study. *S.S. indicates that a steady-state version of the model is used in the corresponding layer.*

	PE	**RTO**	**NMPC**
Objective function	$\|\hat{\boldsymbol{z}} - \bar{\boldsymbol{z}}\|_{\boldsymbol{K}^{-1}}{}^2$	Eq. (6-45)	$\sum_{i=1}^{200} \|\boldsymbol{y_{sp}} - \hat{\boldsymbol{y}}_{\boldsymbol{t+i}}\|_{\boldsymbol{Q}}^2 + \sum_{j=1}^{200} \|\Delta \boldsymbol{u}_{\boldsymbol{t+j}}\|_{\boldsymbol{R}}^2$

Decision variables	$\boldsymbol{\theta} = [UA_2]^T$	$\boldsymbol{y} = [X_2 \quad P_2 \quad T_2]^T$	$\boldsymbol{u_{t+1}} = [P_{100,t+1} \quad F_{200,t+1} \quad F_{3,t+1}]^T$
Model	Eqs. (5-33)–(5-44). S.S. model	Eqs. (5-33)–(5-44). S.S. model	Eqs. (5-33)–(5-44). Dynamic model
Constraints	Eq. (5-51)	Eqs. (5-46)–(5-50)	Eqs. (5-46)–(5-50)
Inputs	$\bar{\boldsymbol{z}} = [\bar{X}_2 \quad \bar{P}_2 \quad \bar{T}_2 \quad \bar{T}_3]^T$ $\bar{\boldsymbol{u}} = [\bar{P}_{100} \quad \bar{F}_{200} \quad \bar{F}_3]^T$ $\bar{\boldsymbol{d}} = [\bar{F}_1 \quad \bar{T}_1 \quad \bar{X}_1]^T$	$\boldsymbol{\theta} = [UA_2]^T$ $\boldsymbol{d} = [F_1 \quad T_1 \quad X_1]^T$	$\boldsymbol{x_0} = [X_2 \quad P_2]^T$ $\boldsymbol{y_{sp}} = [X_{2,sp} \quad P_{2,sp} \quad T_{2,sp}]^T$ $\boldsymbol{d_t} = [F_{1,t} \quad T_{1,t} \quad X_{1,t}]^T$

The CPU time of each challenger problem is $\sim 0.03\ seconds$, which is significantly less than the sampling time. Accordingly, the sampling time dictates the computational burden of the information content procedure as per equation (5-30) and the RTO sample size is set to $M = 60$ as per equation (5-31). All scenarios tested required $k = 4$ sets of challenger problems as shown in Table 5-2, which corresponds to an actual computational burden of $\sim 3.3\ hours$ (to perform all challenger problems), which is well within the RTO period of $16\ hours$, thus enough data can be collected within the RTO period to perform the information content procedure with no delay.

The uncertain parameter is assumed to materialize in the interval $[(1-\alpha)\theta_{nom}, (1+\alpha)\theta_{nom}]$, where $\alpha = 0.1$, for simplicity. The nominal parameter value (corresponding to the initial operating point) can be found in Table B-1 (Appendix B). In each scenario, the true plant parameter manifests at a value from the five uniformly spaced points shown in the first row of Table 5-2. It should be noted that the scheme can be used to estimate any realization of the "true" parameter value; however, the five scenarios in Table 5-2 were chosen such that they would be representative of the entire uncertain parameter domain while limiting the number of scenarios required for testing.

Table 5-2: Results for parameter scenarios in the evaporator case study under low-variance and regular RTO implementations.

	Scenario 1 (S1)	Scenario 2 (S2)	Scenario 3 (S3)	Scenario 4 (S4)	Scenario 5 (S5)
$UA_2\ (kW/K)$	$0.9\theta_{nom}$	$0.95\theta_{nom}$	θ_{nom}	$1.05\theta_{nom}$	$1.1\theta_{nom}$
$\sigma_{\theta,lv}\ (K)$	0.67	0.61	0.03	0.28	0.65
$\sigma_{\theta,r}\ (K)$	1.85	1.17	0.82	0.82	2.45
$\bar{P}_{RTO\ (lv-PE)}\ (\$/s)$	272.77	343.11	270.71	270.39	370.00
$\bar{P}_{RTO}\ (\$/s)$	245.20	272.18	303.32	261.73	255.52
$SAV_{RTO\ (lv-PE)}\ (\%)$	2151.51	21310.10	3878.97	5407.98	4023.45
$SAV_{RTO}\ (\%)$	229805.00	186815.60	160069.42	146878.65	179640.75
k	4	4	4	4	4

Figure 5-5a displays the process losses for several of the scenarios listed in Table 5-2. It should be observed that the losses and average price rate ($\bar{P}$) in all scenarios (except S3) are lower (i.e., favourable) for the regular RTO

implementation than the lv-PE/RTO. This occurs despite the lower variation in the parameter estimates (σ) for all scenarios achieved by the lv-PE/RTO as summarized in Table 5-2. Figure 5-5b elucidates that the regular RTO is achieving this decreased cost through violation of the composition constraint in equation (5-46); this is also reflected in substantially lower SAV when the lv-PE/RTO is implemented. The SAV, as defined in equation (5-32), ranges from one to two orders of magnitude lower when using the lv-PE/RTO than those achieved when using the regular RTO; this results in significant less product being off-specification. The constraint violation occurs as the RTO and NMPC models, which have the estimated parameters, are mismatched from the plant, which has the "true" parameters. Thus, the set points for the RTO and control actions for the NMPC, which appear constraint-abiding in their corresponding optimization problems, are not so when implemented in the plant. As a result, the better (i.e., lower) price rates of the regular RTO are misleading as the product being produced in the constraint-violating periods will not meet the required specifications. In reality, off-specification product such as that produced in the regular RTO implementation would have to be reprocessed, thereby increasing the processing costs. As the re-processing cost is not considered herein, the regular RTO misleadingly appears to be economically superior in all scenarios (except for S3, where the true parameter was set to their nominal value). In contrast, Figure 5-5b also shows that the lv-PE/RTO generally operates the plant directly at the constraint and does not vary the set point for X_2 as it does with the set points for T_2 and P_2 as shown in Figure 5-5c and Figure 5-5d, respectively. As such, most constraint violation that occurred using the lv-PE/RTO was likely owed to noisy plant fluctuations and not to the proposed parameter estimation scheme.

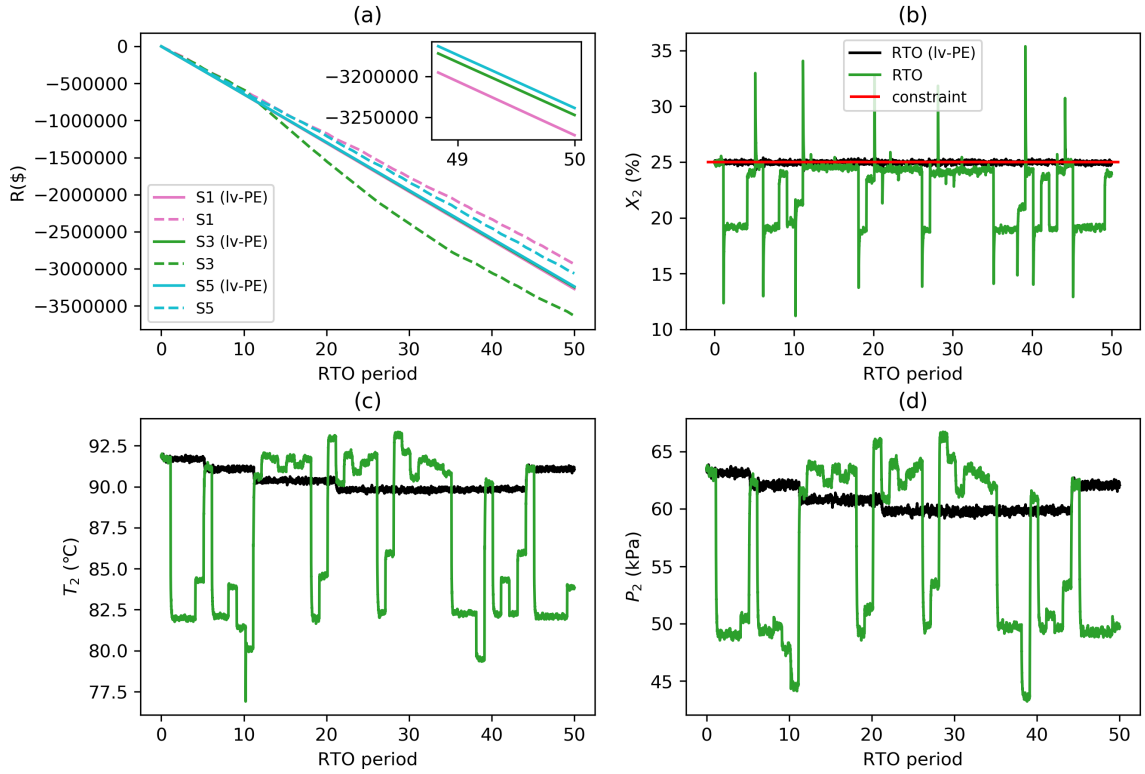

Figure 5-5: Economics and controlled variables for the evaporator case study. a) losses ($), b) product composition, c) product temperature, d) evaporator pressure.

This variation caused by the parameter on the RTO operation is seen most prominently on Figure 5-5c and Figure 5-5d whereby the product temperature and evaporator pressure controlled variables vary when using the regular RTO

compared to a significantly more consistent operation produced by the lv-PE/RTO. This variation has a significant impact on the process cost as observed in the sub-window of Figure 5-5a, where the optimal cost for the lv-PE RTO implementation does not actually vary significantly with respect to the true parameter realizations while the cost of the PE/RTO does despite only a single parameter being assumed to be uncertain in this process. Aside from the constraint violation observed for this case study, the increased variability of the regular RTO also leads to a more active control layer, which is undesirable from an operation and maintenance perspective.

5.3.2. Williams-Otto CSTR

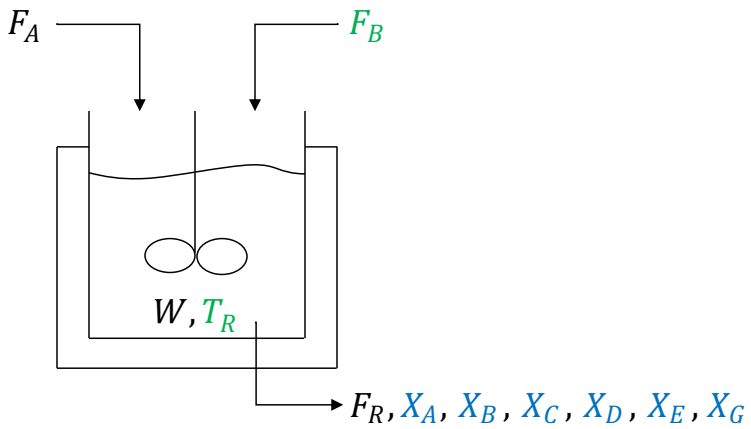

Figure 5-6: Williams-Otto CSTR. Blue denotes controlled variables and green denotes manipulated variables as implemented in the present study.

The continuous stirred-tank reactor (CSTR) first described by Williams and Otto (1960) is another common system used for real-time optimization and control studies (e.g., Amrit et al., 2013; Matias and Le Roux, 2018; Miletic and Marlin, 1998). This system has been used as a benchmark example for many economic optimization methods as it provides a relatively small but nonlinear setting that can be used to highlight potential economic improvements. The process is depicted in Figure 5-6 and consists of two pure inlet streams of substrates A and B with mass flowrates F_A and F_B (kg/s), respectively. While the former flowrate is a disturbance variable, the latter serves as a manipulated variable. Three reactions occur in the system as shown in equations (5-52)–(5-54) whereby D and E are the desired products while C and G are intermediate and undesirable biproducts, respectively:

$$A + B \xrightarrow{k_1} C\colon\ k_1 = A_1 e^{-E_1/T_R} \tag{5-52}$$

$$B + C \xrightarrow{k_2} D + E\colon\ k_2 = A_2 e^{-E_2/T_R} \tag{5-53}$$

$$C + D \xrightarrow{k_3} G\colon\ k_3 = A_3 e^{-E_3/T_R} \tag{5-54}$$

where k_1, k_2, and k_3 (s^{-1}) are the reaction rate constants as expressed by the rate laws with pre-exponential factors (A_1, A_2, $A_3(s^{-1})$) and activation energies (E_1, E_2, $E_3(K)$). The activation energies in this case study are in units of

temperature as converted using ideal gas constant. These rate laws depend on the tank temperature $T_R(K)$. The process dynamic and steady state behaviour are modelled using the equations:

$$W\frac{dX_A}{dt} = F_A - F_R X_A - r_1 \tag{5-55}$$

$$W\frac{dX_B}{dt} = F_B - F_R X_B - r_1 - r_2 \tag{5-56}$$

$$W\frac{dX_C}{dt} = -F_R X_C + 2r_1 - 2r_2 - r_3 \tag{5-57}$$

$$W\frac{dX_D}{dt} = -F_R X_D + r_2 - 0.5r_3 \tag{5-58}$$

$$W\frac{dX_E}{dt} = -F_R X_E + r_2 \tag{5-59}$$

$$W\frac{dX_G}{dt} = -F_R X_G + 1.5r_3 \tag{5-60}$$

where X_A, X_B, X_C, X_D, X_E, and X_G (kg/kg) are the respective component mass fractions. W (kg) is the mass holdup in the tank, which is assumed to be constant such that the tank material is always at steady state, i.e.,

$$F_R = F_A + F_B \tag{5-61}$$

where the tank outlet flowrate is $F_R(kg/s)$. The reactions proceed according to the substrate concentrations as follows:

$$r_1 = k_1 X_A X_B W \tag{5-62}$$

$$r_2 = k_2 X_B X_C W \tag{5-63}$$

$$r_3 = k_3 X_C X_D W \tag{5-64}$$

where r_1, r_2, and $r_3(s^{-1})$ are the reaction rates. The manipulated variables for this process are the inlet flowrate of B and tank temperature (i.e., $\boldsymbol{u} = [F_B \quad T_R]^T$). The controlled variables, states, and initial measurements are the component mass fractions (i.e., $\boldsymbol{z}_0 = \boldsymbol{y} = \boldsymbol{x} = [X_A \quad X_B \quad X_C \quad X_D \quad X_E \quad X_G]^T$). The model uncertain parameters considered in this case study are the activation energies (i.e., $\boldsymbol{\theta} = [E_1 \quad E_2 \quad E_3]^T$). The process revenue is to be maximized in this case according to the following objective function:

$$\Phi = P_D F_R X_D + P_E F_R X_E - P_A F_A - P_B F_B - P_T T_R \tag{5-65}$$

where P_D, P_E, P_A, and P_B are the prices of the products and substrates in Table B-2 (Appendix B).
The RTO and NMPC problems (5-5) and (5-6) are subject to constraints on the controlled variables:

$$0 \leq y_i(kg/kg) \leq 1 \qquad \forall i \in \{1, \dots, n_y\} \tag{5-66}$$

Moreover, the RTO and NMPC problems are also subject to constraints on the manipulated variables:

$$2 \leq F_B(kg/s) \leq 10 \tag{5-67}$$

$$323.15 \leq T_R(K) \leq 423.15 \tag{5-68}$$

Lastly, following constraints are imposed on the estimated parameters in problems (5-7) and (5-19):

$$0.1 \leq E_1, E_2, E_3(K) \leq 50{,}000 \tag{5-69}$$

Table B-2 (Appendix B) contains the model parameters and nominal values as used in this study.

The proposed scheme was implemented for the present case study with the model, controlled variables, manipulated variables, constraints and uncertainty parameters described above. The system is operated for $500\ h$ with an RTO period of $\Delta T = 6.5\ h$ and a sampling interval of $\Delta t = 3\ min.$ $n_{z,min} = 3$ was determined based on preliminary identifiability analysis and the process and measurement noises ($\boldsymbol{w}, \boldsymbol{v}$) are additive and zero-mean with 10% of the nominal state values as variance $\mathcal{N}(0, (0.1\boldsymbol{x_{nom}})^2)$. The NMPC controller tuning for formulation (5-6) is $\boldsymbol{Q} = diag(1,1,1,2,1,2)$, $\boldsymbol{R} = diag(3, 0.03)$, and $P = C = 10\Delta t$, based on preliminary manual controller tuning. Table 5-3 presents the formulations to the corresponding optimization problems (5-5), (5-6), and (5-7) associated with this case study.

*Table 5-3: PE, RTO, and NMPC formulations for evaporator case study. *S.S. indicates that a steady-state version of the model is used in the corresponding layer. $S = \{A, B, C, D, E, G\}$ is the set of all species.*

	PE	**RTO**	**NMPC**
Objective function	$\|\hat{\boldsymbol{z}} - \bar{\boldsymbol{z}}\|_{\boldsymbol{K}^{-1}}{}^2$	Eq. (6-65)	$\sum_{i=1}^{10} \|\boldsymbol{y_{sp}} - \hat{\boldsymbol{y}}_{\boldsymbol{t+i}}\|_{\boldsymbol{Q}}^2 + \sum_{j=1}^{10} \|\Delta \boldsymbol{u}_{\boldsymbol{t+j}}\|_{\boldsymbol{R}}^2$
Decision variables	$\boldsymbol{\theta} = [E_1 \quad E_2 \quad E_3]^T$	$\boldsymbol{y} = [X_i \forall i \in S]^T$	$\boldsymbol{u_{t+1}} = [F_{B,t+1} \quad T_{R,t+1}]^T$
Model	Eqs. (5-52)–(5-64). S.S. model	Eqs. (5-52)–(5-64). S.S. model	Eqs. (5-52)–(5-64). Dynamic model
Constraints	Eq. (5-69)	Eqs. (5-66)–(5-68)	Eqs. (5-66)–(5-68)
Inputs	$\bar{\boldsymbol{z}} = [\bar{X}_i \forall i \in S]^T$ $\bar{\boldsymbol{u}} = [\bar{F}_B \quad \bar{T}_R]^T$ $\bar{\boldsymbol{d}} = [\bar{F}_A]^T$	$\boldsymbol{\theta} = [E_1 \quad E_2 \quad E_3]^T$ $\boldsymbol{d} = [F_A]^T$	$\boldsymbol{x_0} = [X_{i,t} \forall i \in S]^T$ $\boldsymbol{y_{sp}} = [X_{i,sp} \forall i \in S]^T$ $\boldsymbol{d_t} = [F_{A,t}]^T$

In the present case study, each challenger RTO problem required ~0.02 s to perform and, as with the previous case study, this implies that $\Delta t > \Delta t_{dummy}$. Thus, $M = 20$ according to equation (5-31) to avoid delays. As stated in Table 5-4, all scenarios required either $k = 5$ or $k = 6$ sets of challenger problems to be performed, leading to a total computational time of 5 and 6 $hours$ (to perform all challenger problems), respectively. This is within the RTO period time; thus, enough data can be collected, and the challenger problems can be performed with no computational delay to the RTO as determined with equation (5-31).

Each uncertain parameter is assumed to materialize only at a low (l), nominal (n), and high (h) value in the interval $[(1-\alpha)\boldsymbol{\theta_{nom}}, (1+\alpha)\boldsymbol{\theta_{nom}}]$, where $\alpha = 0.1$ and the nominal parameters listed in Table B-2 (Appendix B). To the authors' knowledge, this represents the largest parameter uncertainty region to have been considered for the Williams-Otto plant. Hence, a total of 3^3 possible uncertainty scenarios were possible from which the 9 scenarios Table 5-4 were randomly selected as a representative sample. As with the previous case study, the discretization of the uncertainty was done for simplicity and the proposed scheme can be used to estimate any parameter combination within the aforementioned interval (i.e., it is not limited to any particular set of parameter realizations).

Table 5-4: Results for parameter combination scenarios in the Williams-Otto case study under low-variance and regular RTO implementations.

	S1	S2	S3	S4	S5	S6	S7	S8	S9
E_1	h	h	n	h	h	l	h	n	n
E_2	n	l	n	h	h	l	l	l	n
E_3	h	l	h	n	h	l	n	h	l
$\sigma_{\theta,lv}\ (K)$	99	106	51	59	66	71	201	250	128
$\sigma_{\theta,r}\ (K)$	3325	3734	1964	3678	3513	4693	4973	5198	4978
$\bar{P}_{RTO(lv-PE)}\ (\$/s)$	2.99	−4.83	5.17	−6.39	−2.40	−1.69	1.21	7.90	−6.33
$\bar{P}_{RTO}\ (\$/s)$	2.44	−5.01	5.00	−7.19	−2.77	−3.18	1.01	7.29	−7.51
$\%improvement_{\bar{P}}$	18.39	3.73	3.29	12.52	15.42	88.16	16.53	7.72	18.64
k	6	6	6	5	6	6	6	6	5

Figure 5-7 displays the process revenue/losses for several non-overlapping scenarios from Table 5-4 calculated using equation (5-28). As can be observed, the parameter combination affects whether the process will operate at a revenue or loss; the Williams-Otto plant is only profitable in some cases. Nevertheless, the lv-PE/RTO always results in a more economical operation. This is reflected in the average profit rates ($\bar{P}$) for both schemes as shown in Table 5-4 whereby the lv-PE/RTO has lower average rates in all scenarios as quantified in the %improvement. These improved economics are a result of the decreased variation in the parameter estimates over the 80 RTO periods analyzed, which are observed to generally have decreased by one or two orders of magnitude as per the σ values in Table 5-4. Depending on the parameter combination, the lv-PE/RTO can lead to modest (e.g., 3.28% for S3) or significant (e.g., 88.16% for S6) improvements on revenue/loss with respected to the regular RTO.

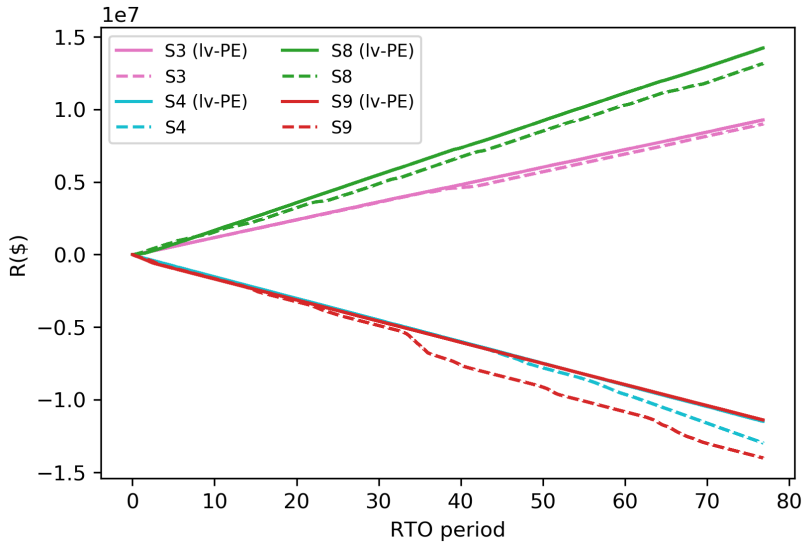

Figure 5-7:Revenue/loss ($) for several of the scenarios in the Williams-Otto case study.

The effect of variance manifests most directly on the manipulated variables, as shown for S8 and S9 in Figure 5-8 and Figure 5-9, respectively. Figure 5-8 exemplifies the effect that measurement noise has on the NMPC and RTO via the parameter updates in an operating scenario without active constraints. As displayed therein, both manipulated variables have brief spikes that correspond to the cases when parameters and set points are changed through execution of the PE and RTO. This is primarily due to the sudden change in controller parameters, which momentarily sends the system on a transient, but also corresponds to small set point corrections. These spikes were observed to be significantly smaller for the lv-PE/RTO than the regular RTO; the resulting transients, which are shorter when the lv-PE/RTO is employed, ensure that the system operates near its optimum for a longer period, thus improving economic performance. The lv-PE/RTO can be observed to result in a far more consistent performance, thus damping the effect of the noisy measurements on the scheme. Figure 5-9 is an atypical scenario where the optimal operating policy occurs at the lower bounds of the manipulated variables in equations (5-67) and (5-68); however, this further elucidates how the lv-PE/RTO can maintain the system at its bound with smaller and less frequent deviations. Another consequence observed therein is the effect of the filter-step of the lv-PE/RTO to avoid periods where the system is operating at non-optimal points. This is also observed between $T = 30$ and $T = 40$ in Figure 5-9 whereby both manipulated variables are not operating at their bounds (i.e., the economic optimum); meaning that the regular RTO was passed an significantly suboptimal set of set points and parameters, which did not reflect the current operating conditions.

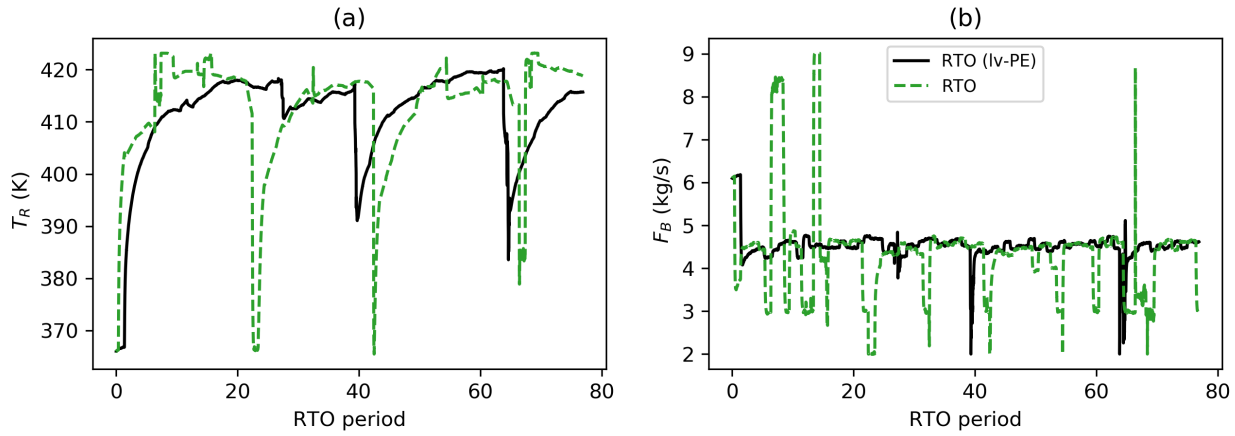

Figure 5-8: Manipulated variables for S8 of the Williams-Otto case study under the lv-PE/RTO and the regular RTO implementations. (a) reactor temperature, (b) inlet flowrate of substrate "B".

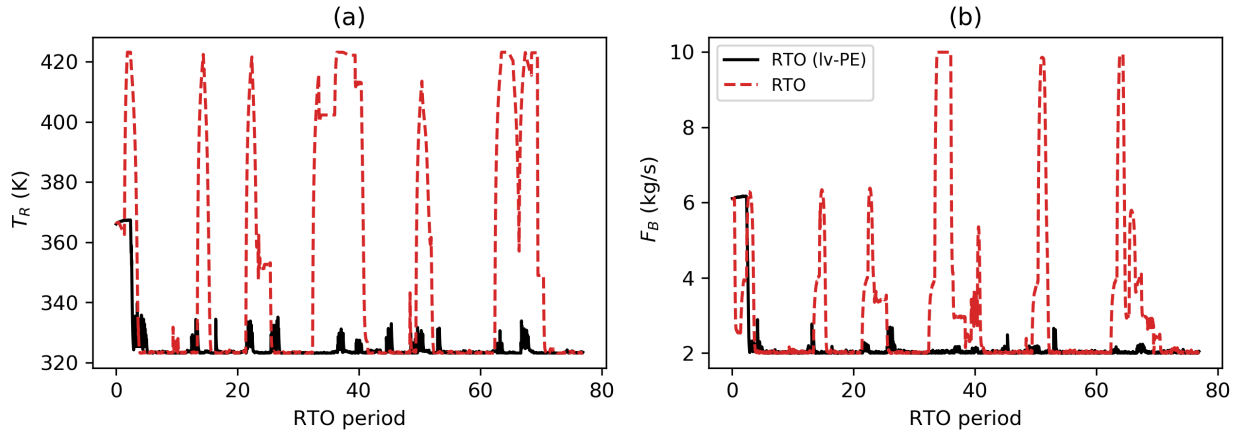

Figure 5-9: Manipulated variables for S9 of the Williams-Otto case study under the lv-PE/RTO and the regular RTO implementations. (a) reactor temperature, (b) inlet flowrate of substrate "B".

Figure 5-10 provides contours of the process profit rates (i.e., $\$/time$) for S8 and S9. These were constructed using the true plant parameters such that they are the "true" profit rate contours. Since these are the "true" contours that correspond to the true parameters in S8 and S9, the performance of the PE scheme can be assessed by how closely they approach the top elevations therein. If the steady-state combinations of manipulated variables are treated as a sampled quantity, the confidence ellipsoids for these manipulated variables in both regular RTO and lv-PE/RTO can be constructed. By superimposing these ellipsoids on the contours, the precision and accuracy of the PE schemes is visualized through the size and closeness to the true optimum, respectively. Figure 5-10 shows these ellipses being centered in the contour region with the most economical profit rates as per the black-shaded elevations, this confirms that the RTO is indeed operating generally near the optimum. However, in both scenarios, the confidence ellipse for the lv-PE/RTO can be observed to be inside the confidence ellipse for the regular RTO; this confirms that the variance in the steady-state manipulated variables has decreased, and in some cases by a significant amount (e.g., S9). The statistical interpretation follows that if many different samples were taken to replicate the construction of the ellipses, then 95% of the constructed ellipses would contain the mean; as such small ellipses imply lower variation in the

sampled quantities — in this case, the manipulated variables. Accordingly, the improvement in process economics occurs through this decrease in variation.

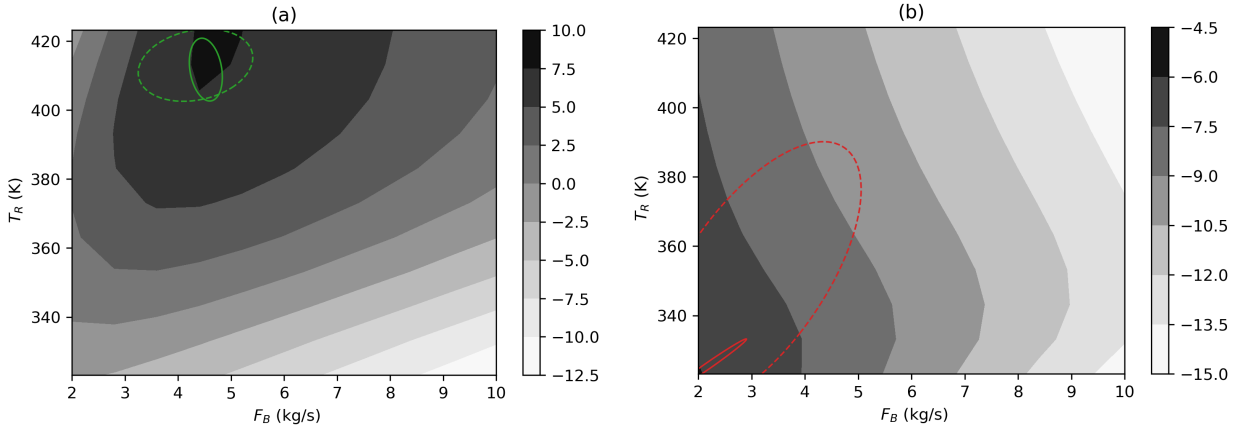

Figure 5-10: Contour plots with the process profit rates ($/s) on the elevations and manipulated variables on the axes for the Williams-Otto case. (a) S8, (b) S9. 95% confidence ellipsoids shown for the manipulated variables under the regular RTO (dashed lines) and lv-PE/RTO (solid lines).

5.4 Summary

Noisy measurements and model uncertainty are inevitable when operating chemical processes, which may lead to poor RTO performance. As RTO attempts to address model uncertainty by adapting model parameters, noisiness can propagate to these parameter estimates leading to poor process performance. An algorithm for reducing noise propagation from the measurements to the parameter estimates is introduced herein; with an error bound step to ensure high quality estimates are obtained. The scheme is motivated through an analysis of RTO economics as affected by set point error owed to parameter inaccuracy. Moreover, the potential computational cost of the scheme is analyzed to avoid any delays are incurred as a result. In two case studies, the estimated parameters are passed to both RTO and NMPC layers as to impact operation significantly. The proposed scheme was found to improve process economics with set points closer to the true plant optima and improved constraint adherence.

6. Parameter Estimation and Robust Optimization of a CO_2 Capture System

Based on the literature review in Section 2.3, uncertainty in the real-time optimization of PCC plants has not been explicitly addressed. To the authors' knowledge, noisiness also remains an open issue as it pertains to PCC estimation schemes and no method has been tested to abate its effects in CO_2 capture systems; hence, the effect of parameter fidelity on model-based control and optimization performance for PCC has not been reported. In addition, parameter and economic robustness have not been jointly addressed in the online optimization of PCC. In particular, the previous work in Chapter 4, which is the most comprehensive RTO implementation in PCC to date, did not consider any type of uncertainty and a very limited set of disturbances. Accordingly, a detailed exploration of the optima across possible disturbances ranges, the addition of novel parameter estimation, and robust optimization layers, will provide new insights on the remaining computational challenges (i.e., uncertainty and noise) that could inhibit the deployment of online economic optimization in PCC plants. The specific objectives considered in the present study are as follows:

1. A high-fidelity framework is proposed for the estimation of uncertainties in high noise environments without requiring data reconciliation. Uncertainty in the thermodynamic parameters and flue gas compositions for post-combustion carbon capture is estimated in the context of RTO.
2. The proposed estimation scheme is compared to standard PE and DR via their respective impacts on PCC performance. These analyses are performed on a long (i.e., month) timescale to assess the impact of real-time decisions on long-term PCC operation.
3. A sensitivity analysis is performed for the optimal cost and rate of carbon capture. The effect of disturbances and economic incentives are quantified for the optimal operation of PCC.
4. A new robust RTO scheme is presented along with an update strategy for PCC set points under diurnal operation. The proposed estimation scheme is also used for uncertainty quantification to yield robust solutions. This new robust RTO scheme explicitly and simultaneously considers uncertainty in the economic parameters and in the operational parameters of the CO_2 capture plant.

This work is structured as follows: Section 6.1 details the formulation for the PE scheme and the robust RTO formulation; Section 6.2 briefly overviews PCC and introduces assessment metrics and constraints for the proposed scheme; Section 6.3 exhibits the test scenarios on the proposed scheme; and Section 6.4 summarizes the insights gained from this study and outlines future works.

6.1. Proposed Scheme and Formulations

RTO is a model-based optimization method that has been proposed in the literature (e.g., Darby et al., 2011) to achieve the economically optimal steady-state operation of process systems. As the models used for RTO are subject to uncertainty, the two-step RTO approach is deployed, which continually updates the model via estimation of parameters. The estimation step, which uses available steady-state process measurements, can address parametric uncertainties in the phenomenological model parameters and external disturbances. In addition to parametric uncertainty, uncertainty also manifests through measurement noise. If the system is noisy, this can adversely impact the fidelity of estimates acquired using the measurements; no practical method or assessment of this issue has been proposed in the context of PCC. This section presents the general formulation for RTO under uncertainty, a noise-abatement scheme to ensure estimates are indeed reliable, and a robust RTO to address price fluctuations.

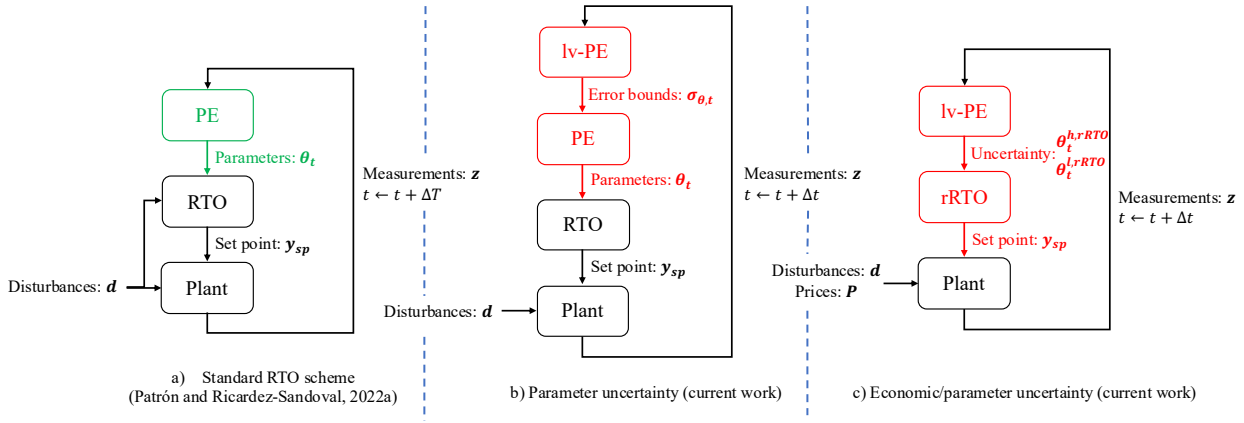

Figure 6-1: Potential RTO architectures. a) parameter uncertainty considered; previous PCC works omitted green block and no uncertainty, b) parameter uncertainty considered using the method in Section 6.1.1, c) parameter and price uncertainties considered using the method in Section 6.1.2. Novel layers considered in this study are shown in red.

RTO-operated systems work in the manner depicted in ca. The RTO computes controlled variable set points, which are passed to the controller. The controller (which could be PID, MPC, NMPC, etc., omitted for brevity) acts by receiving feedback from the plant in the form of state measurements and regulating the plant towards the RTO-defined set point through the manipulated variables, making the scheme closed loop. On a longer timescale, known as the RTO period ΔT, the parameter estimation (PE) problem is executed such that uncertain parameters are updated and the RTO can re-compute the set points under changes in operating conditions.

Generally, RTO is used to optimize process economics such that the process operating conditions can be adjusted as a response to varying disturbances. The formulation for RTO economic optimization with uncertain parameters can be found in Section 5.1, equation (5-5). In the context of energy systems, the economic function Φ could represent emissions, energy consumption, or a comprehensive economic function. Moreover, measurable disturbances ($\boldsymbol{d_t}$) may include changes in electricity demands, fuel grades, or regulatory constraints. The uncertain parameters ($\boldsymbol{\theta_t}$) can include any experimentally determined phenomenological constants (e.g., kinetics, thermodynamics, and equilibrium) or unmeasured disturbances (e.g., compositions) that are built into the model $\boldsymbol{f_s}$. While the uncertain parameters are inherent to the process model, the unmeasured disturbances are external (i.e., a function of factors outside the plant). For PCC, model parameters can include activity coefficients or reaction kinetic parameters, while unmeasured disturbances can include inlet compositions. In process systems, the uncertain model parameters and unmeasured disturbances can both be treated as uncertain parameters, thus necessitating an estimation scheme.

6.1.1. Low-variance PE Formulation (lv-PE)

As mentioned above, uncertain parameters are treated as inputs to the RTO model. Rather than assuming these parameters are fixed, they are updated at regular intervals in the two-step RTO implementation. Moreover, there are many external factors that can be considered as unmeasured disturbances in energy and CO_2 capture systems, which are highly dependent on human behaviour, environmental factors, and process inputs. For instance, energy demands may vary diurnally as in Chapter 4, government production incentives may change as in Chapter 3, or process inputs material grades and types may fluctuate (e.g., Hodžić et al., 2016; Loeffler and Anderson, 2014). These unpredictable changes may result in changes in flue gas composition, which may be difficult or inaccurate to measure. These

unmeasured disturbances can also be treated as uncertain parameters. The uncertain parameters $\boldsymbol{\theta}$ as defined in this work, are time-invariant, i.e., they do not change as an explicit function of the sampling interval but can vary because of the external factors, e.g., changes in the operating conditions. As such, they are updated every RTO period ΔT prior to the set point update. Moreover, the uncertain parameters are bounded such that they are assumed to materialize within a certain range determined *a priori* and constraints on their estimates can be considered in the PE problem to provide a search space. The uncertain parameters herein are classified into two subsets $\boldsymbol{\theta} = [\boldsymbol{\theta_d} \quad \boldsymbol{\theta_p}]^T$. $\boldsymbol{\theta_d} \in \mathbb{R}^{n_{\theta_d}}$ are the uncertain parameters that come from external sources (e.g., unmeasured disturbance) while $\boldsymbol{\theta_p} \in \mathbb{R}^{n_{\theta_p}}$ are parameters that are inherent to the process model (e.g., physical properties); accordingly, $n_\theta = n_{\theta_d} + n_{\theta_p}$.

As mentioned previously, the estimated uncertain parameters ($\boldsymbol{\theta}$) are passed to the RTO formulation in equation (5-1) at time t as depicted in Figure 6-1a and can also be passed to a controller with a matching model to the RTO. These are updated at every RTO period ΔT such that the plant and model are consistently being reconciled. However, the estimation scheme requires noisy measurements ($\boldsymbol{z_t}$) that will inherently include noise that may be propagated from the measurements to the parameter estimates. If the RTO economics are sensitive to these estimated quantities, substantial economic losses may occur. In a system such as PCC, this could manifest through increased energy consumption, resource use, or emissions, which are costly and have prices that accrue over time. Accordingly, the low variance estimation (lv-PE) method proposed in Chapter 5 is deployed herein to abate the propagation of noise from measurements to estimates. The lv-PE method uses formulation (5-19) to determine a measurement set that results in the lowest errors in $\boldsymbol{\theta_t}$ *a prior* to the PE problem. Within the lv-PE algorithm, many PE problems are executed offline via a bootstrapping method. The standard deviations in estimates given multiple different measurement sets are compared to determine which measurements result in the highest precision. Additionally, lv-PE uses the statistics acquired by the bootstrap to provide error bounds and filter the estimates $\boldsymbol{\theta_t}$ *a posteriori* to the online PE problem. Interestingly, lv-PE has yet to be applied to a large-scale system like PCC; thus, its benefit on this class of systems with many inputs and slow dynamics is unknown. PCC, for which uncertainty has not been addressed in online economic optimization, is well-suited to lv-PE as it has infrequent set point changes resulting in long periods at steady state. The measurements acquired at steady state will enable the repeated data collection required for the bootstrapping that lv-PE entails; as such, high-fidelity parameter estimates can be computed to operate the system near its true optima. Moreover, the mechanistic PCC has been shown to exhibit parameter sensitivity (e.g., Cerrillo-Briones and Ricardez-Sandoval, 2019; Hughes at al., 2022). The exchange of information between the lv-PE and PE layers are shown in Figure 6-1b while the full algorithm can be found in Section 5.2.2.

6.1.2. Robust RTO (rRTO)

In addition to the uncertain parameters ($\boldsymbol{\theta_t}$), the RTO presented in equation (5-5) can also manifest uncertainty in the economics. In this case, the economic function is denoted as $\Phi(\hat{\boldsymbol{x}}_t, \boldsymbol{P_t})$ where $\boldsymbol{P_t} \in \mathbb{R}^p$ are the economic uncertainties at time t. When economic uncertainty occurs, the operator may want to find an operating point that works well for a range of uncertain economic scenarios. For instance, when the economics ($\boldsymbol{P_t}$) and parameters ($\boldsymbol{\theta_t}$) are frequently fluctuating, a single solution that works well regardless of the actual realization of uncertainties that happen in the future may be advantageous (i.e., a robust solution that is also suitable for the short-term future); however, this robust

solution may sacrifice performance if uncertainties remain fixed and an accurate parameter estimation scheme is available. As mentioned in Section 2.3, previous studies have considered economic robustness in PCC; however, those schemes make decisions in scheduling and planning timescales, not in real-time. In this economically robust paradigm, one can also address uncertainty in the parameters by bypassing the PE problem and formulating a problem that is robust to both parameter and economic uncertainties.

To achieve RTO robustness with uncertainty in both economics and model parameters (in contrast to uncertainty in parameters only as in Section 6.1.1), the multi-scenario approach can be employed where various model realizations are solved. This approach has been employed in PCC design (Cerrillo-Briones and Ricardez-Sandoval, 2019) and control (Chapter 3), but never considered in an online real-time economic optimization context such as RTO. As such, the multi-scenario approach is applied for robust RTO (rRTO) herein at time t as follows:

$$
\begin{aligned}
&\min_{\widehat{\boldsymbol{y}}_t} \textstyle\sum_{j=1}^{n_r} \omega_{t,j} \Phi\left(\widehat{\boldsymbol{x}}_{\boldsymbol{t,j}}, \boldsymbol{P}_{\boldsymbol{t,j}}\right) \\
&s.t. \\
&\boldsymbol{f}_{\boldsymbol{s,j}}\left(\widehat{\boldsymbol{x}}_{\boldsymbol{t,j}}, \widehat{\boldsymbol{y}}_{\boldsymbol{t,j}}, \boldsymbol{u}_{\boldsymbol{t,j}}, \boldsymbol{d}_{\boldsymbol{t}}, \boldsymbol{\theta}_{\boldsymbol{t,j}}\right) = \boldsymbol{0} && \forall j \in \{1, \dots, n_r\} \\
&\boldsymbol{g}_{\boldsymbol{s,j}}\left(\widehat{\boldsymbol{x}}_{\boldsymbol{t,j}}, \boldsymbol{u}_{\boldsymbol{t,j}}, \boldsymbol{d}_{\boldsymbol{t}}\right) \leq \boldsymbol{0} && \forall j \in \{1, \dots, n_r\} \qquad (6\text{-}1) \\
&\boldsymbol{y}^{\boldsymbol{l}} \leq \widehat{\boldsymbol{y}}_{\boldsymbol{t,j}} \leq \boldsymbol{y}^{\boldsymbol{h}} && \forall j \in \{1, \dots, n_r\} \\
&\boldsymbol{u}^{\boldsymbol{l}} \leq \boldsymbol{u}_{\boldsymbol{t,j}} \leq \boldsymbol{u}^{\boldsymbol{h}} && \forall j \in \{1, \dots, n_r\} \\
&\widehat{\boldsymbol{y}}_{\boldsymbol{t,1}} = \cdots = \widehat{\boldsymbol{y}}_{\boldsymbol{t,j}} = \cdots = \widehat{\boldsymbol{y}}_{\boldsymbol{t,n_r}}
\end{aligned}
$$

where all variables and functions have the additional index $j \in \{1, \dots, n_r\}$. This index represents individual scenarios being considered, which generates various instances of the process model; each instance *j* represents a realization of the uncertain parameters. Accordingly, the last constraint in formulation (6-1) ensures the set point decision variables for all realizations are equivalent. Through the set point equivalence, a single set point is found that is optimal for all realizations; this is the set point that is provided to the control layer as shown in Figure 6-1c.

To choose which uncertainty combinations are featured in *j*, the uncertain parameters are assumed to manifest within $[\boldsymbol{\theta}_{\boldsymbol{t}}^{\boldsymbol{l,rRTO}}, \boldsymbol{\theta}_{\boldsymbol{t}}^{\boldsymbol{h,rRTO}}]$, which represents the lower and upper bounds of the parameter uncertainty region, respectively. As with the uncertain parameters, the objective function Φ has the dependence on $\boldsymbol{P}_{\boldsymbol{t,j}}$, which can manifest within the region $[\boldsymbol{P}_{\boldsymbol{t}}^{\boldsymbol{l}}, \boldsymbol{P}_{\boldsymbol{t}}^{\boldsymbol{h}}]$. Accordingly, n_r, which corresponds to the index j, is the number of scenarios considered within these regions upon discretization of the intervals. Note that the bounds of the regions are indexed in t such that they may expand or contract across RTO periods to accommodate for changing levels of uncertainty. The scenarios encompass the bounds of the uncertainty region; however, the choice of discretization for the uncertainty regions is a user-defined choice that balances computational efficiency with robustness. As more scenarios are included, the model size grows but represents a better approximation of the continuous uncertainty region between the bounds.

Owing to the parameter and economic uncertainty region discretization described above, the economics of the various model realizations are minimized jointly in the rRTO objective function in equation (6-1). Each objective function term is weighed by $\omega_{t,j}$, which corresponds to the probability of a given realization occurring such that $\sum_{j=1}^{n_r} \omega_{t,j} = 1$; these must be established *a priori* based on the underlying statistical distribution that the uncertain parameters and

economics obey. As with the uncertainty regions above, the weights are indexed in t to reflect changing realization probabilities.

While $\boldsymbol{P_t^l}$ and $\boldsymbol{P_t^h}$ must be established based on knowledge of the economic process incentives, the size of the parameter uncertainty region (defined by $\boldsymbol{\theta_t^{l,rRTO}}$, $\boldsymbol{\theta_t^{h,rRTO}}$) are typically difficult to quantify and are based on process knowledge rather than a systematic uncertainty quantification method. However, the lv-PE method presented in Section 5.2.2 presents a bootstrap method that acquires data at every sampling period Δt to quantify the parameter uncertainty region via the parameter standard deviations generated therein. As such, the parameter uncertainty region for the rRTO problem is defined as $\left[\boldsymbol{\theta_t^{l,rRTO}}, \boldsymbol{\theta_t^{h,rRTO}}\right] = [\overline{\boldsymbol{\theta}}_{\boldsymbol{t}} - \frac{\tau}{\sqrt{M}}\boldsymbol{\sigma}_{\boldsymbol{\theta_t}}, \overline{\boldsymbol{\theta}}_{\boldsymbol{t}} + \frac{\tau}{\sqrt{M}}\boldsymbol{\sigma}_{\boldsymbol{\theta_t}}]$ where $\overline{\boldsymbol{\theta}}_{\boldsymbol{t}}$, $\boldsymbol{\sigma}_{\boldsymbol{\theta_t}}$, and M are the sample mean, standard deviation and size, respectively, as defined by the algorithm in Chapter 5. As the quantities acquired in the lv-PE procedure are indexed in time t to accommodate for changing levels of uncertainty across RTO periods, these bounds also reflect changing uncertainty. Moreover, τ allows for the use of confidence intervals to reflect the error tolerance of the user and can be retrieved from a two-sided t-distribution; this gives statistical significance to the robustness in formulation (6-1). The parameter uncertainty region $\left[\boldsymbol{\theta_t^{l,rRTO}}, \boldsymbol{\theta_t^{h,rRTO}}\right]$ differs from the PE optimization bounds in Chapter 5 as it is acquired from the lv-PE algorithm while PE bounds are defined based on process knowledge.

By bypassing the PE step in problem (5-7) and only conveying parameter bounds to problem (6-1), the rRTO formulation finds robust solutions that account for economics fluctuations and parameters uncertainties. Accordingly, the rRTO formulation (6-1) can be deployed instead of the hierarchical approach that uses formulations (5-5) and (5-7). This exchange of information is shown in Figure 6-1c.

6.2. Scheme Implementation and Assessment

A pertinent application of the methods outlined in previous sections is PCC; a technology whose global industrial adoption is currently limited by its unfavourable process economics. Figure 6-2 shows the PCC plant and the uncertainties therein.

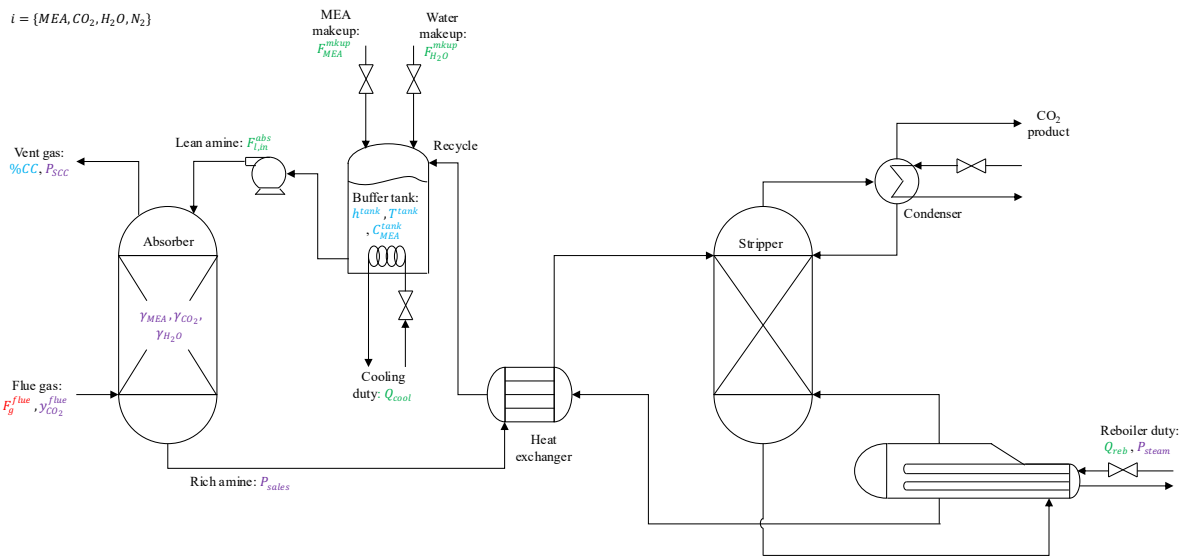

Figure 6-2: PCC plant layout. Blue denotes controlled variables, green denotes manipulated variables, red denotes disturbances, purple denotes uncertainties.

The two-layer RTO and rRTO schemes outlined in Sections 6.1.1 and 6.1.2, respectively, are deployed on the PCC plant. Figure 6-1a shows the scheme deployed in Chapter 4; as shown therein, the previous RTO implementation for PCC assumes measurable disturbances and does not account for uncertainty, which are restrictive assumptions that could lead to significantly suboptimal operation. As summarized in the literature review, previous works did not consider the two-layer architecture shown in Figure 6-1a as the green parameter estimation layer was omitted. Consequently, no previous work considered a noise-abatement scheme (e.g., Figure 6-1b) as outlined in the introduction. In contrast, the two schemes proposed in Figure 6-1b and Figure 6-1c lift these assumptions to explicitly account for noise , model, and economic robustness to the operation of the PCC plant..

Information regarding the manipulated and controlled variables, with their corresponding nominal values, can be found in Section 4.2.3. As noted earlier, uncertain parameters can be segmented into physical properties and unmeasured disturbances, which will be assessed individually through their respective estimates on the RTO scheme. In the PCC plant, both the flue gas flowrate and CO_2 content entering the absorber are typical disturbances. Both disturbances are typically measurable in power plants (e.g., via a flowmeter and a katharometer, respectively). Although the accuracy of the katharometer is generally adequate for monitoring of emissions (e.g., $\pm 0.5\ mol\%$ in absolute terms; ABB, 2003), it may not be adequate for RTO where the optimum is sensitive to the carbon content of the flue gas. Accordingly, an estimation scheme is proposed for the flue gas CO_2 and H_2O concentrations (i.e., $\boldsymbol{\theta_d} = \begin{bmatrix} y_{CO_2}^{flue} & y_{H_2O}^{flue} \end{bmatrix}^T$) while flue gas flowrate is assumed to be a measured disturbance (i.e., $\boldsymbol{d} = \begin{bmatrix} F_0^g \end{bmatrix}^T$). The estimated unmeasured disturbances are treated as uncertain parameters ($\boldsymbol{\theta_d}$) and provided to the RTO layers such that high-fidelity composition estimates are generated and lead to high-fidelity set points. Only these two component fractions are taken as disturbances as the nitrogen fraction is fixed since it is inert in the upstream combustion process, and the MEA is assumed to be unevaporable. The nominal values for the measurable and unmeasured disturbances are $\boldsymbol{d_{nom}} = [4.012\ mol/s]^T$ and $\boldsymbol{\theta_{d,nom}} = [0.175\ mol/mol \quad 0.025\ mol/mol]^T$, respectively. Moreover, activity coefficients are assumed to be the cause of the parametric uncertainties in the PCC model and, as such, are considered uncertain

parameters (i.e., $\boldsymbol{\theta_p} = [\gamma_{MEA} \quad \gamma_{CO_2} \quad \gamma_{H_2O}]^T$). While these parameters are assumed to be constant in the process model (i.e., time-invariant), their true values are not precisely known and are designed to capture non-idealities in fluid behaviour, which may vary over time as the operation of PCC is highly nonlinear. Accordingly, it is important to update the parameters on a regular basis as operating conditions change. The nominal values for the uncertain parameters are $\boldsymbol{\theta_{p,nom}} = [0.381 \quad 0.677 \quad 0.974]^T$).

The present analysis assumes that only 12 measurements are available for estimation, which are denoted as $\boldsymbol{z} = \left[\boldsymbol{C_H^g}^T \quad \boldsymbol{C_0^l}^T \quad T_{g,0} \quad T_{g,H} \quad T_{l,0} \quad T_{l,H}\right]^T$. These include the liquid ($\boldsymbol{C_0^l}$) and gas ($\boldsymbol{C_H^g}$) compositions and temperatures at the bottom and top of the absorber column. Only a single set of gas and liquid absorber concentration measurements along the absorber height are used; thus, it is assumed that these are accessible at the column top and bottom outlets, respectively. This is done as sampling of inlet and outlet streams is more practical than sampling along the column height; moreover, good estimate quality was observed with these sampling locations in Chapter 4. The sample size assumed to be $M = 40$ such that the estimation schemes can provide good estimates while not incurring any delays in the execution of the RTO. This sample size was chosen based on preliminary simulations and ensures significant measurement averaging occurs such that increasing beyond this size makes little difference. Conversely, significantly smaller sample sizes may allow noise propagation as they do not benefit from averaging effects. In addition to these measurements, the following bounds are also given to the PE problem (5-7) in the case of uncertain model parameters ($\boldsymbol{\theta_p}$):

$$0 < \gamma_{MEA}, \gamma_{CO_2}, \gamma_{H_2O} < 2 \tag{6-2}$$

The upper bound of equation (6-2) is chosen as to match the activity coefficient range for mixed amine solutions loaded with CO_2 presented in Kaewsichan et al. (2001). Furthermore, the following constraints are included in the PE problem in the case of unmeasured disturbances ($\boldsymbol{\theta_d}$):

$$\begin{aligned} &y_{CO_2}^{flue} + y_{H_2O}^{flue} = 0.2 \\ &0 < y_{CO_2}^{flue}, y_{H_2O}^{flue} < 0.2 \end{aligned} \tag{6-3}$$

The former fixes the total amount of CO_2 and water in the flue gas (since nitrogen is assumed to be 80 $mol\%$ of the flue gas), while the latter provides upper and lower bounds for the mole fractions. Equation (6-3) encompasses the potential carbon dioxide fraction of typical PCC power plants (Danaci et al., 2021). The lower and upper bounds for the PE problems establish a finite estimation search space and are not included in the RTO economic optimization problem as the disturbances and parameters are not decision variables in the RTO formulation. Similar constraints on manipulated and controlled variables in PCC can be found in Section 4.2.3.

The foremost factor motivating the deployment of RTO is the process economics; thus, each scheme and scenario will be analyzed by their cumulative cost $C(\$CAD)$ across N RTO periods tested, defined as follows:

$$C_{PCC} = \Delta T \sum_{i=0}^{N} \phi_i \tag{6-4}$$

where $\phi_i(\$CAD/hour)$ is the price of operating the PCC according to equation (6-4) at every RTO period i.

In addition to considering the cost of the PCC system, the effect that the reboiler has on the upstream power plant must also be accounted for. The reboiler requires steam that comes from the power plant, resulting in a reduction of the power generation capacity. This is accounted for by considering the cumulative energy penalty $C_{energy}(\$CAD)$ across N RTO periods tested in each scenario, defined as follows:

$$C_{energy} = \Delta T \sum_{i=0}^{N} Q_{reb,i}(P_{elec} - P_{steam})\eta \tag{6-5}$$

where $Q_{reb,i}(kW)$ denotes the reboiler duty, P_{elec} and $P_{steam}(\$CAD/kWh)$ denote the electricity price rate and the steam price rate, respectively, while $\eta = 0.4$ (Mac Dowell and Shah, 2013) denotes the efficiency of converting steam to electricity in the power plant. The difference between energy sales and steam prices corresponds to the energy price markup upon sale. These are multiplied by the reboiler duty through an efficiency factor to quantify the profit loss incurred by using the steam in the PCC reboiler instead of using it in the power plant turbines.

In addition to quantifying the potential economic and energy effects of the RTO. The environmental effects are also of utmost importance. To do this, the cumulative mass of CO_2 emitted $m_{CO_2}^{emitted}(tn)$ over N RTO operating periods is calculated as follows:

$$m_{CO_2}^{emitted} = \Delta T M_{CO_2} \sum_{i=0}^{N} F_{g,i}^{vent} y_{CO_2,i}^{vent} \tag{6-6}$$

where $F_{g,i}^{vent}(mol/hr)$ and $y_{CO_2,i}^{vent}(mol/mol)$ are the vent gas flowrate and CO_2 fraction for each RTO period, respectively, and $M_{CO_2}(tn/mol)$ is the molar mass of CO_2. In addition, an influencing factor in the PCC economics is the amount of MEA makeup added in the tank (as shown in Chapter 4). Accordingly, this is also considered in the assessment of the RTO across N RTO periods tested in each scenario, i.e.,

$$m_{MEA}^{mkup} = \Delta T M_{MEA} \sum_{i=0}^{N} F_{MEA,i}^{mkup} \tag{6-7}$$

where $m_{MEA}^{mkup}(tn)$ is the amount of makeup MEA used and $M_{MEA}(tn/mol)$ is the molar mass of MEA.

6.3. Results

The formulations outlined in Sections 6.1.1 and 6.1.2 are implemented in the PCC system described in Chapter 4. Measurement noise is inserted to the estimation scheme via the steady-state measurement samples $\{\boldsymbol{z_{t-i}}\}_{i=0}^{M}$ and is assumed to be additive zero-mean Gaussian noise with a standard deviation of 5% of the nominal measurement values (i.e., $\mathcal{N}(0, (0.05\boldsymbol{z_{nom}})^2)$, such that the noise can substantially affect estimate quality. $\boldsymbol{z_{nom}}$ is the measurement vector corresponding to the nominal operating conditions outlined in Section 4.2.3. The sensitivity of the cost-optimal process operation is studied in Scenario A. Moreover, the proposed operating scheme in Section 6.1.1 is assessed in Scenario B and Scenario C. Furthermore, the proposed operating scheme in Section 6.1.2 is assessed in scenario D. Both schemes are evaluated through their effects on a long (months) timescale according to the metrics defined in Section 6.2.

6.3.1. Scenario A: Sensitivity of Cost-optimal Operation

Power plants often follow a diurnal schedule whereby the electricity produced observes a time-of-use (TOU) pricing model. TOU works such that price of energy is changed over the day so that providers can disincentivize excessive consumption through periods of peak demand.

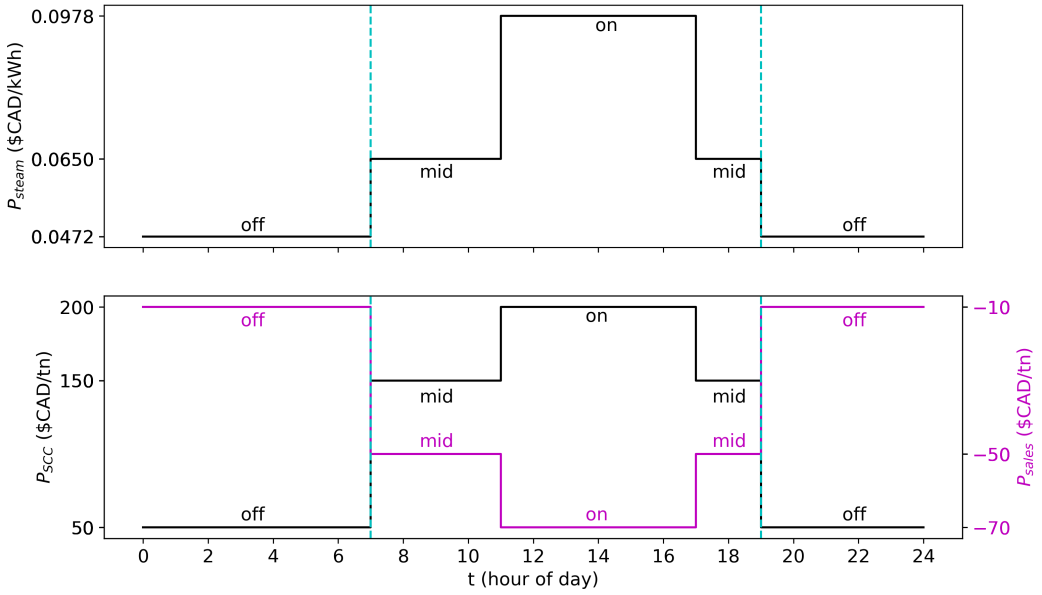

Figure 6-3: TOU variation in steam price (top), SCC and carbon sales (bottom). Cyan dotted lines denote update times for Scenario C.

Consumer pricing fluctuation amplitudes and timings were retrieved from the Ontario Energy Board [61] for a 24-hour summer cycle. These amplitudes were incorporated into the steam price reported in Karimi et al. [60]. As such, electrical losses via steam consumption to the PCC plant vary in the same manner as electricity price to consumer; this is depicted in Figure 6-3 (top). Moreover, SCC [18] and carbon sales rates [59] were also assumed to vary in the same schedule and amplitude with high, medium, and low values taken from the literature (Figure 6-3, bottom). These are scheduled to incentivize removal during on-peak hours of high demand, with lesser incentives in off-peak hours of low demand.

A sensitivity analysis was performed for the cost-optimal PCC operation under variation of the disturbances of flue gas inlet flowrate (F_0^g) and flue gas CO_2 content ($y_{CO_2}^{flue}$). This is done as previous studies only consider a limited set of disturbance realizations, which are far more limited than the ranges typically observed in the literature (e.g., Danaci et al. [16]). The flue gas flowrate is assumed to vary within a symmetric $\pm 15\%$ interval centred around its nominal value (reported in Section 4.3.2), i.e., $F_0^g = \alpha \boldsymbol{d_{nom}}$ where $\alpha \in [0.85, 1.15]$. Furthermore, the flue gas CO_2 content can manifest between the range $y_{CO_2}^{flue} \in [0.12, 0.175]$. In addition to variation of disturbances, the prices can manifest at the three levels (off, mid, on) corresponding to TOU as depicted in Figure 6-3. For this scenario, the uncertain mode parameters are assumed to be perfectly known and manifesting at their nominal values as reported in Section 6.2. Figure 6-4 shows the sensitivity analysis performed of the cost optimal operation.

Generally, a trend of increasing and sensitive capture rates is observed with increasing flue gas CO_2 content as evidenced in the first row of Figure 6-4. These increased optimal rates are coupled with a decreased process cost (second row of Figure 6-4) as the PCC process can operate more efficiently with a more concentrated inlet (i.e., a more concentrated flue gas has similar effect to a more concentrated solvent). In contrast, lower removal rates are coupled with lower removal costs as the flue gas flowrate increases; however, the sensitivity to this disturbance is significantly less than the sensitivity to flue gas composition. This is owed to less efficient operation as increased throughput of flue gas requires a commensurate increase in amine concentration or reboiler duty, which is economically disadvantageous. Accordingly, in situations of higher flue gas flowrates, the optimal operating policy is to settle for low removal to minimize cost. An exception to the behaviours listed above occurs for the process cost under the off-peak regime (bottom-left pane of Figure 6-4). Herein, it is observed that low flue gas compositions and flowrates result in lower costs and there is little sensitivity to either disturbance. This occurs due to the weak economic incentives in the low carbon and energy costs. Accordingly, the off-peak operating regime sees only small changes in optimal pricing regardless of the disturbance combination observed.

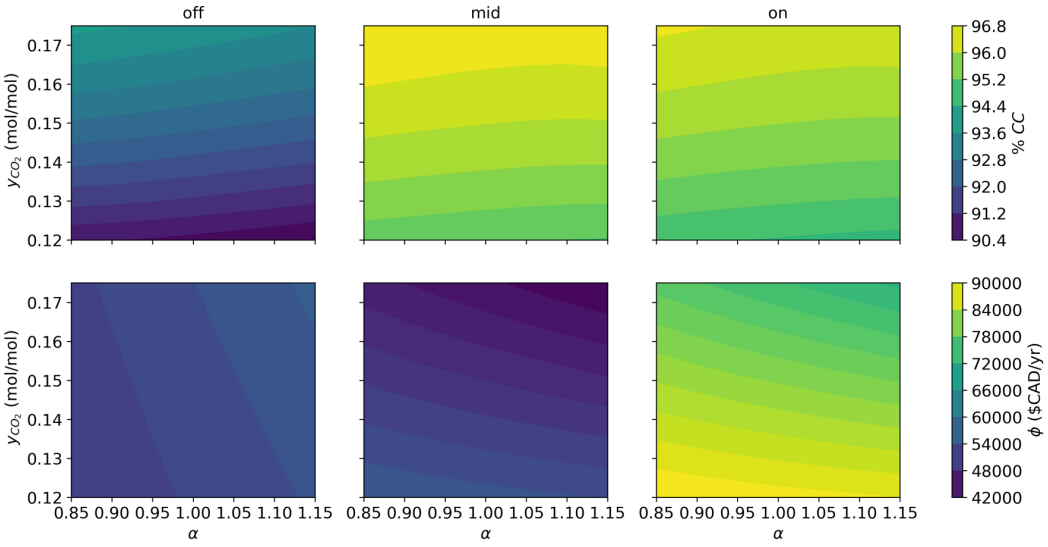

Figure 6-4: Cost-optimal rate of carbon capture (first row) and process cost (second row) under varying disturbances and TOU. The columns represent the TOU prices.

With respect to the TOU economic incentives, the off-peak prices result in the lowest overall capture rates with middling process costs. This occurs as the off-peak prices favour conservative operation due to low carbon costs (Figure 6-3); again, the off-peak prices result in decreased cost sensitivity to disturbances. This implies that the energy price dominates the operation during off-peak hours whereby low capture is favorable as there is little removal incentive and high energy detriment from excessive removal. In contrast, on-peak prices result in high capture rates with the highest costs due to the increased carbon and energy prices. In this case, reasonably high capture is achieved despite the high energy prices because the carbon prices are dominant. However, the highest removal rates and lowest prices in the TOU pricing scenarios are achieved using mid-peak incentives, which balance removal and process costs with middling carbon and energy pricing. The mid-peak incentives have unit costs that are sufficiently low to warrant high removal rates while not being low enough to drastically increase reboiling or makeup (Figure C-1, Appendix C).

The optimal price and rates of carbon capture are sensitive to both upstream disturbances and the economic incentives on the process; this is reflected in an 6.4% range in removal rates and a 48,000 $\$CAD/yr$ range in annualized process cost (see the corresponding colour bars in Figure 6-4). Accordingly, variation and uncertainty in these disturbances and prices will have a significant effect on the operation of PCC; thus, are suitable for parameter estimation and robust optimization in the forthcoming sections.

6.3.2. Scenario B: Estimation of Flue Gas Carbon Content ($\boldsymbol{\theta_d}$)

Flue gas compositions to the PCC plant may vary with respect to time as feedstock to the upstream power plant varies in grade (e.g., changes in the type of coal being used). Moreover, this variation is expected to occur in power plants that employ cofiring (e.g., Hodžić et al., 2016; Loeffler and Anderson, 2014), whereby various fuel types are used within the same power unit. This necessitates an operating scheme that is flexible to different flue gas composition profiles such that the process economics are optimized despite variation.

Scenario B considers a parameter estimation approach as outlined in Section 6.1.1., whereby the uncertain parameters are provided to the RTO and control models. To explore the effect of measurement noise on scheme effectiveness, this scenario compares four RTO implementations: 1) RTO with a standard PE and no noise-abating step (denoted PE); this represents the scheme deployed in Chapter 4 with an additional PE layer, 2) RTO with traditional least-squares DR (e.g., Albuquerque and Biegler, 1996; denoted DR-PE), 3) RTO with low-variance PE considering information content and estimation filters (denoted lv-PE), and 4) RTO with knowledge of the true value of the CO_2 content (denoted TV). The latter of these cases is unrealistic as composition measurements of the flue gas are difficult to perform online in practice; however, it provides an upper bound to economic performance as it results in an RTO model with no mismatch from the plant.

The PE/RTO is run for 100 RTO periods of $\Delta T = 8\ hours$ (i.e., 33 $days$) as to have a large sample of RTO executions and sufficiently long RTO periods as suggested in Chapter 4. The main unmeasured disturbance/estimated parameter ($\boldsymbol{\theta_d}$ as defined in Section 6.2) is the flue gas CO_2 content ($y_{CO_2}^{flue}$), which is varied for each RTO period. Danaci et al. (2021) provides a breakdown of the flue gas CO_2 compositions for different fuel types/grades; based on the range reported therein, the flue gas CO_2 molar fraction was sampled from a uniform distribution between 0.12 and 0.175 mol/mol (i.e., $y_{CO_2}^{flue} \sim \mathcal{U}(0.12,0.175)$). The PE deployed in this scenario must estimate this content such that it can provide the RTO and control models with accurate information regarding the disturbance. The results from these implementations are shown in Figure 6-5.

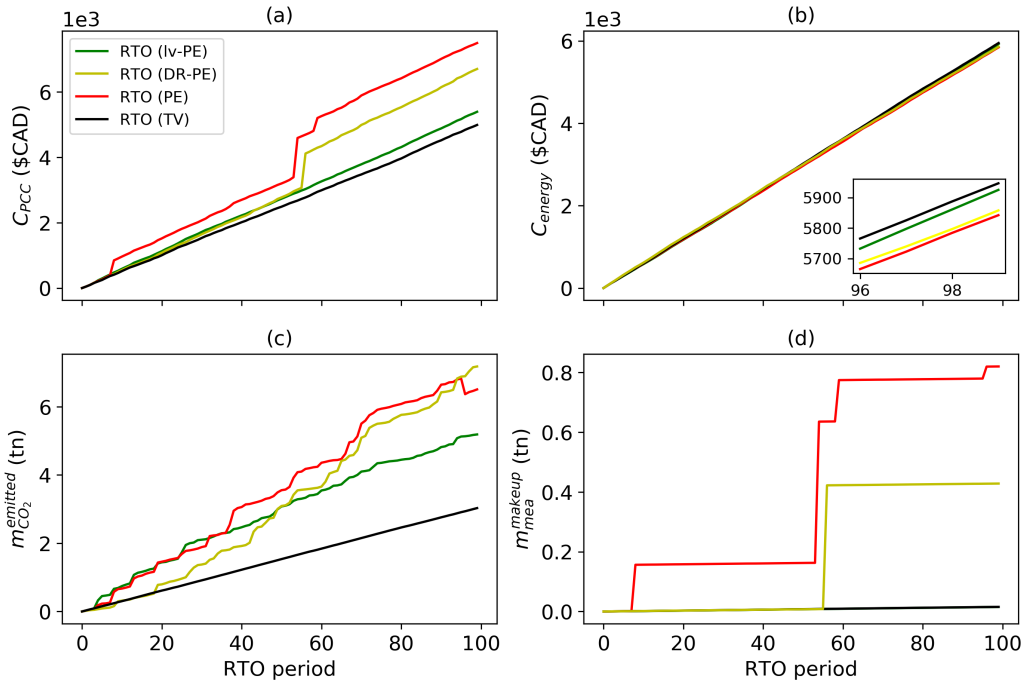

Figure 6-5: Cumulative a) PCC cost, b) energy penalty, c) CO_2 emissions, d) fresh MEA used for scenario B.

As illustrated in Figure 6-5a, the cumulative PCC cost, as defined in equation (6-4), over the 100 RTO periods tested is significantly more expensive for the PE and DR-PE than the lv-PE (~39% and ~25% more expensive, respectively). With respect to the TV case, the PE, DR-PE and lv-PE experience economic losses of ~50%, ~34%, and ~8%, respectively; as such, the lv-PE is the most cost-effective, followed by the DR-PE, and the PE. Comparing the benchmark DR-PE with the proposed lv-PE in Figure 6-5a, it can be observed that the two schemes indeed have similar performance until period 55 whereby the economic profiles diverge. This is owed to an erroneous parameter estimate, which was discarded by the lv-PE scheme by the filter bounds. In contrast, this does not occur with the DR-PE scheme, leading to an expensive period of operation. Moreover, the estimation schemes make subtle difference in abating energy penalties as in Figure 6-5b (in fact, the TV case and lv-PE incur a slightly higher energy penalty). This is likely the main driver of decreased emissions (i.e., increased removal) observed in Figure 6-5c, whereby higher reboiler duty leads to increased removal.

In contrast, as shown in Figure 6-5c and d respectively, the CO_2 emissions and MEA consumption can vary substantially depending on the scheme used. The emissions over the 100 RTO periods tested are ~115%, ~137%, and ~70% higher when using the PE, DR-PE, and lv-PE, respectively, over the TV case. This constitutes another improvement of the lv-PE and a deterioration of the DR-PE with respect to the PE case. While the lv-PE performs better than the PE and DR-PE, it is worse than the measurable disturbance case. This suggests that the CO_2 emissions predictions generated by the PCC model are highly sensitive to uncertainties in flue gas composition, which is reasonable as the upstream composition will directly impact the outlet compositions. Moreover, the DE/RTO and DR-PE/RTO require a significantly higher amount of fresh MEA that the lv-PE and TV cases. Indeed, this appears to be the main factor elevating the PCC cost in the PE and DR-PE schemes as steps in the MEA consumption depicted in

Figure 6-5d align with steps in cost depicted in Figure 6-5a. As mentioned above, these are likely caused by outlier parameter estimates in the PE implementation, which are filtered by the lv-PE such that an unnecessary makeup is not used. This finding also aligns with our previous work, where the MEA makeup was shown to be a major source of PCC cost. In addition to the cumulative plots, the average parameter error across the three estimation schemes tested are ~30%, ~35%, and ~40% for the lv-PE, DR-PE, and PE schemes, respectively. Notably, the limitations of our previous work in Chapter 4 are shown in the PE case, whereby its economic and emissions performance are worse under uncertainty (~42% and ~45% additional deterioration with respect to the true parameter case, respectively). A sample set point transition using the controller/estimator from Chapter 4 with the estimated parameters for one RTO period is shown in Appendix C.

As reported in Chapter 4, the averaged CPU time for the RTO is 4.33 s. Additionally, the mean PE CPU time as determined in this study is 4.45 s. As such, RTO and PE models are fit for online use.

6.3.3. Scenario C: Estimation of Activity Coefficients ($\boldsymbol{\theta_p}$)

Thermodynamic parameters are critical to capture non-idealities in behaviour, which are often nonlinear for PCC systems. Accordingly, the precise activity coefficients will never be exactly known and must be estimated to ensure model fidelity; as such they are considered uncertain for this scenario. As with the previous scenario, the main disturbance, flue gas CO_2 content ($y_{CO_2}^{flue}$) is varied for each RTO period and sampled from a uniform distribution between 0.05 and 0.2 mol/mol (i.e., $y_{CO_2}^{flue} \sim \mathcal{U}(0.05,0.2)$). However, this scenario assumes that the disturbance is measurable and accurate (i.e., does not have to be estimated) and, instead, requires PE to be deployed to estimate the activity coefficients ($\boldsymbol{\theta_p}$) as defined in Section 6.2) such that they can be provided to the RTO and control models. The true parameter values are assumed to be constant and equal to the nominal parameter vector presented in Section 6.2.

As with scenario B, the PE/RTO is run for 100 RTO periods of $\Delta T = 8\, hours$ (i.e., 33 $days$) and four RTO implementations are compared (PE, DR-PE, lv-PE, TV). The TV case herein is unrealistic as activities are not usually truly known; however, it provides an upper bound to economic performance since it assumes a perfect RTO model parameters with respect to the plant. Figure 6-6 shows the results from these implementations.

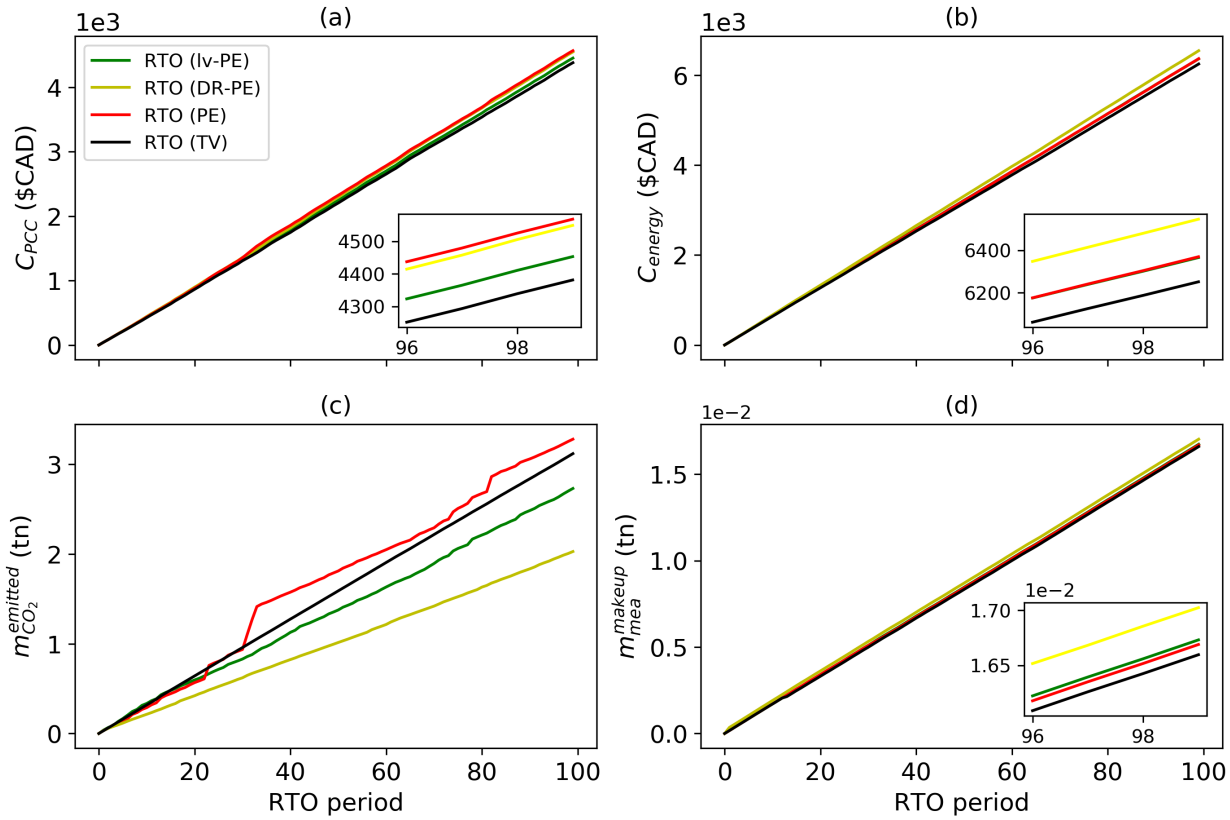

Figure 6-6: Cumulative a) PCC cost, b) energy penalty, c) CO_2 emissions, d) fresh MEA used for scenario C.

As shown in Figure 6-6a, all estimation schemes experience substantially less deterioration in cost with respect to the TV case (~4.25%, ~3.81%, and ~1.63% for the PE, DR-PE, and lv-PE, respectively). This suggests that the PCC process is less sensitive to the accuracy of parameter estimates than the disturbance estimates. Nevertheless, the lv-PE still outperforms the regular PE and DR-PE by ~2.51% and ~2.15%, respectively, over the 100 RTO periods observed. While these improvements are more modest than in scenario B, it should be noted that this difference would only continue to increase over time. In terms of energy penalty, all cases perform similarly as depicted in Figure 6-6b. This reinforces the notion that the RTO does not take the power plant effect into consideration and is in line with the operational scheme design in Chapter 4.

There is a more significant difference in terms of CO_2 emissions (Figure 6-6c) between the four cases whereby the lv-PE emits ~16.74% and ~12.44% less than the PE and TV, respectively, and ~34.52% more than the DR-PE. Accordingly, the lv-PE and DR-PE RTOs are both over-removing while the PE RTO is under-removing CO_2 with respect to the TV case with the true parameters. This is likely the largest dividing factor between the economic profiles in Figure 6-6a. Additionally, Figure 6-6d shows subtle differences with regard to the MEA consumed by the RTO in the four schemes; the TV case uses the least fresh MEA, followed by the PE case, the lv-PE case, then the DR-PE case. While the differences in energy consumption and MEA usage are subtle; they likely contribute to the benefits of the lv-PE observed herein, which occur more gradually than in the large jumps observed in scenario B. Accordingly, the lv estimation scheme is achieving its benefit through the lowered IC rather than the filters as in the previous

scenario. In addition to the plotted results, the average parameter error for the estimated parameters across the three estimation schemes tested are ~32%, ~40%, and ~67% for the lv-PE, DR-PE, and PE schemes, respectively.
On aggregate, the accumulation of these lower steady-state costs is reflected in Figure 6-6a, where the benefit of lv-PE scheme accrues across many RTO periods resulting in more an economical PCC operation. A sample set point transition using the controller/estimator from Chapter 4 with the estimated parameters for one RTO period is shown in Appendix C.

6.3.4. Scenario D: rRTO Under Diurnal Economic Variation and Activity Coefficient Uncertainty

In this scenario, the TOU pricing model in Figure 6-3 was considered to formulate an update strategy for the PCC that considers prices that vary at irregular intervals. Scenario C considers the rRTO update strategy described in Section 6.1. and is assessed across 100 $days$ worth of operation. The cyan vertical dotted lines in Figure 6-3 denote RTO update times; 12-hour periods lengths were chosen as the long and expensive transients observed in Chapter 4 prohibit frequent set point updating, especially in cases where prices vary quickly. The update strategy assumes the RTO is executed at the beginning of the off-peak night operation (19: 00) as shown in Figure 6-3, whereby the RTO can exploit the constant low overnight price. The second update occurs at the beginning of daytime (7: 00), which begins a succession of price changes to mid-peak (denoted m) and on-peak (denoted o) consumption levels. Both strategies are subject to the economic fluctuations ($\boldsymbol{P_t}$) depicted in Figure 6-3 as well as uncertainty in $\boldsymbol{\theta_p}$ (i.e., the thermodynamic activity coefficients as described in Section 6.2.).
Three contrasting RTO schemes were compared. An RTO with knowledge of the true parameter values (labelled tRTO) was implemented and uses a "live" price (i.e., the price at the time at which the RTO is executed). The tRTO is unrealistic since the true parameter values are never known; however, it provides an upper bound for the system's performance. Moreover, a "naïve" update strategy (labelled nRTO henceforth) was also deployed, which updates the RTO set point based on the live price and updates the parameters using the two-step approach without making use of the lv estimation formulation (this is equivalent to Chapter 4 with an added PE layer). Lastly, a robust strategy (labelled rRTO henceforth) updates the set point based on the expectation that the price will vary a few times in the coming 12-hour period and that the uncertain parameters manifest with a uniform distribution. Accordingly, the rRTO formulation in equation (6-1) is deployed with the following weights:

$$\omega_{t,k} = \frac{t_k}{\sum_{k=1}^{n_p} t_k} \times \frac{n_p}{n_r} \tag{6-8}$$

where t_k denotes the operating length associated with each economic scenario $k \in \{1, \dots, n_p\}$ and n_r is the total number of parameter scenarios. The operating times (t_k) weigh the scenarios in the objective function such that prices which are operated at for longer are prioritized; these timings known *a priori* as TOU timings schedules are pre-determined by the Ontario Energy Board (2021). In the daytime period where the costs vary within a short amount of time, this formulation is deployed such that a single operating point that is robust to the prices is used rather than using an operating point that is optimal for a short period of time and subsequently suboptimal. To restrict the model size when using the multi-scenario formulation, the uncertain parameters are assumed to manifest at their 95% confidence interval lower ($\boldsymbol{\theta^l_{p,t}}$) and upper ($\boldsymbol{\theta^h_{p,t}}$) bounds as defined in Section 6.1. Respective scenarios used in the formulation,

denoted as l and h, are shown in Table 6-1. These bounds are determined by the lv-PE algorithm using the parameter estimate statistics prior to the execution of the rRTO and are updated at new operating points to accommodate varying levels of uncertainty. Moreover, the uncertain economics are also assumed to manifest at the mid-peak (m) and on-peak (o) prices when performing the daytime set point update, respectively $\boldsymbol{P_t^l = P_t^m}$ and $\boldsymbol{P_t^h = P_t^o}$, as shown in Figure 6-3. Table 6-1 shows the economic scenarios considered in the present rRTO.

The RTO-operated system is simulated for 100 $days$ to generate costs/savings of the deployment of the rRTO with respect to the RTO; these are shown in Table 6-2 for clarity (plots can also be found in Figure C-2, Supplementary Information).

Table 6-1: Realization in uncertain parameters and economic function for rRTO.

Uncertainty	S1	S2	S3	S4	S5	S6	S7	S8	S9	S10	S11	S12	S13	S14	S15	S16
γ_{MEA}	h		h		h		h		l		l		l		l	
γ_{CO_2}	h		h		l		l		l		l		h		h	
γ_{H_2O}	h		l		h		l		l		h		l		h	
ϕ	m	o	m	o	m	o	m	o	m	o	m	o	m	o	m	o

Table 6-2: Cumulative results for Scenario C over the testing period.

Scheme	Period	C_{PCC} ($CAD)	C_{energy}($CAD)	$m_{CO_2}^{emitted}$ (tn)	m_{MEA}^{makeup} (kg)
rRTO	Daytime	8148.80	9056.14	4.48	25.12
	Overnight	7119.14	8286.15	7.95	21.31
nRTO	Daytime	8271.48	9108.18	4.65	23.88
	Overnight	7207.64	8393.87	7.73	21.44
tRTO	Daytime	8076.01	9006.85	4.52	24.05
	Overnight	7117.63	8629.10	7.82	21.40

A summarized in Table 6-2, the rRTO scheme only experiences total of ~0.48% economic performance deterioration with respect to the tRTO case whereas the nRTO deteriorates by ~1.9% over the time observed herein. The former is achieved through a ~1.7% reduction in energy penalty enabled by ~2.2% higher MEA consumption, which results in ~0.75% higher CO_2 emissions when compared to the tRTO. Distinguishing between daytime and overnight periods, the rRTO is found to only experience ~0.9% deterioration in the former and ~0.02% in the latter. When compared to the corresponding ~2.4% and ~1.3% daytime and overnight deteriorations for the nRTO, the benefit of economic robustness becomes apparent. During the daytime period when prices fluctuate, the multi-scenario economic function of the rRTO outperforms that of the nRTO and results in a larger discrepancy between the two schemes.

The economic benefits of using a robust approach are less than those when the parameter update scheme is deployed for flue gas composition as in scenario B. This suggests that the PCC process is less sensitive to the activity coefficient estimates despite them being uncertain in reality. Moreover, this is consistent with the "price of robustness", whereby a robust solution must sacrifice performance of a specific scenario for optimality in the uncertainty region. However,

small improvements can result in significant savings if the process is expensive as with PCC and longer time periods allow for further accretion of economic benefit. Extrapolating to a year's worth of operation (this simulation length would be computationally prohibitive), the rRTO scheme would continue to outperform the nRTO leading to ~5% annual process cost improvement. This would result in total savings of ~2,250 $\$CAD$ over an extrapolated annual PCC cost of a ~45,000 $\$CAD/yr$. As the PCC plant studies herein is a pilot plant, the benefits of would be even more significant in an industrial scale plant where costs are higher.

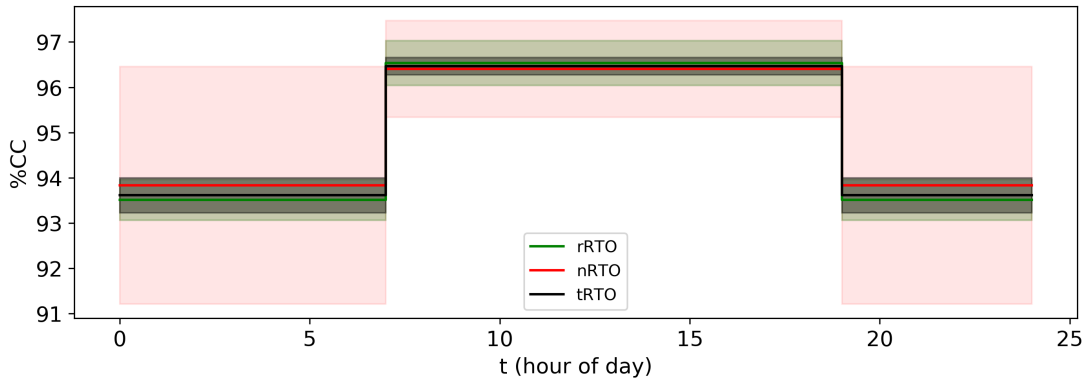

Figure 6-7: %CC set point trajectory statistics over 100-day testing period.

In terms of set point, the $\%CC$ set point is lower in the overnight period as shown in Figure 6-7. This occurs as there is less incentive for carbon removal as reflected in the low overnight SCC and sales rates in Figure 6-3 (bottom). In contrast, the $\%CC$ set point are significantly (~3%) higher during the daytime when the removal incentives are stronger. As the nRTO finds the daytime set point with the live 7: 00 prices, this under-incentivizes the removal during the daytime period where the prices increase owing to the TOU fluctuations. In contrast, the robust formulation in the rRTO takes this variation into account and chooses higher daytime removal set point to account for periods of high carbon prices, hence the higher $\%CC$ set point. Additionally, the nRTO is over-removing CO_2 in the overnight period where removal incentives are not as strong, hence a higher $\%CC$ set point; this is owed to increased error in parameter estimates when using the traditional PE approach when compared to a robust approach like the rRTO.

As the rRTO does not produce parameter estimates, the $\%CC$ is used as a proxy for operational variability. Figure 6-7 shows the statistics of the capture level's diurnal schedule over the testing period, with lines representing means and shaded regions representing standard deviations for each scheme considered in this scenario. As displayed therein, the daytime set points under the rRTO, nRTO, and tRTO are $96.53 \pm 0.50\%$, $96.40 \pm 1.06\%$, and $96.46 \pm 0.19\%$, respectively. Furthermore, the overnight set points under the rRTO, nRTO, and tRTO are $93.51 \pm 0.45\%$, $93.83 \pm 2.62\%$, and $93.61 \pm 0.38\%$, respectively. Accordingly, operation variability (as reflected in the standard deviations) is significantly reduced using the rRTO with respect to the nRTO. In contrast, the nRTO set points experience higher deviation than the rRTO set points despite being subject to the same disturbances and the same lv estimation scheme. As observed in the previous scenarios and in Chapter 4, reduced dynamic operation that results from reduced set point variability can impact operational costs. While the tRTO remains the best-performing scheme in terms of economics and set point variability, the rRTO appears to show only small economic deterioration and set point variability (recall that tRTO is an idealistic scenario as discussed above). The latter is desirable from a controllability standpoint as the

controller is put under less burden while maintaining relatively inexpensive process economics. Finally, the price robustness of the rRTO appears to have an effect under the quickly fluctuating daytime price profiles explored herein, which are typical in the diurnal operation of power plants. Again, the use of the lv-PE layer to provide robustness provides performance benefits with respect to our work in Chapter 4; these are reflected in the improvement rRTO provides over nRTO with respect to cost, resource use, and emissions shown in Table 6-2 and Figure 6-7.

6.4. Summary

This work presents the first estimation scheme for the RTO of PCC systems under uncertainty. This is achieved through the flue gas composition and activity coefficients; however, the scheme is stated generically such that it can be applied to uncertainties that are identifiable given the measurements available. Additionally, the lv-PE approach is deployed, which is designed to abate the propagation of measurement noise to parameter estimates. lv-PE finds the best subset of measurements for each estimation task and filters high-error estimates, resulting in better estimation accuracy and precision over time. This is also the first noise-abatement data processing scheme deployed in the literature for PCC. The performance of the proposed schemes is assessed in terms of the steady-state economic and environmental outcomes. Furthermore, a robust RTO along with an update strategy for the diurnal operation of PCC systems are proposed to be used jointly with the lv-PE scheme, which serves to quantify the parametric uncertainty.
The findings herein indicate that the lv-PE schemes are more successful in their estimation with respect to the traditional DR scheme and approach the true economic optima with an $\sim 8\%$ loss compared to a known parameter case; this is contrasted with $\sim 34\%$ loss for the DR scheme. Moreover, the emissions and solvent consumption of the lv estimation scheme was also found to be consistently lower than the DR/estimation scheme. The results indicate that, while estimation scheme with DR can work well, the use of lv-PE can significantly improve the system performance. Furthermore, the RTO with lv-PE can come very close to the theoretical limit (i.e., RTO with true parameter knowledge), thus resulting in nearly optimal performance observed in previous studies where uncertainties were left unaddressed. Over the period tested, the present study also found that the use of the rRTO updating strategy for periods of high price fluctuations can result in cost savings of about $\sim 1.4\%$ and up to $\sim 80\%$ set point variability reduction over the two-step approach. All case studies observe economic improvements of real-time decision-making on long timescales. With respect to our previous work (Patrón and Ricardez-Ssndoval, 2022a), the results herein indicate that a simple PE layer is insufficient to consistently provide high-quality operating points in noisy environments with fluctuating economics; this is seen through consistent improvements in cost, environmental performance, and resource use. Accordingly, the proposed schemes impart the necessary robustness to deal with these realistic scenarios.

7. Partial Modifier Adaptation

In this work, we propose an MA variant for frequently disturbed periodic systems. Instead of adapting the MA problem with respect to all process inputs modifiers, the subset of modifiers is chosen that have the largest economic effects on the operating point. The proposed approach is shown to be a special case of dMA where the modified directions are limited to only include single inputs. While past approaches like dMA have used dimensionality reduction to address plant-model mismatch in many-input systems, we propose that dimensionality reduction can also be used in frequently-disturbed periodic systems, which has not been previously investigated in the context of dMA. The decreased experimental burden enabled by dimensionality reduction enables quicker action in the proposed approach. Moreover, an ancillary optimization problem is also proposed, which uses available plant and gradient information to drive the system to constraint adhering regions between MA iterations. To the authors' knowledge, the work presented in this study is the first dMA scheme to choose modification directions based on both model and plant (as opposed to only model) economics; thus, choosing modification directions based on plant knowledge (i.e., not solely based on model quantities). Moreover, it is the first dMA approach to address the effect of frequent periodic disturbances. This is also the first MA study in which constraint satisfaction during modifier refinement has been addressed through an optimal approach. Algorithms are outlined to integrate the partial modification and constraint satisfaction problems into a joint scheme referred from henceforth as partial modifier adaptation (pMA). The pMA algorithms determine: 1) which inputs to use for adaptation such that perturbation time is reduced, 2) when and by how much to adjust the operating point to ensure constraint satisfaction, 3) the number of directions to modify for a given disturbance frequency. Using the proposed method, the system can approach the economic optimum before the occurrence of a new disturbance while improving constraint satisfaction at each iteration. The proposed scheme is evaluated through two case studies, which investigate the effect of number of modifiers, disturbance period, and filtering on cost optimality and constraint satisfaction.

This work is structured as follows: Section 7.1 reviews the standard MA formulation, implementation procedure, and assumptions in this work; Section 7.2 builds on this formation and provides the pMA formulation, the constraint adjustment formulation, pMA properties, determination of modification directions, and corresponding algorithms; Section 7.3 tests the pMA schemes in a variety of systems; and conclusion are outlined in Section 7.4.

7.1. Modifier Adaptation

The standard steady-state economic optimization problem is formulated as follows:

$$\begin{aligned} &\min_{\boldsymbol{u_t}} \phi_t \\ &\boldsymbol{f}(\boldsymbol{x_t}, \boldsymbol{u_t}, \boldsymbol{d_t}) = 0 \\ &\boldsymbol{g}(\boldsymbol{x_t}, \boldsymbol{u_t}, \boldsymbol{d_t}) \leq 0 \\ &\boldsymbol{u_{lb}} \leq \boldsymbol{u_t} \leq \boldsymbol{u_{ub}} \end{aligned} \tag{7-1}$$

where $\boldsymbol{x_t} \in \mathbb{R}^{n_x}$, $\boldsymbol{u_t} \in \mathbb{R}^{n_u}$, and $\boldsymbol{d_t} \in \mathbb{R}^{n_d}$ denote the model-predicted process states, inputs, and measured/estimated disturbances, respectively, at time t (i.e., the current time at which the solution will be conveyed to the plant). $\phi_t \in \mathbb{R}$ denotes economic objective function (e.g., steady-state cost, energy consumption); in this work we take the convention of minimization, however maximization is equally valid through the requisite reformulations. $\boldsymbol{f}: \mathbb{R}^{n_u} \times \mathbb{R}^{n_d} \to \mathbb{R}^{n_x}$ denotes steady-state process model, which maps the disturbances and inputs to the states (this model must fulfil the

adequacy conditions like a positive definite Lagrangian Hessian matrix as outlined in Marchetti et al. (2009)). $\boldsymbol{u_l} \in \mathbb{R}^{n_u}$ and $\boldsymbol{u_u} \in \mathbb{R}^{n_u}$ denote the lower and upper bounds, respectively, for the process inputs. $\boldsymbol{g}: \mathbb{R}^{n_x} \times \mathbb{R}^{n_u} \times \mathbb{R}^{n_d} \rightarrow \mathbb{R}^{n_g}$ denotes the process inequality constraints (e.g., grade requirements, safety specifications). Formulation (7-1) does not address uncertainty and is susceptible to model inaccuracies as $\boldsymbol{f}$ may not fully match the true plant $\boldsymbol{f_p}$. Accordingly, MA adjusts the inequality constraints as follows:

$$\boldsymbol{g_{MA,t}} \coloneqq \boldsymbol{g}(\boldsymbol{u_t}, \boldsymbol{d_t}) + \boldsymbol{\varepsilon_{g,t}} + \boldsymbol{\mu_{g,t}^T}(\boldsymbol{u_t} - \boldsymbol{u_{t-1}}) \tag{7-2}$$

where $\boldsymbol{\varepsilon_{g,t}} \in \mathbb{R}^{n_g}$ are 0th order modifiers (i.e., bias terms) and $\boldsymbol{\mu_{g,t}} \in \mathbb{R}^{n_u \times n_g}$ are 1st order modifiers (i.e., gradient correction terms). Moreover, $\boldsymbol{u_{t-1}} \in \mathbb{R}^{n_u}$ denotes the inputs from the previous MA execution with which the plant is operating prior to solving the updated MA problem. The 1st order modifiers, as will be explained later in this section, capture the difference between plant and model gradients (i.e., gradient error); hence the use of an input difference in equation (7-2). Additionally, MA modifies the objective function as follows:

$$\phi_{MA,t} \coloneqq \phi_t + \boldsymbol{\mu_{\phi,t}^T u_t} \tag{7-3}$$

where $\boldsymbol{\mu_{\phi,t}} \in \mathbb{R}^{n_u}$ are 1st order modifiers. Note that the objective function is only adapted in the constraint gradients with respect to the decision variables (as opposed to the difference between the inputs and previous inputs). This occurs as objective bias terms ($\boldsymbol{\varepsilon_{\phi,t}}$) and modifiers with respect to prior inputs ($\boldsymbol{\mu_{\phi,t}^T u_{t-1}}$) would be constant terms, thus would not contribute to the objective function as they would contribute to the feasible region via the constraints in equation (7-2) (Marchetti et al., 2016).

Plant quantities are denoted with subscript p while model quantities are denoted with the subscript m. The 0th order modifiers are the difference between the plant and model constraint predictions at the pre-update operating point defined by the previous MA iteration, defined as follows:

$$\boldsymbol{\varepsilon_{g,t}} = \boldsymbol{g_{p,t-1}} - \boldsymbol{g_{m,t-1}} \tag{7-4}$$

where $\boldsymbol{g_{p,t-1}} \in \mathbb{R}^{n_g}$ and $\boldsymbol{g_{m,t-1}} \in \mathbb{R}^{n_g}$ denote the plant and model constraints under the inputs ($\boldsymbol{u_{t-1}}$) from the previous MA execution. Similarly, the 1st order modifiers are the difference between plant and model gradient predictions at the current time, i.e.,

$$\boldsymbol{\mu_{g,t}} = \boldsymbol{J_{g_p(u_{t-1})}} - \boldsymbol{J_{g_m(u_{t-1})}} \tag{7-5}$$

$$\boldsymbol{\mu_{\phi,t}} = \nabla_{\boldsymbol{u_{t-1}}} \phi_p - \nabla_{\boldsymbol{u_{t-1}}} \phi_m \tag{7-6}$$

where $\nabla_{\boldsymbol{u_{t-1}}}$ denotes the gradient operator applied to scalar-valued plant and model economic functions (ϕ_p and ϕ_m, respectively) at the operating point corresponding to $\boldsymbol{u_{t-1}}$. $\boldsymbol{J_{g_p(u_{t-1})}} \in \mathbb{R}^{n_g \times n_u}$ and $\boldsymbol{J_{g_m(u_{t-1})}} \in \mathbb{R}^{n_g \times n_u}$ denote, respectively, the Jacobian matrices of the plant and model constraints with respect to the inputs at $\boldsymbol{u_{t-1}}$. The modifiers in equations (7-5) and (7-6) are calculated by perturbing the inputs around the operating point (i.e., corresponding to $\boldsymbol{u_{t-1}}$) and using a gradient estimation method. For this study, finite difference approximation (FDA) is used as it has

been found to perform adequately in past studies (Marchetti et al., 2016); however, other techniques exist, which have been previously compared in the literature (Mansour and Ellis, 2003). Accordingly, the gradients from FDA, which populate the Jacobian and gradients in equations (7-5) and (7-6) are defined as follows:

$$\frac{\partial g_i}{\partial u_j} = \frac{g_{i,j,pert} - g_{i,nom}}{\delta u_j} \qquad \forall i \in \{1, \dots, n_g\}, \quad \forall j \in \{1, \dots, n_u\} \qquad (7\text{-}7)$$

$$\frac{\partial \phi}{\partial u_j} = \frac{\phi_{j,pert} - \phi_{nom}}{\delta u_j} \qquad \forall j \in \{1, \dots, n_u\} \qquad (7\text{-}8)$$

where δu_j denotes a small change (i.e., a perturbation) in the j^{th} input u_j. Note that the subscript $pert$ and nom refer to the perturbed (i.e., post-perturbation) and nominal (i.e., pre-perturbation) quantifies, respectively.

Furthermore, modifiers are also passed through first-order filters to abate the effect of measurement noise and ensure a smooth convergence to the true plant optimum; this also prevent sudden operating point changes that may be impractical from an instrumentation perspective (i.e., overly aggressive control actions). The filters are defined as follows:

$$\boldsymbol{\varepsilon}^{\boldsymbol{f}}_{\boldsymbol{g,t}} = (\boldsymbol{I}_{\boldsymbol{n_g}} - \boldsymbol{\lambda}_{\boldsymbol{\varepsilon}})\boldsymbol{\varepsilon}^{\boldsymbol{e}}_{\boldsymbol{g,t}} - \boldsymbol{\lambda}_{\boldsymbol{\varepsilon}}\boldsymbol{\varepsilon}^{\boldsymbol{f}}_{\boldsymbol{g,t-1}} \qquad (7\text{-}9)$$

$$\boldsymbol{\mu}^{\boldsymbol{f}}_{\boldsymbol{g,t}} = \left(\mathbf{1}_{n_g \times n_u} - \boldsymbol{\lambda}_{\boldsymbol{g}}\right) \odot \boldsymbol{\mu}^{\boldsymbol{e}}_{\boldsymbol{g,t}} - \boldsymbol{\lambda}_{\boldsymbol{g}} \odot \boldsymbol{\mu}^{\boldsymbol{f}}_{\boldsymbol{g,t-1}} \qquad \forall j \in \{1, \dots, n_u\} \qquad (7\text{-}10)$$

$$\boldsymbol{\mu}^{\boldsymbol{f}}_{\boldsymbol{\phi,t}} = (\boldsymbol{I}_{\boldsymbol{n_\phi}} - \boldsymbol{\lambda}_{\boldsymbol{\phi}})\boldsymbol{\mu}^{\boldsymbol{e}}_{\boldsymbol{\phi,t}} - \boldsymbol{\lambda}_{\boldsymbol{\phi}}\boldsymbol{\mu}^{\boldsymbol{f}}_{\boldsymbol{\phi,t-1}} \qquad (7\text{-}11)$$

where $\boldsymbol{\lambda}_{\boldsymbol{\varepsilon}} \in \mathbb{R}^{n_g \times n_g}$ and $\boldsymbol{\lambda}_{\boldsymbol{\phi}} \in \mathbb{R}^{n_u \times n_u}$ are diagonal weighting matrices, which act on their respective modifers via matrix multiplication. The e and f superscripts denote estimated (via FDA) and filtered modifiers, respectively. Moreover, $\boldsymbol{\lambda}_{\boldsymbol{g}} \in \mathbb{R}^{n_g \times n_u}$ is a nonzero weighting matrix and $\mathbf{1}_{n_g \times n_u} \in \mathbb{R}^{n_g \times n_u}$ is a matrix of ones; these act on its modifiers via the element-wise multiplication $\odot$. The elements of the filter matrices $\lambda \in [0,1)$ are user-defined tunable parameters that determines the rate of convergence of the MA scheme.

Figure 7-1 illustrates the standard MA procedure whereby the filtered modifiers are initialized at zero, n_u perturbations occur, modifiers are calculated and filtered, the operating point is updated, and iterative refinement of the modifiers occurs.

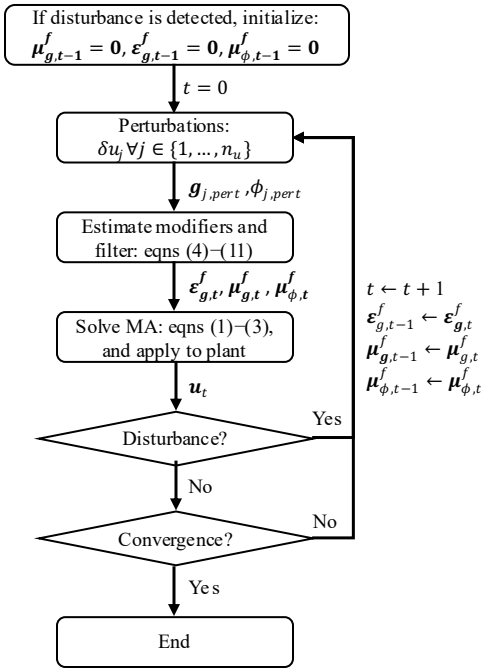

Figure 7-1: Depiction of the standard MA algorithm.

The standard MA procedure as depicted in Figure 7-1, and all the methods presented hereafter, are subject to the following assumptions for this work:

1. The plant experiences periodic disturbance (i.e., they occur at fixed time intervals).
2. Uncertain model parameters and their distributions are unknown as the plant only contains structural mismatch.
3. Disturbances can be readily detected.

Assumption 1 is applicable to many plants whereby inlet raw material grades are updated on a regular basis. These are treated as disturbances, which vary diurnally, seasonally, or according to upstream production schedules. Examples of periodic disturbances include: energy systems (industrial boilers: Yip and Marlin, 2004), chemical plants (ethylene production: Tian et al, 2013; polyamine production, distillation: Pan and Lee, 2003), biological systems (nitrification/denitrification: Kornaros et al., 2012), and agricultural systems (greenhouse: Pawlowski et al., 2011). Assumption 2 is generally the case in models that are not mechanistic whereby simplifying assumptions are made for the model to be solvable. A process operator may deliberately choose to omit phenomena from a process model to make it more parsimonious or the modeler may have formulated a mismatched model as complex analytical expressions can cause problems in optimization programs. In any case, most models have some degree of structural mismatch. Assumption 3 assumes that disturbance/steady-state detection is readily available; this means that the operating mode (i.e., transient or steady) can be ascertained at any given time. While this is a non-trivial problem, it is outside the scope of the current study. Examples of disturbance/steady-state detection use test statistics (Cao and Rhinehart, 1995), Monte Carlo sampling (Hou et al., 2016) and Wavelet transforms (Jiang et al., 2003).

7.2. Partial Modifier Adaptation

A new variant on the standard MA scheme outlined in Section 7.1 is proposed whereby only some input modifiers are continually refined; thus, achieving quicker action in the presence of frequent periodic disturbances. This scheme is denoted as partial modifier adaptation (pMA) and is depicted in Figure 7-2.

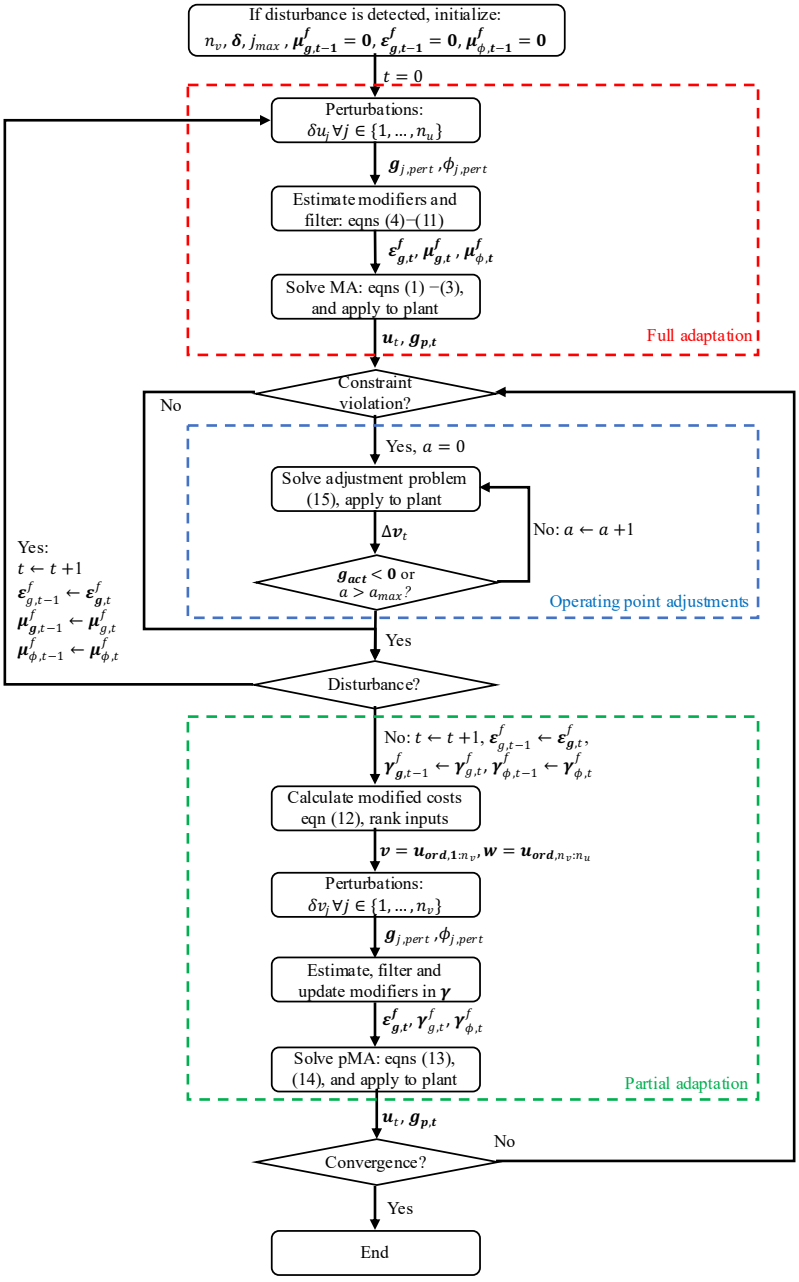

Figure 7-2: Depiction of the pMA algorithm.

7.2.1. pMA Formulations and Algorithm

As shown in Figure 7-2, there are three distinct operations that can occur within the proposed algorithm. Prior to the first pMA iteration, initialization occurs whereby the filtered modifier values are defined as zero and the number of gradient modifiers n_v is chosen; the choice of this term is discussed in section 7.2.3. Furthermore, we introduce $\boldsymbol{\alpha}$ and a_{max}, which are defined for the operating point adjustment at the outset; these are discussed in depth later. For $t = 0$ the MA procedure proceeds as usual through the full MA (i.e., red block in Figure 7-2); n_u perturbations are made and the corresponding modifiers $\boldsymbol{\varepsilon}^{\boldsymbol{f}}_{\boldsymbol{g,t}}$, $\boldsymbol{\mu}^{\boldsymbol{f}}_{\boldsymbol{g,t}}$, and $\boldsymbol{\mu}^{\boldsymbol{f}}_{\boldsymbol{\phi,t}}$ are computed as depicted in Figure 7-2.

After every operating point update, the new operating point is checked for constraint violations. If violations are detected, the algorithm proceeds through the operating point adjustment (blue block in Figure 7-2), which is discussed later. If no violations are present, the system is checked for any new disturbances; a new disturbance would trigger the full adaptation procedure as depicted in Figure 7-2, otherwise the partial adaptation scheme is engaged as depicted in the green block in Figure 7-2.

Assuming no disturbances and no constraint violations, the partial adaptation can begin after the initial iteration (i.e., $t > 0$). The modifiers corresponding to $n_v \in \{\mathbb{Z}^+ : n_v < n_u\}$ inputs are iteratively refined; these are chosen based on their impact on the economic predictions of the MA problem such that the inputs with the largest effect are chosen. This leverages the fact that not all inputs have the same effect on optimality and choosing the appropriate inputs will yield a sufficiently good operating point without taking as much perturbation time. To evaluate the impact of individual input modifiers on economic predictions, the "modified costs" are introduced herein to choose which n_v inputs modifiers should be used. Since all modifiers are calculated in the first full MA iteration, they can be used to make process predictions at the current operating point; accordingly, the modified costs are defined as follows:

$$\hat{\phi}_{j,t} \coloneqq \mu_{\phi,t,j} u_{t,j} \qquad \forall j \in \{1, \dots, n_u\} \qquad (7\text{-}12)$$

where the modified costs are sorted into the ordered set (i.e., sequence) $U = \{\hat{\phi}_{j,t}\}_{j=0}^{n_u}$ and $\boldsymbol{u_{ord}} \in \mathbb{R}^{n_u}$ is the corresponding vector of inputs sorted by modified cost. The modified cost in equation (7-12) is used to rank possible single-input modifications using the most recently available modifiers. Accordingly, the pMA scheme uses both plant and model information to choose the inputs with respect to which the cost gradient has the largest gradient error (i.e., the largest modifiers). This modifier is then multiplied by the most recent input value to normalize gradient with respect to the input magnitude. Accordingly, the inputs that are chosen by equation (7-12) are those that will lead to the largest corrections in the cost gradient. The modified cost of each input will be different owing to their distinct values and gradients. However, a situation may arise in which the difference is relatively small. Even if the small difference is owed to numerical or process noise, both inputs in question will have similar effects on plant-model mismatch so the choice of either input will have similar adaptation effects on the system.

With the minimization convention, the first n_v elements of $\boldsymbol{u_{ord}}$ are stored in the vector $\left(\boldsymbol{v} = \boldsymbol{u_{ord,1:n_M}}\right) \in \mathbb{R}^{n_v}$ as these inputs yield the lowest modified costs; these correspond to the set of modified costs $V = \{U : j \leq n_v\}$. Moreover, the remaining $n_u - n_v$ elements of $\boldsymbol{u_{ord}}$ are stored in the vector $\left(\boldsymbol{w} = \boldsymbol{u_{ord,n_M:n_u}}\right) \in \mathbb{R}^{(n_u - n_v)}$; these correspond to the set of modified costs $W = \{U : j > n_v\}$. In other words, the input variable vector is decomposed into two

subvectors. $\boldsymbol{u} = [\boldsymbol{v} \quad \boldsymbol{w}]^T$ and the sequence of modified costs is such that $U = V \cup W$. The inputs in $\boldsymbol{v}$ are those whose modifiers lead to the best predicted economics (i.e., the least predicted costs); thus, only the modifiers corresponding to $\boldsymbol{v}$ are adapted with respect to in the next partial MA execution. Thus, the partial adaptation objective function becomes:

$$\phi_{pMA,t} \coloneqq \phi_t + \boldsymbol{\gamma}_{\boldsymbol{\phi},t}^T \boldsymbol{v}_t + \boldsymbol{\omega}_{\boldsymbol{\phi},t}^T \boldsymbol{w}_t \tag{7-13}$$

where $\boldsymbol{\gamma}_{\boldsymbol{\phi},t} \in \mathbb{R}^{n_v}$ and $\boldsymbol{\omega}_{\boldsymbol{\phi},t} \in \mathbb{R}^{(n_u - n_v)}$ are the 1st order objective function modifiers corresponding to $\boldsymbol{v}$ and $\boldsymbol{w}$, respectively. Accordingly, like the input vector, the vector of objective function modifiers is decomposed into two subvectors $\boldsymbol{\mu}_\phi = [\boldsymbol{\gamma}_\phi \quad \boldsymbol{\omega}_\phi]^T$.

Likewise, the adapted constraints become:

$$\boldsymbol{g}_{\boldsymbol{pMA},\boldsymbol{t}} \coloneqq \boldsymbol{g}(\boldsymbol{u}_t, \boldsymbol{d}_t) + \boldsymbol{\varepsilon}_{g,t} + \boldsymbol{\gamma}_{g,t}^T (\boldsymbol{v}_t - \boldsymbol{v}_{t-1}) + \boldsymbol{\omega}_{g,t}^T (\boldsymbol{w}_t - \boldsymbol{w}_{t-1}) \tag{7-14}$$

where $\boldsymbol{\gamma}_{g,t} \in \mathbb{R}^{n_v \times n_g}$ and $\boldsymbol{\omega}_{g,t} \in \mathbb{R}^{(n_u - n_v) \times n_g}$ are the 1st order constraint modifiers corresponding to $\boldsymbol{v}$ and $\boldsymbol{w}$, respectively. Accordingly, like the input vector, the matrix of gradient modifiers is decomposed into two block matrices, i.e., $\boldsymbol{\mu}_g = [\boldsymbol{\gamma}_g \quad \boldsymbol{\omega}_g]^T$.

At each partial adaptation iteration, the members of V and W **(**and their corresponding vectors $\boldsymbol{v}$ and $\boldsymbol{w}$**)** are refined according to the ranked modified cost sequence in equation (7-12) as described above. This sequence is updated using the newly updated economic function gradient modifiers ($\boldsymbol{\gamma}_\phi$) along with the outdated modifiers ($\boldsymbol{\omega}_\phi$). This allows for iterative refinement of the inputs that have the largest effect on economic function adaptation until convergence to their final modifiers and final membership of V and W. This process of refinement is depicted in the "rank inputs" block of Figure 7-2. We note that, the ability to change modification directions through V and the modified cost is present in pMA but not the standard dMA (Costello et al., 2016); the latter can yield myopic behaviour owed to its directional inflexibility.

If a disturbance is detected after any partial adaptation iteration, the previous members of V and W are no longer valid as the operating point has changed and the gradients may be different in the new operating neighbourhood. This triggers the disturbance block in Figure 7-2 that toggles between the full and partial adaptation schemes. The toggling of schemes allows for a full set of modifiers $\boldsymbol{\mu}_\phi$ and $\boldsymbol{\mu}_g$ to be computed such that an entirely new U and its corresponding $\boldsymbol{u}_{\boldsymbol{ord}}$ can be found at the new operating point.

As only plant economics are considered in the input ranking equation (7-12), constraint satisfaction is unaddressed at each partial adaptation iteration. Furthermore, constraint satisfaction upon convergence is not guaranteed when using partial modification (i.e., no KKT matching). Even with consideration of the Lagrangian as in directional MA (Costello et al., 2016), iteration satisfaction is not guaranteed. Indeed, full MA schemes (i.e., not only pMA) only ensure constraint satisfaction at convergence; hence, the "path" to the optimum may be subject to iterations where violations occur (Marchetti, 2022). Thus, recourse action is needed to avoid constraint violations at pMA iterations and upon convergence where these violations could lead to safety or economic concerns (e.g., violation of temperature

limits or production below purity specification). In systems with frequent disturbances, it is advantageous to satisfy constraints along the path as convergence to a final steady state may never be achieved.

To minimize these iterative constraint violations, operating point "adjustments" ancillary problems are proposed to be solved after every adaptation iteration where constraint violations are detected. These are depicted in the blue block of Figure 7-2. The adjustment problems use process measurements and the plant gradient data available from the partial adaptation perturbations to formulate of a quadratic problem (QP) that reduces or altogether closes the constraint violation gap.

The partial adaptation section of the algorithm features adjustments occurring after the solution is applied to the plant. As shown in Figure 7-2, these adjustments only occur if a constraint violation is detected. Once this occurs, the following problem is solved:

$$
\begin{aligned}
&\min_{\Delta \boldsymbol{v}} \|\widehat{\boldsymbol{g}}_{\boldsymbol{act}}\|_{\boldsymbol{QA}}{}^2 \\
&\widehat{\boldsymbol{g}} = \boldsymbol{g_p} + \boldsymbol{J}_{\boldsymbol{g}(\boldsymbol{v_{t-1}})} \Delta \boldsymbol{v} \\
&\widehat{\boldsymbol{g}}_{\boldsymbol{act}} = \boldsymbol{A}\widehat{\boldsymbol{g}} \\
&\widehat{\boldsymbol{g}}_{\boldsymbol{in}} = (\boldsymbol{I}_{n_g} - \boldsymbol{A})\widehat{\boldsymbol{g}} \\
&\widehat{\boldsymbol{g}}_{\boldsymbol{in}} \leq \boldsymbol{0} \\
&\boldsymbol{Q} = diag(g_{p,1} \quad \cdots \quad g_{p,n_g}) \\
&\boldsymbol{A} = diag(a_1 \quad \cdots \quad a_{n_g}) : a_i = \begin{cases} 1 & g_{p,i} > 0 \\ 0 & g_{p,i} \leq 0 \end{cases} \\
&-\boldsymbol{\alpha} \leq \Delta \boldsymbol{v} \leq \boldsymbol{\alpha}
\end{aligned}
\tag{7-15}
$$

where $\widehat{\boldsymbol{g}}$ and $\boldsymbol{g_p} \in \mathbb{R}^{n_g}$ are the linear model-predicted and current (measured) plant operating point for all constraints. $\boldsymbol{J}_{\boldsymbol{g}(\boldsymbol{v_{t-1}})} \in \mathbb{R}^{n_g \times n_v}$ is the Jacobian of the constraints with respect to the subset of process inputs used in the partial adaptation step; this is constructed using the most recent partial plant perturbation results. Using the most recently calculated plant Jacobian, a local approximation of the constraint-input relationship is generated such that small input adjustments can be computed. This differs from a constraint adaptation scheme (e.g., Chachuat et al., 2009) since it uses a linear model with a satisfaction objective as opposed to a nonlinear model with an economic objective; moreover, the adjustment step is used to compliment the pMA problem defined above, which acts on an economic basis. The model-predicted constraint vector is partitioned into active and inactive constraints using the matrix $\boldsymbol{A} \in \mathbb{R}^{n_g \times n_g}$ and its identity matrix difference $\boldsymbol{I} - \boldsymbol{A}$ where $\boldsymbol{I}_{n_g} \in \mathbb{R}^{n_g \times n_g}$. $\boldsymbol{A}$ contains diagonal identity elements to indicate if the plant constraint $g_{p,i} \forall i \in \{1, \dots, n_g\}$ has been violated. Using the $\boldsymbol{A}$ matrix, the inactive constraint entries are set to zero in the vector $\widehat{\boldsymbol{g}}_{\boldsymbol{act}} \in \mathbb{R}^{n_g}$; conversely, the active constraint entries are set to zero in the vector $\widehat{\boldsymbol{g}}_{\boldsymbol{in}} \in \mathbb{R}^{n_g}$. Using the inactive constraint predictions $\widehat{\boldsymbol{g}}_{\boldsymbol{in}}$, the linearized model can be used such that they remain inactive using the inequality constraint in formulation (7-15). Moreover, the objective function in (7-15) features a minimization term for the active constraints $\widehat{\boldsymbol{g}}_{\boldsymbol{act}}$ whereby their predicted value is minimized; this serves to bring their value to zero as constraints in MA are posed such that the RHS is zero. This objective is weighted by a diagonal matrix of the constraint violation magnitudes for the active constraints $\boldsymbol{QA} \in \mathbb{R}^{n_g \times n_g}$; this way larger violations are prioritized over smaller violations. The decision variable for this problem is the vector of process inputs adjustments $\Delta \boldsymbol{v} \in \mathbb{R}^{n_v}$, which are bounded by the user-specified $\boldsymbol{\alpha} \in \mathbb{R}^{n_v}$ mentioned in the initialization section above. The adjustment bounds are designed to be small through the choice of $\boldsymbol{\alpha}$, thus requiring little computational or transient time. Also required in

initialization are the maximum number of constraint adjustments a_{max}; this is imposed on the scheme such that there is little delay in returning to the partial adaptation loop. Accordingly, $\boldsymbol{\alpha}$ and a_{max} are user defined but should be small (i.e., since they are assumed to be adjustments and not large changes). We note that the disturbance block is checked at every iteration of the pMA algorithm as shown in Figure 7-2. Whether or not a constraint violation is detected, disturbances must be checked to accommodate for their potential effect of suddenly changing the memberships in V and W. The timeliness of this check is ensured by capping the number of adjustment iterations at a_{max}.

While the operating point adjustment problem (7-15) focuses solely on constraint attenuation, the main pMA objective in equations (7-13) and (7-14) is still to minimize plant-model mismatch through its modifiers. The reason for the additional adjustments is to decrease potential constraint violations in the modifier refinement process whereby the plant-model mismatch is not accounted for to its full possible extent within the pMA paradigm. Through the adjustment subproblem (7-15), constraint-violating operating points may be abated quickly. Firstly, the measurement of $\boldsymbol{g_p}$ serves to localize problem (7-15) in the current constraint-space of the plant. This measurement is updated at every adjustment problem iteration such that the local linear prediction of constraints $\hat{\boldsymbol{g}}$ begins at the correct state. Additionally, only the inputs contained within $\boldsymbol{v}$ are used for the constraint adjustment step as only the local plant gradients for these inputs are updated as part of the pMA algorithm. Despite no guarantee being available for whether violation will be avoided (this would require controllability of all states via all inputs); problem (7-15) uses readily available information via $\boldsymbol{g_p}$ and $\boldsymbol{J_{g(v_{t-1})}}$ as opposed to other constraint-feasibility approaches that require additional data be estimated from the system (e.g., Hessian matrices). Note that problem (7-15) constitutes a discrete time one-step-ahead linear-quadratic regulator whereby no control-move suppression terms are used, and the state matrix is an identity matrix. In principle, such a linear quadratic regulator is solvable for an explicit feedback law using the dynamic Ricatti equation; however, the inactivity constraints prohibit this for the system shown in equation (7-15).

The pMA algorithm is summarized as follows:

pMA operation:	
	Initialize: define n_v, $\boldsymbol{\alpha}$, a_{max}, $\boldsymbol{\mu^f_{g,t-1}} = \mathbf{0}$, $\boldsymbol{\varepsilon^f_{g,t-1}} = \mathbf{0}$, $\boldsymbol{\mu^f_{\phi,t-1}} = \mathbf{0}$.
1.	For $t = 0$: perform full MA and apply to plant.
2.	Are constraints being violated?
a.	Yes: $a = 0$, activate constraint adjustment, go to step 3.
b.	No: proceed to step 5.
	Operating point adjustments
3.	Solve problem (15) and apply to plant.
4.	$\boldsymbol{g_{viol}} < \mathbf{0}$ or $a > a_{max}$?
a.	Yes: Proceed to step 5.
b.	No: $a \mathrel{+}= 1$, return to step 3.
5.	New disturbance?
a.	Yes: $t \mathrel{+}= 1$, activate full MA, go to step 6.

b.	No: $t+=1$, activate partial adaptation, go to step 9.
	Full adaptation
6.	Perturb n_u inputs.
7.	Estimate n_u modifiers and filter.
8.	Solve full MA problem using equations (2) and (3). Return to step 2.
	Partial adaptation
9.	Perturb n_v inputs.
10.	Estimate n_v modifiers and filter.
11.	Re-evaluate "modified costs" in equation (12) and refine modifiers in $\boldsymbol{v}$.
12.	Solve partial adaptation using equations (13) and (14).
13.	Has the scheme converged to an operating point
a.	Yes: end.
b.	No: continue refining modifiers and return to step 2.

The benefit to the proposed pMA approach is twofold: firstly, using $n_v < n_u$ input modifiers result in a faster acting scheme that prioritizes economic modification; secondly, the adjustment step will enable iterates to be constraint abiding without any additional information (e.g., Hessian matrix). On the other hand, the adjustment step in the proposed pMA scheme is designed to act quickly and only take small steps. Accordingly, the system may not be able to close the constraint gap if the adjustment step begins far from the constraint as the number of adjustment iterations is limited in quantity and size. Crucially, the selection of n_v is not a trivial and an algorithm that leverages disturbance periodicity to determine the number of modification directions is presented in Section 7.2.3.

We note that pMA is not mutually exclusive other approaches in the literature; indeed, the modified cost metric introduced in this work can be used similarly to the sensitivity matrix in dMA to compute privileged directions (i.e., not limited to partial derivatives). Moreover, the dual methods and the use transient measurements introduced by Costello et al. (2016) and François and Bonvin (2014), respectively, can also be incorporated into the pMA scheme proposed in this work.

7.2.2. pMA Properties

The vector $\boldsymbol{v_t}$ of inputs used in the pMA approach can alternatively be represented by the block matrix $\boldsymbol{V_t} \in \mathbb{R}^{n_u \times n_v}$, i.e.:

$$\boldsymbol{V_t} = \begin{bmatrix} diag(u_1, \dots, u_{n_v}) \\ \mathbf{0}_{(n_u - n_v) \times n_v} \end{bmatrix} \tag{7-16}$$

where $\mathbf{0}_{(n_u - n_v) \times n_v} \in \mathbb{R}^{(n_u - n_v) \times n_v}$ denotes a zero matrix. Similarly, dMA defines its directions using the block matrix $\boldsymbol{U_t} \in \mathbb{R}^{n_u \times n_v}$, i.e.:

$$\boldsymbol{U_t} = [\boldsymbol{\delta u}_1 \quad \cdots \quad \boldsymbol{\delta u}_{n_v}] \tag{7-17}$$

where ($\boldsymbol{\delta u}_j \in \mathbb{R}^{n_u}$) $\forall j \in \{1, \dots, n_v\}$ are the vectors containing input directions whereby a subset of the inputs elements is chosen for each direction. From equations (7-16) and (7-17), it is evident that $\boldsymbol{V_t}$ is a special case of $\boldsymbol{U_t}$ whereby only the diagonal elements in the top block are used. This represents an analogue to multivariable calculus whereby partial derivatives represent a special case of directional derivatives. Since pMA implies a special case of dMA, some properties of the latter can be applied to pMA.

Theorem 1: (Plant optimality for chosen input adaptations). Consider the pMA algorithm without measurement noise and perfect estimation of plant derivatives in n_v inputs. If the algorithm converges to the fixed point ($\boldsymbol{u}_\infty, \boldsymbol{\varepsilon}_{\boldsymbol{g},\infty}, \boldsymbol{\gamma}_{\boldsymbol{g},\infty}, \boldsymbol{\gamma}_{\boldsymbol{\phi},\infty}$), this corresponds to a KKT point of the modified optimization problem in equations (7-13) and (7-14), then $\boldsymbol{u}_\infty$ will be optimal for the plant in these n_v directions.

Proof: See Costello et al. (2018), Theorem 3.1. ■

An advantage of pMA is that inputs are chosen based on readily available plant data whereby the information necessary to compute the modified costs is found as part of the pMA algorithm during the perturbation step. Instead of using model sensitivities with respect to uncertain parameters to determine $\boldsymbol{U_t}$, the modified cost metric in equation (7-12) uses the cost gradient modifiers (i.e., the plant-model cost gradient error) to determine the inputs to which the cost is most sensitive (i.e., $\boldsymbol{V_t}$). These modifiers are multiplied by the latest-acquired input values to normalize their magnitude; thus, pMA chooses the directions of highest normalized input error. Note that Costello et al. (2016) normalize the sensitivity matrix with uncertain parameter ranges; however, this does not abide by assumption 2 (Section 7.1). Moreover, the approach presented offers benefits with respect to the active approach proposed by Singhal et al. (2018); namely, it does not rely on parameter uncertainty being present or access to a probability density as stated in assumption 2 (Section 7.1). With the approach presented in this work, we only consider the cost gradient sensitivities, which are equivalent to the Lagrangian gradient in the case of no active constraints. Only cost sensitivities are considered (as opposed to Lagrangian sensitivities) because the plant Lagrange multipliers cannot be readily measured.

7.2.3. Disturbance Periodicity and the Number of Modification Directions

The aforementioned weaknesses in the standard MA scheme can be seen most saliently in equations (7-7) and (7-8), which depend on the index $\forall j \in \{1, \dots, n_u\}$ and correspond to the perturbation block in Figure 7-1. As previously noted, these perturbations delay the operating point updates as they may be time-consuming. To analyze the refinement time that the MA scheme requires, we introduce a user-defined perturbation time τ (i.e., the required to perform a single perturbation), a system-defined settling time T (i.e., the time required to reach a new operating point upon modifier refinement), and an externally defined disturbance period ΔT (i.e., the time between subsequent disturbances). The use of different τ and T reflects the fact that small perturbations (of τ duration) may not require the same settling time as an operating point change (of T duration). This occurs as perturbations are meant to be small (i.e., a fraction of an input's value) while operating point changes are potentially large (i.e., a completely different set of input values). Accordingly, if n_u, τ, or T are large, the MA refinement procedure will be time-consuming. Furthermore, if ΔT is small, convergence to the true optimum may not occur before a new disturbance is imposed.

That is, if the MA scheme requires n_{MA} iterations to converge to the optimum, the following inequality must hold if convergence is to occur:

$$n_{MA}n_u\tau + n_{MA}T \leq \Delta T \tag{7-18}$$

However, this inequality may not be fulfilled if n_u and τ are large, or ΔT small as mentioned previously. By treating equation (7-18) as an equality we can express the maximum number of MA iteration necessary to reach convergence as follows:

$$n_{MA} = \frac{\Delta T}{n_u\tau + T} \tag{7-19}$$

This ratio is not practically useful as many of these quantities are not known *a priori*; however, it serves for theoretical discussion of the MA schemes in periodic settings. In contrast to MA equation (7-19), the number of iterations to reach convergence for pMA is defined as follows:

$$n_{pMA} = \frac{\Delta T}{n_v\tau + T} \tag{7-20}$$

since $n_v < n_u$ perturbations are performed on most iterations, a larger number of pMA iterations may be performed (i.e., $n_{pMA} > n_{MA}$). This results in quicker modifier refinement, which is the working principle of pMA. These refinements will work towards the directional optimum given the chosen modification directions; as a full set of modifiers is not refined until convergence, the pMA scheme will not converge to the plant KKT points as noted for dMA (Costello et al., 2016). However, the directional optimum will certainly be better than a "do-nothing" case and convergence to this optimum may occur more quickly (i.e., within a given disturbance period).

Recalling equations (7-19) and (7-20), which quantify the number of MA and pMA iterations that a given scheme must perform to reach convergence, we propose a scheme-independent metric to assess the efficacy of various pMA and MA schemes on a given system. While the number of modified inputs is scheme-dependent and the settling time is not known *a priori*, thus rendering equations (7-19) and (7-20) impractical; they elucidate how the number of iterations of each scheme is dependent on the disturbance period (i.e., $n_{pMA} = f(\Delta T)$). Thus, for a given plant, the best number of inputs modified with respect to can be expressed as piecewise function of the disturbance period:

$$n_v = \begin{cases} 1 & \Delta T \leq \zeta_1 \\ \vdots & \zeta_k < \Delta T \leq \zeta_{k+1} \\ n_u & \Delta T > \zeta_{n_u} \end{cases} \tag{7-21}$$

where n_v is segmented into n_u regimes such that $n_v \in \{1, \dots, n_u\}$ can be determined based on prior operation of the system. $\zeta_j \ \forall j \in \{1, \dots, n_u\}$ are the corresponding disturbance period boundaries that define the how many modifiers j are suitable for refinement. According to equation (7-21), the number of inputs to be modified for (thus perturbed) could be tuned using the disturbance frequency. Determination of the regime boundaries ζ_j can be performed through preliminary system runs, whereby data are collected for various frequencies such that equation (7-21) can be fully defined for a given process; however, this may be impractical. Establishing regimes for n_u also allows for disturbances to be approximately periodic. Put concretely, disturbances that have periods within the same period regime use the same number of modifiers, thus exact periodicity is not needed for pMA to be applicable.

A limitation of dMA is that the number of privileged directions must be pre-specified by the user such that $n_v \leq n_\theta$. With the pMA approach, we leverage the periodicity of the disturbances to determine the number of inputs for adaptation as a function of the disturbance period. The following algorithm enables the systematic determination of n_v for a given disturbance period ΔT under a performance metric PM and a minimization convention:

Determination of n_v for a disturbance period ΔT	
	Initialize: define $n_v = 1$, $l = 1$, $\boldsymbol{\alpha}$, a_{max}, B, $\boldsymbol{\mu}^{f}_{g,t-1} = \mathbf{0}$, $\boldsymbol{\varepsilon}^{f}_{g,t-1} = \mathbf{0}$, $\boldsymbol{\mu}^{f}_{\phi,t-1} = \mathbf{0}$.
1.	Deploy pMA algorithm for n_v modifiers.
2.	B disturbance elapsed?
a.	Yes: Calculate PM for B previous disturbance period, go to step 3.
b.	No: $t \leftarrow t + \Delta t$, go to step 2.
3.	$l > 2$?
a.	Yes: $l \mathrel{+}= 1$, go to step 4.
b.	No: $l \mathrel{+}= 1$, go to step 1.
4.	$PM_l < PM_{l-1}$?
(7-1)	Yes: $n_v \mathrel{+}= 1$, go to step 1.
(7-2)	No: $n_v = l - 1$, end.

The n_v-determination algorithm initial assumes that only one modification direction is being used ($n_v = 1$). The user defines an allowable computational budget B along with all other pMA operational parameters. Once B disturbances have elapsed, R or P_{prod} can be computed for unconstrained and constrained systems, respectively. After the initial B disturbance periods, another input direction is assumed to be available; hence $n_v \mathrel{+}= 1$. This allows for comparison between the previous B and the next B disturbance periods on the basis of a user-defined PM whereby a modification dimension is added until there is no significant improvement in the process cost (assuming a minimization convention). Examples of performance metrics are provided in the next section for constrained and unconstrained MA-operated systems.

7.3. Case Studies

The proposed scheme was tested using two case studies: the Williams-Otto CSTR (Williams and Otto, 1960) and the forced circulation evaporator (Lee et al., 1989). The former case study explored partial adaptation on a two-input system such that the effect of filtering and disturbance period can be isolated and assessed on an entirely economic basis. The latter case study provides a setting in which to test partial adaptation on a three-input system with active constraints such that the effect of number of adapted inputs and constraint satisfaction can be quantified on process economics and throughput, respectively. Moreover, the evaporator also provides a constrained setting in which to assess the proposed pMA against dMA. As stated in the introduction, we aim to improve on the aggregate performance of MA across many disturbances; hence, showing any iteration is not very instructive. Instead, we introduce the following performance metrics (PM), which summarize aggregate process performance over time.

Accordingly, the cumulative process economics $R(\$)$ are calculated as follows:

$$R = \sum_{k=0}^{T_f} \phi_k \tag{7-22}$$

where $T_f(time)$ is the final scenario length and ϕ_k are the instantaneous process economics at time k. Additionally, the time operating at constraint violating points is used as a measure to directly quantify constraint violation. This is defined as follows:

$$t_{viol} = \sum_{\forall k \in \{0,\dots,T_f-1\} | g_k > 0} \Delta t_k \tag{7-23}$$

where Δt_k are the sampling interval lengths; accordingly, the cumulative time at constraint violation over a test scenario is quantified. Furthermore, constraint violations influence the quantity of material processed (i.e., throughput); especially in cases where below-specification product may be produced. The cumulative mass of material process $m\ (mass)$ is defined as follows:

$$m = \sum_{\forall k \in \{0,\dots,T_f\} | g_k \leq 0} m_k \tag{7-24}$$

where m_k is the instantaneous mass throughput at time k and the expression in equation (7-24) sums over constraint-satisfying product. Lastly, the cost per mass rate P_{prod} is defined using equations (7-22) and (7-24) as follows:

$$P_{prod} = \frac{R}{m} \tag{7-25}$$

The production metrics in equations (7-22)–(7-25) are computed *a posteriori* to the scenarios tested for each case study.

7.3.1 Williams-Otto CSTR

The CSTR proposed by Williams and Otto, which is depicted in Figure 5-6 and presented in Section 5.3.2, serves as a benchmark for MA. Its small size and nonlinearity make it a good example to examine price variation as a function of the operating conditions.

The model in equation (5-52)–(5-62) captures the complete species dynamics and represents the Williams-Otto plant. In addition to this plant model, a simplified steady-state model has also been formulated for the Williams-Otto CSTR. The abbreviated model omits species C and uses the follow two-reaction scheme to approximate the system:

$$A + 2B \overset{k_1}{\rightarrow} D + E\colon k_1 = (2.189 \times 10^8) e^{\left(\frac{-8077.6}{T_R}\right)} \tag{7-26}$$

$$A + B + D \overset{k_2}{\rightarrow} G\colon k_2 = (4.310 \times 10^{13}) e^{\left(\frac{-12438}{T_R}\right)} \tag{7-27}$$

where all variables are defined as in Section 5.3.2 and the two-reaction scheme corresponds to the following steady-state material balances:

$$0 = F_A - F_R X_A - k_1 X_A X_B{}^2 W - k_2 X_A X_B X_D W \tag{7-28}$$

$$0 = F_B - F_R X_B - 2k_1 X_A {X_B}^2 W - k_2 X_A X_B X_D W \quad (7\text{-}29)$$

$$0 = -F_R X_D + k_1 X_A {X_B}^2 W - k_2 X_A X_B X_D W \quad (7\text{-}30)$$

$$0 = -F_R X_E + k_1 X_A {X_B}^2 W \quad (7\text{-}31)$$

$$0 = -F_R X_G - 3k_2 X_A X_B X_D W \quad (7\text{-}32)$$

The inputs to the system are $\boldsymbol{u} = [F_B \quad T_R]^T$ and the disturbance is $\boldsymbol{d} = [F_A]$. The nominal input and disturbance values for the system are $\boldsymbol{u_{nom}} = [6.1 \quad 366.15]^T$ and $\boldsymbol{d_{nom}} = [1.8]$. The inputs have the bounds $F_B \in [3,6]$ and $T_R \in [343.15, 373.15]$ and the economic objective is to maximize the profit produced by the product species. This is denoted using the following minimization (note the negative to convert maximization to minimization) objective function:

$$-\phi = F_R(1143.38X_D + 25.92X_E) - 76.23F_A - 114.34F_B \quad (7\text{-}33)$$

The mismatched model in equations (7-28)–(7-32) is deployed using the regular MA and pMA schemes shown in Figure 7-1 and Figure 7-2, respectively. Since only two inputs are available in this system, the pMA will only ever adapt with respect to one of them while the MA will adapt with respect to both. These competing schemes are evaluated on an economic basis using the cumulative profit function shown in equation (7-33) (i.e., $PM = R$). The disturbance variable is changed every period (ΔT) from the distribution $\boldsymbol{d} \sim [\mathcal{U}(0.3,3)]$**.** All necessary 0$^{\text{th}}$ order system information for MA is assumed to be measurable and sampled every $\Delta t = 3\ minutes = 1\ time\ interval$. The perturbation sizes for these inputs are $\boldsymbol{\delta} = 0.001\boldsymbol{u_t}$ (i.e., 0.1% of the current input value) and they are assumed to last $\tau = 50$ time intervals.

Three test scenarios are performed, which feature forty disturbance realizations $\boldsymbol{d_l}\ \forall l \in \{1, \dots, B\}$, $B = 40$, each occurring every ΔT sampling intervals, such that the effect of the scheme can be analyzed over a long period of time and over a wide range of operating conditions.

Scenario 1 has $\Delta T = 250$. The filter matrices in equations (7-9)–(7-11) are assumed to all use an equivalent filter constant λ. This filter constant is varied for each simulation, which features a different random disturbance sequence for each filter run. This allows for the performance of the scheme to be assessed across a wide array of disturbance trajectories.

Scenario 2 sets $\Delta T = 250$ and varies the filter constant (λ). However, this scenario has the same disturbance sequence for all filters runs. This way the efficacy of the scheme with respect to λ can be extricated from the disturbance trajectory. This filter is important in the performance of the scheme as it affects the speed at which the modifiers are updated (and can thus inhibit the speed of pMA).

Scenario 3 has varying disturbance periods (ΔT), a filter constant of $\lambda = 0.01$, and the same disturbance sequence for each run. This extricates the effect of disturbance frequency on the scheme as it is designed to work best for increased frequencies.

Results from Scenario 1 are summarized in Table 7-1, where the pMA outperforms the standard MA scheme for small filter constants based on the total process revenue. Aside from $\lambda = 0.01$, the benefit of the pMA scheme appears to be increasing as the modifiers are filtered less; this suggests that the filters indeed inhibit the speed at which the proposed scheme finds an economically preferable operating point. Furthermore, a break-even point between full MA and pMA occurs between $\lambda = 0.075$ and $\lambda = 0.1$ whereby full MA is best for higher filtering and pMA for lower. This likely occurs as increased filtering inhibits the ability of pMA to act quickly, thus eliminating its advantage over full MA. A conflating factor of this scenario is the random and varying disturbance sequence used for each filter run, which makes the improvement of the proposed scheme a function of the filter and the specific disturbance sequence; to extricate the former from the latter, scenario 2 keeps the same disturbance sequence for all filter runs.

Table 7-1: Results for all scenarios in the Williams-Otto case study. %I denotes the percent improvement (difference) in R of pMA with respect to MA.

Scenario 1				**Scenario 2**				**Scenario 3**			
λ	R (\$) MA	R (\$) pMA	$\%I$	λ	R (\$) MA	R pMA	$\%I$	ΔT	R (\$) MA	R (\$) pMA	$\%I$
0.01	108,988	111,719	2.50	0.01	106,784	129,272	21.06	150	46,555	72,673	56.10
0.025	113,289	128,535	13.46	0.025	113,289	128,535	13.46	200	63,667	92,379	45.10
0.05	127,230	138,401	8.78	0.05	114,611	128,404	12.03	250	106,784	129,272	21.06
0.075	147,091	152,130	3.42	0.075	116,983	123,814	5.84	300	150,076	115,675	−23.26
0.1	198,767	190,434	−4.19	0.1	122,488	117,857	−3.78				

The results from Scenario 2 are shown in Table 7-1, whereby the trend in improvement of the pMA over the standard MA scheme is more clearly appreciable than in Scenario 1 owed to the equivalent disturbance sequence in all filter runs. This is also illustrated in the time domain by Figure 7-3, where the cost trajectories corresponding to the filter runs are displayed. As shown therein, the respective process revenues of pMA and MA diverge as time progresses. This is owed to the accretion of revenue over time and would continue further for longer scenarios. As the filter constant is increased, the revenue dynamics of the two implementations become increasingly similar whereby the pMA and standard MA show more overlap. As in Scenario 1, a break-even point occurs between $\lambda = 0.075$ and $\lambda = 0.1$ whereby the full MA becomes more favourable than the pMA as increased filtering inhibits convergence speed. This scenario illustrates the merit of allowing the pMA to adapt with respect to a single input. As exemplified by better performance for lower filter constants, Scenario 2 verifies the notion also observed in Scenario 1 that the advantage the pMA has over the standard MA is inhibited by aggressive filtering.

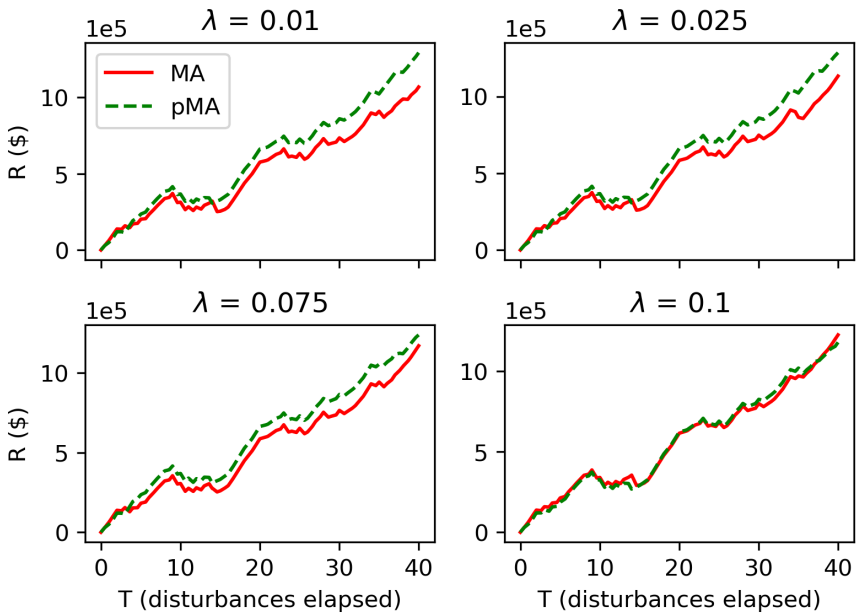

Figure 7-3: Profit accretion profiles for Williams-Otto case study, scenario 2, increasing filter constant.

The results from scenario 3 are also shown in Table 7-1, whereby a trend of increasing improvement of pMA over the standard MA is shown for runs with decreasing disturbance periods. This is also depicted transiently in Figure 7-4, whereby the revenue trajectories diverge increasingly as the disturbance period decreases (i.e., increased disturbance frequency). Note that the plots in Figure 7-4 are compressed/elongated to show the forty disturbance periods in the same range despite their varying period. As in the previous scenarios, a break-even point between the two schemes exists between $\Delta T = 250$ and $\Delta T = 300$. From this, we can conclude that the input-number regime for this system from equation (7-21) is as follows:

$$n_v = \begin{cases} 1 & \Delta T \leq 250 \\ n_u & \Delta T > 300 \end{cases} \tag{7-34}$$

Once the disturbance period becomes sufficiently large (i.e., infrequent disturbances), the pMA loses its competitive advantage of acting quickly as the standard MA has sufficient time to approach and benefit from economically superior operating points. Nevertheless, for short disturbance periods, the advantage can be significant (e.g., $\Delta T = 150$ with 56.1% cost improvement); this exemplifies the applicability of the scheme for constantly disturbed systems as proposed in the outset.

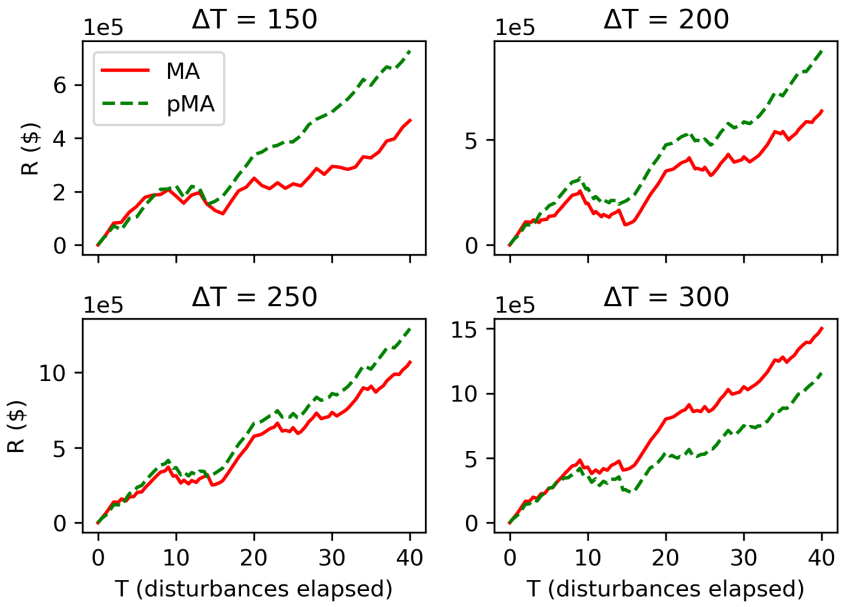

Figure 7-4: Profit accretion profiles for Williams-Otto case study, scenario 3, increasing disturbance periods.

A couple conclusions can be made from the Williams-Otto case. Firstly, the filters are found to inhibit, or conversely incite, the pMA scheme to perform better than the MA scheme through quick action. As this is a tuning parameter, we conclude that pMA should use as little filtering as possible. Moreover, the disturbance period was found to affect the efficacy of the pMA scheme as quick adaptation is more suitable for quick disturbances.

While the Williams-Otto case-study explored herein is excellent as a benchmark as it has been used in multiple studies, it contains inherent features that leave some aspects of pMA unanswered. Firstly, it is a two-input system, which is the bare minimum requirement for pMA. While this number of inputs provides a simple way to assess the system, most industrial systems have more inputs. In this case study, only one of the two inputs is chosen for partial adaptation; in other systems, a subset (as opposed to only one) input can be chosen for this task. Moreover, the Williams-Otto optimization problem does not require any inequality constraints to be adapted; hence, the effect of the operating point adjustment step was not observed; these aspects will be addressed in the next case study.

7.3.2 Forced Circulation Evaporator

The forced circulation evaporator, depicted in Figure 5-4 and presented in Section 5.3.1, is another nonlinear industrial system that has been used for multiple model-based control and optimization studies. This system provides a different perspective from the previous case study as its optima occur at an active constraint, making is a good setting in which to observe potential constraint violations.

Equations (5-33)–(5-44) represent the mechanistic (i.e., "perfect") evaporator model. For the purposes of this study, equation and parameter values were changed to introduce a plant-model mismatch. Accordingly, the mismatched model uses $\kappa = 35.5\ (kW \cdot min)/kg$ in equations (5-38) and (5-44), $\kappa_s = 34.6 (kW \cdot min)/kg$ in equation (5-42), and substitutes equation (5-41) for the following:

$$UA_1 = 0.16F_3 \tag{7-35}$$

Notably, the product composition is subjected to the following constraint to ensure a sufficiently high-quality product is generated by the evaporator:

$$X_2 \geq 25\% \tag{7-36}$$

The disturbance and manipulated variables for the forced circulation evaporator system are $\boldsymbol{d} = [X_1 \quad F_1 \quad T_1 \quad T_{200}]^T$ and $\boldsymbol{u} = [P_{100} \quad F_{200} \quad F_3]^T$, respectively. The nominal disturbance and input values are $\boldsymbol{d_{nom}} = [5 \quad 10 \quad 40 \quad 25]^T$ and $\boldsymbol{u_{nom}} = [200 \quad 200 \quad 50]^T$. The inputs have the bounds $P_{100} \in [10{,}400]$, $F_{200} \in [10, 400]$, and $F_3 \in [1{,}100]$. The objective of this system is to minimize the cost expressed as follows:

$$\Phi = 0.1009(F_2 + F_3) + 60F_{200} + 60P_{100} \tag{7-37}$$

The disturbance variables are changed every period (ΔT) from individual uniform distributions that serve as multipliers for the nominal disturbance values i.e., $\boldsymbol{d}\sim[\mathcal{U}(0.8{,}1.2) \cdot 5 \quad \mathcal{U}(0.8{,}1.2) \cdot 10 \quad \mathcal{U}(0.8{,}1.2) \cdot 40 \quad \mathcal{U}(0.8{,}1.2) \cdot 25]^T$. All necessary 0[th] order system information for MA is assumed to be measurable and sampled every $\Delta t = 1\ minute = 1\ time\ interval$; moreover, a varying number of modifier directions are used for different scenarios in the case study. The perturbation sizes for these inputs are $\boldsymbol{\delta} = 0.001\boldsymbol{u_t}$ (i.e., 0.1% of the current input value) and assumed to last $\tau = 300$ time intervals. Moreover, the system is limited to only ten adjustment iterations $j_{max} = 10$ of $\boldsymbol{\alpha} = 0.01\boldsymbol{v_{t-1}}$ such that the next operating point update is not delayed significantly.

A few scenarios were performed for this case study, which features ten disturbances $\boldsymbol{d_l}\ \forall l \in \{1, \dots, B\}$, $B = 10$, each occurring every ΔT sampling intervals. The disturbance period (ΔT), number of inputs modified with respect to (n_v), and scheme (MA vs. pMA) are varied such that the timing and degree of modification can be analyzed. In addition to the full MA and pMA, a version of the pMA without the operating point adjustment step (blue block of Figure 7-2) is also deployed and denoted pMA(-); this scheme is impractical in practice but serves to observe the effect of the adjustment step for active constraints proposed in this scheme. A number after pMA denotes the number of modifiers being continually refined; for instance, pMA1(-) denotes that a single input is being modified with respect to and that the constraint adjustment scheme is not being deployed.

The data for this scenario is shown in Appendix D, Supplementary Material for Chapter 7

Table D-1. Figure 7-5 shows the cumulative cost calculated using equation (7-22) of the competing scheme under various disturbance periods. It should be noted first that the full MA is unable to ever perform a single iteration in the $\Delta T = 2000$ case; this occurs as performing n_u perturbations is too protracted and a new disturbance always occurs before they finish. Moreover, longer disturbance periods entail longer simulation times, thus increasing values of R with increasing ΔT, as shown in Figure 7-5. Nevertheless, as observed therein, the full MA outperforms the pMA and pMA(-) schemes on a cumulative cost minimization basis for all disturbance periods where it can perform an iteration. On this cumulative cost basis, there seems to be relatively little difference between pMA and pMA(-) as indicated by their nearly equivalent trajectories. However, this superficial interpretation does not consider constraint violations, thus the economic analysis should be adjusted to consider process throughput.

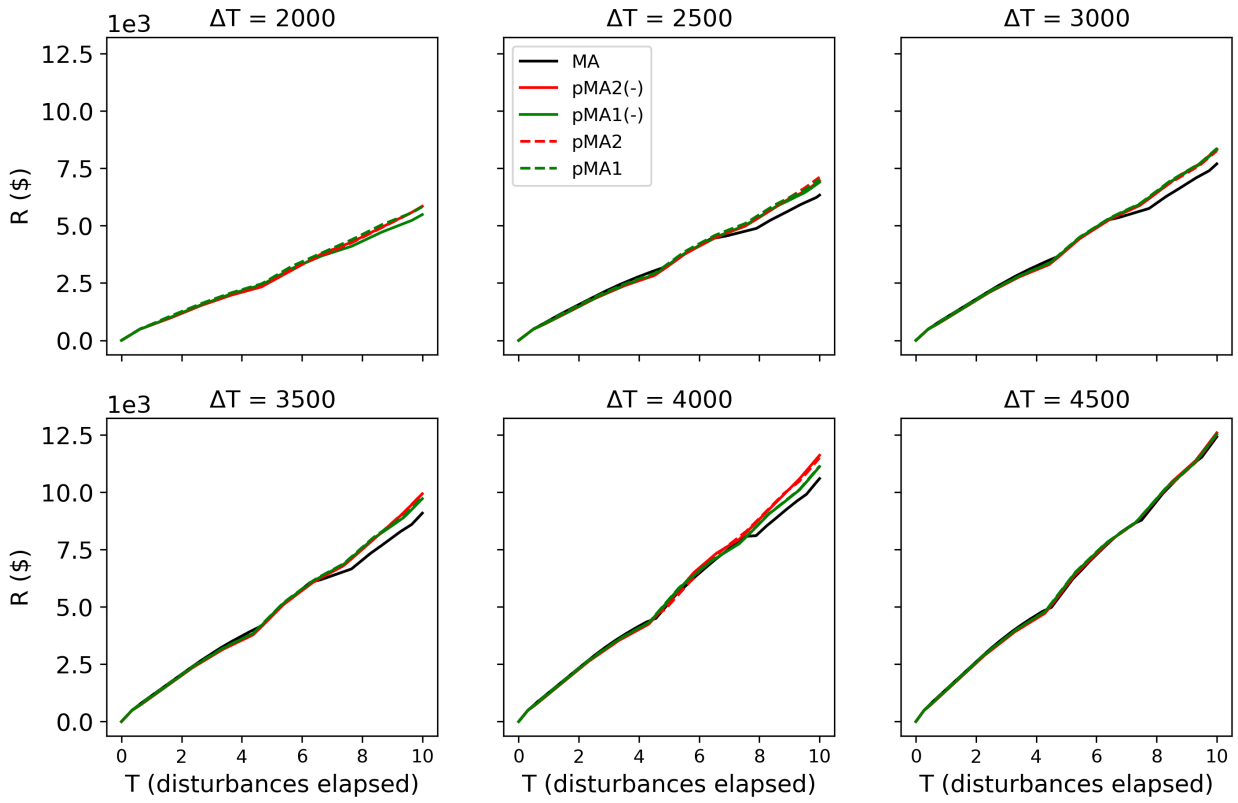

Figure 7-5: Cost accretion profiles for evaporator case study, increasing disturbance periods.

As outlined in the introduction, basic MA schemes do not guarantee constraint satisfaction during modifier refinement; moreover, as this study uses frequent periodic disturbances, the constraint satisfaction upon convergence property is not observed since convergence is not reached. Table 7-2 summarizes the cumulative time at constrain violation as defined in equation (7-23) while Figure 7-7 displays the throughput for all competing schemes as defined in equation (7-24). Additionally, the constrain trajectories for all scenarios can be found in Figure D-1 (Appendix D). In terms of times at constrain violation and throughput, the analysis favours the partial schemes until the disturbance period is increased to $\Delta T = 4500$. Regardless of the disturbance period, the pMA schemes are shown to always outperform their pMA(-) counterparts on a constraint violation and mass processed basis. This is owed to the constraint adjustment step, which ensures that the pre-perturbation operating point abides with the product purity requirement in equation (32); thus, the pMA iterations produce above-specification product while their pMA(-) equivalents may not. This effect of the adjustment step is further evident when comparing pMA to full MA whereby the former also outperforms the latter on constraint violation and throughput bases. As illustrated in Table 7-2, the cumulative time at constraint violation as defined in equation (7-23) is highest for the full MA scheme for all scenario except where the disturbances are sufficiently spaced at $\Delta T = 4000$. With more frequent disturbances, even the pMA(-) without adjustments outperforms the full MA on constraint satisfaction; thus, the quick action given by the partial adaptation alone is observed to have the effect of staying in constraint violating points for less time.

Table 7-2: Cumulative time (min) at constraint violation t_{viol} for evaporator case study, increasing disturbance periods.

	$\Delta T = 2000$	$\Delta T = 2500$	$\Delta T = 3000$	$\Delta T = 3500$	$\Delta T = 4000$	$\Delta T = 4500$
MA	–	240	302	328	310	281
pMA2	148	176	233	237	249	286
pMA2(-)	165	207	251	255	255	320
pMA1	119	146	205	255	3222	349
pMA1(-)	167	209	254	303	364	411

Analyzing a subset of constraint trajectories from Figure D-1 (Appendix D) more closely, Figure 7-6 displays the results for the best (pMA1) scheme, its counterpart without the adjustment set (pMA1(-)), and the full MA scheme for $\Delta T = 2500$. In these trajectories, the result of the constraint adjustment step is more clearly appreciable. In several time instances (e.g., $T \sim 0.7, 4.6, 7.6$), the adjustment step is activated to bring the composition above the quality constraint. The effects of the adjustment step with respect to constraint satisfaction are accrued over time, thus generating the operational differences between pMA and pMA(-) schemes observed in in Table 7-2; these will continue to accrue as the process operation evolves in time.

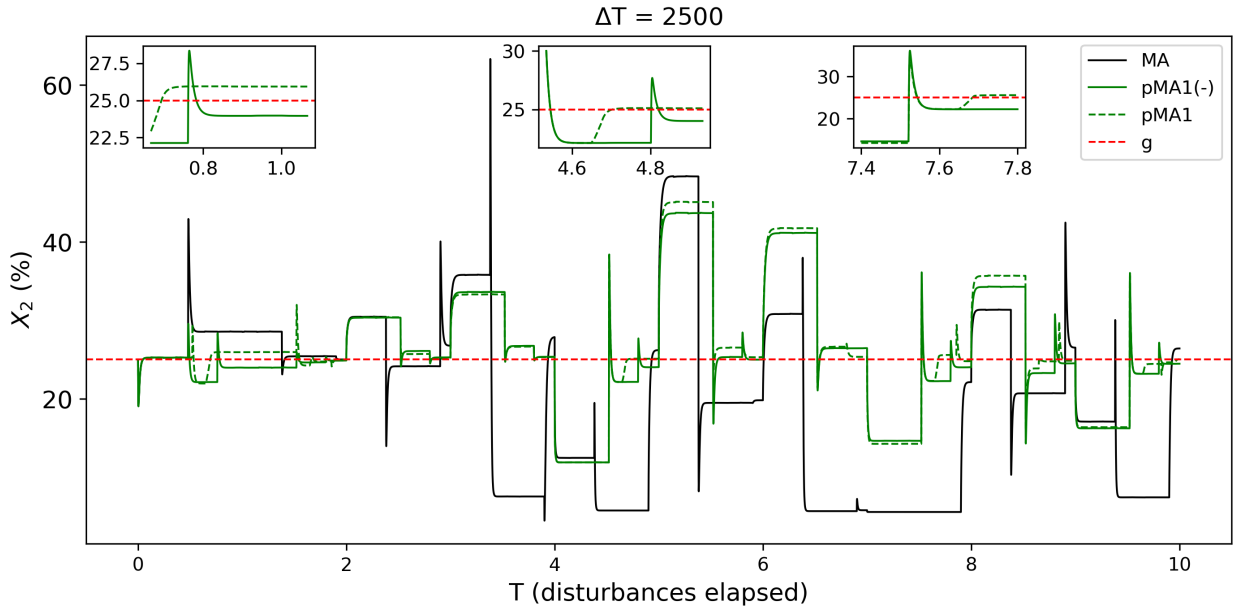

Figure 7-6: Product quality trajectory for $\Delta T = 2500$ scenario in evaporator case study.

Figure 7-7 illustrates how the number of inputs modified with respect to (n_v) can impact the efficacy of the pMA scheme. For short disturbance periods (i.e., $\Delta T = 2000$, $\Delta T = 2500$, and $\Delta T = 3000$), the pMA1 (i.e., $n_v = 1$) scheme are best. This occurs as the disturbance happen frequently enough to require more iterations of the pMA that are facilitated by the pMA1 schemes. For intermediate disturbance periods (i.e., $\Delta T = 3500$ and $\Delta T = 4000$), the pMA2 (i.e., $n_v = 2$) scheme is the best. In this case, the disturbances happen less frequently as to allow for more iterations of the pMA schemes performed in pMA2; however, they still occur frequently enough as to not favour the

full MA scheme. Furthermore, for long disturbance periods (i.e., $\Delta T = 4500$), the full MA scheme dominates as enough time between disturbances occurs for the full MA to arrive near the plant optima.

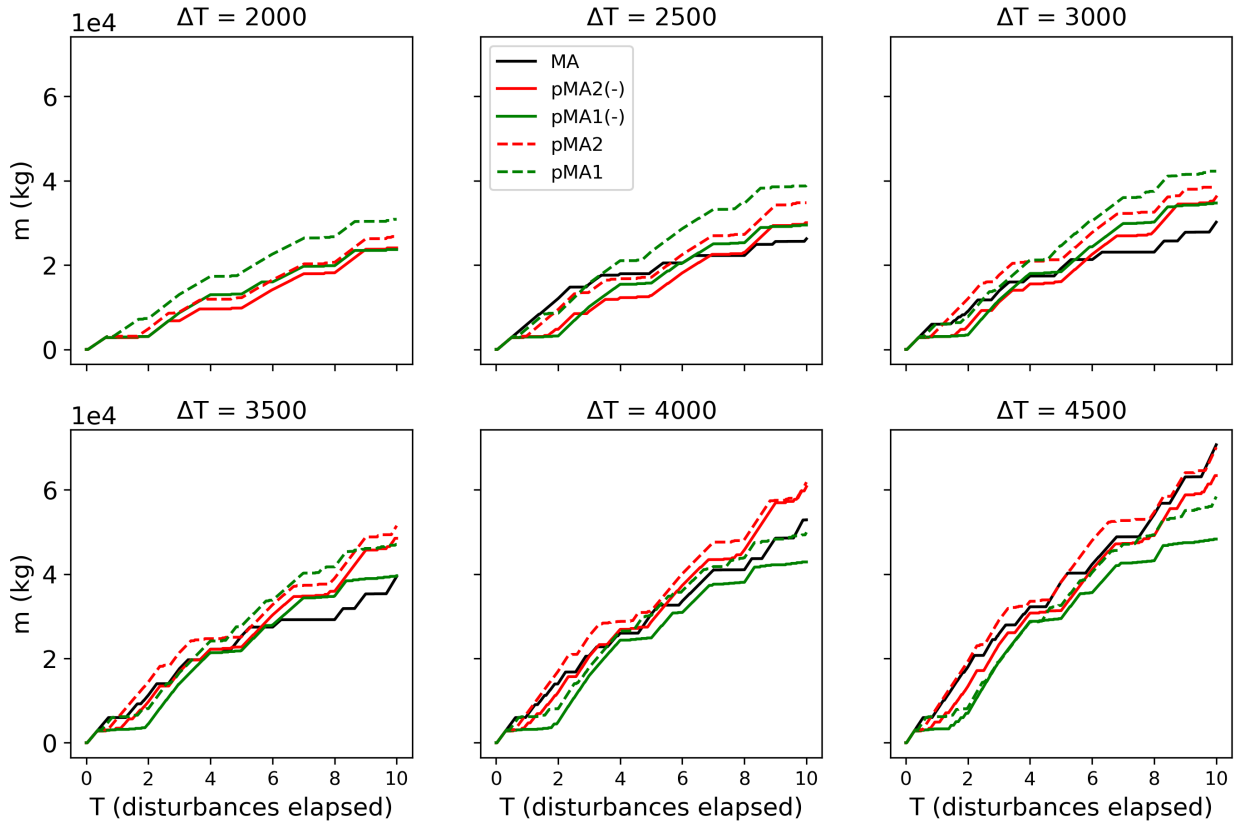

Figure 7-7: Material production profiles for evaporator case study, increasing disturbance periods.

Figure 7-8 summarizes the aggregate effect of cost (Figure 7-5) and throughput (Figure 7-7) as defined in equation (7-25) (i.e., $PM = P_{prod}$). As with the throughput, a clear pattern emerges whereby the pMA schemes are superior to the pMA(-) schemes, which are superior to the full MA scheme. Thus, for the evaporator case, the following regimes are established for the number of inputs modified with respect to:

$$n_v = \begin{cases} 1 & \Delta T \leq 3000 \\ 2 & 3500 < \Delta T \leq 4000 \\ n_u & \Delta T > 4000 \end{cases} \tag{7-38}$$

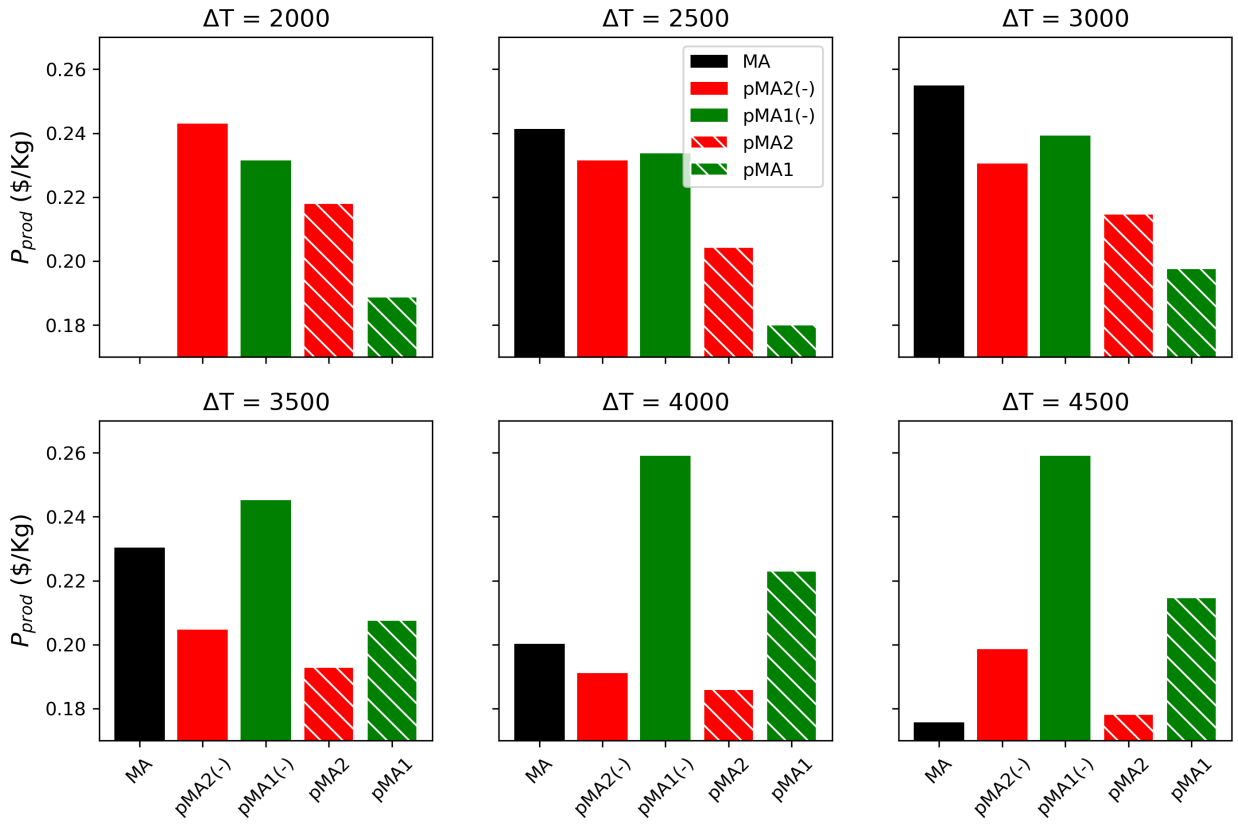

Figure 7-8: Cost per unit weight for evaporator case study, increasing disturbance periods.

In contrast to the William-Otto scenario, the evaporator exemplifies the potential economic importance of producing constraint-adhering product as affected by increased production. Moreover, we observe the effect of different number of input modifications more concretely and its relationship to the disturbance period.

While pMA was shown to outperform the traditional MA scheme in the case of frequent periodic disturbances, many MA variants could have similar benefits to pMA under these conditions; one such variant is dMA (Costello et al., 2016). As noted previously, dMA can choose multi-input directions for adaptation but requires the one-time local computation of a parameter/input sensitivity matrix. While pMA can only use single-input adaptation directions, sensitivities are computed locally; thus, a potential tradeoff is present between the schemes, making them apt for comparison.

After determining the suitable number of modifier directions (i.e., $n_v = 1$) using the n_v-determination algorithm for a disturbance period of ΔT =2000, several dMA scenarios were performed for the same ten-disturbance sequence was imposed on the pMA. The results from the dMA approach can be found in Table 7-3 whereby each scenario differs in the point around which the model sensitivity matrix is identified (as noted in Costello et al., 2016; this matrix is required for determining the privileged dMA directions $\boldsymbol{U_t}$.

Table 7-3: Performance of dMA scenarios with sensitivity matrix calculated at different operating point, $n_v = 1$, and ΔT = 2000.

Scenario	**Sensitivity matrix point**	$\boldsymbol{R}$ ($)	$\boldsymbol{m(kg)}$	$\boldsymbol{P_{prod}}$ ($/$\boldsymbol{kg}$)
1	$\boldsymbol{d} = [6.0 \quad 9.8 \quad 37.9 \quad 23.2]^T$	6926.08	38404.97	0.180

	$\boldsymbol{u} = [350 \quad 200 \quad 40]^T$			
2	$\boldsymbol{d} = [4.1 \quad 12.7 \quad 37.1 \quad 23.5]^T$ $\boldsymbol{u} = [350 \quad 200 \quad 50]^T$	6314.30	24860.15	0.254
3	$\boldsymbol{d} = [5.1 \quad 9.7 \quad 51.0 \quad 20.9]^T$ $\boldsymbol{u} = [166 \quad 183 \quad 98]^T$	7004.76	38474.18	0.182
4	$\boldsymbol{d} = [5.1 \quad 12.9 \quad 37.0 \quad 23.2]^T$ $\boldsymbol{u} = [390 \quad 200 \quad 50]^T$	6724.96	33030.24	0.204
5	$\boldsymbol{d} = [5.2 \quad 8.8 \quad 49.8 \quad 24]^T$ $\boldsymbol{u} = [148 \quad 133 \quad 95]^T$	7024.16	38483.14	0.182
6	$\boldsymbol{d} = [5.6 \quad 8.4 \quad 43.3 \quad 24.5]^T$ $\boldsymbol{u} = [335 \quad 80 \quad 32]^T$	6418.26	28182.64	0.228
7	$\boldsymbol{d} = [4.1 \quad 9.6 \quad 46.7 \quad 22.8]^T$ $\boldsymbol{u} = [324 \quad 150 \quad 54]^T$	6928.07	36818.15	0.188
8	$\boldsymbol{d} = [5.8 \quad 8.8 \quad 54.0 \quad 28.3]^T$ $\boldsymbol{u} = [218 \quad 126 \quad 41]^T$	6477.56	30165.92	0.21
dMA average	–	6727.27	33552.42	0.204
pMA	–	5827.37	30852.88	0.189

As shown in Table 7-3, and Figure D-2 (Appendix D), the performance of the dMA scheme on the evaporator is highly dependent on which point the sensitivity matrix is computed through the direction it chooses. Compared to the pMA, which is not dependent on this matrix, the dMA can perform moderately better (e.g., scenario 1; ∼4.8% improvement) or significantly worse (e.g., scenario 2; ∼34.4% deterioration). Note that pMA does not rely on a parameter distribution being known *a priori*, thus this assumption is alleviated by the proposed approach. Moreover, the potential variability in performance owed to the sensitivity matrix point is abated by using pMA. On aggregate, pMA outperforms dMA (∼7.4% improvement in using pMA over the average in dMA), as shown in Table 7-3. Conversely, the dMA is shown to be able to outperform pMA if the sensitivity matrix is computed at an adequate point; thus, there is a tradeoff in the two schemes between average and variability in performance. As discussed above, this is mostly owed to the use of multi-input directions compared to the ability to update directions online.

7.4. Summary

MA is a commonly used method to abate model uncertainty, but its gradient estimation step can cause delays in the update of operating points. The pMA scheme presented in this chapter only modifies with respect to a subset of the inputs chosen using the modified cost metric. This subset is refined as the pMA scheme progresses such that the modifications are chosen to have the largest effect on the process economics. Additionally, pMA employs an operating point adjustment step, which drives constraint-violating systems into constraint adhering regions prior to the perturbation step. The proposed scheme was deployed on the Williams-Otto plant where it was found to be superior to the full MA for small disturbance periods and small filter constants; thus, leveraging modifier refinement speed to its economic advantage. Moreover, the pMA scheme was deployed for an evaporator case study with active constraints whereby it was shown to increase material throughput through decreased constraint violation compared to the full MA. Increased throughput was shown to also result in improved process economics. The evaporator case also exemplified how the best number of modifiers is dependent on the disturbance period such that different numbers of modifiers can be used in different disturbance regimes. With respect to dMA, pMA was found to lead to an average performance improvement owed to its lack of dependence on the initial sensitivity matrix. Conversely, some dMA

scenarios were found to outperform pMA if the initial sensitivity matrix was computed around certain operating points; thus, there is a tradeoff in robustness and performance between the two methods.

8. Conclusions and Recommendations

This PhD thesis has developed various practical algorithms for the online model-based economic optimization of processes under uncertainty as well as economic operating schemes for processes that will contribute to sustainable development. In an increasingly competitive world, the ability to update processes online gives operators an edge in to addressing external disturbances and incentive changes. The core ideas developed herein revolve around RTO, which continually updates process operating conditions with the assistance of ancillary layers (i.e., PE, MPC, MHE). Two principal approaches are taken for steady-state economic optimization of processes: the two-step RTO and MA. In two-step RTO, uncertain model parameters are updated prior to the economic optimization step; to this end, the quality of set points is dependent on the fidelity of the parameter estimates. Approaches like DR have been developed to help in the PE step; however, these aim to make measurements consistent with the model and are not selective of measurements that may be inhibiting PE performance. In the MA approach, bias and gradient-correction (i.e., modifiers) terms are used to reconcile the optimization model with the plant. The gradient-correction terms require perturbation to the plant in their estimation procedure, thus delaying the economic optimization of the plant. This delay is especially salient in frequently disturbed systems and approaches like directional MA have been proposed to modify a with respect to a subset of inputs and alleviate this delay. However, no approach in the open literature uses a purely economic criterion in the input selection process and no approach has been designed to correct for constraint violation in the modifier refinement process.

In addition to the algorithmic gaps defined above, practical gaps remain in the economic optimization of sustainable many systems; in particular, this work concerns itself with PCC and RAS. While PCC has been widely studied from many perspectives, the online economic optimization literature is scant. Some RTO and EMPC approaches have been proposed but neither has considered the wide range of economic factors in PCC. Moreover, no PCC RTO scheme has been fully implementable beyond simulation owed to lack of state estimation and a method to deal with model uncertainty. Likewise, no online economic optimization schemes for RAS exist, primarily owing to the lack of process models to use in an optimization program. For this reason, no effort has been afforded to formulating an economic function and very little attention has been paid to treating RAS using a process controls/operations approach.

This PhD thesis sought to advance the corresponding fields of the gaps mentioned above by providing efficient and practical algorithms for RTO under uncertainty as well as using economic incentives to operate novel processes cheaply and incite their further development. The principal conclusions gained from this work are outlined as follows:

- A robust NMPC for a post-combustion CO_2 capture absorber was presented in Chapter 3. The robust operation of the absorber under parametric and process uncertainty using the robust NMPC controller was compared against that of nominal and plant-model mismatched NMPCs for various disturbance rejection scenarios. The controllers were assessed in a simulated plant with plant-model mismatch to elucidate the benefits of the multi-scenario approach used in the design of the robust NMPC. As expected, the computational demands of the robust NMPC controllers were found to be increasing with increasing size of uncertainty regions and increasing number scenarios considered by the controller. Moreover, a larger uncertainty region was found to exhibit more conservativism in the control moves leading to offset. Nevertheless, it was found that for short simulation times the robust NMPCs generally led to better average

performance and less variability in performance across plants in which the controllers were tested. Further, for long simulations, where error can accrue over time; the performance of a robust NMPC controller was found to be significantly better than that of the NMPCs with no robustness.

- A novel operational scheme was proposed and implemented for PCC plants in Chapter 4. This includes RTO, NMPC, and MHE layers. The RTO was found to provide consistent steady-state cost improvements across all scenarios tested. These cost improvements always exceeded the energy penalty imposed on the upstream power plant by the PCC plant; resulting in net gains despite any additional energy expended. In terms of resource used, the MEA cost was found to be large following disturbance rejection and when operating dynamically. Conversely, the MEA cost was found to be low when operating at the RTO-defined set points while allowing for low reboiler duty to be necessary. CO_2 sales were found to significantly lessen the process cost in all scenarios. From an operational standpoint, the MHE was found to provide acceptable estimates to the NMPC, leading to good control performance that resulted in economically attractive operating points. Moreover, the NMPC was observed to perform well under an array of large disturbances through its use of the makeup streams and its coordination of control objectives.
- Chapter 5 proposed a novel low-variance parameter estimation (lv-PE) scheme applied to RTO for noisy processes. The proposed scheme uses the information content (IC) metric, as well as establishing parameter bounds for filtering; these novelties reduce the variability in parameter estimates over time and eliminates poorly estimated parameters, respectively. The proposed scheme was implemented in two case studies, namely a forced circulation evaporator and the Williams-Otto CSTR. The evaporator displayed the ability of the proposed scheme to avoid constraint violations by one to two orders in magnitude, while the Williams-Otto case study showed the improvement yielded by the proposed scheme on process economics ranging from $\sim$4 to 88%, depending on the scenario. Although the benefit provided by the lv-PE to each case study was different, both were observed to result in significant reduction in parameter variation owing to the lv-PE/RTO of one to two orders of magnitude.
- Chapter 6 presents the first estimation scheme for the RTO of PCC systems under uncertainty. Both physical properties and external disturbances are estimated through the approach proposed in Chapter 5. Moreover, the lv-PE algorithm is used for uncertainty quantification to formulate an rRTO. In both estimation cases (physical property and disturbance), the lv-PE is shown to improve the quality of the set points achieved via their economics; this is compared with respect to traditional PE as well as PE with DR. The rRTO formulation was also found to result in modest cost savings with a large reduction in set point variability, which would reduce control burden.
- The pMA scheme presented in Chapter 7 uses a directional approach to speed up the gradient estimation step in MA. This is suitable for frequent periodic disturbance where modifier convergence may not be achieved. A secondary constrain-adjustment problem is also presented to abate constrain violations and an algorithm is presented to determine the number of adjustment directions for a given disturbance frequency. The proposed scheme was found to provide up to $\sim$56% improvement with respect to the standard MA scheme

in the Williams-Otto CSTR for short disturbance periods. Moreover, pMA was also found to outperform standard MA and dMA scheme in an evaporator case study.

8.1. Recommendations for Future Research

Despite the advances outlined in this thesis, gaps remain in the literature that should be addressed. Furthermore, some of the works presented herein have opened avenues for new areas of inquiry. These are as follows:

- There remain a few issues to be solved before an approach using the NMPC in Chapter 3 becomes tractable. Namely, a reduction in CPU time is necessary for online implementation of the NMPCs presented in this study. This computational effort reduction can be achieved with fast NMPC algorithms, which use model reduction (Yu et al., 2015) and advanced step strategies (Zavala and Biegler, 2009). However, model reduction strategies may not be able to capture process nonlinearities and may not be able to consider parametric uncertainty in the same level of detail as presented in this study. Thus, advanced dynamic optimization decomposition techniques may be considered to reduce the computational effort.
- Likewise, as shown in this work, the robust NMPC controllers do not have perfect performance and result in some set-point offset. A natural extension of the multi-scenario-based robust controller to further reduce this conservatism is the design of a multi-stage robust controller (Lucia and Engell, 2012).
- The single-layer approach should also be considered by through the PCC objective function proposed in Chapter 4 through deployment of EMPC.
- The significant effect of the PCC stripper reboiler in terms of cost was observed in this study through a simplified model. This finding warrants further investigation as to how the explicit inclusion of the reboiler could aid the control layer in conjunction with MEA makeup manipulation as proposed herein. Additionally, the loss of power plant efficiency resulting from steam used in reboiler heating also needs to be studied.
- In PCC there exists a trade-off between changing the set point and the dynamics that ensue as a result, which are often expensive. These economic trade-offs and the computational effort involved should be compared to those frameworks that consider the process economics in the transient domain, i.e., EMPC. By adapting the novel economic function proposed herein to a dynamic optimization problem that considers transient costs in an approach like EMPC, a more comprehensive understanding of the connection between dynamics and process cost could be established. Moreover, steady state and dynamical operational approaches can then be compared such that the best PCC operational schedules and schemes can be determined for different power plant operational scenarios.
- Corrosion is also assumed to be negligible in the present study but is an important factor preventing the uptake of PCC. A suitable control approach that explicitly models corrosion as noted in Rúa et al. (2021b), could potentially mitigate these effects by considering corrosion minimization as an additional operational incentive; this will be a topic of future work.
- The mechanistic PCC model used in this work was developed using data from a pilot plant and, accordingly, the operating conditions, dynamics, and cost reflect this scale. In the future, a scale-up of this model must be performed to assess the operational advantages of the scheme in an industrial system. The results obtained

from this work also reflect the current economic incentives as manifested in the prices used. With scaled-up conditions as well as future process developments that change the economic incentives (e.g., energy-efficient solvents, increased carbon prices, decreased energy prices), the process can be re-optimized and reassessed through the economic framework developed in this work, thus resulting in an optimal operation that can simultaneously capture CO_2 at low operational costs.

- The concept of IC to pre-process measurements and generate parameter bounds could be adapted for a state, parameter, or disturbance estimation procedure (or a joint estimation procedure). Moreover, the respective estimators could also be adapted as dynamic problems to address issues such as parameter drift or frequent unmeasurable disturbances.
- As noted in Section 5.2.2, another direction for future work is the extension of the current lv-PE methodology for joint estimation variance reduction and GED.
- The pMA scheme proposed in Chapter 7 has been implemented using the traditional perturbation method; however, gradients acquisition can be made more efficient through dual MA. Future works will also investigate the joint use of pMA and dual MA, which could lead to further benefits in speeding up modifier refinement. The pMA scheme can be inhibited by filtering, this limits its applicability to low noise environments; thus, an alternative noise abatement scheme must be proposed to make the scheme suited to noisy measurements (e.g., the lv-PE scheme in Chapter 5).
- Furthermore, pMA in Chapter 7 was only tested in systems whereby preliminary runs may be performed for tuning; this may not be achievable or desirable in all systems. Accordingly, online tuning and tuning budget sizing for pMA requires further attention. The case studies presented in Chapter 7 were selected such that they provide clear illustrations of the benefits and limitations of the proposed scheme. However, industrial plants are usually more complex; future works will thus deploy pMA in high-dimensional constrained chemical plants (i.e., those involving many inputs and constraints).

Letters of Copyright Permissions

A robust nonlinear model predictive controller for a post-combustion CO2 capture absorber unit

Author: Gabriel D. Patron,Luis Ricardez-Sandoval
Publication: Fuel
Publisher: Elsevier
Date: 1 April 2020

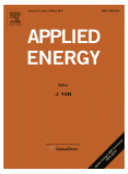

An integrated real-time optimization, control, and estimation scheme for post-combustion CO2 capture

Author: Gabriel D. Patrón,Luis Ricardez-Sandoval
Publication: Applied Energy
Publisher: Elsevier
Date: 15 February 2022

Low-Variance Parameter Estimation Approach for Real-Time Optimization of Noisy Process Systems

Author: Gabriel D. Patrón, Luis Ricardez-Sandoval
Publication: Industrial & Engineering Chemistry Research
Publisher: American Chemical Society
Date: Nov 1, 2022

References

ABB. (2013). Measurement of CO_2 in Flue Gases. SS/6515_2. https://library.e.abb.com/public/ad9b40c4540c82c7c1257b0c005402f8/SS_6515_2.pdf.

Adetola, V., Guay, M. (2010). Integration of real-time optimization and model predictive control. *J. Process Control*, 20(2), 125–133. https://doi.org/10.1016/j.jprocont.2009.09.001.

AESO. (2019). Ets.aeso.ca. Alberta Electric System Operator: Current and Historical Market Reporting. [online] Available at: http://ets.aeso.ca/ [Accessed Aug 14. 2019].

Afshari, H., Gadsden, S., Habibi, S. (2017). Gaussian filters for parameter and state estimation: A general review of theory and recent trends. *Signal Process.,* 135, 218–238. https://doi.org/10.1016/j.sigpro.2017.01.001.

Ahmed, N., Turchini, G. (2021). Recirculating aquaculture systems (RAS): Environmental solution and climate change adaptation. *J. Clean. Prod*., 297, 126604. https://doi.org/10.1016/j.jclepro.2021.126604.

Åkesson, J., et al. (2012). Nonlinear Model Predictive Control of a CO_2 Post-Combustion Absorption Unit. *Chem. Eng. Technol.,* 35(3), 445–454. https://doi.org/10.1002/ceat.201100480.

Akinola, O., Oko, E., Wu, X., Ma, K., Wang, M. (2020). Nonlinear model predictive control (NMPC) of the solvent-based post-combustion CO_2 capture process. *Energy*, 213, 118840. https://doi.org/10.1016/j.energy.2020.118840.

Akula, P., Eslick, J., Bhattacharyya, D., Miller, D. (2021). Model Development, Validation, and Optimization of an MEA-Based Post-Combustion CO_2 Capture Process Under Part-Load and Variable Capture Operations. *Ind. Eng. Chem. Res.,* 60(14), 5176–5193. https://doi.org/10.1021/acs.iecr.0c05035.

Albuquerque, J., Biegler, L. (1996). Data reconciliation and gross-error detection for dynamic systems. *AIChE J.,* 42(10), 2841–2856. https://doi.org/10.1002/aic.690421014.

Allgöwer, F., Badgwell, T., Qin, J., Rawlings, J., Wright, S. (1999). Nonlinear Predictive Control and Moving Horizon Estimation — An Introductory Overview. In: Frank, P.M. (eds) *Advances in Control*. Springer, London. https://doi.org/10.1007/978-1-4471-0853-5_19.

Altan, A., Karasu, S., Zio, E. (2021). A new hybrid model for wind speed forecasting combining long short-term memory neural network, decomposition methods and grey wolf optimizer. *Appl. Soft Comp*., 100, 106996. https://doi.org/10.1016/j.asoc.2020.106996.

Amrit, R., Rawlings, J., Angeli, D. (2011). Economic optimization using model predictive control with a terminal cost. *Annu. Rev. Control*, *35*(2), 178–186. https://doi.org/10.1016/j.arcontrol.2011.10.011.

Amrit, R., Rawlings, J., Biegler, L. (2013). Optimizing process economics online using model predictive control. *Comput. Chem. Eng.,* 58, 334–343. https://doi.org/10.1016/j.compchemeng.2013.07.015

Angeli, D., Amrit, R., Rawlings, J. (2011). On average performance and stability of economic model predictive control. *IEEE Trans. Automat. Contr.*, *57*(7), 1615–1626. 10.1109/TAC.2011.2179349.

Arora, N., Biegler, L. (2001). Redescending estimators for data reconciliation and parameter estimation. *Comput. Chem. Eng.,* 25(11), 1585–1599. https://doi.org/10.1016/S0098-1354(01)00721-9.

AUC. (2019). Auc.ab.ca. Current rates and terms of conditions. [online] Available at: http://www.auc.ab.ca/Pages/current-rates-electric.aspx [Accessed 10 Oct. 2019.].

Austgen, D., Rochelle, G., Peng, X., Chen, C. (1989). Model of vapor-liquid equilibria for aqueous acid gas-alkanolamine systems using the electrolyte-NRTL equation. *Ind. Eng. Chem. Res.*, 28(7), 1060–1073. https://doi.org/10.1021/ie00091a028.

Babu, P., Kumar, R., Linga, P. (2013). Pre-combustion capture of carbon dioxide in a fixed bed reactor using the clathrate hydrate process. *Energy*, 50, 364–373. https://doi.org/10.1016/j.energy.2012.10.046.

Bahakim, S., Ricardez-Sandoval, L. (2014). Optimal Steady-state Design of a Post-combustion CO_2 Capture Plant Under Uncertainty. *Energy Procedia*, 63, 1608–1616. https://doi.org/10.1016/j.egypro.2014.11.171.

Bahakim, S., Ricardez-Sandoval, L. (2015). Optimal Design of a Postcombustion CO_2 Capture Pilot-Scale Plant under Process Uncertainty: A Ranking-Based Approach. *Ind. Eng. Chem. Res.*, 54(15), 3879–3892. https://doi.org/10.1021/ie5048253.

Bedelbayev, A., Greer, T., Lie, B. (2008). Model Based Control of Absorption Tower for CO_2 Capturing. *Proc. SIMS 2008,* 166–176. https://www.scansims.org/media-files/sims2008/21.pdf.

Bhat, S., Saraf, D. (2004). Steady-State Identification, Gross Error Detection, and Data Reconciliation for Industrial Process Units. *Ind. Eng. Chem. Res*., 43, 4323–4336. https://doi.org/10.1021/ie030563u.

Bottari, A., Zumoffen, D., Marchetti, A. (2020). Economic Control Structure Selection for Two-Layered Real-Time Optimization Systems. *Ind. Eng. Chem. Res.,* 59(49), 21413–21428. https://doi.org/10.1021/acs.iecr.0c02591.

BP p.l.c. (2019). BP Statistical Review of World Energy 2019. https://www.bp.com/content/dam/bp/business-sites/en/global/corporate/pdfs/energy-economics/statistical-review/bp-stats-review-2019-full-report.pdf.

Bunin, G., François, G., Srinivasan, B., Bonvin, D. (2011). Input Filter Design for Feasibility in Constraint-Adaptation Schemes. *IFAC. Proc. Vol*., 44(1), 5585–5590. https://doi.org/10.3182/20110828-6-IT-1002.02937.

Canada.ca. (2019). Pricing carbon pollution in Canada: how it will work. [online] Available at: https://www.canada.ca/en/environment-climate-change/news/2017/05/pricing_carbon_pollutionincanadahowitwillwork.html [Accessed 10 Oct. 2019].

Cao, S., Rhinehart, R. (1995). An efficient method for on-line identification of steady state. *J. Process Control*, 5(6), 363–374. https://doi.org/10.1016/0959-1524(95)00009-F.

Cerrillo-Briones, I., Ricardez-Sandoval, L. (2019). Robust optimization of a post-combustion CO_2 capture absorber column under process uncertainty. *Chem. Eng. Res. Des*., 44, 386–396. https://doi.org/10.1016/j.cherd.2019.02.020.

Chachuat, B., Srinivasan, B., Bonvin, D. (2009). Adaptation strategies for real-time optimization. *Comput. Chem. Eng.,* 33(10), 1557–1567. https://doi.org/10.1016/j.compchemeng.2009.04.014.

Chan, L., Chen, J. (2018). Economic model predictive control of an absorber-stripper CO_2 capture process for improving energy cost. *IFAC-PapersOnLine*, 51(18), 109–114. https://doi.org/10.1016/j.ifacol.2018.09.284.

Chansomwong, A., Douglas, P., Croiset, E., Zanganeh, K., Shafeen, A., Ricardez-Sandoval, L. (2014a). Control of An Oxy-fuel Capture and Purification Unit For Coal-Based Power Plants. *Energy Procedia*, 63, 476–483. https://doi.org/10.1016/j.egypro.2014.11.051.

Chansomwong, A., Zanganeh, K., Shafeen, A., Douglas, P., Croiset, E., Ricardez-Sandoval, L. (2014b). Dynamic modelling of a CO_2 capture and purification unit for an oxy-coal-fired power plant. *Int. J. Greenh. Gas Control*, 22, 111–122. https://doi.org/10.1016/j.ijggc.2013.12.025.

Chen, C., Joseph, B. (1987). On-Line Optimization Using a Two-Phase Approach: An Application Study. *Ind. Eng. Chem. Res.,* 26(9), 1924–1930. https://doi.org/10.1021/ie00069a034.

Chen, W., O'Reilly, J., Balance, D. (2000). Model predictive control of nonlinear systems: Computational burden and stability. *IEE. Proc. D*, 147(4), 387–394. 10.1049/ip-cta:20000379.

Costello, S., François, G., Bonvin, D. (2016). A Directional Modifier-Adaptation Algorithm for Real-Time Optimization. *J. Process Control,* 39, 64–76. https://doi.org/10.1016/j.jprocont.2015.11.008.

Cox, H. (1964). On the Estimation of State Variables and Parameters for Noisy Dynamic Systems. *IEE Trans. Automat. Contr*., 9(1), 5–12. 10.1109/TAC.1964.1105635.

D'Agaro, E., Gibertoni, P., Esposito, S. (2022). Recent Trends and Economic Aspects in the Rainbow Trout (Oncorhynchus mykiss) Sector. *Appl. Sci.*, 12(17), 8773. https://doi.org/10.3390/app12178773.

Danaci, D., Bui, M., Petit, C., Mac Dowell, N. (2021). En Route to Zero Emissions for Power and Industry with Amine-Based Post-combustion Capture. *Environ. Sci. Technol*., 55(15), 10619–10632. https://doi.org/10.1021/acs.est.0c07261.

Darby, M., Nikolaou, M., Jones, J., Nicholson, D. (2011). RTO: An overview and assessment of current practice. *J. Process Control*, 21(6), 874–884. https://doi.org/10.1016/j.jprocont.2011.03.009.

de Avila Ferreira, T., François, G., Marchetti, Bonvin, D. (2017). Use of Transient Measurements for Static Real-Time Optimization. *IFAC-PapersOnLine*, 50(1), 5737–5742. https://doi.org/10.1016/j.ifacol.2017.08.1130

Decardi-Nelson, B., Liu, S., Liu, J. (2018). Improving Flexibility and Energy Efficiency of Post-Combustion CO_2 Capture Plants Using Economic Model Predictive Control. *Processes*, 6(9), 135. https://doi.org/10.3390/pr6090135.

Decardi-Nelson, B., Liu, J. (2022). Robust Economic MPC of the Absorption Column in Post-Combustion Carbon Capture through Zone Tracking. *Energies*, 15(3), 1140. https://doi.org/10.3390/en15031140.

del Rio Chanona, A., Petsagkourakis, P., Bradford, E., Alves Graciano, J., Chachuat, B. (2021). Real-time optimization meets Bayesian optimization and derivative-free optimization: A tale of modifier adaptation. *Comput. Chem. Eng.*, 147, 107249. https://doi.org/10.1016/j.compchemeng.2021.107249.

Dering, D., Swartz, C. (2022). Dynamic Real–Time Optimization with Closed-Loop Prediction for Nonlinear MPC–Controlled Plants. *Comput. Aided Chem. Eng.,* 51, 1099–1104. https://doi.org/10.1016/B978-0-323-95879-0.50184-3.

Diehl, M., Amrit, R., Rawlings, J. (2010). A Lyapunov function for economic optimizing model predictive control. *IEEE Trans. Automat. Contr.*, *56*(3), 703–707. 10.1109/TAC.2010.2101291.

Diehl, M., et al. (2002). Real-time optimization and nonlinear model predictive control of processes governed by differential-algebraic equations. *J. Process Control*, 12(4), 577–585. https://doi.org/10.1016/S0959-1524(01)00023-3.

D'Orbcastel, E., Blancheton, J., Aubin J. (2009). Towards environmentally sustainable aquaculture: Comparison between two trout farming systems using Life Cycle Assessment. *Aquac. Eng.*, 40, 113–119. https://doi.org/10.1016/j.aquaeng.2008.12.002.

Dorris, C., Lu, E., Park, S., Toro F. (2016). High-Purity Oxygen Production Using Mixed Ionic-Electronic Conducting Sorbents. *Senior Design Reports (CBE)*, 78. https://repository.upenn.edu/cbe_sdr/78/.

Dos Santos, A., Attramadal K., Skogestad, S. (2022). Optimal Control of Water Quality in a Recirculating Aquaculture System. *IFAC-PapersOnLine*, 55(8), 328–333. https://doi.org/10.1016/j.ifacol.2022.07.465.

Dugas, E. (2006). Pilot plant study of carbon dioxide capture by aqueous monoethanolamine. *Masters thesis*, University of Texas at Austin.

Ellis, M., Durand, H., Christofides, P. (2014). A tutorial review of economic model predictive control methods. *J. Process Control,* 24(8), 1156–1178. https://doi.org/10.1016/j.jprocont.2014.03.010.

Fagiano, L., Teel, A. (2013). Generalized terminal state constraint for model predictive control. *Automatica*, *49*(9), 2622–2631. https://doi.org/10.1016/j.automatica.2013.05.019.

Faramarzi, L., et al. (2017). Results from MEA Testing at the CO_2 Technology Centre Mongstad: Verification of Baseline Results in 2015. *Energy Procedia*, 114, 1128–1145. https://doi.org/10.1016/j.egypro.2017.03.1271.

Fernandes, P., Pedersen, L., Pedersen, P. (2017). Influence of fixed and moving bed biofilters on micro particle dynamics in a recirculating aquaculture system. *Aquac. Eng.*, 78(A), 32–41. https://doi.org/10.1016/j.aquaeng.2016.09.002.

Food and Agriculture Organization of the United Nations (FAO). (2022a). The State of World Fisheries and Aquaculture: Towards Blue Transformation. FAO, Rome. https://doi.org/10.4060/cc0461en.

Food and Agriculture Organization of the United Nations (FAO). (2022b). *GLOBEFISH European Price Dashboard. FAO*. https://www.fao.org/in-action/globefish/prices/en/ (Accessed: 15 October 2022).

Forbes, J.F., Marlin, T.E. (1994). Model Accuracy for Economic Optimizing Controllers: The Bias Update Case. *Comput. Ind. Eng. Chem. Res.* 33(8), 1919–1929. https://doi.org/10.1021/ie00032a006

Forbes, J.F., Marlin, T.E. (1996). Design cost: a systematic approach to technology selection for model-based real-time optimization systems. *Comput. Chem. Eng.*, 20(6–7), 717–734. https://doi.org/10.1016/0098-1354(95)00205-7.

François, G., Bonvin, D. (2014). Use of Transient Measurements for the Optimization of Steady-State Performance via Modifier Adaptation. *Ind. Eng. Chem. Res.*, 53(13), 5148–5159. https://doi.org/10.1021/ie401392s.

Galan, A., et al. (2019) Implementation of RTO in a large hydrogen network considering uncertainty. *Optim. Eng.*, 20, 1161–1190. https://doi.org/10.1007/s11081-019-09444-3.

Gao, W., Engell, S. (2005). Iterative set-point optimization of batch chromatography. *Comput. Chem. Eng.* 29(6), 1401–1409. https://doi.org/10.1016/j.compchemeng.2005.02.035.

Gao, W., Wenzel, S., Engell, S. (2016). A reliable modifier-adaptation strategy for real-time optimization. *Comput. Chem. Eng.,* 91, 318–328. https://doi.org/10.1016/j.compchemeng.2016.03.019.

Gaspar, J., Ricardez-Sandoval, L., Jorgensen, J., Fosbøl, P. (2016). Dynamic simulation and analysis of a pilot-scale CO_2 post-combustion capture unit using piperazine and MEA. *IFAC-PapersOnLine*, 49(7), 645–650. https://doi.org/10.1016/j.ifacol.2016.07.246.

Gaspar, J., Ricardez-Sandoval, L., Jørgensen, J., Fosbøl, P. (2017). Design, Economics and Parameter Uncertainty in Dynamic Operation of Post-combustion CO_2 Capture Using Piperazine (PZ) and MEA. *Energy Procedia*, 114, 1444–1452. https://doi.org/10.1016/j.egypro.2017.03.1269.

Geankoplis, C. (2003). Transport processes and separation process principles. 4th ed. Upper Saddle River, NJ: Prentice Hall.

Govatsmark, M., Skogestad, S. (2001). Control structure selection for an evaporation process. *Comput. Aided Chem. Eng.,* 9, 657–662. https://doi.org/10.1016/S1570-7946(01)80104-8.

Guillaume, H., et al. (2019). Introductory overview of identifiability analysis: A guide to evaluating whether you have the right type of data for your modeling purpose. *Environ. Model. Softw.,* 119, 418–432. https://doi.org/10.1016/j.envsoft.2019.07.007.

Haimour, N., Sandall, O. (1984). Absorption of carbon dioxide into aqueous methyldiethanolamine. *Chem. Eng. Sci., 1*39(12), 1791–1796. https://doi.org/10.1016/0009-2509(84)80115-3.

Hart, W., Watson, J. and Woodruff, D. (2011). Pyomo: modeling and solving mathematical programs in Python. *Math. Program. Comput*., 3(3), 219–260. https://doi.org/10.1007/s12532-011-0026-8.

Harun, N., Nittaya, T., Douglas, P., Croiset, E., Ricardez-Sandoval, L. (2012). Dynamic simulation of MEA absorption process for CO_2 capture from power plants. *Int. J. Greenh. Gas Control*, 10, 295–309. https://doi.org/10.1016/j.ijggc.2012.06.017.

Haseltine, E., Rawlings, J. (2005). Critical Evaluation of Extended Kalman Filtering and Moving-Horizon Estimation. *Ind. Eng. Chem. Res.,* 44(8), 2451–2460. https://doi.org/10.1021/ie0343081.

He, Z., Hossein Sahraei, M., Ricardez-Sandoval, L. (2016). Flexible operation and simultaneous scheduling and control of a CO_2 capture plant using model predictive control. *Int. J. Greenh. Gas Control*, 48, 300–311. https://doi.org/10.1016/j.ijggc.2015.10.025.

He, Z., Sahraei, M., Ricardez-Sandoval, L. (2016). Flexible operation and simultaneous scheduling and control of a CO_2 capture plant using model predictive control. *Int. J. Greenh. Gas Control*, 48, 300–311. https://doi.org/10.1016/j.ijggc.2015.10.025.

Heidarinejad, M., Liu, J. and Christofides, P. (2012). Economic model predictive control of nonlinear process systems using Lyapunov techniques. *AIChE J.*, *58*(3), 855–870. https://doi.org/10.1002/aic.12672.

Helei L, Tantikhajorngosol P, Chan C, Tontiwachwuthikul P. (2021). Technology development and applications of artificial intelligence for post-combustion carbon dioxide capture: Critical literature review and perspectives. *Int. J. Greenh. Gas Control*, 108, 103307. https://doi.org/10.1016/j.ijggc.2021.103307.

Hikita, H., Asai, S., Ishikawa, H., Honda, M. (1977). The kinetics of reactions of carbon dioxide with monoethanolamine, diethanolamine and triethanolamine by a rapid mixing method. *Chem. Eng. J*., 13(1), 7–12. https://doi.org/10.1016/0300-9467(77)80002-6.

Hilliard, M. (2008). A Predictive Thermodynamic Model for an Aqueous Blend of Potassium Carbonate, Piperazine, and Monoethanolamine for Carbon Dioxide Capture from Flue Gas**.** *PhD thesis*, University of Texas at Austin.

Hodžić, N., Kazagić, A., Smajević, I. (2016). Influence of multiple air staging and reburning on NOx emissions during co-firing of low rank brown coal with woody biomass and natural gas. *Appl. Energy*, 168, 38–47. https://doi.org/10.1016/j.apenergy.2016.01.081.

Hoff, K., Juliussen, O., Falk-Pedersen, O., Svendsen, H. (2004). Modeling and Experimental Study of Carbon Dioxide Absorption in Aqueous Alkanolamine Solutions Using a Membrane Contactor. *Ind. Eng. Chem. Res.*, 43(16), 4908–4921. https://doi.org/10.1021/ie034325a.

Hossein Sahraei, M., Ricardez-Sandoval, L. (2014). Controllability and optimal scheduling of a CO_2 capture plant using model predictive control. *Int. J. Greenh. Gas Control*, 30, 58–71. https://doi.org/10.1016/j.ijggc.2014.08.017.

Hou, Y., Wu, J., Chen, Y. (2016). Online Steady State Detection Based on Rao-Blackwellized Sequential Monte Carlo. *Qual. Reliab. Eng. Int.,* 32(8), 2667–2683. https://doi.org/10.1002/qre.2067.

HSL. A collection of Fortran codes for large scale scientific computation. http://www.hsl.rl.ac.uk.

Huang, B., et al. (2010). Industrial test and techno-economic analysis of CO_2 capture in Huaneng Beijing coal-fired power station. *Appl. Energy*, 87(11), 3347–3354. https://doi.org/10.1016/j.apenergy.2010.03.007.

Huang, R., Biegler, L., Harinath, E. (2012). Robust stability of economically oriented infinite horizon NMPC that include cyclic processes. *J. Process Control*, *22*(1), 51–59. https://doi.org/10.1016/j.jprocont.2011.10.010.

Huang, R., Patwardhan, S., Biegler, L. (2009). Multi-Scenario-Based Robust Nonlinear Model Predictive Control with First Principle Models. *Comput. Aided Chem. Eng*., 27, 1293–1298. https://doi.org/10.1016/S1570-7946(09)70606-6.

Hughes, R., Kotamreddy, G., Bhattacharyya, D., Omell, B., Matuszewski, M. (2022). Modeling and Bayesian Uncertainty Quantification of a Membrane-Assisted Chilled Ammonia Process for CO_2 Capture. *Ind. Eng. Chem. Res.*, 61(11), 4001–4016. https://doi.org/10.1021/acs.iecr.1c04601.

Idem, R., et al. (2006). Pilot Plant Studies of the CO_2 Capture Performance of Aqueous MEA and Mixed MEA/MDEA Solvents at the University of Regina CO_2 Capture Technology Development Plant and the Boundary Dam CO_2 Capture Demonstration Plant. *Ind. Eng. Chem. Res.*, 45(8), 2414–2420. https://doi.org/10.1021/ie050569e.

IEA. (2020). Key World Energy Statistics 2020. *IEA*. [Online] https://www.iea.org/reports/key-world-energy-statistics-2020.

Jayarathna, S., Lie, B., Melaaen, M. (2013). Amine based CO_2 capture plant: Dynamic modeling and simulations. *Int. J. Greenh. Gas Control*, 14, 282–290. https://doi.org/10.1016/j.ijggc.2013.01.028.

Jiang, T., Chen, B., He, X., Stuart, P. (2003). Application of steady-state detection method based on wavelet transform. *Comput. Chem. Eng.*, 27(4), 569–578. https://doi.org/10.1016/S0098-1354(02)00235-1.

Jung, H., Heo, S., Lee, J. (2021). Model predictive control for amine-based CO_2 capture process with advanced flash stripper. *Control Eng. Pract*., 114, 104885. https://doi.org/10.1016/j.conengprac.2021.104885.

Jung, H., Im, D., Heo, S., Kim, B., Lee, J. (2020). Dynamic analysis and linear model predictive control for operational flexibility of post-combustion CO_2 capture processes. *Comput. Chem. Eng.*, 140, 106968. https://doi.org/10.1016/j.compchemeng.2020.106968.

Kaewsichan, L., Al-Bofersen, O., Yesavage, V., Selim, M. (2001). Predictions of the solubility of acid gases in monoethanolamine (MEA) and methyldiethanolamine (MDEA) solutions using the electrolyte-UNIQUAC model. *Fluid Phase Equilib.*, 183–184, 159–171. https://doi.org/10.1016/S0378-3812(01)00429-0.

Kalman, R. (1960). A New Approach to Linear Filtering and Prediction Problems. *J. Basic Eng.*, 82(1), 35–45 https://doi.org/10.1115/1.3662552.

Kamali, S., Ward V., Ricardez-Sandoval L. (2022). Dynamic modeling of recirculating aquaculture systems: Effect of management strategies and water quality parameters on fish performance. *Aquac. Eng.*, 99, 102294. https://doi.org/10.1016/j.aquaeng.2022.102294.

Kamali, S., Ward, V., Ricardez-Sandoval, L. (2023). Closed-loop operation of a simulated recirculating aquaculture system with an integrated application of nonlinear model predictive control and moving horizon estimation. *Comput. Electron. Agric.*, 209, 107820. https://doi.org/10.1016/j.compag.2023.107820.

Karasu, S., Altan, A., Bekiros, S., Ahmad, W. (2020). A new forecasting model with wrapper-based feature selection approach using multi-objective optimization technique for chaotic crude oil time series. *Energy,* 212, 118750. https://doi.org/10.1016/j.energy.2020.118750.

Karimi, M., Hillestad, M., Svendsen, H. (2011). Capital costs and energy considerations of different alternative stripper configurations for post combustion CO_2 capture. *Chem. Eng. Res. Des.*,89(8), 1229–1236. https://doi.org/10.1016/j.cherd.2011.03.005.

Ko, J., Tsai, T., Lin, C., Wang, H, Li, M. (2001). Diffusivity of Nitrous Oxide in Aqueous Alkanolamine Solutions. *J. Chem. Eng. Data*, 46(1), 160–165. https://doi.org/10.1021/je000138x.

Kornaros, M., Dokianakis, S.N., Lyberatos, G. (2010). Partial Nitrification/Denitrification Can Be Attributed to the Slow Response of Nitrite Oxidizing Bacteria to Periodic Anoxic Disturbances. *Environ. Sci. Technol.*, 44(19), 7245–7253. https://doi.org/10.1021/es100564j.

Krasławski, A. (1989). Review of applications of various types of uncertainty in chemical engineering. *Chem. Eng. Process.*, 26(3), 185–191. https://doi.org/10.1016/0255-2701(89)80016-9.

Kravaris, C., Hahn, J., Chu, Y. (2013). Advanced and selected recent developments in state and parameter estimation. *Comput. Chem. Eng.,* 51, 111–123. https://doi.org/10.1016/j.compchemeng.2012.06.001.

Krishnamoorthy, D., Foss, B., Skogestad, S. (2018). Steady-state real-time optimization using transient measurements. *Comput. Chem. Eng.,* 115, 34–45. https://doi.org/10.1016/j.compchemeng.2018.03.021.

Kvamsdal, H., Jakobsen, J., Hoff, K. (2009). Dynamic modeling and simulation of a CO_2 absorber column for post-combustion CO_2 capture. *Chem. Eng. Process.*, 48(1), 135–144. https://doi.org/10.1016/j.cep.2008.03.002.

Kvamsdal, H., Rochelle, G. (2008). Effects of the Temperature Bulge in CO_2 Absorption from Flue Gas by Aqueous Monoethanolamine. *Ind. Eng. Chem. Res.*, 47(3), 867–875. https://doi.org/10.1021/ie061651s.

Lawal, A., Wang, M., Stephenson, P., Yeung, H. (2009). Dynamic modelling of CO_2 absorption for post combustion capture in coal-fired power plants. *Fuel*, 88(12), 2455–2462. https://doi.org/10.1016/j.fuel.2008.11.009.

Lee, P., Newell, R., Sullivan, G. (1989). Generic Model Control – A Case Study. *Can. J. Chem. Eng*., 67, 478–484. https://doi.org/10.1002/cjce.5450670320.

Le Quéré, C., et al. (2018). Global Carbon Budget. *Earth Syst. Sci. Data*, 10, 2141–2194. https://doi.org/10.5194/essd-10-2141-2018.

Li, Z., Ierapetritou, M. (2008). Robust Optimization for Process Scheduling Under Uncertainty. *Ind. Eng. Chem. Res.,* 47(12), 4148–4157. https://doi.org/10.1021/ie071431u.

Li, K., Leigh, W., Feron, P., Yu, H., Tade, M. (2016). Systematic study of aqueous monoethanolamine (MEA)-based CO_2 capture process: Techno-economic assessment of the MEA process and its improvements. *Appl. Energy,* 165, 648–659. https://doi.org/10.1016/j.apenergy.2015.12.109.

Linga, P., Kumar, R., Englezos, P. (2007). The clathrate hydrate process for post and pre-combustion capture of carbon dioxide. *J. Hazard. Mater*., 149(3), 625–629. https://doi.org/10.1016/j.jhazmat.2007.06.086

Liu, J., et al. (2021) Simultaneous State and Parameter Estimation: The role of Sensitivity Analysis. *Ind. Eng. Chem. Res*., 60, 2971–2982. https://doi.org/10.1021/acs.iecr.0c03793.

Loeffler, D., Anderson, N. (2014). Emissions tradeoffs associated with cofiring forest biomass with coal: A case study in Colorado, USA. *Appl. Energy,* 113, 67–77. https://doi.org/10.1016/j.apenergy.2013.07.011.

Lucia, S., Engell, S. (2012). Multi-stage and Two-stage Robust Nonlinear Model Predictive Control. *IFAC Proc. Vol.,* 45(17), 181–186. https://doi.org/10.3182/20120823-5-nl-3013.00015.

Lucia, S., Finkler, T., Engell, S. (2013). Multi-stage nonlinear model predictive control applied to a semi-batch polymerization reactor under uncertainty. *J. Process Control,* 23(9), 1306–1319. https://doi.org/10.1016/j.jprocont.2013.08.008.

Lucio, M., Ricardez-Sandoval, L. (2020). Dynamic modelling and optimal control strategies for chemical-looping combustion in an industrial-scale packed bed reactor. *Fuel*, 262, 116544. https://doi.org/10.1016/j.fuel.2019.116544.

Luu, M., Abdul Manaf, N., Abbas, A. (2015). Dynamic modelling and control strategies for flexible operation of amine-based post-combustion CO 2 capture systems. *Int. J. Greenh. Gas Control*, 39, 377–389. https://doi.org/10.1016/j.ijggc.2015.05.007.

Mac Dowell, N., Samsatli, N., Shah, N. (2013). Dynamic modelling and analysis of an amine-based post-combustion CO_2 capture absorption column. *Int. J. Greenh. Gas Control*, 12, 247–258. https://doi.org/10.1016/j.ijggc.2012.10.013.

Mac Dowell, N., Shah, N. (2013). Identification of the cost-optimal degree of CO_2 capture: An optimisation study using dynamic process models. *Int. J. Greenh. Gas Control,* 13, 44–58. https://doi.org/10.1016/j.ijggc.2012.11.029.

MacKinnon, L., Li, H., Swartz, C. (2021). Robust model predictive control with embedded multi-scenario closed-loop prediction. *Comput. Chem. Eng.,* 149, 107283. https://doi.org/10.1016/j.compchemeng.2021.107283.

MacKinnon, L., Ramesh, P., Mhaskar, P., Swartz, C. (2022). Dynamic real-time optimization for nonlinear systems with Lyapunov stabilizing MPC. *J. Process Control, 114*, 1–15. https://doi.org/10.1016/j.jprocont.2022.03.009.

Mandur, J., Budman, H. (2014). Robust optimization of chemical processes using Bayesian description of parametric uncertainty. *J. Process Control, 24(2)*, 422–430. https://doi.org/10.1016/j.jprocont.2013.10.004.

Mandur, J.S., Budman, H. (2015). Simultaneous model identification and optimization in presence of model-plant mismatch. *Chem. Eng. Sci., 129*, 106–115. https://doi.org/10.1016/j.ces.2015.02.038.

Mansour, M., Ellis, J. (2003). Comparison of methods for estimating real process derivatives in on-line optimization. *Appl. Math. Model.,* 27(4), 275–291. https://doi.org/10.1016/S0307-904X(02)00124-5.

Marchetti, A. (2022). Feasibility in real-time optimization under model uncertainty. The use of Lipschitz bounds. *Comput. Chem. Eng.,* 168, 108057. https://doi.org/10.1016/j.compchemeng.2022.108057.

Marchetti, A., Chachuat, B., Bonvin, D. (2009). Modifier-Adaptation Methodology for Real-Time Optimization. *Ind. Eng. Chem. Res.* 48(13), 6022–6033. https://doi.org/10.1021/ie801352x.

Marchetti, A., Chachuat, B., Bonvin, D. (2010). A dual modifier-adaptation approach for real-time optimization. *J. Process Control,* 20(9), 1027–1037. https://doi.org/10.1016/j.jprocont.2010.06.006.

Marchetti, A.G., de Avila Ferreira, T., Costello, S., Bonvin, D. (2020). Modifier Adaptation as a Feedback Control Scheme. *Ind. Eng. Chem. Res.*, 59(6), 2261–2274. https://doi.org/10.1021/acs.iecr.9b04501.

Marchetti, A.G., Faulwasser, T., Bonvin, D. (2017a). A feasible-side globally convergent modifier-adaptation scheme. *J. Process Control* 54, 38–46. https://doi.org/10.1016/j.jprocont.2017.02.013.

Marchetti, A., François, G., Faulwasser, T., Bonvin, D. (2016). Modifier Adaptation for Real-Time Optimization–Methods and Applications. *Processes,* 4(4), 55. https://doi.org/10.3390/pr4040055.

Marchetti, A., Singhal, M., Faulwasser, T., Bonvin, D. (2017b). Modifier adaptation with guaranteed feasibility in the presence of gradient uncertainty. *Comput. Chem. Eng.,* 98, 61–69. https://doi.org/10.1016/j.compchemeng.2016.11.027.

Matias, J., Le Roux, G. (2018). Real-time optimization with persistent parameter adaptation using online parameter estimation. *J. Process Control*, 68, 195–204. https://doi.org/10.1016/j.jprocont.2018.05.009.

Mayne, D. (2014). Model predictive control: Recent developments and future promise. *Automatica*, 50(12), 2967–2986. https://doi.org/10.1016/j.automatica.2014.10.128.

Mayne, D. (2016). Robust and stochastic model predictive control: Are we going in the right direction? *Annu. Rev. Control*, *41*, 184–192.

Mechleri, E., Lawal, A., Ramos, A., Davison, J., Mac Dowell, N. (2017). Process control strategies for flexible operation of post-combustion CO 2 capture plants. *Int. J. Greenh. Gas Control*, 57, 14–25. https://doi.org/10.1016/j.ijggc.2016.12.017.

Mendiola-Rodriguez, T., Ricardez-Sandoval, L. (2022). Robust control for anaerobic digestion systems of Tequila vinasses under uncertainty: A Deep Deterministic Policy Gradient Algorithm. *Digital Chem. Eng.,* 3, 100023. https://doi.org/10.1016/j.dche.2022.100023.

Mendoza-Serrano, D., Chmielewski, D. (2012). December. HVAC control using infinite-horizon economic MPC. In: *2012 IEEE 51st IEEE Conference on Decision and Control (CDC),* 6963–6968. 10.1109/CDC.2012.6426071.

Mesbah, A. (2016). Stochastic Model Predictive Control: An Overview and Perspectives for Future Research. *IEEE Control Syst*., 36(6), 30–44. https://doi.org/10.1109/mcs.2016.2602087.

Miletic, I., Marlin, T. (1998). On-line Statistical Results Analysis in Real-Time Operations Optimization. *Ind. Eng. Chem. Res*., 37(9), 3670–3684. https://doi.org/10.1021/ie9707376.

Navia, D., Briceño, L., Gutiérrez, G., de Prada, C. (2015). Modifier-Adaptation Methodology for Real-Time Optimization Reformulated as a Nested Optimization Problem. *Ind. Eng. Chem. Res.,* 54(48), 12054–12071. https://doi.org/10.1021/acs.iecr.5b01946.

Navia, D., Villegas, D., Cornejo, I., de Prada, C. (2016). Real-time optimization for a laboratory-scale flotation column. *Comput. Chem. Eng.*, 86, 62–74. https://doi.org/10.1016/j.compchemeng.2015.12.006.

Negnevitsky, M., Mandal, P., Srivastava, A. (2009). Machine Learning Applications for Load and Price Forecasting and Wind Power Prediction in Power Systems. *International Conference on Intelligent Systems Applications to Power Systems (ISAP),* 1–6. 10.1109/ISAP.2009.5352820.

Nittaya T. (2014). Dynamic Modelling and Control of MEA. *Masters thesis*. University of Waterloo. http://hdl.handle.net.proxy.lib.uwaterloo.ca/10012/8128.

Nittaya, T., Douglas, P., Croiset, E., Ricardez-Sandoval, L. (2014). Dynamic Modeling and Evaluation of an Industrial-Scale CO_2 Capture Plant Using Monoethanolamine Absorption Processes. *Ind. Eng. Chem. Res.*, 53(28), 11411–11426. https://doi.org/10.1021/ie500190p.

Nordhaus, W. (2017). Revisiting the social cost of carbon. *Proc. Nat. Acad. Sci. U.S.A*., 114(7), 1518–1523. https://doi.org/10.1073/pnas.1609244114.

Nwaoha, C., Tontiwachwuthikul, P. (2019). Carbon dioxide capture from pulp mill using 2-amino-2-methyl-1-propanol and monoethanolamine blend: Techno-economic assessment of advanced process configuration. *Appl. Energy*, 250, 1202–1216. https://doi.org/10.1016/j.apenergy.2019.05.097.

OEB: Ontario Energy Board. (2021). Electricity rates, https://www.oeb.ca/rates-and-your-bill/electricity-rates. [accessed 31 August 2021].

Olivier, J., Peters, J. (2018). Trends in Global CO_2 and Total Greenhouse Gas Emissions: 2018 Report. PBL Netherlands Environmental Assessment Agency. The Hague. https://www.pbl.nl/en/publications/trends-in-global-co2-and-total-greenhouse-gas-emissions-2018-report.

Onda, K., Takeuchi, H., Okumoto, Y. (1968). MASS TRANSFER COEFFICIENTS BETWEEN GAS AND LIQUID PHASES IN PACKED COLUMNS. *J. Chem. Eng. Jpn*., 1(1), 56–62. https://doi.org/10.1252/jcej.1.56.

Özyurt, D., Pike, R. (2004). Theory and practice of simultaneous data reconciliation and gross error detection for chemical processes. *Comput. Chem. Eng.,* 28(3), 381–402. https://doi.org/10.1016/j.compchemeng.2003.07.001.

Pan, Y., Lee, J.H. (2003). Identification and Control of Processes with Periodic Operations or Disturbances. *Ind. Eng. Chem. Res.* 42(9), 1938–1947. https://doi.org/10.1021/ie020313y.

Panahi, M., Skogestad, S. (2012). Economically efficient operation of CO_2 capturing process. Part II. Design of control layer. *Chem. Eng. Process*., 52, 112–124. https://doi.org/10.1016/j.cep.2011.11.004.

Patrón, G., Ricardez-Sandoval, L. (2020a). A robust nonlinear model predictive controller for a post-combustion CO_2 capture absorber unit. *Fuel*, 265, 116932. https://doi.org/10.1016/j.fuel.2019.116932.

Patrón, G., Ricardez-Sandoval, L. (2020b). Real-Time Optimization and Nonlinear Model Predictive Control for a Post-Combustion Carbon Capture Absorber. *IFAC-PapersOnLine,* 53(2), 11595–11600. https://doi.org/10.1016/j.ifacol.2020.12.639.

Patrón, G., Ricardez-Sandoval, L. (2022a). An integrated real-time optimization, control, and estimation scheme for post-combustion CO_2 capture. *Appl. Energy*, 308, 118302. https://doi.org/10.1016/j.apenergy.2021.118302.

Patrón, G., Ricardez-Sandoval, L. (2022b). Low-Variance Parameter Estimation Approach for Real-Time Optimization of Noisy Process Systems. *Ind. Eng. Chem. Res*., 61(45), 16780–16798. https://doi.org/10.1021/acs.iecr.2c02897.

Pawlowski, A., Guzmán, J.L., Rodríguez, F., Berenguel, M., Normey-Rico, J.E. (2011). Predictive Control with Disturbance Forecasting for Greenhouse Diurnal Temperature Control. *IFAC. Proc. Vol*. 44(1), 1779–1784. https://doi.org/10.3182/20110828-6-IT-1002.00857.

Poling, B., Prausnitz, J., O'Connell, J. (2007). The properties of gases and liquids. New York: McGraw-Hill.

Quelhas, A., de Jesus, N, Pinto, J. (2013). Common vulnerabilities of RTO implementations in real chemical processes. *Can. J. Chem. Eng.,* 91(4), 652–668. https://doi.org/10.1002/cjce.21738

Rafiei, M., Ricardez-Sandoval, L. (2020). Integration of design and control for industrial-scale applications under uncertainty: a trust region approach. *Comput. Chem. Eng.*, 141, 107006. https://doi.org/10.1016/j.compchemeng.2020.107006.

Rahimi, M., Moosavi, S., Smit, B., Hatton, T. (2021). Toward smart carbon capture with machine learning. *Cell Rep. Phys. Sci.,* 2(4), 100396. https://doi.org/10.1016/j.xcrp.2021.100396.

Ramesh, P., Swartz, C., Mhaskar, P. (2021). Closed-loop dynamic real-time optimization with stabilizing model predictive control. *AIChe J*., 67(10), e17308. https://doi.org/10.1002/aic.17308.

Rangel-Martinez, D., Nigam, K., Ricardez-Sandoval, L. (2021). Machine learning on sustainable energy: A review and outlook on renewable energy systems, catalysis, smart grid and energy storage. *Chem. Eng. Res. Des.*, 174, 414–441. https://doi.org/10.1016/j.cherd.2021.08.013.

Rhinehart, R. (2013). Automated steady state and transient state identification in noisy processes. American control conference. 10.1109/ACC.2013.6580530.

Roberts, P., Williams, T. (1981). On an algorithm for combined system optimisation and parameter estimation. *Automatica*, 17(1), 199–209. https://doi.org/10.1016/0005-1098(81)90095-9.

Rodrigues, D., Marchetti, A.G., Bonvin, D. (2022). On improving the efficiency of modifier adaptation via directional information. *Comput. Chem. Eng.*, 164, 107867. https://doi.org/10.1016/j.compchemeng.2022.107867.

Rúa, J., Hillestad, M., Nord, L.O., (2021a). Model predictive control for combined cycles integrated with CO2 capture plants. *Comput. Chem. Eng.* 146, 107217. https://doi.org/10.1016/j.compchemeng.2020.107217.

Rúa, J., Verheyleweghen, A., Jäschke, J., Nord, L. (2021b). Optimal scheduling of flexible thermal power plants with lifetime enhancement under uncertainty. *Appl. Therm. Eng.,* 191, 116794. https://doi.org/10.1016/j.applthermaleng.2021.116794.

Sahraei, M., Ricardez-Sandoval, L. (2014). Simultaneous Design and Control of the MEA Absorption Process of a CO_2 Capture Plant. *Energy Procedia*, 63, 1601–1607. https://doi.org/10.1016/j.egypro.2014.11.170.

Saltık, M., Özkan, L., Ludlage, J., Weiland, S., Van den Hof, P. (2018). An outlook on robust model predictive control algorithms: Reflections on performance and computational aspects. *J. Process Control*, *61*, 77–102. https://doi.org/10.1016/j.jprocont.2017.10.006.

Salvinder, K. et al. (2019). An overview on control strategies for CO_2 capture using absorption/stripping system. *Chem. Eng. Res. Des*, 147, 319–337. https://doi.org/10.1016/j.cherd.2019.04.034.

Santander, O., Elkamel, A., Budman, H. (2016). Economic model predictive control of chemical processes with parameter uncertainty. *Comput. Chem. Eng.*, 95, 10–20. https://doi.org/10.1016/j.compchemeng.2016.08.010.

Schneider, R., Kenig, E., Górak, A. (1999). Dynamic Modelling of Reactive Absorption with the Maxwell-Stefan Approach. *Chem. Eng. Res. Des.*, 77(7), 633–638. https://doi.org/10.1205/026387699526683.

Schöbel, A., Zhou-Kangas, Y. (2021). The price of multiobjective robustness: Analyzing solution sets to uncertain multiobjective problems. *Eur. J. Oper. Res.*, 291, 782–793. https://doi.org/10.1016/j.ejor.2020.09.045.

Shah, G., Engell, S. (2011). Tuning MPC for desired closed-loop performance for MIMO systems. In: *Proceedings of the 2011 American Control Conference,* 4404–4409. 10.1109/ACC.2011.5991581.

Singh, D., Croiset, E., Douglas, P., Douglas, M. (2003). Techno-economic study of CO_2 capture from an existing coal-fired power plant: MEA scrubbing vs. O_2/CO_2 recycle combustion. *Energy Convers. Manag.*, 44(19), 3073–3091. https://doi.org/10.1016/S0196-8904(03)00040-2.

Singhal, M., Marchetti, A.G., Faulwasser, T., Bonvin, D. (2018). Active directional modifier adaptation for real-time optimization. *Comput. Chem. Eng.*, 115, 246–261. https://doi.org/10.1016/j.compchemeng.2018.02.016.

Smith, J., Van Ness, H., Abbott, M. (2005). Introduction to Chemical Engineering Thermodynamics. 7th International Edition, McGraw-Hill Chemical Engineering Series. McGraw-Hill, Boston.

Straathof, A., Bampouli, A. (2017). Potential of commodity chemicals to become bio-based according to maximum yields and petrochemical prices. *Biofuels Bioprod. Biorefining,* 11(5), 798–810. https://doi.org/10.1002/bbb.1786.

Tejeda-Iglesias, M., Lappas, N., Gounaris, C., Ricardez-Sandoval, L. (2019). Explicit model predictive controller under uncertainty: An adjustable robust optimization approach. *J. Process Control*, 84, 115–132. https://doi.org/10.1016/j.jprocont.2019.09.002.

Tian, Y., Du, W., Qian, F. (2013). Fault Detection and Diagnosis for Non-Gaussian Processes with Periodic Disturbance Based on AMRA-ICA. *Ind. Eng. Chem. Res.* 52(34), 12082–12107. https://doi.org/10.1021/ie400712h.

Tian, X., Negenborn, R., van Overloop, P., María Maestre, J., Sadowska, A., van de Giesen, N. (2017). Efficient multi-scenario Model Predictive Control for water resources management with ensemble streamflow forecasts. *Adv. Water Resour.,* 109, 58–68. https://doi.org/10.1016/j.advwatres.2017.08.015.

Vaidya P., Kenig, E. (2007). CO_2-Alkanolamine Reaction Kinetics: A Review of Recent Studies. *Chem. Eng. Technol*., 30(11), 1467–1474. https://doi.org/10.1002/ceat.200700268.

Valencia-Marquez, D., Flores-Tlacuahuac, A., Ricardez-Sandoval, L. (2015). Technoeconomic and Dynamical Analysis of a CO_2 Capture Pilot-Scale Plant Using Ionic Liquids. *Ind. Eng. Chem. Res.,* 54(45), 11360–11370. https://doi.org/10.1021/acs.iecr.5b02544.

Valipour, M., Ricardez-Sandoval, L. (2021). Assessing the Impact of EKF as the Arrival Cost in the Moving Horizon Estimation under Nonlinear Model Predictive Control. *Ind. Eng. Chem. Res.,* 60(7), 2994–3012. https://doi.org/10.1021/acs.iecr.0c06095.

Valluru, J., Patwardhan, S. (2019). An Integrated Frequent RTO and Adaptive Nonlinear MPC Scheme Based on Simultaneous Bayesian State and Parameter Estimation. *Ind. Eng. Chem. Res*., 58(18), 7561–7578. https://doi.org/10.1021/acs.iecr.8b05327.

Vrugt, J., Bouten, W., Weerts, A. (2001). Information Content of Data for Identifying Soil Hydraulic Parameters from Outflow Experiments. *Soil Sci. Soc. Am. J*., 65(1), 19–27. https://doi.org/10.2136/sssaj2001.65119x.

Wächter, A. and Biegler, L. (2005). On the implementation of an interior-point filter line-search algorithm for large-scale nonlinear programming. *Math. Program*, 106(1), 25–57. https://doi.org/10.1007/s10107-004-0559-y.

Wang, H., Ricardez-Sandoval, L. (2020). Dynamic optimization of a pilot-scale entrained-flow gasifier using artificial recurrent neural networks. *Fue*l, 272, 117731. https://doi.org/10.1016/j.fuel.2020.117731.

Wang, Y., Zhao, L., Otto, A., Robinius, M., Stolten, D. (2017). A Review of Post-combustion CO_2 Capture Technologies from Coal-fired Power Plants. *Energy Procedia*, 114, 650–665. https://doi.org/10.1016/j.egypro.2017.03.1209.

Weiland, R., Dingman, J., Cronin, D, Browning, G. (1998). Density and Viscosity of Some Partially Carbonated Aqueous Alkanolamine Solutions and Their Blends. *J. Chem. Eng. Data,* 43(3), 378–382. https://doi.org/10.1021/je9702044.

Williams, T., Otto, R. (1960). A generalized chemical process model for the investigation of computer control. *IEEE Trans. Commun*., 79(5), 458–473. 10.1109/TCE.1960.6367296.

Wu, Q., Lin, Q., Wang, X., Zhai, M. (2015). An inexact optimization model for planning regional carbon capture, transportation and storage systems under uncertainty. *Int. J. Greenh. Gas. Control,* 42, 615–628. https://doi.org/10.1016/j.ijggc.2015.09.017.

Würth, L., Rawlings, J., Marquardt, W. (2009). Economic dynamic real-time optimization and nonlinear model-predictive control on infinite horizons. *IFAC Proc. Vol.*, *42*(11), 219–224. https://doi.org/10.3182/20090712-4-TR-2008.00033.

Xuan, A., Shen, X., Guo, Q., Sun, H. (2022). Two-stage Planning for Electricity-Gas Coupled Integrated Energy System with Carbon Capture, Utilization, and Storage Considering Carbon Tax and Price Uncertainties. *IEEE Trans. Power Appar. Syst.*, 1–13. 10.1109/TPWRS.2022.3189273.

Yang, B., et al. (2019). Life cycle environmental impact assessment of fuel mix-based biomass and co-firing plants with CO_2 capture and storage. *Appl. Energy*, 252, 113483. https://doi.org/10.1016/j.apenergy.2019.113483.

Yin, X., Decardi-Nelson, B., Liu, J. (2019). Distributed monitoring for the absorption column of a post-combustion CO_2 capture plant. *Int. J. Adapt. Control Signal Process*., 34(6), 757–776. https://doi.org/10.1002/acs.3074.

Yip, W.S., Marlin, T.E. (2004). The effect of model fidelity on real-time optimization performance. *Comput. Chem. Eng.*, 28(1–2), 267–280. https://doi.org/10.1016/S0098-1354(03)00164-9.

You, H., Yuan, Y., Li, J., Ricardez-Sandoval, L. (2018). A Multi-scale model for CO_2 capture: A Nickel-based oxygen carrier in Chemical-looping Combustion. *IFAC-PapersOnLine*, 51(18), 97–102. https://doi.org/10.1016/j.ifacol.2018.09.264.

Yu, M., Miller, D., Biegler, L. (2015). Dynamic Reduced Order Models for Simulating Bubbling Fluidized Bed Adsorbers. *Ind. Eng. Chem. Res.*, 54(27), 6959–6974. https://doi.org/10.1021/acs.iecr.5b01270.

Yuan, Y., Khatibisepehr, S., Huang, B., Li, Z. (2015). Bayesian Method for Simultaneous Gross Error Detection and Data Reconciliation. *AIChe J.*, 68(3), 3232–3248. https://doi.org/10.1002/aic.14864.

Zantye, M., Arora. A, Faruque Hasan, M. (2019). Operational power plant scheduling with flexible carbon capture: A multistage stochastic optimization approach. *Comput. Chem. Eng.*, 130, 106544. https://doi.org/10.1016/j.compchemeng.2019.106544.

Zavala, V., Biegler, L. (2009). The advanced-step NMPC controller: Optimality, stability and robustness. *Automatica*, 45(1), 86–93. https://doi.org/10.1016/j.automatica.2008.06.011.

Zhang, Y., Monder, D., Forbes, J. (2002). Real-time optimization under parametric uncertainty: a probability constrained approach. *J. Process Control*, 12(3), 373–389. https://doi.org/10.1016/S0959-1524(01)00047-6.

Zhang, Q., Turton, R., Bhattacharyya, D. (2018). Nonlinear model predictive control and H robust control for a post-combustion CO_2 capture process. *Int. J. Greenh. Gas Control*, 70, 105–116. https://doi.org/10.1016/j.ijggc.2018.01.015.

Zhang, S., Zhuang, Y., Liu, L., Zhang, L., Du, J., 2019. Risk management optimization framework for the optimal deployment of carbon capture and storage system under uncertainty. *Renew. Sust. Energ. Rev.* 113, 109280. https://doi.org/10.1016/j.rser.2019.109280.

Appendix A - Supplementary Material for Chapter 4

Supplementary Figures

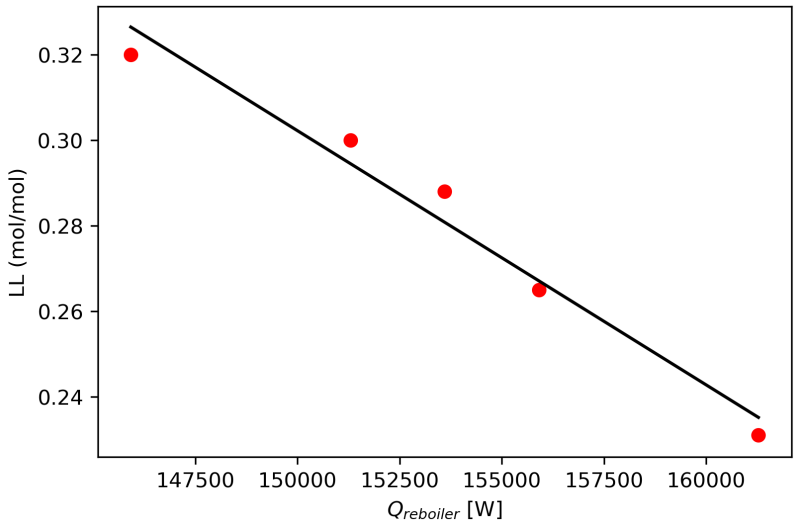

Figure A-1: Data and linear regression fit for recycle lean loading duty correlation.

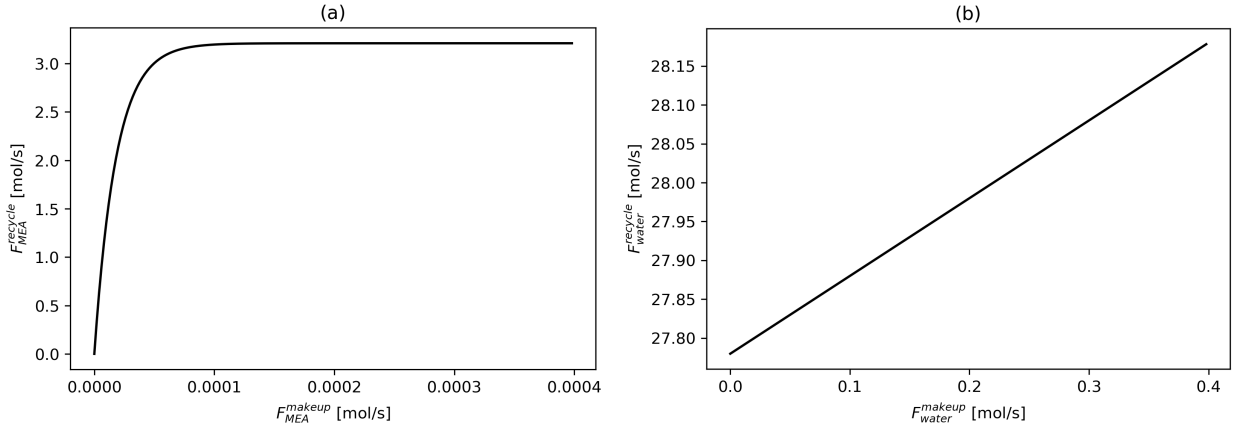

Figure A-2: Recycle stream correlations for a) MEA b) water, assuming nominal water content in the flue gas

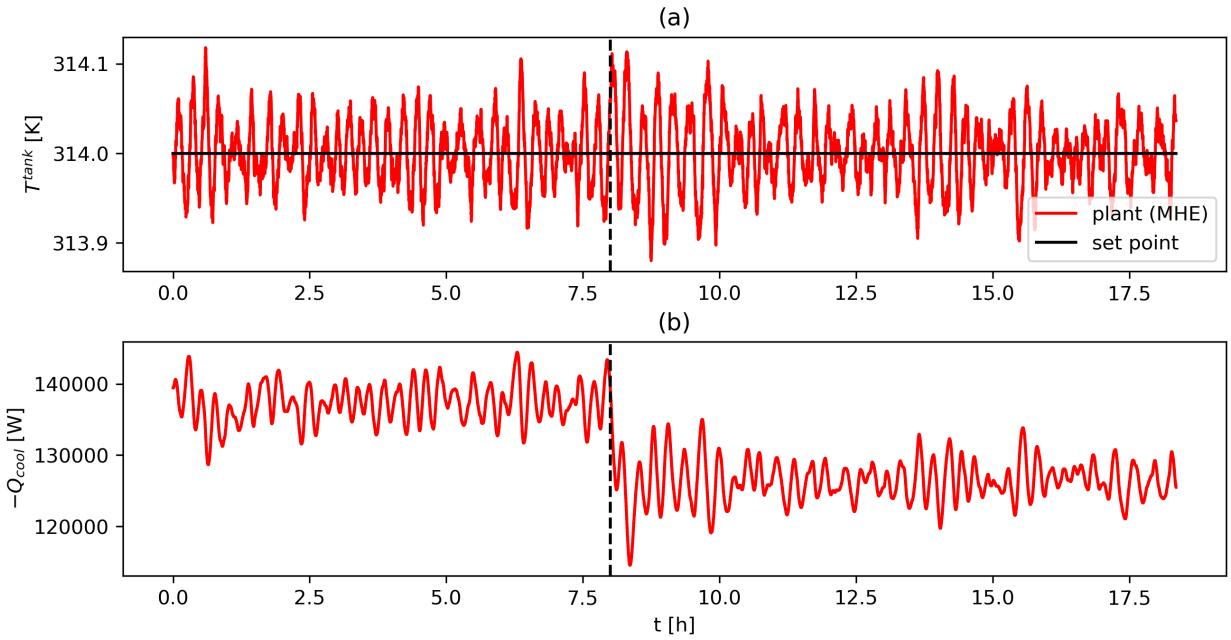

Figure A-3: Scenario A plots of a) tank temperature and b) cooling duty. Dashed lines denote RTO executions.

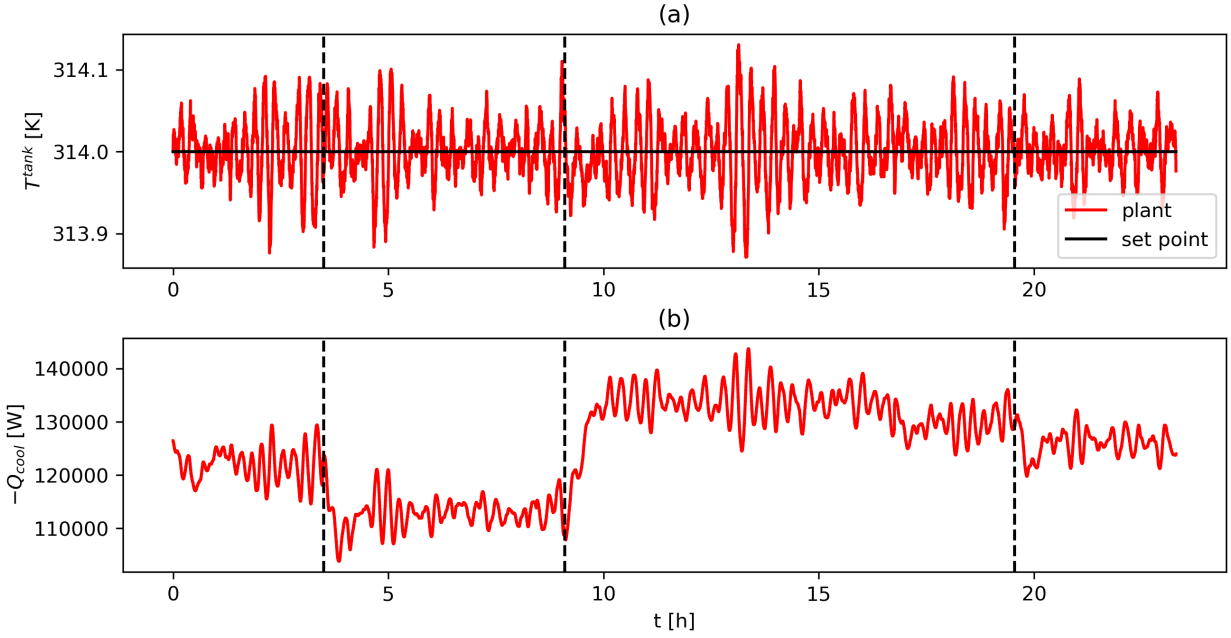

Figure A-4: Scenario B plots of a) tank temperature and b) cooling duty. Dashed lines denote RTO executions.

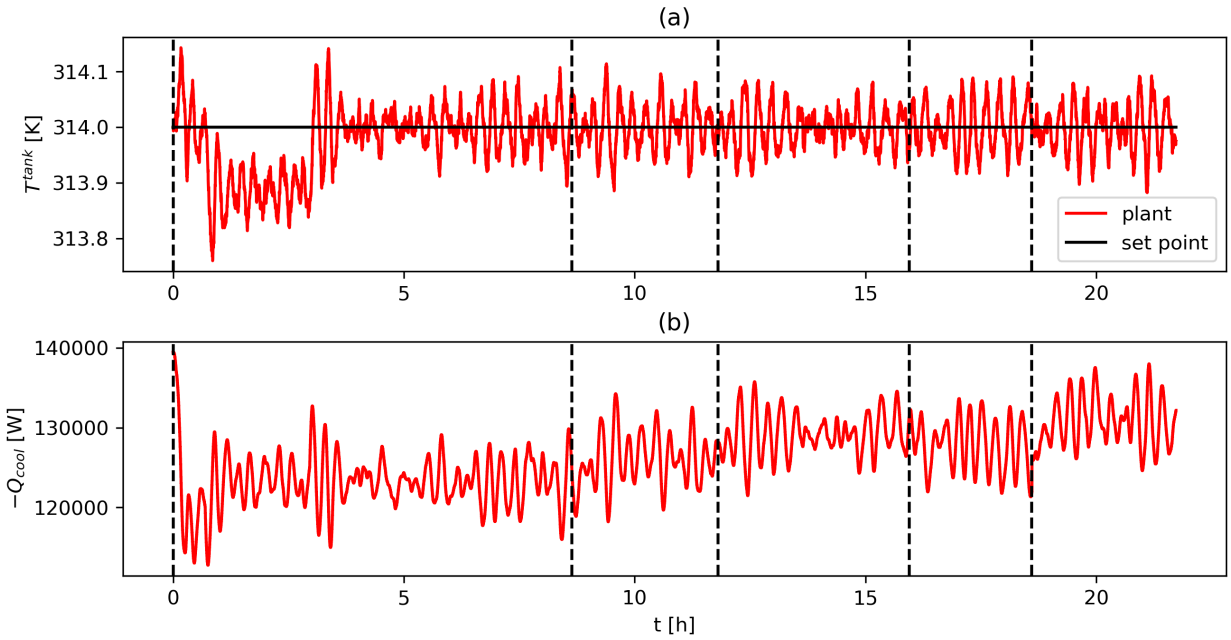

Figure A-5: Scenario C plots of a) tank temperature and b) cooling duty. Dashed lines denote RTO executions.

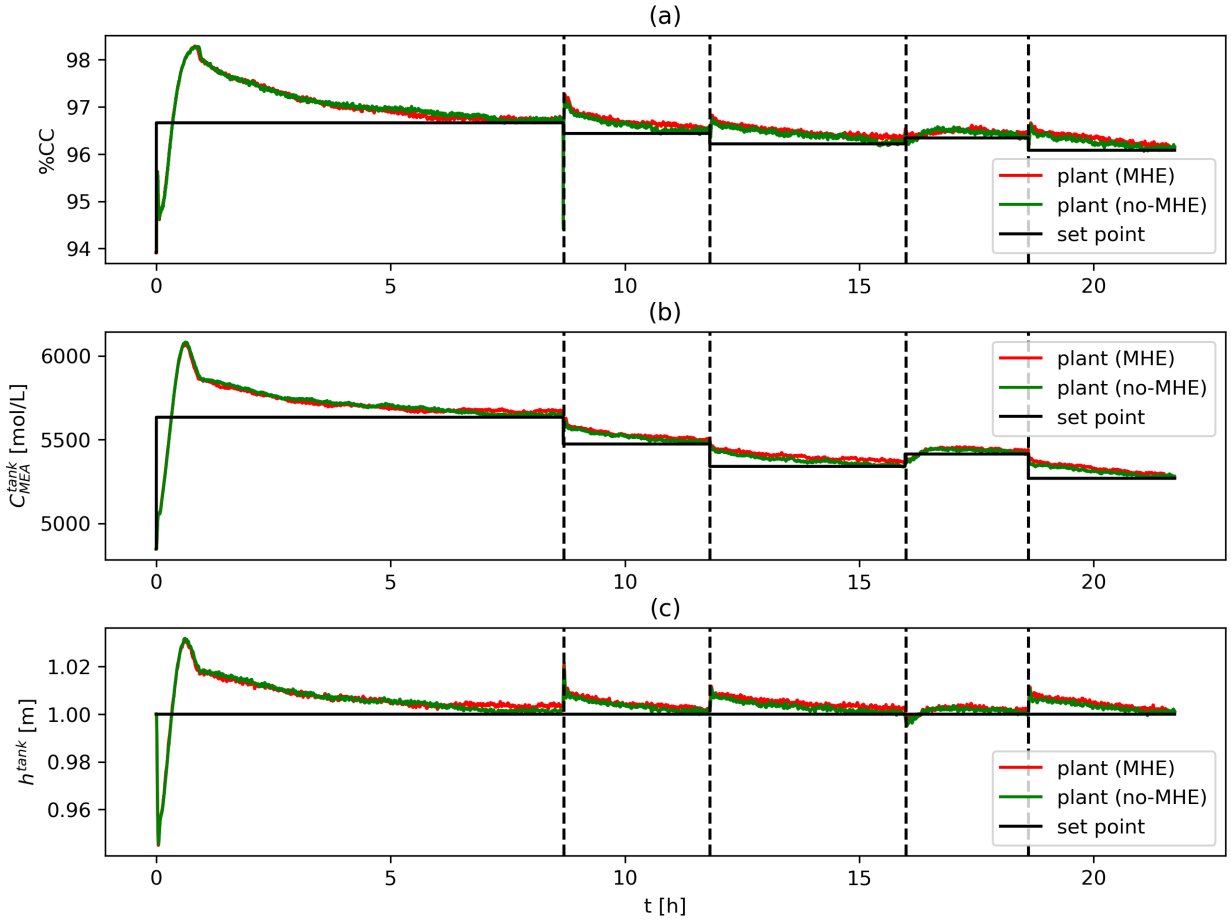

Figure A-6: Controlled variables in MHE and no-MHE cases for Scenario C. Dashed lines denote RTO executions.

Table A-1: Nominal stream conditions for the present model.

	Recycle stream	**Fresh MEA**	**Fresh water**	**Tank outlet (lean solvent)**	**Flue gas**	**Vent gas**	**Rich solvent**
Temperature (K)	366.50	298.00	298.00	314.00	319.71	314.06	318.43
Flowrate (mol/s)							
MEA	3.2098	0.0002	0.0000	3.2100	0.0000	0.0000	3.2098
CO_2	0.9800	0.0000	0.0000	0.9800	0.7020	0.0427	1.6393
Water	27.780	0.0000	0.2000	27.980	0.1000	0.2340	27.846
N_2	0.0000	0.0000	0.0000	0.0000	3.2100	3.2100	0.0000
Total	31.9698	0.0002	0.2000	32.170	4.0120	3.4869	32.6951

Table A-2: Validation cases and conditions for the present model against data from Harun et al. (2012).

						Composition (mol/mol)			
Case #		**Temperature (K)**		**Flowrate (mol/s)**		**Lean solvent**	**Flue gas**		
Current study	[42]	Lean solvent	Flue gas	Lean solvent	Flue gas	LL	Water	CO_2	Packing height (m)
1	32	314	320	29.0	3.52	0.279	0.013	0.177	5.00
2	43	313	327	29.3	5.28	0.231	0.022	0.170	7.80
3	28	313	321	58.2	7.07	0.287	0.016	0.165	5.85
4	39	313	328	60.0	7.02	0.228	0.016	0.169	6.10

Table A-3: Effect of MHE on control and economic performance for scenario C.

Controlled variable	***SSE*** **(MHE)**	***SSE*** **(no-MHE)**	**Performance loss** (%)
$\%CC$ (%)	5240	4975	5.327
C_{MEA}^{tank} (mol/L)	2.747×10^8	2.732×10^8	0.549
$h^{tank}(m)$	1.704	1.628	4.668
Economics	**Cost (MHE)**	**Cost (no-MHE)**	
$\int_0^{18h} C_{process} dt$ $(\$CAD)$	4790	4636	3.322

Preliminary RTO Design

The study herein employs the model and nominal controller used in Chapter 3 and proposes a novel RTO formulation to employ the two-layer approach for the PCC absorber. The RTO is accompanied by a nonlinear MPC (NMPC), both of which use a mechanistic model of the PCC absorber. To the authors' knowledge, this is the first work that makes use of an RTO/NMPC formulation for the PCC absorber. In addition to the RTO/NMPC scheme, a Kalman filter (KF) is used to provide state estimates to the layers, another novelty for the PCC absorber. Moreover, this study also investigates the effects of time-varying carbon tax on the RTO/NMPC under transient changes in the operation of the CO_2 capture absorber unit, which has also not been considered previously. Such carbon taxes are becoming increasingly prevalent as CO_2 emission deterrents and their prices may fluctuate subject to market conditions.

Scheme Formulations

In this work, the two-layer approach was used to maintain the PCC absorber unit near its economic optimum. Moreover, a KF is used to provide state estimates from measurement. The RTO and NMPC are both formulated as nonlinear optimization problems (NLPs). These are employed in conjunction to affect the plant as depicted in Figure A-7.

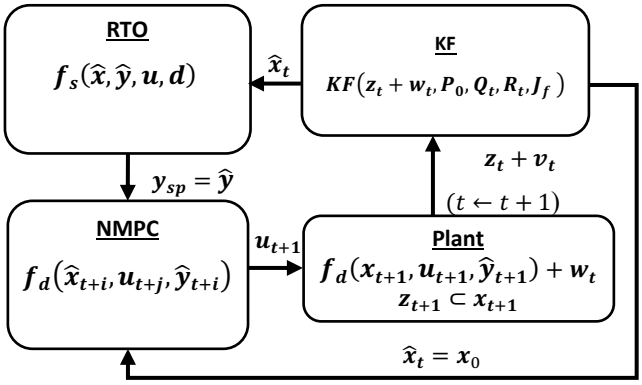

Figure A-7: Arrangement of exchange of information between the RTO, NMPC, KF, and the plant

RTO Formulation

The aim of the RTO in the operation of a process is to minimize the operating cost by computing an economically optimal set point at steady state. The RTO designed for the absorber model is formulated as follows:

$$\min_{\hat{y}} P_{MEA}\dot{m}^{l}_{CO_2,out}(\hat{x}) + P_{CO_2}\dot{m}^{g}_{CO_2,out}(\hat{x}) + P_e W_{pump}(\hat{x})$$
$$s.t. \qquad \text{(A-1)}$$
$$f_s(\hat{x}, \hat{y}, u, d) = 0$$
$$u^l \leq u \leq u^h$$

where $\hat{x} \in \mathbb{R}^{n_x}$, $\hat{y} \in \mathbb{R}^{n_y}$, $u \in \mathbb{R}^{n_u}$, and $d \in \mathbb{R}^{n_d}$ are the estimated state, controlled variables, manipulated variable, and disturbance vectors, respectively. $\dot{m}^{l}_{CO_2,out}(tn/s)$ and $\dot{m}^{g}_{CO_2,out}(tn/s)$ are the liquid and gas outlet CO_2 mass flowrates, respectively, which are contained in the state vector $\hat{x}$. Moreover, W_{pump} (kWh/s) is the pump power

needed to drive the inlets into the absorber, which is contained in the state vector $\hat{\boldsymbol{x}}$. Further, $\boldsymbol{y_{sp}} = \hat{\boldsymbol{y}} \in \mathbb{R}^{n_y}$ is the optimization variable that is passed down as the set point to the NMPC framework, as depicted in Figure A-7. In the case of the PCC absorber column, the optimization variable is the CO_2 removal percentage, defined as in equation (3-13).

In this study, the economic objective was formulated as the sum of three terms as shown in (6). These correspond to MEA degradation cost (P_{MEA}), the carbon tax cost (P_{CO_2}), and the cost of electricity (P_e). The specific rates for these economic terms are $P_{MEA} = 2.99\ \$CAD\ /tn\ CO_2\ captured$ (adjusted for inflation and converted to \$CAD from Singh et al., 2003); $P_{CO_2} = 50\ \$CAD/tn\ CO_2\ emitted$ (Canada.ca, 2019); and $P_e = 0.066\ \$CAD/kWh$ (AUC, 2019), respectively. The MEA degradation cost is incurred owing to the addition of fresh MEA to make up for solvent losses in the process. The carbon tax cost is imposed by state regulatory bodies for releasing CO_2 into the atmosphere. The aforementioned carbon tax rate serves as a nominal value; however, the effect of price variations of this tax will be studied. Lastly, the electricity cost comes from pumping the solvent from an upstream holding tank to the absorber.

$\boldsymbol{f_s}: \mathbb{R}^{n_u} \times \mathbb{R}^{n_d} \longrightarrow \mathbb{R}^{n_x} \times \mathbb{R}^{n_y}$ represents the set of mass, energy balances and algebraic equations shown in Chapter 3. These are solved as a steady-state optimization problem for the RTO.

In the case of the absorber model, the states are phase component concentration and temperatures as stated in Chapter 3 and the manipulated variable for the absorber is the solvent flowrate into the column (F_{in}^{l}). $\boldsymbol{u^l}$ and $\boldsymbol{u^h} \in \mathbb{R}^{n_u}$ are the lower ($10\ mol/s$) and upper ($80\ mol/s$) bounds of the manipulated variable, respectively. These bounds are the same as those used in the NMPC framework and reflect the physical limitations of the controller. While these are not necessary to execute the RTO, they are included in the formulation to ensure that the set points determined by the RTO are reachable by the controller. This ensures that the economically optimal set points are feasible by the overall two-layer scheme.

The steady state model was discretized into ten finite elements in the axial domain using finite differences. Model validation showed that the implementation of the absorber model was in good agreement with previous implementations of the model. For the purposes of this study, the RTO is executed at a fixed 100 NMPC sampling intervals (~21 minutes). Preliminary simulations found that this was sufficient time for the NMPC to reach the setpoints dictated by the RTO for the sizes of disturbances in this study; thus, no steady-state detection measure was used. Furthermore, this study assumes that the model parameters do not change substantially during operation, thus no data reconciliation step is implemented. These two issues will be addressed in future work.

KF Formulation

The axially discretized absorber model has 110 states, which are required to execute the RTO and NMPC. The NMPC deployed herein is the nominal realization of the controller described in Section 3.2. However, it is unlikely that all the states will be available for measurement during the operation of the absorber. Accordingly, a Kalman filter (KF) was used as a state estimator in the proposed scheme. In the current KF scheme, access to all temperatures, gas concentrations, as well as inlet and outlet (boundary) states is assumed, totalling to 74 states. Contrastingly, all interior liquid states, totalling to 36, are estimated. The measured states $\boldsymbol{z_t} \in \mathbb{R}^{n_z}$, where $\boldsymbol{z_t} \subset \boldsymbol{x_t}$, are used to predict all of states $\hat{\boldsymbol{x}}_{\boldsymbol{t}} \in \mathbb{R}^{n_x}$. Additionally, randomly sampled process ($\boldsymbol{w_t} \in \mathbb{R}^{n_x}$) and measurement ($\boldsymbol{v_t} \in \mathbb{R}^{n_z}$) noises were

introduced to the plant. These noises introduce uncertainty and plant-model mismatch into the system. The nonlinear mechanistic model was used to perform *a priori* state predictions, while the discretized equations were symbolically differentiated to produce the Jacobian matrix $\boldsymbol{J_f} \in \mathbb{R}^{n_x \times n_x}$ for the KF to yield *a posteriori* estimates. The initial state covariance matrix $\boldsymbol{P_{0,KF}} \in \mathbb{R}^{n_x \times n_x}$, the process covariance matrix $\boldsymbol{Q_{t,KF}} \in \mathbb{R}^{n_x \times n_x}$, and measurement covariance matrix $\boldsymbol{R_t} \in \mathbb{R}^{\mathrm{N_z} \times \mathrm{N_z}}$ were defined as follows:

$$\boldsymbol{P_{0,KF}} = {\sigma_{P_{0,KF}}}^2 diag({x_{1,nom}}^2, \dots, {x_{n_x,nom}}^2)$$

$$\boldsymbol{Q_{t,KF}} = {\sigma_{Q_{t,KF}}}^2 diag({x_{1,nom}}^2, \dots, {x_{n_x,nom}}^2)$$

$$\boldsymbol{R_{t,KF}} = {\sigma_{R_{t,FK}}}^2 \mathrm{diag}({z_{1,nom}}^2, \dots, {z_{n_z,nom}}^2)$$

where $x_{i,nom} \forall i \{1, \dots, n_x\}$ and $z_{i,nom} \forall i \{1, \dots, n_z\}$ are the states and measurements during nominal operation, described in the following section. $\sigma_{P_{0,KF}} = \sigma_{Q_{t,KF}} = 1e^{-5}$ and $\sigma_{R_t} = 1e^{-6}$ are the corresponding matrix weights. The complete KF scheme is denoted as $\boldsymbol{KF}: \mathbb{R}^{n_z} \rightarrow \mathbb{R}^{n_x}$ for brevity in Figure A-7. As with the NMPC, the KF was executed every sampling interval (12.5 s).

Results

Three test scenarios were implemented to assess the performance of the RTO/NMPC implementation. The scenarios were subjected to the series of disturbances $\boldsymbol{d}$ depicted in Figure A-8. These disturbances impose different sizes and directions of steps every 100 NMPC sampling intervals and were chosen to represent substantial variation around the nominal inlet flue gas flowrate (from 0.8 to 1.2 times its nominal value of $4.012\ \mathrm{mol/s}$), which can be considered as the main disturbance that will affect the operation of this unit. The test scenarios included observing the effects of a fixed and a varying carbon tax; the fixed price tax case used a price of $50\$CAD/tn\ CO_2$ emitted, while the varying carbon tax cost features subsequent $5\$CAD$ steps up from the base price of $50\$CAD/tn\ CO_2$ emitted as displayed in Figure A-9.

The test scenarios, presented next, correspond to 1) no RTO implemented (only regulation by NMPC to the initial nominal set-point), 2) RTO /NMPC framework (Figure A-7) with a fixed carbon tax, and 3) RTO/NMPC framework with a varying carbon tax (Figure A-9). In all scenarios, the disturbance followed the trajectory shown in Figure A-8 whereby it is at its nominal value for 25 sampling intervals (~5 minutes) and a step change is introduced every 100 sampling intervals (~21 minutes) thereafter. The inlet solvent flowrate (manipulated variable) and percent carbon captured (controlled variable) results for these scenarios are shown in Figure A-10 and Figure A-11, respectively.

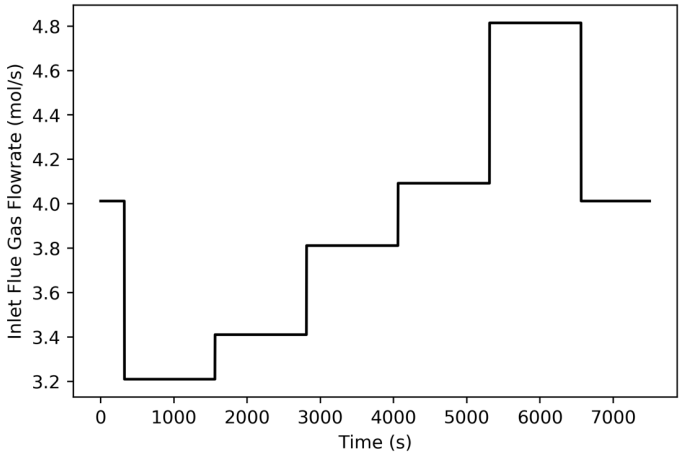

Figure A-8: Inlet flue gas flowrate (disturbance).

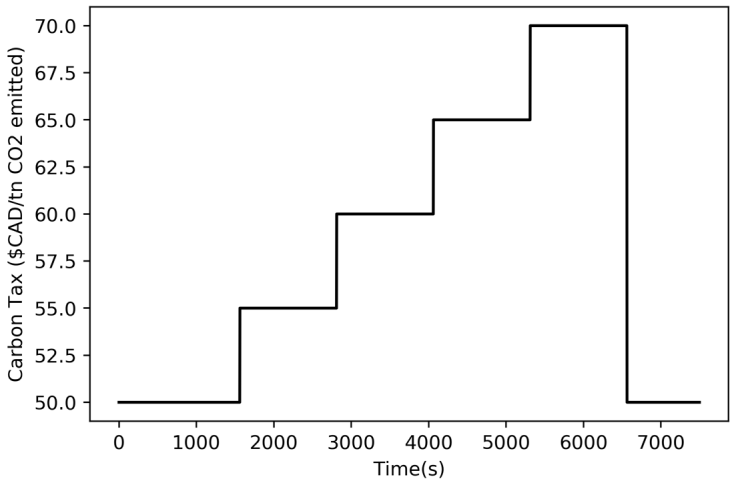

Figure A-9: Carbon tax profile for varying tax case.

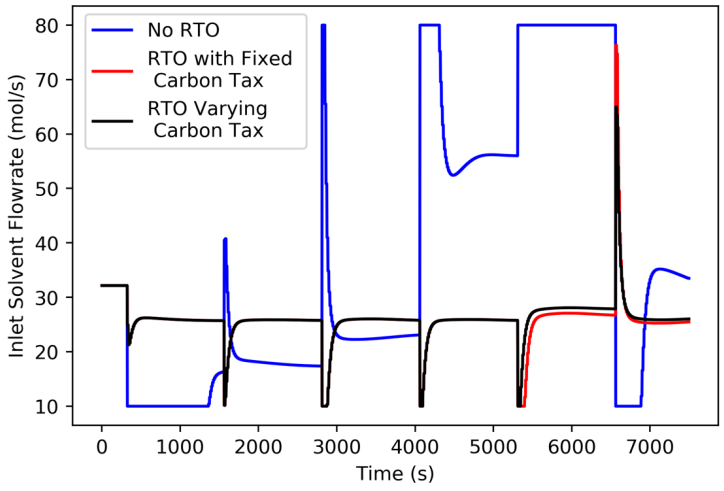

Figure A-10: Inlet solvent flowrate (manipulated variable) for the scenarios tested.

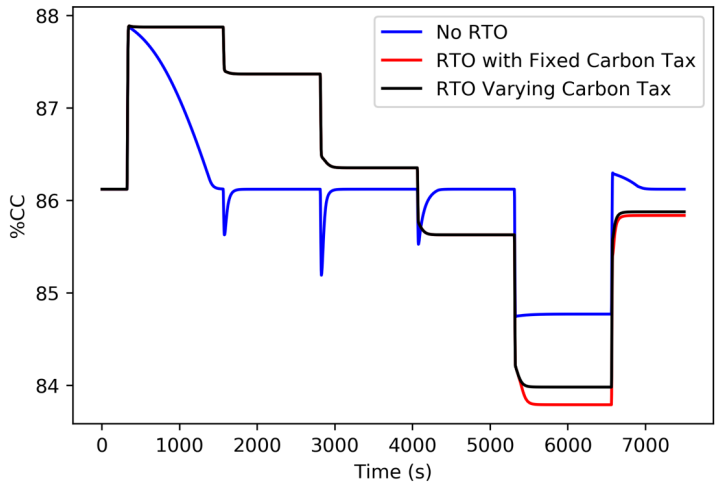

Figure A-11: Percent carbon captured (controlled variable) for the scenarios tested.

The scenarios were assessed on the basis of their process cost from the first to the final disturbance, these results are displayed in Table A-4. The costs were calculated using the expression employed in the RTO objective function shown in (6). This instantaneous price rate is multiplied by the time interval lengths to give a total process cost comprised of the MEA degradation, carbon tax, and electricity cost over the operating period considered in this study. The total cost is also broken down into its aforementioned sources. The results for each scenario are discussed next.

Table A-4. Process cost for scenarios tested ($CAD).

Scenario	**Total Cost**	**Tax Cost**	**MEA Cost**	**Electrical Cost**
No RTO (fixed tax)	13.46	6.31	7.13	0.01
No RTO (varying tax)	14.64	7.50	7.13	0.01
RTO (fixed tax)	11.98	6.31	5.67	0.01
RTO (varying tax)	13.23	7.51	5.70	0.01

NMPC Only (no RTO)

The NMPC was implemented without the RTO to regulate the set point subject to the disturbances shown in Figure A-8. The 86.12 %CC set point in this case corresponds to the steady state operation of the absorber using the nominal inlet flue gas fractions reported in Harun et al. (2012). The objective of this case was to establish a "do-nothing" baseline cost, in which no set point updates based on process economics are considered.

It can be observed in Figure A-11 that the controller is able to successfully regulate to the set point for all except one of the disturbances introduced. This exception occurs in the 5th disturbance interval (from ~5300 seconds to ~6600 seconds) and corresponds to a large +18% step-up in the disturbance variable with respect to its nominal value, as shown in Figure A-8. During this period, Figure A-10 shows that the controller holds the manipulated variable at its upper bound (80 mol/s) and despite this, the set point appears to be unreachable as the %CC reaches an asymptote in Figure A-11. This unreachable set point occurs because it becomes increasingly difficult to achieve the same %CC

for flue gas flowrates that are largely increased due to the upper bound of the manipulated variable. For this upper solvent flowrate bound and concentration, the solution has been saturated with CO_2 and has no remaining absorption capacity. Typically, the flue gas flowrate serves as a manipulated variable for smaller disturbances (i.e. $\pm 10\%$). Larger disturbances in the system would be handled by a downstream reboiler or upstream MEA make-up stream that would enrich the concentration of the MEA solvent fed to the absorber, thereby increasing the CO_2 absorption capacity. It is important to note that the issue of unreachable set points could have been avoided by executing RTOs when each disturbance was introduced. This will be shown in the next section.

Using the results from the no-RTO scenario, the process costs were calculated for the fixed and varying tax rates. As noted in Table A-4, the cost of this experiment is about 8.77% higher in the varying cost case than the fixed cost case. This increase comes entirely from carbon tax. The increased cost occurs as the fixed cost case considers only the minimum cost in the varying cost case. This disparity would widen with longer periods of operation where the cost can accrue over time.

NMPC and RTO

The NMPC tested in the previous section was implemented along with the RTO for fixed and varying carbon taxes. From Figure A-10, it is clear that the NMPC is not required to perform as aggressive of control actions in the RTO/NMPC scheme compared to the no-RTO scheme. This is shown in the manipulated variable, which is at bounds substantially less than in the no-RTO scenario. Furthermore, it can be observed in Figure A-11 that the controller successfully tracks the new set points supplied by the RTO before the next disturbance enters the system for all intervals. In fact, steady state is generally reached quickly, resulting in short transition times. Generally, the control profiles (Figure A-10) for both the RTO/NMPC cases (fixed and varying carbon tax) look similar in shape; however; it can be observed that the RTO selects slightly different removal set points in Figure A-11 for the 5^{th} and 6^{th} disturbances (from ~5300 s to ~7800 s). The 5^{th} disturbance corresponds to a combination in the highest carbon tax rate ($70\$CAD$) and disturbance ($4.814\ mol/s$) entering the process. The confluence of these factors results in the largest RTO set point disparity between the fixed and variable tax cost cases. The 6^{th} disturbance is another large step down in both the flue gas flowrate (-20%) and carbon tax rate (-40%). Aside from these two periods, however, there is not a marked difference between the set points determined by the fixed and varying tax RTOs. This suggests that the RTO is insensitive to carbon tax and disturbance variable changes unless they are large.

The RTO scenario with varying carbon tax incurred significantly (10.43%) more cost than the fixed carbon tax scenario This is to be expected as the tax is increasing from its nominal value, which was considered in the fixed tax case. Nonetheless, the economic benefit of employing the RTO is evident in Table A-4, which shows cost reductions of 11.00% and 9.63% for the fixed and varying carbon tax cases, respectively, with respect to the no-RTO cases. Moreover, as shown in Table A-4, the RTO in both tax cases gains most of its economic benefit by decreasing the MEA degradation cost, which is reflected in the similar tax cost incurred in these cases. This reinforces the idea that the RTO chooses to reduce costs via the MEA degradation cost and is insensitive to the carbon tax rate unless it is subjected to large changes. These results show economic differences over the short operational time of ~130 min. This would be even further apparent over a longer operational period of hours or days, which a PCC system would

experience in real operation. Moreover, this study considers the operation of a pilot-scale unit, the magnitude of these costs would be much higher in industrial-scale.

Summary

An RTO/NMPC implementation for a PCC absorber is presented. The implementation of a nonlinear mechanistic dynamic model used to formulate an RTO and an NMPC in tandem is a novelty for this process. The RTO simultaneously considers carbon taxes, energy prices, and solvent degradation; this is the most complete economic function used in online optimization of PCC to date. The proposed scheme leads to improved steady state process economics across disturbance and price change scenarios.

Appendix B - Supplementary Material for Chapter 5

Payback Period

Decomposing the RTO period revenues as in Section 5.2.1 for a single RTO period, the following expressions can be constructed for a system in which the set point is changed at $t = 0$:

$$R_f = P_f\left(T_f - \tau\right) + R_t \tag{B-1}$$

And a system where the set point remains the same $t = 0$:

$$R_i = P_i T_f \tag{B-2}$$

where R_f and R_i (\$) in the LHS denote the revenue after and before the set point change, respectively. P_f and P_i ($\$/time$) on the RHS denote the steady-state profit/price rates before and after the set point is changed, respectively. τ $(time)$ denotes the transient time and R_t (\$) denotes the transient revenue. T_f $(time)$ denotes the total operating time.

If the transient between set points (R_t) is expensive or less profitable, the revenue obtained when changing the set point can be compared to the revenue obtained if the system had remained at the old set point:

$$R_f - R_i = P_f\left(T_f - \tau\right) + R_t - P_i T_f \tag{B-3}$$

As such, the equivalence (i.e., break-even) point occurs when:

$$0 = P_f\left(T_f - \tau\right) + R_t - P_i T_f \tag{B-4}$$

which allows for the payback period $T_{payback}(time)$ to be expressed as:

$$T_{payback} \equiv T_f = \frac{P_f \tau - R_t}{P_f - P_i} \tag{B-5}$$

as P_f, P_i, R_t, and τ become known after the system reached its new set point, this expression can be used for the prediction of the length of time for a set point change to be economically justified.

Supplementary Data

*Table B-1: Model parameters for the forced-circulation evaporator. * denotes nominal value(s) for uncertain parameter(s).*

Parameter	Value
Mass holdup	$H = 20\ kg$
Unit conversion constant	$K = 4\ kg/kPa$
Condenser heat transfer coefficient*	$UA_2 = 4\ kW/°C$
Heat capacity of water	$C_p = 0.07(kW \cdot min)/(kg \cdot °C)$
Latent heat of evaporation (water)	$\kappa = 38.5\ (kW \cdot min)/kg$
Latent heat of evaporation (saturated steam)	$\kappa_s = 36.6\ (kW \cdot min)/kg$
Price of electricity (pumping)	$P_e = 0.001009\ \$/kg$
Price of steam	$P_s = 0.60\ \$/kg$
Price of cooling water	$P_w = 0.60\ \$/kg$

*Table B-2: Model parameters associated with the Williams-Otto CSTR as implemented in this study. * denotes nominal value(s) for uncertain parameter(s).*

Parameter	Value
Mass holdup	$W = 2104.7\ kg$
Pre-exponential factor 1	$A_1 = 1.6599 \times 10^6\ s^{-1}$
Pre-exponential factor 2	$A_2 = 7.2117 \times 10^8\ s^{-1}$
Pre-exponential factor 3	$A_3 = 2.6745 \times 10^{12}\ s^{-1}$
Nominal activation energy 1*	$E_1 = 6666.7\ K$
Nominal activation energy 2*	$E_2 = 8333.3\ K$
Nominal activation energy 3*	$E_3 = 11111\ K$
Price of substrate *A*	$P_A = 0.7623\ \$/kg$
Price of substrate *B*	$P_B = 5.5542\ \$/kg$
Price of heating tank	$P_T = 0.01\ \$/(s.K)$
Sales price of product *D*	$P_D = 11.4338\ \$/kg$
Sales price of product *E*	$P_E = 0.2592\ \$/kg$

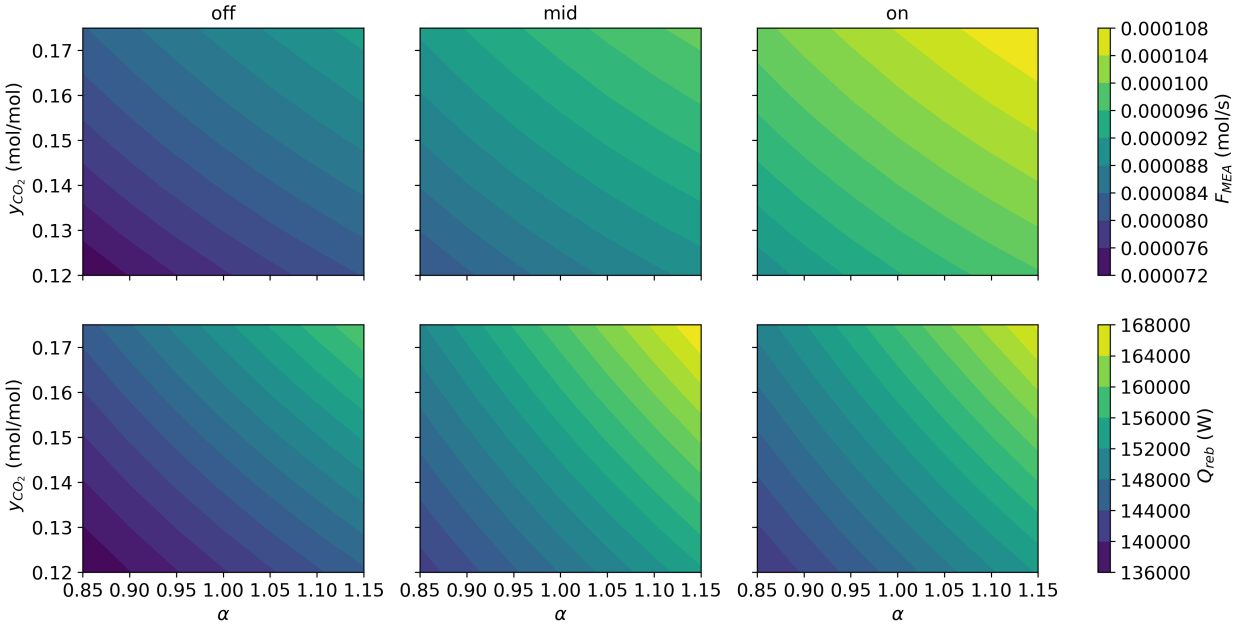

Figure C-1: Optimal manipulated variables under the sensitivity analysis Scenario A.

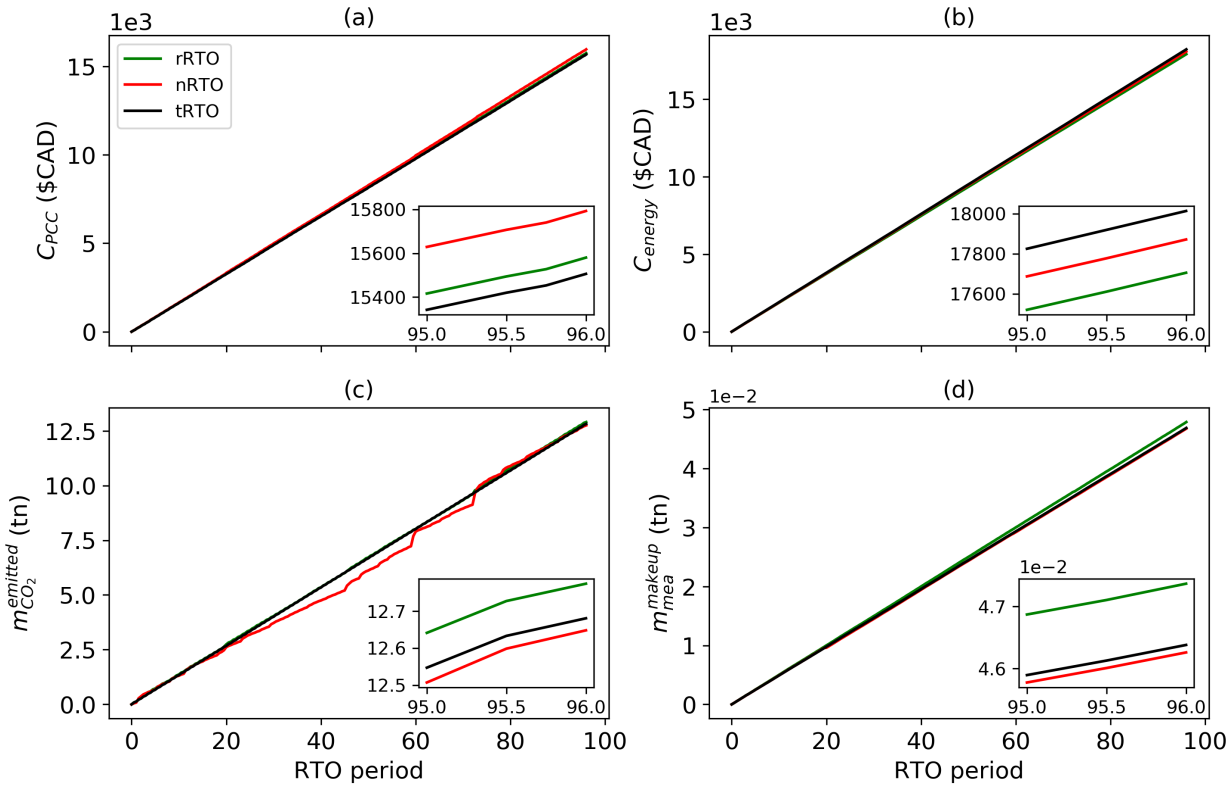

Figure C-2:Cumulative a) PCC cost, b) energy penalty, c) CO_2 emissions, d) fresh MEA used for scenario D.

Dynamic Transition

The control and estimation structure deploys a nonlinear model predictive controller (NMPC) and moving horizon estimator (MHE), respectively. The sampling interval is assumed to be $12.5\,seconds$ to capture quick process dynamics and allow for good feedback control. The NMPC and MHE employ the dynamic mechanistic model ($\boldsymbol{f_d}$) outlined in the supplementary information along with a least-squares objective; for brevity, the respective formulations are omitted herein. As depicted in Figure 4-1, the NMPC layer uses the manipulated variables to regulate the PCC plant towards the RTO-defined set points, while the MHE uses the available measurements to estimate states as feedback to the NMPC; together these layers to achieve closed-loop dynamic operation of the PCC plant. As it pertains to the assessment of the control scheme under different disturbance and parameter estimates, the sum of squared errors with respect to the true set point is used here to quantify control performance:

$$SSE_y = \sum_{i=1}^{n} \left(y_i - y_{sp}^{true}\right)^2 \tag{C-1}$$

where y and y_{sp}^{true} denote a controlled variable and its set point, respectively, as described in Chapter 4. In particular, the dynamics of the key performance variables $\%CC$ and C_{MEA}^{tank} will be analyzed here as they will primarily dictate the removal performance of the absorber.

Dynamics Example (Scenario B)

From a dynamic performance standpoint, the transition between PCC periods 14 and 15 were observed as illustrated in Figure C-3 for the key performance variables and Figure C-4 for ancillary variables. The true flue gas CO_2 composition (i.e., disturbance) in period 14 is $y_{CO_2}^{flue} = 0.154$. In period 15, the true disturbance value is $y_{CO_{2,TV}}^{flue} = 0.164$ and the estimated values are $y_{CO_{2,DE}}^{flue} = 0.137$ and $y_{CO_2,lv-DE}^{flue} = 0.163$. Accordingly, the lv-PE leads to a significantly lower relative estimation error of ~0.6% (~0.09 $mol\%$ in absolute terms) while the regular PE leads to an estimation error ~16.4% for this period. As noted above, higher estimation error results in significant losses in steady state economics over long periods of time but also deterioration in control performance as shown in Figure C-3.

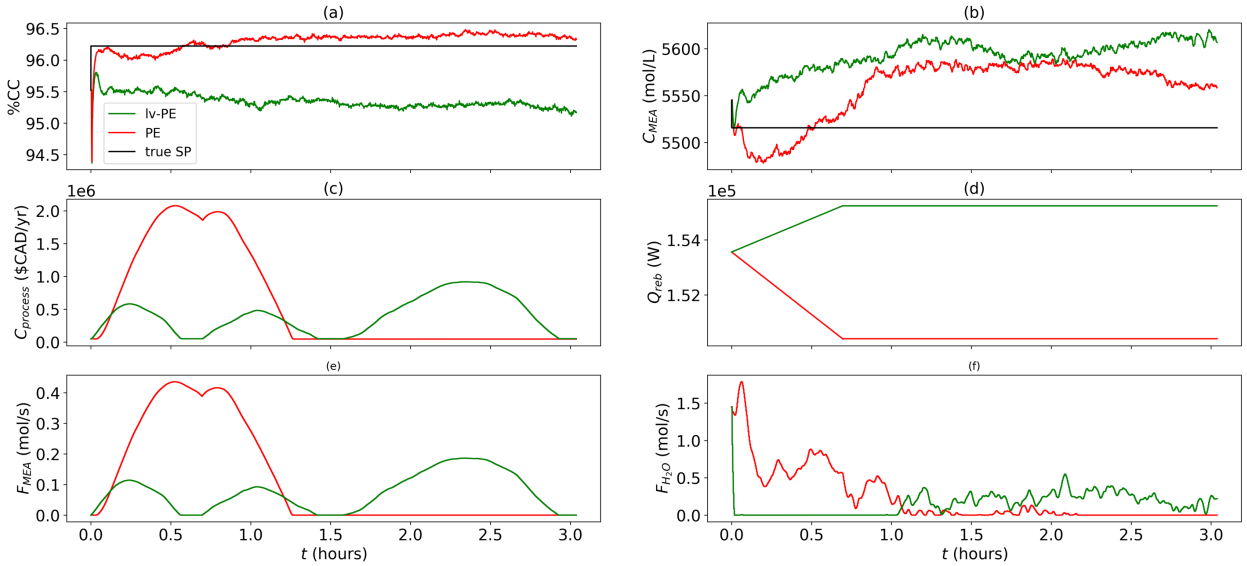

Figure C-3: Dynamic performance of transition between RTO periods 14 and 15.

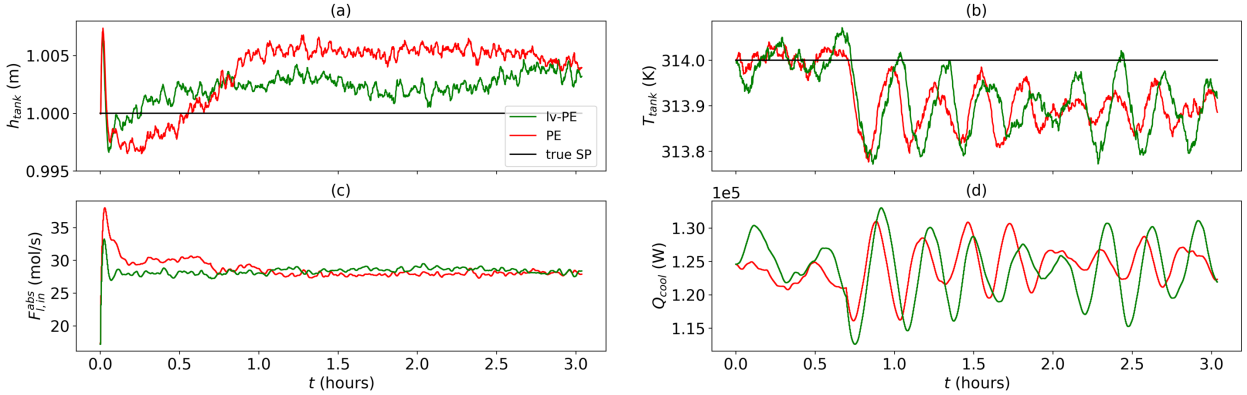

Figure C-4: Dynamic performance of ancillary controlled and manipulated variables in scenario B.

Moreover, as defined in equation (13), the sums of squared errors are provided in Table C-1.

Table C-1: Dynamic tracking metrics for transition between RTO periods 14 and 15.

	PE	lv-PE
$SSE_{\%CC}$	2709	93.01
$SSE_{C_{MEA}^{tank}}$	21.64×10^6	9.962×10^6

The SSE for $\%CC$ and C_{MEA}^{tank} is two and one order of magnitude lower for the lv-DE scheme than the DE scheme, respectively; this is attributable to the improved accuracy of the $y_{CO_2}^{flue}$ estimate for lv scheme. The lower estimation error results in the final operating conditions in Figure C-3a and b being closer to the true set points (i.e., less offset) in the controlled variables as affected by the NMPC and MHE whereby better disturbance estimates are provided to the dynamic mechanistic models used for control and estimation, respectively. Figure C-3c shows the dynamic cost for the competing schemes in which both schemes subject the system to temporary increases in cost through increased MEA makeup (Figure C-3e trajectory coincides with that of Figure C-3c). In the control scheme with lv-PE, the

elevated cost occurs through a single rapid ($\sim 1.25\ hr$) peak in MEA makeup, while the elevated cost in the PE/control scheme come from three consecutive long peaks in the MEA makeup. Both makeups eventually go to effectively zero as the steady state makeup burden is mostly achieved by solvent regeneration in the stripper-side reboiler in Figure C-3d.

While the lv-PE RTO chooses to increase reboiler duty, the DE RTO chooses to decrease it. This results in lower recycle CO_2 concentration, thus lower lean loading (i.e., CO_2 content in the lean solvent) in the lv-PE control scheme. Moreover, Figure C-3f shows that the lv-PE control scheme also effectively adds zero water at the new steady state, while the PE control scheme continues adding water to the system, thus diluting the lean amine solution. In aggregate, these factors lead to the higher removal rate achieved by the lv-PE control scheme despite a lower MEA concentration in the buffer tank. The higher removal rate and higher carbon sales rate offset the higher reboiler duty used by the lv-DE scheme with a low annualized steady-state operating cost of $50{,}224\ \$CAD/yr$ compared to a higher $51{,}994\ \$CAD/yr$ achieved by the PE.

Dynamic Example (Scenario C)

Dynamically, the transition between PCC periods 5 and 6 were observed as illustrated in Figure C-5. The flue gas CO_2 composition (i.e., disturbance) in period 5 is $y_{CO_2}^{flue} = 0.170$ while the disturbance value in period 6 is $y_{CO_2}^{flue} = 0.188$. In this scenario, the PE must estimate the model parameters given in Chapter 6 (i.e., $\boldsymbol{\theta_{p,nom}} = [0.381 \quad 0.677 \quad 0.974]^T$) to pass to the NMPC and MHE. The lv-PE yielded an estimate of $\widehat{\boldsymbol{\theta}}_{\boldsymbol{p,lv-PE}} = [0.380 \quad 0.345 \quad 0.983]^T$ while the regular PE yielded $\widehat{\boldsymbol{\theta}}_{\boldsymbol{p,PE}} = [0.363 \quad 0.236 \quad 1.136]^T$. These estimates correspond to percent errors of $[0.2 \quad 49 \quad 0.9]^T$ and $[4.7 \quad 65 \quad 17]^T$, respectively, thus the lv-PE scheme improves estimate quality across all parameters. It should be noted that the estimate for $\theta_2 = \gamma_{CO_2}$ is poor in both cases, suggesting that the sensitivity of the measurement predictions to this parameter is low. This occurs as the mass transfer model for CO_2 is more elaborate and makes less simplifications than that of the other species; thus, it is less reliant on the activity coefficient for prediction accuracy. Moreover, mass transfer of CO_2 is dictated greatly by the enhancement factor that is considered in the mass transfer coefficient calculation [9], not in the equilibrium pressure as effected by the activity coefficient. Nevertheless, the control performance is found to be adequate, as shown in Figure C-5 for the key performance variables and Figure C-6 for the ancillary variables.

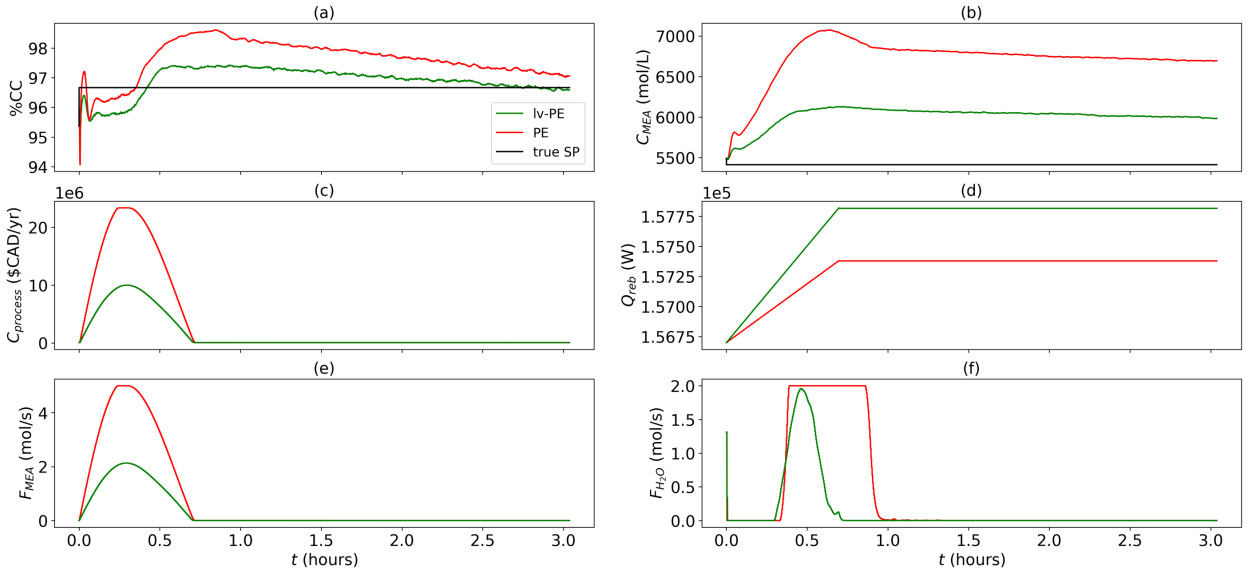

Figure C-5: Dynamic performance of transition between RTO periods 5 and 6.

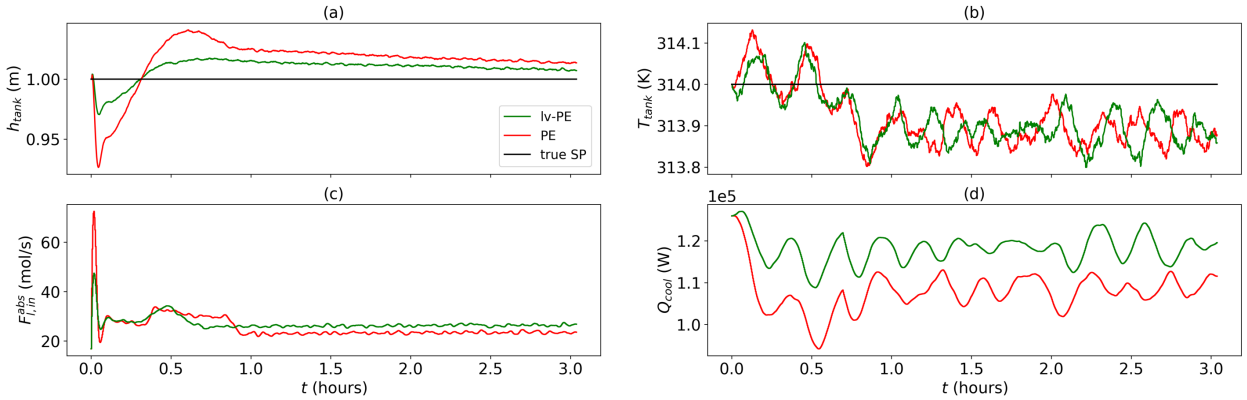

Figure C-6: Dynamic performance of ancillary controlled and manipulated variables in scenario C.

The sums of squared errors and dynamic costs are provided in Table C-2.

Table C-2: Dynamic tracking metrics for transition between RTO periods 5 and 6.

	PE	lv-PE
$SSE_{\%CC}$	4687	986.3
$SSE_{C_{MEA}^{tank}}$	6221×10^6	1312×10^6

Figure C-5a show the improvements in control performance of $\%CC$, which is the key performance variable in this system, whereby the lv-PE control scheme can track the set point almost exactly in the given time while the regular PE scheme remains with a mismatch. This is also reflected in the $SSE_{\%CC}$ in Table C-2, which is an order of magnitude lower for the lv-PE control scheme. Moreover, while there remains significant offset for C_{MEA} in Figure C-5b, the tracking performance is also significantly better in the lv-PE control scheme as reflected in $SSE_{C_{MEA}^{tank}}$. As with the previous scenario, the dynamic costs are mainly driven by the MEA makeup as indicated by the matching profiles in Figure C-5c and Figure C-5e, where the lv-PE control scheme uses significantly less MEA, leading to a more economic

transient. A less aggressive control approach is also reflected in the water makeup Figure C-5f, whereby the lv-PE control scheme peaks briefly while the regular PE control scheme applies bang-bang control for a small period of time. The more efficient control exhibited by the lv-PE scheme is facilitated by an increase in the reboiler duty (Figure C-5d) to a higher level that the regular PE scheme whereby less makeup is required as a result.

Eventually, both schemes' makeups (Figure C-5e and f) effectively approach zero as the systems approaches steady state, this is accompanied by a commensurate drop in process cost (Figure C-5c), whereby the final steady state costs for the lv-PE and PE scheme are $46{,}863\ \$CAD/yr$ and $47{,}886\$CAD/yr$, respectively.

Appendix D - Supplementary Material for Chapter 7

Table D-1: Data for the evaporator scenario.

	Mean processing cost $\bar{M}(\$/kg)$					Mass processed $m \times 10^3(kg)$				
T	MA	pMA2+	pMA2	pMA1+	pMA1	MA	pMA2+	pMA2	pMA1+	pMA1
2000	N/A	654	728	566	566	N/A	481	535	473	617
2500	724	613	694	540	540	524	601	695	590	778
3000	764	644	691	593	593	603	723	769	694	845
3500	690	579	614	622	622	789	969	1,029	792	940
4000	600	558	573	669	669	1,057	1,215	1,236	857	998
4500	526	535	595	644	644	1,413	1,267	1,401	966	1,168

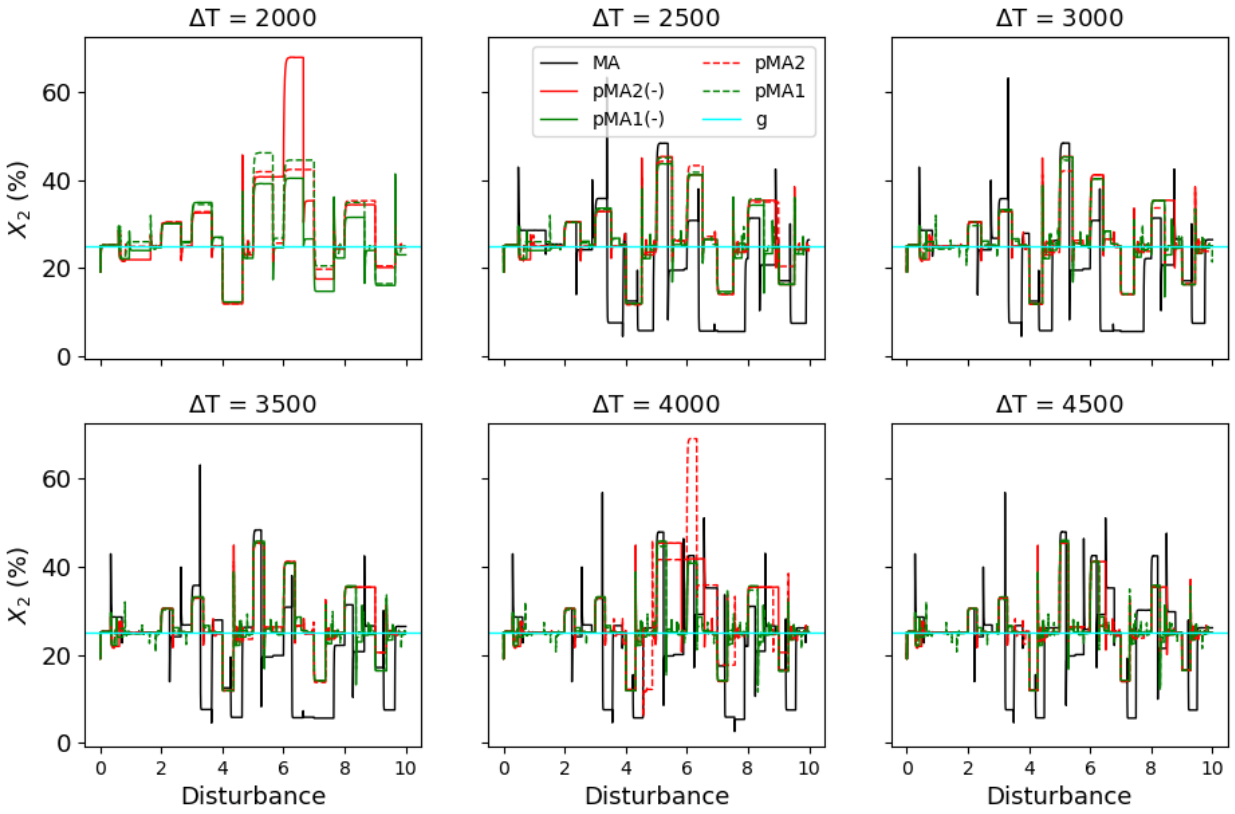

Figure D-1: Constraint trajectories for evaporator case, increasing disturbance periods.

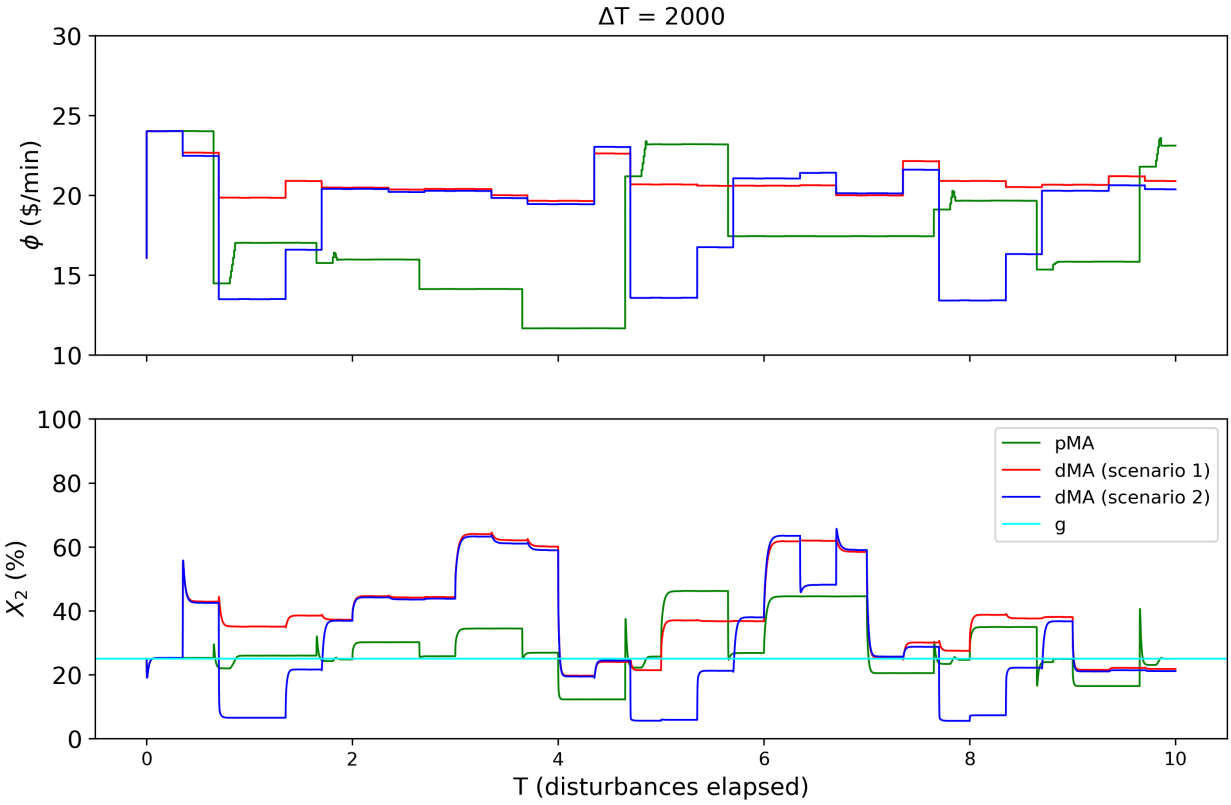

Figure D-2: Profit rate (top) and constraint (bottom) for the evaporator case study under pMA, dMA (scenario 1), and dMA (scenario 2).

Appendix E - Economic Model Predictive Control of a RAS System

Global consumption of seafood has undergone a fivefold increase over the past sixty years (FAO, 2022a). This has prompted advancements in seafood production as wild fisheries are unable to meet the surging demand because of stagnating wild fish populations. Accordingly, aquaculture, the process of human-reared farming of fish, has become an increasingly important means of production, comprising nearly half of worldwide fish capture in 2020 (FAO, 2022a).

Typically, RASs assume that the operational variables of the units outlined above are constant, including feed rates to the fish tank, solid removal fraction, ammonia conversion in the biological reactor, and oxygen flows to the aerators and fish tank. This continues for a fixed amount of time until the fish have reached maturity and are removed from the tank in a batch manner. After removal, the tank is refilled with juveniles, thus starting a new batch. Despite their benefits, RASs has been shown to be expensive as their controlled environment requires increased energy and resource (e.g., oxygen) use; thus, limiting their use to certain stages of the fish production cycle (e.g., hatcheries; D'Agaro *et al*., 2022). To this end, little attention has been paid as to how to optimize the economics of RAS systems in real time. Process systems engineering (PSE) provides systematized approach to generate optimal production strategies for chemical and biological processes. RASs can be modelled as batch processes whereby the products (fish) are processed (grown) for a finite amount of time until they are ready for harvesting. Moreover, RASs encompass the three interacting units outlined previously. In this context, PSE process control techniques have been applied to RASs (e.g., Dos Santos *et al*., 2022; Kamali *et al.,* 2023). The former study implemented an economic control scheme for RAS while the latter implemented a regulatory model predictive control scheme complemented with a state estimator. PSE practitioners have also employed model-based economic optimization approaches for various chemical and energy systems (e.g., Mendiola-Rodriguez and Ricardez-Sandoval, 2022). However, online economic optimization has only been deployed once in the RAS literature (Dos Santos *et al*., 2022). While this constituted a step forward in the PSE for RAS literature, fish growth was not included in the economic model and a simplified process model was used in the control scheme. Mechanistic process models deployed with an economic optimization approach can therefore provide valuable decisions that influence fish growth dynamics and balance sales profits with operational costs. To use PSE tools, many of which are model based, a RAS production model is necessary. Dynamic models of each of the key process units have been developed in the literature. Moreover, fish growth and mortality models are also available. Recently, Kamali *et al*. (2022) combined mechanistic process, fish growth, and fish mortality models to evaluate RAS performance under several disturbance scenarios.

Aquaculture has traditionally occurred in fenced or caged environments where fish and feed waste build-up occurs. The wastewater produced has prompted ecological and sustainability concerns owed to its disposal and resultant makeup water consumption. To allay these issues, the recirculating aquaculture system (RAS) has been proposed. The basic layout for RAS consists of three processes as depicted in Figure E-1: the fish tank, where fish are grown and fed, makeup water is introduced, and fresh oxygen is diffused; the solid removal, where wastewater from the fish tank is filtered to remove solid particles; and the biological reactors, where the water is aerated and dissolved waste is treated with microorganisms to maintain water quality for recycling into the fish tank. This RAS layout can significantly reduce water usage in fish rearing while maintaining fish population health.

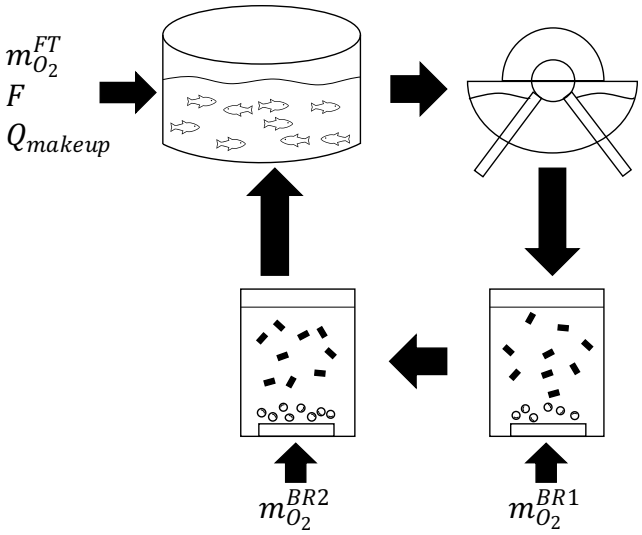

Figure E-1: RAS schematic. Clockwise from top left: fish tank, solid removal drum filter, biological reactors.

As per the literature reviewed above, a gap exists for a rigorous model-based economic optimization scheme applied to aquaculture that considers fish growth and mortality within its decision-making. As such, we propose the use of an economic model predictive control (EMPC) scheme for the operation of a RAS; the model developed by Kamali et al. (2022) will be the basis of the present work. The EMPC proposed uses a novel economic function, which is the first to account for fish sales, utility, and energy usage simultaneously. Another novelty in the current work is the determination of RAS batch length through profit-tracking.

This study is structured as follows: firstly, we outline the RAS model; secondly, we detail the EMPC formulation; thirdly, we test the proposed scheme across several scenarios; and, lastly, we highlight conclusions.

RAS Model

The dynamic mechanistic model presented by Kamali et al. (2022) was adapted for the present work. It consists of a fish tank (FT), two fixed-bed biofilters (FBB1, FBB2), two moving-bed bioreactors with aerators (BR1, BR2), and a drum filter; these units are shown in Figure E-1. The work herein assumes rainbow trout (*Oncorhynchus mykiss*) is being produced. The model was validated in Kamali et al. (2022) where it was found to be consistent with experimental RAS data from Fernandes et al. (2022). For brevity, only the most important features of the RAS model are outlined herein; more details about this model can be found in Kamali et al. (2022). The key assumptions made in developing the model are as follows:

1. The fish tanks are modelled as perfectly mixed reactors.
2. The solid removal is assumed to operate at steady state with constant efficiency.
3. The RAS model does not consider an energy balance; hence, temperature cannot be controlled and is treated as a disturbance.

As described in Kamali et al. (2022), the components being modelled in the system are: soluble inert organic matter (IOM), readily biodegradable substrate (BDS), particulate inert organic matter (POM), slowly biodegradable substrate (SBS), heterotrophic biomass (BH), ammonia oxidizing bacteria (AOB), nitrite oxidizing bacteria (NOB), particulate

products arising from biomass decay (PP), nitrite nitrogen (NO_2), nitrate nitrogen (NO_3), total ammonia nitrogen (NH), soluble biodegradable organic nitrogen (SND), particulate biodegradable organic nitrogen (PND) and alkaline components (ALK). These comprise the set of components I.

Fish Tank

As noted above, a tank to grow fish is one of the RAS units. The changes in fish weight over time are modelled as follows:

$$\frac{dW}{dt} = bF_{fish} - abF_{fish} - KW^n \quad \text{(E-1)}$$

where W(g) is the weight of a single fish and F_{fish}(g/day) is the daily food intake of each fish. a(g/g) is the fraction of food assimilated, b(g/g) is the efficiency of food assimilation, K(g/day) is the catabolism coefficient, and n is a weight/catabolism exponent. The size of fish population is modelled through the following mortality model:

$$\frac{dN}{dt} = -M_{ins}N \quad \text{(E-2)}$$

where N is the total number of fish in the tank and M_{ins}(s^{-1}) is the instantaneous mortality rate. In addition to fish growth and population, waste components build up in the fish tank such that the water becomes contaminated. The concentration of a given waste component in the fish tank is modelled as follows:

$$V_{FT}\frac{dZ_i}{dt} = Q_{FT}\left(Z_{i,in} - Z_i\right) + \omega_i - L_i \quad \text{(E-3)}$$

where Z_i and $Z_{i,in}$(kg/kg) are the bulk and inlet concentrations of components $i \in I$, respectively. V_{FT}(m^3) and $Q_{FT} = Q_{makeup} + Q_{recirculated}$($m^3$/day) are the fish tank volume and inlet flowrate, respectively. ω_i(kg/day) and L_i(kg/day) are the excretion and feed loss rates of components $i \in I$, respectively.

Waste Production and Solid Removal

Fish and feed waste constitute the total waste production in RAS. The waste dynamics are as follows:

$$\tau\frac{d\omega_i}{dt} = F\gamma_i(1 - \varepsilon_{loss}) - \omega_i \quad \text{(E-4)}$$

where τ (days) is the residence time of the fish digestive system, which is treated as a well-mixed reactor. F(kg/day) and ε_{loss} are the total system feeding rate and feed loss fraction, respectively. γ_i denotes the component-specific was fraction of $i \in I$. To remove the waste, a 40 μm drum filter is assumed to work at a 48% removal efficiency.

Biological Reactors

The biological reactors work to convert compounds that are toxic into inert compounds. They are modelled as follows:

$$V_j\frac{dS_i^j}{dt} = Q_j\left(S_{i,in}^j - S_i^j\right) + V_j r_i^j \quad \text{(E-5)}$$

where $j \in \{BR1, BR2\}$. S_i^j and $S_{i,in}^j$(g/m^3) are the bulk and inlet concentrations of components $i \in I$ in unit j, respectively. V_j(m^3) and Q_j(m^3/day) are the bioreactor volume and inlet flowrate, respectively, $r_i{}^j$(g/m^3-day) is the reaction rate of component $i \in I$.

Aeration and Oxygen Addition

As show in Figure E-1, aeration occurs in the two BRs. Additionally, pure oxygen is introduced in the FT to supplement the aeration. Both these processes assist in reoxygenation and remove carbon dioxide from the system. Accordingly, the oxygen and carbon dioxide concentrations in units $j \in \{FT, BR1, BR2\}$ are modelled as follows:

$$V_j \frac{dS_{O_2}^j}{dt} = Q_j\left(S_{O_2,in}^j - S_{O_2}^j\right) - r_{O_2}^j + m_{O_2}^j \tag{E-6}$$

$$V_j \frac{dS_{CO_2}^j}{dt} = Q_j\left(S_{CO_2,in}^j - S_{CO_2}^j\right) + r_{CO_2}^j - m_{CO_2}^j \tag{E-7}$$

where $S_{O_2}^j$(kg/m^3), $S_{O_2,in}^j$(kg/m^3), $r_{O_2}^j$(kg/day), and $m_{O_2}^j$(kg/day) are the bulk concentration, inlet concentration, oxygen consumption rate, and fresh flowrate of oxygen, respectively, in unit j. Moreover, $S_{CO_2}^j$(kg/m^3), $S_{CO_2,in}^j$(kg/m^3), $r_{CO_2}^j$(kg/day), and $m_{CO_2}^j$(kg/day) are the bulk concentration, inlet concentration, carbon dioxide production rate, and removal flowrate of carbon dioxide, respectively. The carbon dioxide is removed as the water becomes increasingly aerated.

Model Parameters and Implementation

The dynamic model presented in equations (E-1)–(E-7) is denoted henceforth as $\boldsymbol{f}$. The complete RAS model consists of 63 states. Model parameters and algebraic equations are outlined in Table E-1; the latter are part of $\boldsymbol{f}$ but were not detailed for brevity and can be found in Kamali et al. (2022). The inputs to each algebraic variable are also stated in Table E-1. Moreover, the temperature dependence, which is crucial to the present study, occurs in these algebraic variables (e.g., $r_{CO_2}^j$ is a function of temperature T (°C) and fish weight W).

For the RAS control system proposed herein, the manipulated variables available for control are $\boldsymbol{u} = [F \quad Q_{makeup} \quad m_{O_2}^{FT} \quad m_{O_2}^{BR1} \quad m_{O_2}^{BR2}]^{\boldsymbol{T}}$; these are the feeding rate, water makeup rate, oxygen diffusion rate, and aeration rates, which are outlined with their corresponding unit in Figure E-1. The oxygen addition manipulated variables correspond to the $m_{O_2}^j$ value for their respective unit in (E-6). While feed and oxygenation rates affect fish health directly through metabolism and respiration, water makeup impacts water quality. The sampling interval of the RAS is $\Delta t = 0.1$ days. The time-discretized dynamic optimization problem solved for the EMPC proposed in this work constitutes 6,569 variables and 6,519 constraints when discretized using the backward finite difference method. For a single sampling interval, the EMPC problem is solved in an average of 245 seconds; as the computational time is much less than the sampling interval, the control scheme is implementable. Note that the current work assumes full state accessibility (i.e., all feedback states are measurable).

Table E-1: Model parameters and algebraic variables; $\boldsymbol{f}(\cdot)$ denotes variable dependencies

	Description	Value
a	Fraction of food assimilated (g/g)	0.4
n	Body weight exponent	0.81
V_{FT}	FT volume (m^3)	5.5
V_{BR1}, V_{BR2}	BR volume (m^3)	0.4
ε_{loss}	Feed loss fraction	0.05
τ	Feed residence time (days)	0.211
b	Efficiency of food assimilation	$f(W)$
F_{fish}	Daily food intake of one fish	$f(F,T,W)$
K	Catabolism coefficient	$f(T)$
L_i	Component waste fraction	$f(F)$
M_{ins}	Instantaneous mortality rate (s^{-1})	$f(W)$
$r_{CO_2}^j$	CO_2 reaction rate (kg/day)	$f(T,W)$
r_i^j	BR reaction rates (g/m^3-day)	$f(S_i^j)$
$r_{O_2}^j$	O_2 reaction rate (kg/day)	$f(T,W)$
γ_i	Waste fraction of component i	$f(i)$

EMPC Formulation and Deployment

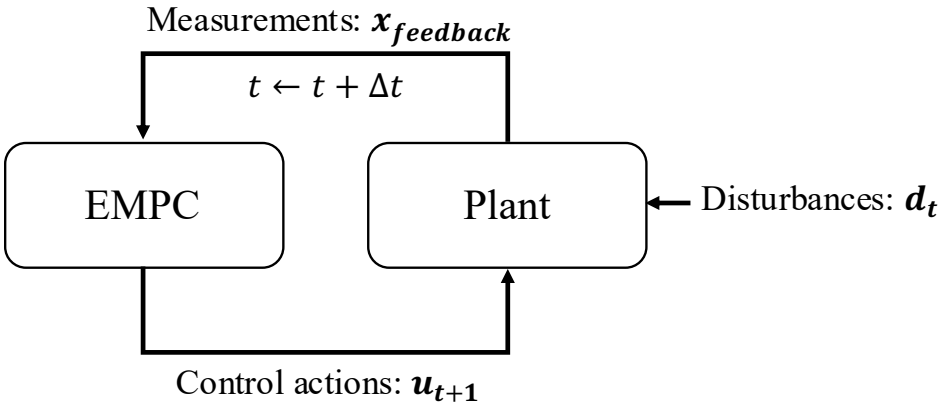

Figure E-2: EMPC exchange of information with plant.

Model predictive control (MPC) is a commonly used method to regulate the operation of variables in closed-loop process systems subject to feasibility constraints. MPC takes the form of an optimization problem that is solved at each sampling instant (Δt). This problem employs a process model to predict future process behaviour and obtain optimal plant control actions to correct for future set point deviations. The MPC formulation is solved at every

sampling interval, whereby the process model is updated via its initial conditions and the optimal control problem is re-solved with the updated state.

EMPC is a variant of MPC that retains the internal predictive model but foregoes set point target tracking for an economic objective (Ellis et al., 2014). EMPC is often implemented as depicted in Figure E-2 wherein it receives measurements (or state estimates) as initial conditions to solve a dynamic optimization problem. The EMPC supplies the plant with manipulated variables, thus regulating plant behaviour towards the achievement of an optimal economy. Note that the EMPC does not use a constant set point like the traditional MPC scheme; rather, its control actions are inherently economical and need not be at steady state (Ellis et al., 2014). The EMPC is solved at every sampling interval Δt such that it constantly obtains feedback from the plant and predicts further into the future, thus making the scheme closed loop. In the present study, the EMPC problem at time t is formulated as follows:

$$
\begin{aligned}
&\max_{\boldsymbol{u_{t+i}} \forall i \in \{1,\dots,P\}} \phi(\boldsymbol{x_{t+i}}, \boldsymbol{u_{t+i}}) - \sum_{i=1}^{C} \|\Delta \boldsymbol{u_{t+i}}\|_{\boldsymbol{K}}^2 \\
&\boldsymbol{f}(\boldsymbol{x_{t+i}}, \boldsymbol{u_{t+i}}, \boldsymbol{\theta}) = \boldsymbol{x_{t+i+1}} && i \in \{0, \dots, C-1\} \\
&\boldsymbol{x_t} = \boldsymbol{x_{feedback}} \\
&\boldsymbol{g}(\boldsymbol{x_{t+i}}, \boldsymbol{u_{t+i}}) \leq \boldsymbol{0} && i \in \{0, \dots, C\} \\
&\boldsymbol{u^l} \leq \boldsymbol{u_{t+i}} \leq \boldsymbol{u^h} && i \in \{0, \dots, C\}
\end{aligned}
\tag{E-8}
$$

where $\boldsymbol{x} \in \mathbb{R}^x$ and $\boldsymbol{u} \in \mathbb{R}^u$ denote the process states and manipulated variables, respectively. Moreover, $\boldsymbol{\theta} \in \mathbb{R}^\theta$ denotes the time-invariant model parameters (i.e., in Table E-1). $\phi: \mathbb{R}^x \times \mathbb{R}^u \to \mathbb{R}$ denotes the economic objective function, which generates economic prediction given the predicted states and manipulated variables. $\boldsymbol{f}: \mathbb{R}^x \times \mathbb{R}^u \times \mathbb{R}^\theta \to \mathbb{R}^x$ denotes the process model, which maps the states and manipulated variables to the future states on the horizon C. $\boldsymbol{u^l}$ and $\boldsymbol{u^h} \in \mathbb{R}^u$ denote the lower and upper bounds, respectively, for the manipulated variables, which define the search space for the optimization problem. $\boldsymbol{g}: \mathbb{R}^x \times \mathbb{R}^u \to \mathbb{R}^g$ denotes the process constrains that must be satisfied by the EMPC solution. $\boldsymbol{x_{feedback}} \in \mathbb{R}^x$ denotes the state measurements (or estimates), which serve as initial conditions to the dynamic optimization problem. The RAS model $\boldsymbol{f}$ is discretized using backward finite differences with a resolution 0.1 days. The control and prediction horizons are equivalent at 5 days (i.e., $C = 50$); this was based on Kamali et al. (2022).

In addition to the economic objective ϕ, the EMPC formulation (E-8) minimizes the rate of change of the manipulated variables (i.e., $\Delta \boldsymbol{u_t} = \boldsymbol{u_t} - \boldsymbol{u_{t-1}}$) in the objective function such that aggressive control actions are penalized. The weighing matrix ($\boldsymbol{K}$) for this term ensures that the dynamics in the manipulated variables are balanced with the economic objective. The tuning matrix for the present RAS system $\boldsymbol{K} = diag(1e^{-2} \quad 1e^{-2} \quad 1e^{-3} \quad 1e^{-3} \quad 1e^{-3})$ was determined using preliminary tuning simulations whereby each term was adjusted individually to yield smooth control actions; each element in this matrix corresponds to a manipulated variable in the vector $\boldsymbol{u}$ defined in Section 8.1.5. The bounds on the manipulated variables imposed on (E-8) provide the feasible region for the EMPC dynamic optimization problem. These bounds are adapted from Kamali et al. (2022) and are as follows:

$$
\begin{aligned}
&0 \leq F(g/day) \leq 3 \\
&0 \leq Q_{makeup}(m^3/day) \leq 3
\end{aligned}
\tag{E-9}
$$

$$0 \leq m_{O_2}^{j}(kg/day) \leq 1$$

The economic function in (E-8) is posed as a profit maximization problem in this work. It is formulated as follows:

$$\phi = \phi_\pi - \phi_\chi \tag{E-10}$$

where ϕ_π and ϕ_χ are the profit and cost elements of the process economics, respectively. For the present RAS system, the profit is directly related to fish production; accordingly:

$$\phi_\pi = P_{fish} W_{t+C} N_{t+C} \tag{E-11}$$

where P_{fish}(\$/g) is the wholesale price of the fish being produced (rainbow trout in the present study). The total live fish mass in the RAS system at the end of the horizon $W_{t+C}N_{t+C}$(kg) is maximized. The endpoint (i.e., final) fish mass at time C is considered as the fish only become products at the end of the batch. The cost element of the economic function is as follows:

$$\phi_\chi = \Delta t \sum_{i=0}^{C} \left(P_f F_{t+i} + P_{O_2} m_{O_2,t+\mathrm{i}}^{FT} + \sum_{k \in E} P_e D_{k,t+i} \right) \tag{E-12}$$

where P_f(\$/g), P_{O_2}(\$/g), and P_e(\$/kWh) denote the feed, oxygen, and electrical prices, respectively. Only oxygen input into the FT is accounted for in the cost function as the BRs receive their oxygen via aeration. $D_{k,t+i}$ denotes the energy duties for $k \in E$ where E is the set of all energy-consuming units (i.e., water pumping, water treatment, aeration, feed distribution, fish handling, fuel, and gas; D'Orbcastel et al., 2009). These utilities and energy are consumed throughout the RAS process in contrast to the fish, which are only capitalized on at the end of each batch. Accordingly, the path summation (as opposed to the endpoint) is considered in the objective function and minimized accordingly. The prices considered in this study are listed in Table E-2.

Table E-2: RAS prices.

Term	Price	Source
P_{fish}	7.35 \$/kg fish	FAO (2022b)
P_f	1550 \$/tn feed	D'Agaro (2022)
P_{O_2}	40 \$/tn oxygen	Dorris et al. (2016)
P_e	0.20 \$/kg fish	D'Orbcastel et al. (2009)

Despite the RAS system being a batch process, it is subject to disturbances and has a long batch length (i.e., in the orders of months); as such, an online method such as EMPC is best suited over formulating a single optimal control problem that considers the complete batch length. However, this implementation does not allow for the batch length to be considered explicitly as a decision variable. Instead, batch length is determined by tracking the cost over the time elapsed (i.e., $R = \phi_\pi(T) - \int_0^T \phi_\chi(t)\, dt$). R is expected to increase initially as fish are quickly growing from juveniles provided that the fish remain in an acceptable environment for growth during the entire batch operation. Subsequently, as fish growth slows down, the profit stagnates as a case of diminishing returns begin to occur. Eventually, the profit will reach a maximum where the production costs (i.e., oxygen, feed, energy) begin to dominate;

and R begins to decrease. The time at which the maximum occurs is therefore chosen as the batch length (t_{batch}) of the RAS process.

Results

Five test scenarios involving the RAS system presented in Section 8.1 are considered in the present study. All scenarios begin by operating the RAS system at their constant nominal manipulated variables, i.e., $\boldsymbol{u_{nom}} = [2 \quad 3 \quad 0.2 \quad 0.4 \quad 0.4]^{\boldsymbol{T}}$ corresponding to $\boldsymbol{u}$. This constant operation is maintained for fifteen sampling intervals (i.e., 1.5 days). The EMPC, tasked with determining the optimal trajectory in the manipulated variables ($\boldsymbol{u}$), is deployed for three constant temperature scenarios at 10°C (scenario 1), 15°C (scenario 2), and 20°C (scenario 3). These temperatures are chosen based on the RAS operating range from Kamali et al. (2022). Moreover, scenario 4 involves an initial RAS operation at 20°C followed by a temperature step disturbance to 15°C at $t = 80$ days. This mid-batch disturbance is imposed such that the EMPC can adjust its operating policy on-line; such a disturbance could occur owing to seasonal ambient temperature changes. Seasonal changes are considered instead of diurnal changes as small daily fluctuations will negate over the timespans simulated herein. Lastly, scenario 5 maintains all manipulated variables at their nominal values until a cost profit maximum is observed. The key process variable and manipulated variable trajectories are displayed in Figure E-3 and Figure E-4, respectively; Table E-3 provides a summary of results. Firstly, it should be noted that scenario 1 is not productive. As shown in Figure E-3a and Figure E-3b, respectively, the fish decrease in weight and the highest population decline is observed. This is because the 10°C temperature is too cold for RAS operation as was noted in Kamali et al. (2022). Nevertheless, the EMPC acts to mitigate losses by imposing low feed conditions (Figure E-4a) and low oxygen diffusion (Figure E-4c) ; the former two settle at non-zero values to slow fish mortality. As this is a poor environment for fish growth, the maximum profit is achieved at the beginning of the batch (Figure E-3c). Accordingly, it is best not to operate the RAS in these conditions as it can only negatively impact the health and growth of the fish population. In this scenario, the batch length is effectively zero and the profit correspond to the sales cost of the juveniles (Table E-3).

Table E-3: Final batch results.

Scenario	Temperature	t_{batch} (days)	R ($)
1	10°C	0	740.18
2	15°C	92.1	958.61
3	20°C	83.4	905.41
4	20 → 15°C	101.2	912.83
5	20°C ($\boldsymbol{u_{nom}}$)	4.9	748.98

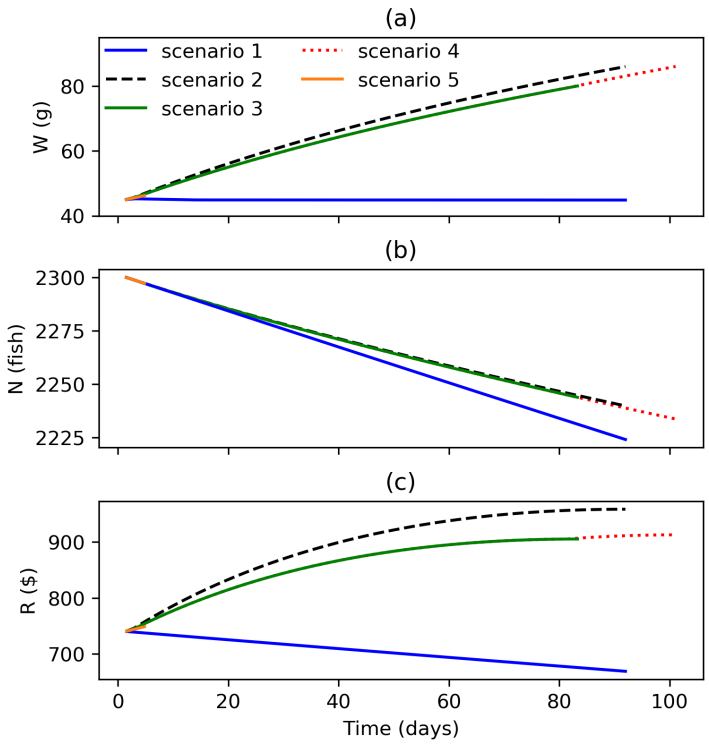

Figure E-3: Key process variable trajectories for scenarios tested.

In contrast to scenario 1, scenarios 2 and 3 result in acceptable environments for fish growth. Both scenarios have maximum feeding (Figure E-4a) and maximum water makeup (Figure E-4b) to encourage fish growth. Moreover, the oxygen diffusion in both scenarios (Figure E-4c) increases as the batch continues; this is to supplement the maximum aeration to the biological reactors (Figure E-4d. and e.) such that the oxygen requirements of increasingly large fish (Figure E-3a) are met. In a typical RAS operation, oxygen diffusion would be kept constant; thus, time-varying diffusion as shown herein has not been previously considered. Despite the similarities in scenarios 2 and 3, it is apparent that the former is a better environment for fish growth. With similar fish mortality rates (Figure E-3b), scenario 2 can result in ~6% higher final batch profit over scenario 3 with only an additional 8.7 days of batch length

(Table E-3, Figure E-3c). With respect to the starting price, scenarios 2 and 3 represent substantial valorisation in the fish, ~30.5% and ~22.3%, respectively; thus, justifying the RAS operation.

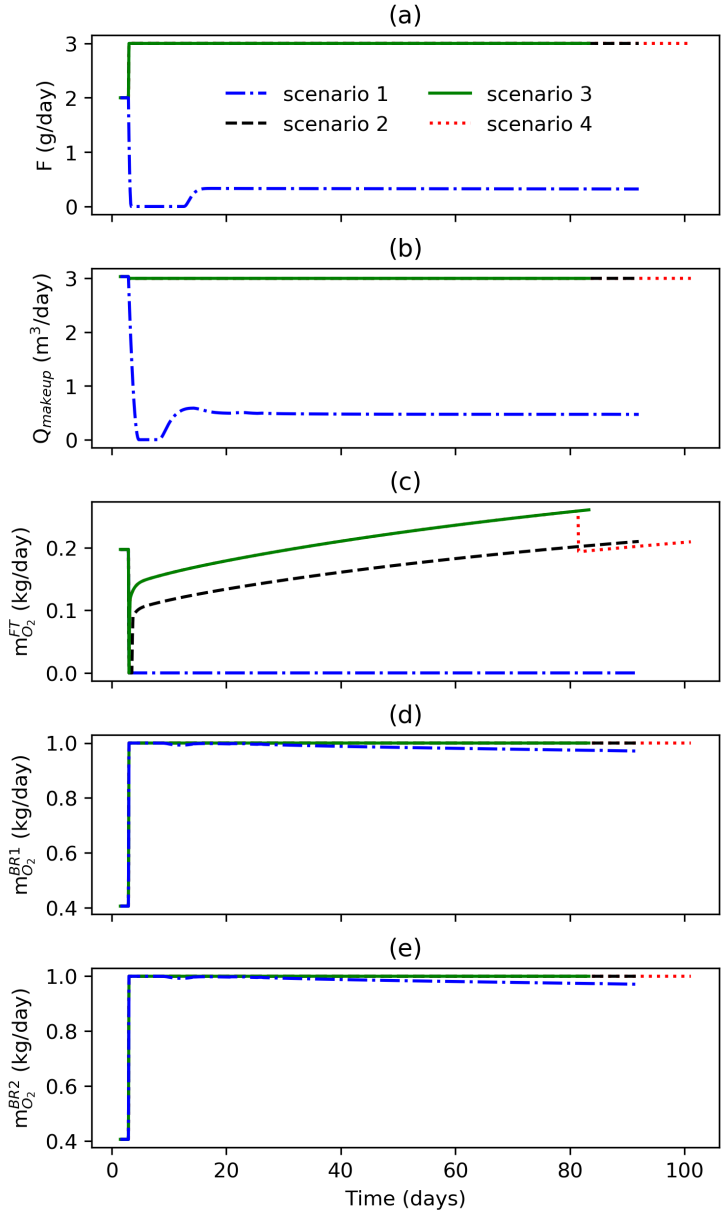

Figure E-4: Manipulated variable trajectories for scenarios tested.

Scenario 4 begins via the trajectories of scenario 3 until the occurrence of the temperature disturbance. At this point, the oxygen diffusion (Figure E-4c) is decreased below the level of scenario 2. The disturbance also causes the batch to be operated for a prolonged length of time as the profit (Figure E-3c) undergoes an upward inflection such that its maximum is delayed. As a result, the batch length of the scenario 4 (Table E-3) is longer that those of the constant temperature scenarios while only achieving small (~0.8%) improvements and large deterioration (~4.8%) with respect to the scenarios 3 and 2, respectively. Accordingly, it can be concluded that the temperature for RAS is best kept constant with tight control if possible. Finally, scenario 5 presents a counterfactual to scenario 3 in which the manipulated variables are kept constant at their nominal values as is typically done. As shown in Table E-3 and Figure

E-3 (omitted from Figure E-4 for simplicity); this results in only slight valorisation of the fish. Thus, the RAS is only profitable for 4.9 days before utility costs begin to dominate, after which continuing operation is not economically advantageous.

Summary

The present study proposes an EMPC scheme for RAS, which considers fish production profits as well as utility costs. The EMPC was applied to various scenarios and was always found to make economic decisions even in the case where conditions were not suited for fish growth. In suitable conditions, the EMPC was able to significantly increase fish profit through weight increase and low mortality rates while minimizing utility usage. In general, fish weights were only increased to ~80 g, which is too small for wholesale. This aligns with the current main use of RAS in the early fish life cycle (D'Agaro *et al*., 2022), whereby fish are graded by size and moved to traditional aquaculture environments to minimize cost.

As shown in Kamali et al. (2020), the RAS model contains uncertainties such that it does not fully match experimental data. As such, an approach to address uncertainty in the EMPC proposed herein is necessary. It is suggested that a batch-to-batch implementation of MA is used for this system and compared to a dynamic parameter estimation procedure. Future works will also incorporate a dynamic energy balance within the current RAS model; accordingly, dynamic temperature control can be potentially implemented and further enhance the economics of this system. Other disturbance scenarios should also be considered for the present EMPC (e.g., aerator failure). Moreover, the relationship batch length and fish growth should be analysed in a multi-batch context such that the trade-off between resuming an old batch and beginning new batch can be understood. The simultaneous selection of design and control decisions (e.g., Rafiei and Ricardez-Sandoval, 2020) for RAS should also be explored as a potential avenue to improve regulatory and economic performance. Finally, the current work is limited to rainbow trout and can be applied to any aquaculture-reared fish.